



University of Pennsylvania
ScholarlyCommons


Publicly Accessible Penn Dissertations

2021

Biofabrication Approaches With Hyaluronic Acid Hydrogels For Cartilage Repair

Jonathan H. Galarraga
University of Pennsylvania

Follow this and additional works at: <https://repository.upenn.edu/edissertations>

 Part of the [Biomedical Commons](#), and the [Mechanics of Materials Commons](#)

Recommended Citation

Galarraga, Jonathan H., "Biofabrication Approaches With Hyaluronic Acid Hydrogels For Cartilage Repair" (2021). *Publicly Accessible Penn Dissertations*. 5481.
<https://repository.upenn.edu/edissertations/5481>

This paper is posted at ScholarlyCommons. <https://repository.upenn.edu/edissertations/5481>
For more information, please contact repository@pobox.upenn.edu.

Biofabrication Approaches With Hyaluronic Acid Hydrogels For Cartilage Repair

Abstract

Current therapies to repair damaged articular cartilage fail to consistently or fully restore the biomechanical function of cartilage. Although cell-based clinical techniques have emerged for the treatment of focal defects in articulating joints, these approaches typically lead to inferior tissue formation when compared to native, healthy cartilage. Alternatively, subchondral microfracture is a surgical procedure that aims to recruit endogenous mesenchymal stromal cells (MSCs) from the underlying bone marrow to facilitate neocartilage formation in focal defects. Similarly, microfracture typically results in the formation of repair cartilage incapable of withstanding the loading environment of the articulating joint over time. New biomaterial-based strategies are therefore in significant demand to improve cartilage tissue formation and maturation within focal defects.

Hyaluronic acid (HA) is a glycosaminoglycan that is found in native cartilage and that shows promise as a biomaterial for cartilage tissue engineering due to its innate bioactivity and ability to form hydrogels, water-swollen polymer networks that may be engineered to mimic the native extracellular matrix (ECM). Moreover, hydrogels may be employed as materials for biofabrication, which involves the use of automated additive manufacturing processes such as 3D printing to fabricate living, biological constructs.

This dissertation describes the design and implementation of HA hydrogels for the biofabrication of articular cartilage towards improving existing therapies for damaged cartilage. Multiple biofabrication approaches, including extrusion bioprinting, melt-electrowriting, and digital light processing are investigated to engineer scaffolds with rationally designed geometries, mechanical properties, porosities, and biodegradability. Conserved across all these approaches is the use of thiol-ene based photochemistry to control the formation and resultant material properties of HA hydrogels modified with norbornene functional groups. Taken together, the employment of these biofabrication approaches for cartilage repair has significantly informed the design and implementation of future therapies for articular cartilage damage.

Degree Type

Dissertation

Degree Name

Doctor of Philosophy (PhD)

Graduate Group

Bioengineering

First Advisor

Jason A. Burdick

Keywords

Biofabrication, Bioprinting, Cartilage, Hyaluronic Acid, Hydrogel, Tissue Engineering

Subject Categories

Biomedical | Mechanics of Materials

**BIOFABRICATION APPROACHES WITH HYALURONIC ACID HYDROGELS FOR
CARTILAGE REPAIR**

Jonathan H. Galarraga

A DISSERTATION

in

Bioengineering

Presented to the Faculties of the University of Pennsylvania

in

Partial Fulfillment of the Requirements for the

Degree of Doctor of Philosophy

2021

Supervisor of Dissertation

Jason A. Burdick, Ph.D., Robert D. Bent Professor of Bioengineering

Graduate Group Chairperson

Yale Cohen, Ph.D., Professor of Bioengineering

Dissertation Committee

Robert L. Mauck, Ph.D., Professor of Orthopaedic Surgery

James Carey, M.D., MPH, Associate Professor of Orthopaedic Surgery

Kacy Cullen, Ph.D., Associate Professor of Neurosurgery

ACKNOWLEDGMENTS

This dissertation work would not have been possible without the help of many people. First and foremost, I'd like to thank my advisor Prof. Jason Burdick and my thesis committee members, Prof. Robert Mauck, Prof. James Carey, and Prof. Kacy Cullen, for all your guidance and support. I greatly appreciate all the insights you have shared with me over the years,

Working with Prof. Burdick has been one of the greatest distinctions of my career, and I will be forever grateful for the mentorship he has offered towards my development as a researcher and an engineer. Moreover, I'd like to express my gratitude for the opportunity he gave me to live out my dream of performing impactful research and helping people in need. Because of Prof. Burdick, I have also met some of the most amazing people. The Burdick Lab is home to some of the most brilliant and talented people that I have ever met. I would like to thank everyone from the lab who ever challenged me to strive for excellence.

The words of encouragement and support that I received from the post-doctorate fellows truly empowered me throughout my time in the lab. I am forever grateful for the time I shared with Kwang Hoon Song, Sebastian Vega, Yi-Cheun Yeh, Adrienne Rosales, Katrina Wisdom, Mikyung Shin, Brendan Purcell, Taimoor Qazi, and Claire Witherel. I would like to especially thank Christopher Highley for instilling in me an appreciation for the culture and all the hard work that preceded my time in the lab, and for sparking my curiosity in the possibilities of biofabrication. I also thank Matthew Davidson and Andrew Daly for the many discussions we shared, which allowed me to confidently explore new ideas and opportunities throughout my dissertation. Finally, I'd like to thank Claudia Loebel for all her mentorship and for the example she set for myself and others in the lab to follow as the consummate lab member.

Of course, this work would not have been possible without my fellow PhD students either. Thank you to Leo Wang, Minna Chen, Mi Kwon, and Joshua Mealy for helping me find my way in lab as I grew through the beginning of this dissertation work. I would also like to thank Selen Uman, Victoria Muir, Margaret Prendergast, Abhishek Dhand, Niko Di Caprio, and Karen Xu, as each of you always knew how to make me smile and made working in the lab truly a joy. It was an honor to work with all of you.

I would like to thank the Master's students and visiting PhD students that also helped to make the lab a joyful place to always work. Thank you to Andrew Rouff, Mu-Huan Lee, James Howard, Liliang Ouyang, Sara Trujillo-Munoz, Bárbara Mendes, Gabe Mickel, Karyll Davis, and Tianbi Duan. I enjoyed the opportunity to work with several undergraduate students during my graduate studies, and I thank them for always bringing enthusiasm to our group. I was especially fortunate to work closely with two talented undergraduates, Claude King III and Bruce Enzmann, who helped me grow both as a mentor and as a person. I thank you both for your trust in me and for the time and effort you concerted towards the work we did together.

Much of the work described throughout this dissertation would not have been possible without the efforts and help of our great collaborators. Thank you to the Mauck lab for always welcoming me into your community. I would especially like to thank Hannah Zlotnick and the amazing team of researchers and surgeons that I was privileged to work with. Thank you to Ryan Locke, Brendan Stoeckl, Sachin Gupta, Natalie Fogarty, Kendall Masada, Jay Patel, Sarah Gullbrand, Matthew Fainor and Sanjana Hemdev. I would also like to thank Brian Cosgrove and Sonia Bansal for all your support over the years.

One of the highlights of my graduate studies was meeting and collaborating with colleagues from across the world. I will be forever grateful for the time I spent visiting

with the Malda and Levato labs at Utrecht University, and I would like to thank Prof. Riccardo Levato, Prof. Miguel Castilho, Prof. Jos Malda, Quentin Peiffer, and Cody Fell for all your help with the development of our composite system. I would also like to thank Prof. Khoon Lim and Prof. Tim Woodfield from the University of Otago, as it was a pleasure to work together on informing the biofabrication community on innovations in light-based bioprinting. I am also extremely thankful for the helpful discussions I shared with Ghodsiehsadat Jahanmir and Prof. Ying Chau on modeling the hydrolysis of degradable DLP resins.

While I learned a great deal from my lab mates and colleagues, I was fortunate to also learn and grow alongside amazing friends. Thank you to Rhea Chitalia, Divya Jain, Joey Newton, Zakary Beach, Sadhana Ravikhumar, Fabiana Zappala, Nickolas Perkons, Sonia Kartha, Christopher Kegelman, Bhavin Gala, and Katie Rose. I would like to especially thank Ryan Leiphart, Andrei Georgescu, Eric Dai, Benjamin Carberry, and Talon Curtis. Each of you regularly inspire me, and I would not have completed this dissertation without your unwavering encouragement.

I would like to thank all the past professors, mentors, and coaches that helped me become the person I am today, making this dissertation work a possibility. To this end, I would like to especially thank Prof. Christopher Kloxin at the University of Delaware, who once took a risk by allowing a wide-eyed, naïve freshman to perform undergraduate research in his lab. Thank you for helping me discover my passion and love for research. I would also like to thank Prof. Ray Peters, who taught me the value in considering how the research we perform brings value and change to our community.

Finally, I'd like to thank my family for their constant love and support. I thank my abuelos, my tios, and the generations that preceded them, as this dissertation would not have been possible without their many sacrifices. Thank you to my sisters, Jennifer,

Jessica, and Jess, who always helped show me the importance of chasing your dreams and abiding by your values. Thank you to all my parents, especially my Mom, Lillian, and my Dad, Humberto, for treating me not as the man I am, but rather the man I aspire to be. Because of you, I have learned to find fulfillment and purpose in life's greatest challenges. Finally, I thank my nieces Sofia, Ellie, and Isabella, and my nephew Milan. Simply put, you all mean the world to me, and I hope this work shows that if you commit yourself wholeheartedly to your dreams, anything is possible.

“There is nothing noble in being superior to your fellow man; true nobility is being superior to your former self.” – Ernest Hemingway

ABSTRACT

**BIOFABRICATION APPROACHES WITH HYALURONIC ACID HYDROGELS FOR
CARTILAGE REPAIR**

Jonathan H. Galarraga

Jason A. Burdick

Current therapies to repair damaged articular cartilage fail to consistently or fully restore the biomechanical function of cartilage. Although cell-based clinical techniques have emerged for the treatment of focal defects in articulating joints, these approaches typically lead to inferior tissue formation when compared to native, healthy cartilage. Alternatively, subchondral microfracture is a surgical procedure that aims to recruit endogenous mesenchymal stromal cells (MSCs) from the underlying bone marrow to facilitate neocartilage formation in focal defects. Similarly, microfracture typically results in the formation of repair cartilage incapable of withstanding the loading environment of the articulating joint over time. New biomaterial-based strategies are therefore in significant demand to improve cartilage tissue formation and maturation within focal defects.

Hyaluronic acid (HA) is a glycosaminoglycan that is found in native cartilage and that shows promise as a biomaterial for cartilage tissue engineering due to its innate bioactivity and ability to form hydrogels, water-swollen polymer networks that may be engineered to mimic the native extracellular matrix (ECM). Moreover, hydrogels may be employed as materials for biofabrication, which involves the use of automated additive manufacturing processes such as 3D printing to fabricate living, biological constructs.

This dissertation describes the design and implementation of HA hydrogels for the biofabrication of articular cartilage towards improving existing therapies for damaged cartilage. Multiple biofabrication approaches, including extrusion bioprinting, melt-electrowriting, and digital light processing are investigated to engineer scaffolds with rationally designed geometries, mechanical properties, porosities, and biodegradability. Conserved across all these approaches is the use of thiol-ene based photochemistry to control the formation and resultant material properties of HA hydrogels modified with norbornene functional groups. Taken together, the employment of these biofabrication approaches for cartilage repair has significantly informed the design and implementation of future therapies for articular cartilage damage.

TABLE OF CONTENTS

ACKNOWLEDGMENTS.....	II
ABSTRACT.....	VI
LIST OF TABLES	XII
LIST OF FIGURES.....	XIII
CHAPTER 1: INTRODUCTION.....	1
1.1. THE BURDEN OF CARTILAGE DAMAGE AND INJURY	1
1.2 DESIGN OF HYDROGELS FOR CARTILAGE TISSUE ENGINEERING	4
1.3 STATE OF THE ART IN BIOFABRICATION FOR CARTILAGE REPAIR	5
1.3.1 Extrusion-Based Bioprinting and Biofabrication.....	6
1.3.1.1 Bioink Design and Implementation	6
1.3.1.2 Multi-Material Extrusion-Based Printing.....	12
1.3.2 Incorporation of Fibrous Materials into 3D Printing.....	16
1.3.3 Inkjet Bioprinting and Biofabrication.....	20
1.3.4 Lithography-Based Bioprinting and Biofabrication	21
1.3.5 Scaffold-Free Biofabrication and Bioassembly	26
1.3.6 Biofabrication for Osteochondral Tissue Engineering	30
1.4 CONCLUSIONS.....	34
1.5 REFERENCES.....	36
CHAPTER 2: RESEARCH OVERVIEW	50
2.1 SPECIFIC AIMS.....	50
2.2 CHAPTER OUTLINE	55
2.3 REFERENCES.....	57
CHAPTER 3: FUNDAMENTALS OF PHOTOCROSSLINKING IN BIOPRINTING	60
3.1 INTRODUCTION.....	60
3.2 OVERVIEW OF PHOTOCROSSLINKING REACTIONS.....	62
3.2.1 Free-Radical Chain Polymerization	63

3.2.2	Thiol-ene Photocrosslinking.....	67
3.2.3	Photo-mediated Redox Crosslinking.....	72
3.3	LIGHT-BASED BIOPRINTING METHODS.....	74
3.3.1	Extrusion-Based Bioprinting.....	75
3.3.1.1	Traditional Fabrication Window.....	75
3.3.1.2	Rheological Additives and Sacrificial Materials.....	77
3.3.1.3	Embedded Printing and Granular Media.....	80
3.3.1.4	In Situ Crosslinking Technique.....	82
3.3.2	Lithography-Based Bioprinting.....	83
3.3.2.1	Engineering Printability in Lithographic Techniques.....	83
3.3.2.2	Computed Axial Lithography Bioprinting.....	88
3.3.2.3	Other Lithographic-Based Printing Techniques.....	89
3.4	OVERVIEW OF MATERIALS IN LIGHT-BASED BIOPRINTING.....	91
3.4.1	Reactive Polymers used for Photocrosslinkable Bioinks and Bioresins.....	91
3.4.1.1	Natural Materials.....	94
3.4.1.2	Synthetic Materials.....	97
3.4.2	Photoinitiators and light sources used for bioinks and bioresins.....	98
3.4.2.1	Free-Radical Photoinitiators.....	99
3.4.2.2	Light Sources used for Bioprinting and Light Attenuation.....	106
3.5	CELLULAR CONSIDERATIONS IN LIGHT-BASED BIOPRINTING.....	107
3.5.1	Shear forces.....	108
3.5.2	Photoirradiation conditions.....	109
3.5.3	Cell Settling.....	111
3.6	CONCLUSIONS.....	112
3.7	REFERENCES.....	116
 CHAPTER 4: 3D BIOPRINTING VIA AN IN SITU CROSSLINKING TECHNIQUE TOWARDS ENGINEERING CARTILAGE.....		131
4.1	INTRODUCTION.....	131
4.2	METHODS.....	135
4.2.1	Materials.....	135
4.2.2	NorHA Synthesis and Characterization.....	135
4.2.3	Hydrogel Formation and Rheological Characterization.....	136
4.2.4	3D Printing of NorHA.....	137
4.2.5	Cell Encapsulation and Viability.....	138
4.2.6	Gene Expression Analysis.....	139
4.2.7	Construct Mechanical and Biochemical Characterization.....	139
4.2.8	Construct Histological Characterization.....	140
4.2.9	Statistical Analysis.....	140
4.3	RESULTS AND DISCUSSION.....	141
4.3.1	Design of <i>In Situ</i> Crosslinking Approach Based on Bioink Formulation.....	141
4.3.2	Photorheology to Identify Permissible Printing Regimes.....	144
4.3.3	<i>In Situ</i> Crosslinking of NorHA Bioink for MSC Encapsulation.....	150
4.3.4	Neocartilage Formation in 3D Printed NorHA Constructs.....	152
4.3.5	Evaluation of <i>In Situ</i> Crosslinking Approach.....	156

4.4	CONCLUSIONS.....	161
4.5	REFERENCES.....	162
CHAPTER 5: FABRICATION OF MSC-LADEN COMPOSITES OF HYALURONIC ACID HYDROGELS REINFORCED WITH MEW SCAFFOLDS FOR CARTILAGE REPAIR.....		168
5.1	INTRODUCTION.....	168
5.2	METHODS	172
5.2.1	Materials.....	172
5.2.2	Hydrogel Fabrication and Characterization	172
5.2.2.1	NorHA Synthesis.....	172
5.2.2.2	Hydrogel Fabrication.....	173
5.2.2.3	Compression Testing.....	174
5.2.3	Cell Culture and Characterization of MSC-Laden Constructs.....	174
5.2.3.1	Cell/tissue Isolation and Culture.....	174
5.2.3.2	Cell Viability.....	174
5.2.3.3	Gene Expression Analysis and Biochemical Assays.....	175
5.2.3.4	Histology and Immunohistochemistry.....	176
5.2.4	Composite fabrication and characterization.....	177
5.2.4.1	MEW of PCL Meshes.....	177
5.2.4.2	Composite Fabrication.....	178
5.2.5	Assessment of ex vivo integration capacity.....	179
5.2.5.1	Fabrication of press-fit constructs in cartilage ring explants.....	179
5.2.5.2	Push-Out Testing.....	179
5.2.5.3	MicroCT and Interfacial Contact Area.....	180
5.2.6	Statistical Analysis	180
5.3	RESULTS AND DISCUSSION	180
5.3.1	Influence of Crosslink Density on Cartilage Formation in NorHA Hydrogels ..	180
5.3.2	Reinforcement of NorHA Hydrogels with MEW Meshes	188
5.3.3	Neocartilage Formation in MEW-Reinforced NorHA Hydrogels.....	190
5.3.4	Integration of Composites Within Cartilage Explants.....	197
5.4	CONCLUSIONS.....	204
5.5	REFERENCES.....	205
CHAPTER 6: EVALUATION OF MEW-NORHA COMPOSITES IN A PORCINE CARTILAGE DEFECT MODEL.....		213
6.1	INTRODUCTION.....	213
6.2	METHODS	216
6.2.1	Materials.....	216
6.2.2	MEW Mesh-NorHA Composite Fabrication and Cell Culture.....	216
6.2.3	Screening of Porcine Donors for pMSC Chondrogenic Potential.....	217
6.2.4	Cell Viability.....	217
6.2.5	Animal Procedures and Stifle Joint Surgery.....	218
6.2.6	Arthroscopy and Gross Observations.....	220
6.2.7	Indentation Testing of Composites and Repair Cartilage.....	220

6.2.8	MicroCT and Histological Evaluation of Cartilage Defects	221
6.2.9	Statistical Analysis	222
6.3	RESULTS AND DISCUSSION	222
6.3.1	pMSC Donor Screen for Chondrogenic Potential	222
6.3.2	Animal Study Design	226
6.3.3	Evaluation of Repair Cartilage	230
6.4	CONCLUSIONS.....	239
6.5	REFERENCES.....	242
CHAPTER 7: DIGITAL LIGHT PROCESSING OF MACROPOROUS AND HYDROLYTICALLY DEGRADABLE NORHA_{CA} HYDROGELS FOR USE WITH AUTOLOGOUS MATRIX-INDUCED CHONDROGENESIS		247
7.1	INTRODUCTION.....	247
7.2	METHODS	250
7.2.1	Materials	250
7.2.2	NorHA _{CA} Synthesis, Hydrogel Fabrication, and Photorheology	250
7.2.3	Compression Testing	252
7.2.4	Characterization of NorHACA Hydrogel Bulk Degradation	252
7.2.5	Modeling of Hydrogel Degradation Behavior.....	253
7.2.6	Preparation of Copolymer Hydrogels	262
7.2.7	Digital Light Processing of Hydrogels	262
7.2.8	Statistical Analysis	263
7.3	RESULTS AND DISCUSSION	263
7.3.1	Rational Design of Degradable Hydrogels for AMIC	263
7.3.2	Characterization and Modeling of Bulk Degradation in NorHA _{CA} Hydrogels ..	265
7.3.3	Digital Light Processing of NorHA _{CA} Hydrogels	272
7.4	CONCLUSIONS.....	279
7.5	REFERENCES.....	281
CHAPTER 8: CONCLUSIONS, LIMITATIONS, AND FUTURE DIRECTIONS.....		288
8.1	OVERVIEW.....	288
8.3	SPECIFIC AIM 2	291
8.4	SPECIFIC AIM 3	294
8.5	SPECIFIC AIM 4	295
8.6	OVERALL SUMMARY	298
8.7	REFERENCES.....	298

LIST OF TABLES

Table 3.1: Representative hydrogels used in bioprinting, including the polymer, introduced reactive group, crosslinking chemistry, and bioprinting technique employed	93
Table 3.2: Photocrosslinking parameters used for various photoinitiators during light-based bioprinting	102
Table 5.1: qRT-PCR bovine Taqman primers	176
Table 7.1: Model inputs for network initialization prior to Monte Carlo simulation	270
Table 7.2: DLP working curve fit parameters for NorHA _{CA} resin.	277

LIST OF FIGURES

Figure 1.1: Overview of the distinct zones and extracellular matrix of articular cartilage	2
Figure 1.2: The traditional biofabrication window for extrusion printing of bioinks	8
Figure 1.3: Extrusion printing for the formation of cartilage	15
Figure 1.4: Incorporation of fibrous materials into 3D printing and biofabrication.	19
Figure 1.5 Inkjet bioprinting for the formation of articular cartilage	21
Figure 1.6: Stereolithography (SLA) and digital light processing (DLP) for the formation of articular cartilage	24
Figure 1.7: Scaffold-free fabrication approaches for articular cartilage formation	27
Figure 1.8: Biofabrication of biphasic, cell-laden scaffolds for the repair of full-thickness osteochondral defects	32
Figure 3.1: Light-based bioprinting techniques	61
Figure 3.2: Overview of free-radical chain polymerization	64
Figure 3.3: Overview of thiol-ene photocrosslinking.	69
Figure 3.4: Overview of photo-mediated redox crosslinking	72
Figure 3.5: Overview of techniques commonly employed in extrusion-based bioprinting	78
Figure 3.6: Representative examples of constructs fabricated with lithography-based bioprinting technologies	84
Figure 3.7: Absorption spectra and molar extinction coefficients of commonly used photoinitiators for light-based bioprinting	101
Figure 4.1: Schematic of <i>in situ</i> crosslinking approach for 3D printing	134
Figure 4.2: ¹ H NMR characterization of NorHA in D ₂ O	136

Figure 4.3: <i>In situ</i> crosslinking technique setup	138
Figure 4.4: NorHA bioink composition and crosslinking	141
Figure 4.5: Influence of light absorbance on printability	143
Figure 4.6: Light attenuation through the capillary	144
Figure 4.7: Rheological properties of bioinks across various light intensities	145
Figure 4.8: Identification of permissible printing conditions via photorheology	146
Figure 4.9: Representative multi-layered constructs printed via <i>in situ</i> crosslinking	148
Figure 4.10: Stability of discs printed via <i>in situ</i> crosslinking technique	148
Figure 4.11: Quantification of printing error associated with <i>in situ</i> crosslinking technique	149
Figure 4.12: Swelling behavior and mechanics of printed versus casted NorHA discs	150
Figure 4.13: Cell viability and distribution in printed constructs	151
Figure 4.14: Relative gene expression of encapsulated MSCs in printed NorHA constructs	152
Figure 4.15: Mechanical characterization and biochemical analysis of printed constructs	153
Figure 4.16: Histological evaluation of printed constructs	154
Figure 4.17: Culture and characterization of printed femoral condyles	155
Figure 5.1: ¹ H-NMR spectra of synthesized NorHA	173
Figure 5.2: NorHA hydrogels with varied crosslink densities	181
Figure 5.3: Viability of NorHA hydrogels with varied crosslink densities	182
Figure 5.4: Influence of NorHA crosslink density on MSC chondrogenesis and neocartilage formation	183
Figure 5.5: Influence of NorHA crosslink density on MSC gene expression	184
Figure 5.6: Representative gross images of MSC-laden NorHA hydrogels	184

Figure 5.7: Influence of NorHA crosslink density on matrix production and distribution	186
Figure 5.8: Alcian Blue and Collagen Immunohistochemistry	187
Figure 5.9: Influence of NorHA crosslink density on type I collagen elaboration and distribution	187
Figure 5.10: PCL meshes reinforce NorHA hydrogels	189
Figure 5.11: MEW Mesh dimensions influence composite mechanical properties	190
Figure 5.12: Influence of MEW meshes on MSC chondrogenesis and neocartilage formation	191
Figure 5.13: Viability within NorHA-MEW Composites	192
Figure 5.14: Influence of MEW Mesh on MSC chondrogenic gene expression	193
Figure 5.15: Compressive moduli of acellular hydrogels and composites	194
Figure 5.16: Representative gross images of MSC-laden 2 kPa hydrogels and composites	195
Figure 5.17: Influence of MEW Meshes on matrix production and distribution	196
Figure 5.18: Influence of MEW Meshes on type I collagen elaboration and distribution	197
Figure 5.19: Integration of composites within explanted cartilage rings	198
Figure 5.20: Representative gross images of constructs press-fit into explanted cartilage rings	199
Figure 5.21: Push-out testing set-up	199
Figure 5.22: Mechanical analysis after push-out testing	200
Figure 5.23: Image filtering of MicroCT scans	200
Figure 5.24: Quantification of composite-cartilage contact area from MicroCT scans	201
Figure 5.25: Characterization of composite-cartilage interfaces	202

Figure 5.26: MicroCT reconstructions of constructs press-fit and cultured within explanted cartilage rings	203
Figure 6.1: <i>In vitro</i> screening of porcine MSC donors	224
Figure 6.2: ECM staining of composites across porcine MSC donors	226
Figure 6.3: Overview of in vivo study design	227
Figure 6.4: Overview of implant distributions for porcine surgeries	229
Figure 6.5: Cell viability of precultured composites for implantation in vivo	230
Figure 6.6: Arthroscopic observation of repair cartilage	231
Figure 6.7: Gross observation of repair cartilage	232
Figure 6.8: Gross observation of the opposing articulating surface	233
Figure 6.9: MicroCT scans of cartilage defects and underlying subchondral bone	235
Figure 6.10: Safranin O /Fast Green staining of repair cartilage	236
Figure 6.11: Indentation testing of repair cartilage	237
Figure 6.12: Mechanical properties of composites before and after implantation	239
Figure 7.1: Overview of hydrolytically degradable NorHA _{CA} hydrogel formation	251
Figure 7.2: Overview of possible crosslink states within NorHA _{CA} hydrogels	255
Figure 7.3: Characterization of NorHA _{CA} hydrogel mechanical properties	265
Figure 7.4: Characterization of NorHA _{CA} hydrogel degradation	266
Figure 7.5: Modeling the degradation behavior of NorHA _{CA} hydrogels via Monte Carlo simulations	269
Figure 7.6: Degradation behavior of NorHA _{CA} :NorHA hydrogels	271
Figure 7.7: Modeling the degradation behavior of NorHA _{CA} :NorHA hydrogels	272
Figure 7.8: Overview of digital light processing (DLP) and considerations for printability	273
Figure 7.9: DLP of NorHACA hydrogels for tissue engineering applications	276

CHAPTER 1: INTRODUCTION

1.1. THE BURDEN OF CARTILAGE DAMAGE AND INJURY

Cartilage is a load bearing connective tissue that is found in articulating joints and permits movement between bones with minimal friction. Cartilage is comprised of four distinct zones: the superficial zone, middle zone, deep zone, and calcified zone.^{1,2} The superficial zone exhibits densely packed collagen II fibrils, flattened elongated cells (oriented by tangential shear stresses), relatively high cellularity, and a low compressive modulus. The middle zone however contains round cells, higher compressive properties and collagen fibers that are randomly arranged. Finally, the deep zone is characterized by columns of ellipsoidal cells that are distributed between radially oriented collagen fibers, while the calcified zone interfaces with underlying subchondral bone. In each of the respective zones of cartilage, proteoglycans are contained within an entangled collagen matrix. While the negatively charged sites found on aggrecan molecules result in swelling, these proteoglycans are aggregated together due to the presence of the collagen matrix. The repulsive forces between negatively charged proteoglycans and the osmotic swelling that occurs within the matrix ultimately yield the impressive compressive properties of cartilage.^{1,3} More generally, the stratified anisotropy of collagens in articular cartilage, taken together with the variable ECM compositions throughout each zone, gives rise to unique mechanical properties,⁴ such as tension-compression non-linearity,⁵ which impart cartilage with its biomechanical function (**Figure 1.1**).⁶

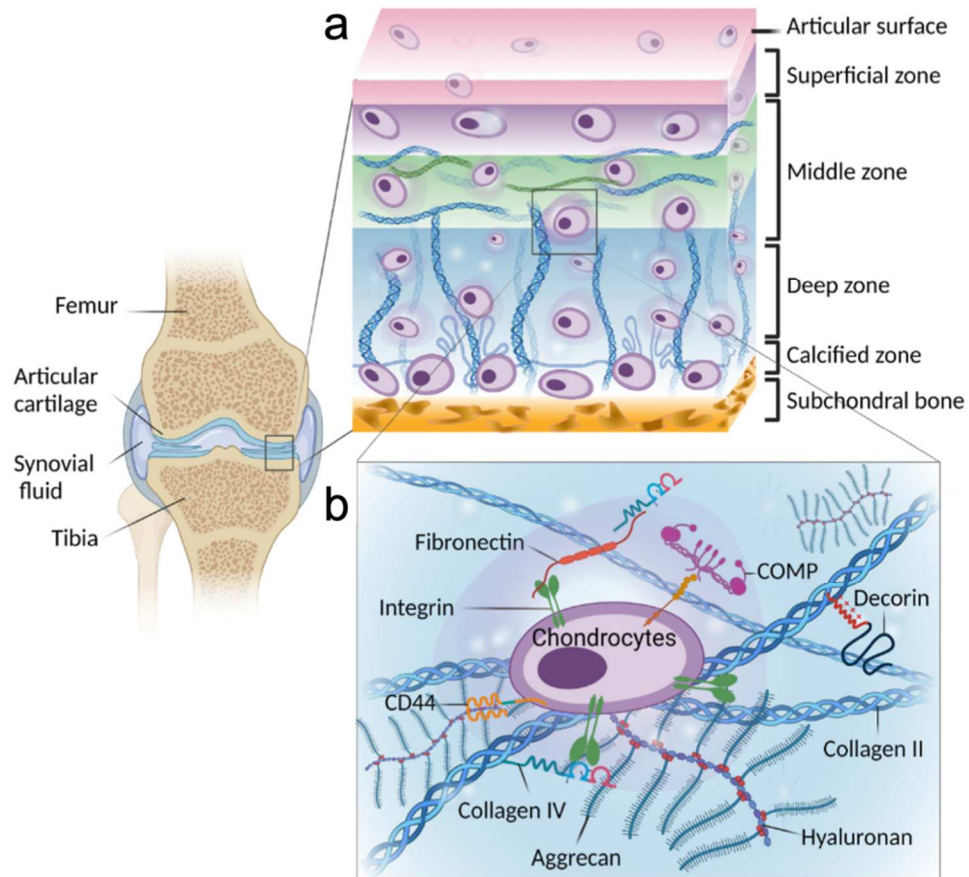


Figure 1.1: Overview of the distinct zones and extracellular matrix of articular cartilage.

A) Articular cartilage is composed of four distinct zones: the superficial, middle, deep, and calcified zones. From the superficial zone to the deep zone of articular cartilage, the orientation of both cells and collagen fiber transitions from parallel to the articulating surface to orthogonal. In addition, relative differences in oxygen content (highest in the superficial zone), collagen cross-links (i.e., lysylpyridinoline (LP), hydroxylysylpyridinoline (HP)), and compressive modulus (highest in the deep zone) are observed throughout different zones.⁷ The calcified zone is marked by the presence of hypertrophic chondrocytes, which undergo endochondral ossification toward the formation of the underlying subchondral bone. B) The extracellular matrix of articular cartilage is composed of collagen fibers (predominantly type II collagen) and negatively charged proteoglycans (predominantly aggrecan), which are entangled together to form a viscoelastic network that imparts resistance to compressive loading. Chondrocytes embedded within the ECM interact with the surrounding environment via interactions between fibronectin and integrin binding receptors and between hyaluronan (i.e., hyaluronic acid) and CD44 surface receptors. Schematics adapted from ².

Articular cartilage degeneration is a pervasive problem that afflicts many people, inhibiting quality of life and joint mobility in over 20 million Americans.⁸ Focal defects on the articulating surface of joints typically form in patients due to trauma, sports injuries, or daily activities associated with joint function.⁹ Unfortunately, native cartilage does not possess any innate healing capacity,¹⁰ such that these defects may lead to the progression of disease throughout the entire joint if left untreated. Furthermore, it is understood that these focal defects may evolve towards pain and ultimately osteoarthritis.¹¹

To this end, a number of clinical approaches have been developed for reconstructing chondral defects, such as microfracture (MFX), mosaicplasty, and matrix-assisted chondrocyte implantation (MACI).¹² Microfracture is a minimally invasive, arthroscopic procedure that involves the formation of holes in underlying subchondral bone via an awl to recruit mesenchymal stromal cells from bone marrow and elicit a healing response.¹³ While microfracture may induce some cartilage repair in small defects (< 2.5 cm²), it often leads to the formation of fibrocartilage,¹⁴ which exhibits inferior mechanical properties when compared to native hyaline cartilage.^{13,15} Alternatively, mosaicplasty may be employed to fill and repair large defects (>4 cm²) via transplantation of autologous tissue from a non-weight bearing region.¹⁴ However, this technique often results in donor site morbidity and poor transplant integration with adjacent tissue.¹⁶ MACI has been employed clinically to deliver autologous chondrocytes within a collagen matrix to promote the repair of cartilage, and has shown marked improvement over microfracture for critical size defects (≥ 3 cm²);^{14,17} however, this procedure has yielded less than satisfactory clinical results, as adequate repair in a subset of cartilage defect patients, possibly due to insufficient matrix properties.¹⁷ With all of this considered, there remains a significant clinical need for the development of new approaches that support the

formation of functional cartilage and enhance the prospects for strategies such as MACI. Specifically, approaches that utilize biomaterials and biofabrication techniques may advance towards the clinical repair of cartilage focal defects, alleviating the burden of pain and costs associated with cartilage degeneration.¹⁷

1.2 DESIGN OF HYDROGELS FOR CARTILAGE TISSUE ENGINEERING

One approach to cartilage repair involves the incorporation of cells within hydrogels, water swollen polymer networks that mimic the native extracellular matrix, to elicit neotissue formation.¹⁵ Although a range of materials have been investigated in this approach, including natural collagen materials with the clinically-used MACI technique, the quality of repair tissue formed in these materials is typically inferior to healthy tissue.¹⁵ Additionally, it is a challenge to fabricate hydrogels that exhibit the necessary mechanical properties for stabilization in defects while still supporting the viability and function of cells.¹⁸

One important class of hydrogels in cartilage tissue engineering are those formed from hyaluronic acid (HA). HA is a non-sulfated glycosaminoglycan found in native cartilage that shows promise as a hydrogel for cartilage repair due to its inherent bioactivity and amenability to facile chemical modification for hydrogel formation.¹⁹ Studies have shown that the presence of distinct physiochemical cues (e.g. network mechanical properties, mesh size, signaling ligands) can appreciably influence ECM formation and distribution by encapsulated cells.²⁰⁻²² As one specific hydrogel example, norbornene-modified HA (NorHA) has proven to be very amenable to tuning hydrogel material properties and has potential in cartilage tissue engineering.

The field of additive manufacturing has also advanced in recent years to improve techniques for the fabrication of cell-laden hydrogels into user-defined geometries, including for cartilage tissue engineering.²³ To understand the complex challenges and

design criteria associated with the use of additive manufacturing for cartilage repair, it is important to first consider recent progress and advancements within the field of biofabrication for cartilage tissue engineering. The aim of this introduction is to outline these advances to provide a general background for the new light-based biofabrication techniques and hyaluronic acid-based scaffolds described in this dissertation.

1.3 STATE OF THE ART IN BIOFABRICATION FOR CARTILAGE REPAIR

Biofabrication generally involves the construction of complex biological products from elementary units such as living cells, bioactive molecules, and biomaterials,²⁴ and has rapidly emerged as one of the leading technological platforms within the fields of tissue engineering and regenerative medicine toward the automated manufacturing of complex, functional tissues and organs.²³⁻²⁶ To build these structures, biofabrication techniques require the implementation of multidisciplinary approaches, combining skills in diverse fields such as cell biology and anatomy, mechanical engineering, and materials science to assemble cells and engineered biomaterials into functional tissue constructs^{23,24} or complex 3D *in vitro* tissue models for high throughput screening and disease modeling.²⁶

Toward recreating complex features within engineered tissues, a range of additive manufacturing techniques have been adapted or developed in recent years, including extrusion-based 3D printing, inkjet printing, lithography-based 3D printing (i.e., stereolithography (SLA), digital light processing (DLP), computed axial lithography (CAL), continuous liquid interface printing (CLIP), two-photon printing (2PP)), laser induced forward transfer (LIFT), and bioassembly.^{23,27-29} Across all of these approaches, the goal is to organize cells and/or physicochemical cues in 3D to elicit desired cellular behaviors, which may include cell proliferation, migration, differentiation, and tissue formation. Bioprinting approaches specifically include instances where cells are directly processed

and organized via 3D printing.³⁰ In cartilage applications, typically chondrocytes, mesenchymal stromal cells, chondroprogenitors, or co-culture of these cells are utilized, such that chondrogenesis and/or ECM production can be mediated through both the selected biofabrication method employed and the presentation of signaling cues. The biofabrication method employed for cartilage tissue engineering often varies, as each approach possesses their own respective advantages and limitations.

Bioprinting has rapidly evolved as a leading and widely adopted additive manufacturing approach for the design and production of living cartilage tissue constructs. By utilizing computer-aided design (CAD), bioprinting permits the automated formation of living materials with desired architectures in a precise and reproducible manner.²⁶ Specifically, the ability to 3D bioprint cells and materials into defined geometries allows the fabrication of constructs that recapitulate the complex organization and structure–function relationships found in native tissues. For example, bioprinting may be leveraged to mimic the anisotropic mechanical properties and zonally stratified regions found in native cartilage.³¹

1.3.1 Extrusion-Based Bioprinting and Biofabrication

1.3.1.1 Bioink Design and Implementation

Extrusion-based bioprinting methods have been widely employed in recent years for the fabrication of cell-laden hydrogel constructs through the extrusion and subsequent stabilization of bioinks. Bioinks are generally any biomaterial that can be processed via 3D printing that also incorporates living cells, cell aggregates/spheroids, organoids, or microtissues.³⁰ The simplicity, diversity and predictability of this printing technique has led to its extensive popularity, with many commercial bioprinters now available. In comparison to other printing approaches such as SLA, DLP, and CAL, extrusion-based bioprinting functions at lower print speeds and resolutions;²⁹ however, the major advantages of

extrusion-based bioprinting include the wide range of printable bioinks, the use of inexpensive equipment, and the minimal loss of the bioink during fabrication. As a result, extrusion-based bioprinting has been the most common biofabrication approach leveraged for cartilage tissue engineering to date.

Many researchers have modified conventional commercial 3D printers for extrusion-based bioprinting or developed custom printing equipment to reduce the costs required for bioprinting. On the other hand, due to the growing demand and development of extrusion-based bioprinters, commercial systems have become widely available and adopted by researchers in academia and industry, which has rapidly enhanced the print quality and speed, as well as the ability to fabricate constructs with a wider range of biomaterials.³²

To successfully support conventional extrusion-based bioprinting, bioinks must be designed with specific properties (**Figure 1.2**).^{29,33}

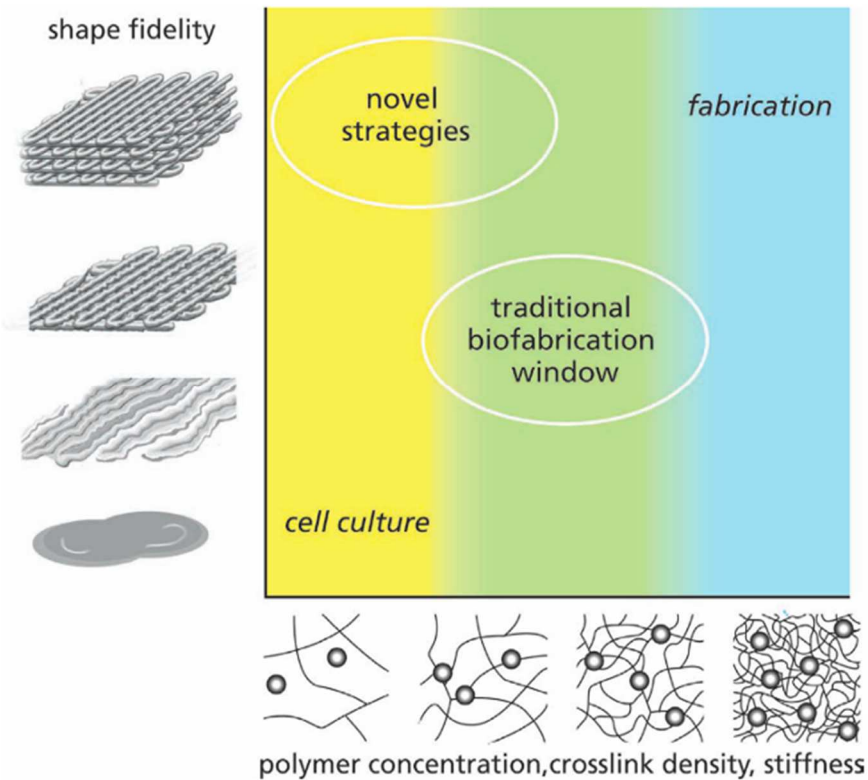


Figure 1.2: The traditional biofabrication window for extrusion printing of bioinks. Generally, bioinks and biomaterial inks employed in extrusion printing must possess suitable rheological properties so that they can readily flow upon application of shear stress, and in tandem exhibit sufficient mechanical integrity to support the deposition of stable filaments in a layer-by-layer manner. Viscous materials that yield hydrogels with higher polymer concentrations, crosslink densities, and stiffness typically meet each of these respective design criteria for ink printability (blue, upper right corner of schematic). However, hydrogels with these properties often exhibit poor cytocompatibility, as they do not possess the mesh sizes needed to support nutrient transport for encapsulated cells. Hydrogels desirable for cell encapsulation and function typically exhibit lower polymer concentrations and crosslink densities (yellow, lower left corner of schematic). To this end, conventional extrusion bioprinting aims to balance ink properties to achieve optimal cellular microenvironments while conserving ink printability and the shape fidelity of printed constructs (green, center of diagram). The development of novel extrusion printing approaches (e.g., embedded 3D printing) is focused on achieving optimal shape fidelity and hydrogel properties for cell culture in parallel (upper left corner of schematic). Schematic adapted from ³⁸.

For example, the viscosity of the bioink can be very important toward successful processing with extrusion-based bioprinting.²⁹ Specifically, extrusion printing requires that biomaterial inks exhibit low enough viscosity so that they can traverse through a print head

without clogging or generating cytotoxic shear forces if cells are included; however, inks must also possess suitable mechanical integrity so that they can be deposited in a layer-by-layer manner. Another important consideration is the influence that cells themselves have on the overall bioink properties. Past studies have demonstrated that the incorporation of cells at high densities (100×10^6 cells/mL) within collagen inks resulted in increased ink viscosities and storage moduli initially, but decreased rates of gelation and storage moduli post-gelation; however, printability can still be conserved at these high cell densities.³⁴

To ensure that encapsulated cells remain functional during the printing process, strategies have been developed to mitigate the influence of shear stresses on cell viability during bioink extrusion. Controlling properties such as ink viscosity (e.g. through material formulation or temperature), printing pressure (or force for screw/piston-based extrusion), nozzle geometry, and nozzle diameter improve the control over applied shear stresses during the printing process.^{35,36} The development of fluid dynamic-based models have further improved the ability to tune shear stresses generated during printing towards ensuring cell viability throughout the printing process.^{35,37}

To achieve the deposition of stable filaments during the extrusion process, the inks employed must be rapidly crosslinked. Bioinks used in extrusion-based bioprinting may be crosslinked with a range of different exogenous triggers including light, temperature, and/or the presence of ions. For instance, co-axial extrusion setups have been leveraged to print methacrylated-gelatin (GelMA), methacrylated-HA (MeHA), and chondroitin sulfate amino ethyl methacrylate (CS-AEMA) as photosensitive inks for cartilage tissue engineering, with ionically crosslinked alginate added to impart initial printability and filament stability. Using this approach, constructs were printed with high viability of embedded MSCs and features on the order $\sim 100 \mu\text{m}$.³⁹ Interestingly, bioinks composed of

alginate, gelatin, and chondroitin sulfate have also been employed to achieve optimal ratios of COLII/COL I and COLII/COLX gene expression by encapsulated cells toward the development of hyaline cartilage; however, ink formulations in the same study with higher macromer concentrations resulted in more hypertrophic gene expression, likely due to the increase in hydrogel crosslink density.³⁹ Dual crosslinking of alginate has also been achieved via modification with thiol and norbornene functional groups, such that the alginate bioink could be initially crosslinked via ionic crosslinking and subsequently stabilized via thiol-ene photocrosslinking.⁴⁰ Additional discussion on the use of light-mediated crosslinking for extrusion bioprinting is included in Chapter 3.

In addition to the myriad of crosslinking chemistries employed for the stabilization of bioinks, a range of different bioinks have been utilized and compared for extrusion bioprinting including both natural biopolymers (e.g., gelatin methacryloyl (GelMA), allylated gelatin (GelAGE)⁴¹, collagen,⁴² chondroitin sulfate,³⁹ gellan gum,⁴³ silk fibroin,⁴⁴ mannan,⁴⁵ fibrinogen,⁴⁶ alginate,⁴⁷ agarose,⁴⁷ and hyaluronic acid⁴⁸) and synthetic polymers (e.g., PEGMA,⁴⁷ Pluronic block copolymer,⁴⁹ allyl-functionalized poly(glycidol)s (P(AGE-co-G))⁵⁰). While synthetic materials typically possess well-defined material properties and tunability, the inherent bioactivity, biodegradability, and biocompatibility of natural materials make them excellent candidate materials for bioinks. In one representative example, platelet-rich plasma was combined with photocrosslinkable GelMA (which interacts with plasma via integrin receptors), to create a patient-specific bioink that presents growth factors to chondrocytes.⁵¹

Decellularized ECM has also been leveraged to provide a local microenvironment to encapsulated cells that is chondroinductive. For example, cartilage ECM particles have previously been combined with gellan gum and alginate based inks in combination with TGF-B3 to increase the matrix production of encapsulated cells (**Figure 1.3a**).⁵² Similarly,

alginate bioinks containing MSCs have also been supplemented with decellularized cartilage extracellular matrix to improve their chondrogenic potential, as evidenced by increases in chondrogenic gene expression (i.e., SOX9, COLII, ACAN) when compared to alginate alone controls.⁵³ Since these gels also demonstrated differentiation consistent with an endochondral pathway (marked by RUNX2 and COLX expression, as well as mineralization), TGF-B3 was included within the ink to improve chondrogenesis toward a hyaline-like phenotype. dECM is an excellent candidate bioink due to the innate physicochemical cues retained within the ECM and its cytocompatibility.⁵⁴ However, variability in sourced ECM, taken together with the challenges posed by processing dECM, storing dECM inks, and potentially scaling dECM manufacturing has led to the implementation of alternative bioinks composed of natural polymers or ECM components.

To improve the overall control over ink properties, hybrid inks composed of both natural and synthetic materials have been employed. For example, triblock copolymers of PEG and methacrylated poly [N-(2- hydroxypropyl) methacrylamide mono/dilactate] were previously utilized as thermally sensitive bioinks, permitting thermal self-assembly of chondrocyte-laden gels to occur concurrently with photocrosslinking during the printing process. Methacrylated-chondroitin sulfate and methacrylated-HA were then preferentially incorporated into these inks to modulate resultant hydrogel mechanical properties and degradation profiles.⁵⁵

Shear-thinning and self-healing materials are commonly employed in extrusion bioprinting since they exhibit viscous flow upon application of shear (i.e., during extrusion) while also recovering their mechanical integrity with the removal of shear stress. Typically, these types of inks incorporate either physically crosslinked polymers, reversible dynamic-covalent chemistries, or components that can physically interact with each other (e.g., Laponite nanosilicates,⁵⁶ nanocellulose^{36,57}) via ionic or intermolecular interactions. For

instance, alginate-based inks have been supplemented with nanocellulose to permit viable extrusion printing of chondrocytes.^{36,57}

Similarly, nanocomposite bioinks containing nanoparticles (NPs) that exhibit dynamic covalent or physical bonding with surrounding polymers are also utilized to improve printability.^{44,58} In one instance, oxidized alginate along with gellan gum (physical crosslinking is achieved with cooling post-printing) was mixed with amine presenting NPs, such that reversible imine bonds could readily form, resulting in interpenetrating networks (IPNs) composed of covalent alginate-NP networks and physically crosslinked gellan gum networks. The inclusion of NPs improved the rheological properties for extrusion printing (e.g., increase of yield stress from 14.5 Pa to 79 Pa with the inclusion of NPs) and mechanical stability of inks when compared to ionically crosslinked alginate alone, which quickly undergoes dissolution. Chondrogenic culture of printed chondrocyte-laden constructs and implantation in nude mice then led to neotissue formation *in vitro* and *in vivo*, respectively.⁵⁸

1.3.1.2 Multi-Material Extrusion-Based Printing

While composite ink formulations may improve overall ink printability or mechanical properties, they do not always fully capture the range of physiochemical properties presented within native tissues. Therefore, to further improve the complexity of scaffolds for cartilage tissue engineering, multi-material printing techniques have been developed. For example, the controlled deposition of GelMA/gellan gum and fugitive alginate inks allowed for the formation of complex overhanging geometries that would otherwise not be readily achieved, improving the ability to recapitulate anatomically relevant features.⁵⁹ Similarly, collagen inks have been used to create constructs with gradients of cell densities, mimicking the relative cellularity of the distinct cartilage zones. Interestingly, printing of chondrocyte-laden gels with gradients of cell densities led to corresponding

gradients in chondrogenic gene expression, as well as the formation of tissue that exhibited gradients of ECM composition.⁴² Moreover, microfluidics have been leveraged as a method to control the temporal deposition of different inks, permitting multi-material printing.⁶⁰ To this end, an extrusion printing setup with seven distinct printheads controlled via pneumatic valves was designed to achieve continuous and rapid deposition of multiple materials in parallel, such that multiple bioinks could be readily and precisely deposited in parallel or in series with each other.⁶¹ Skylar-Scott and colleagues have also coupled microfluidics with multiple print nozzles for high-frequency multi-material printing towards the fabrication of complex, voxelated and heterogeneous structures.⁶² Generally, the ability to combine multiple materials and cell populations in these approaches demonstrates how continued advancements in both printer capabilities and bioink design are enabling the fabrication of constructs that more faithfully emulate cartilage.

One of the limitations of most hydrogel bioinks is their relatively low mechanical properties, which are significantly lower than those of native healthy cartilage. In response to this, multi-material printing has enabled the fabrication of composites of hydrogels and polycaprolactone (PCL) templates to improve construct mechanical properties (**Figure 1.3b**).⁶³ Multihead dispensing systems (MHDS) have been employed for co-printing of PCL and alginate hydrogels encapsulating chondrocytes and TGF- β . Importantly, these composite systems demonstrated significance promise, with no adverse tissue responses and the formation of neocartilage observed 4 weeks after subcutaneous implantation in nude mice.⁶⁴ Since co-printing PCL scaffolds with cell-laden gels is a common approach for cartilage tissue engineering,^{50,53} the influence of PCL molecular weight, scaffold porosity, filament size, filament spacing, and filament orientation on resultant mechanical properties has been characterized.⁶⁵

In another study, cell-laden hybrid ECM gels (gelatin, fibrinogen, HA, glycerol) were co-printed with reinforcing PCL in the presence of sacrificial gels (Pluronic F-127) for stabilization, and the incorporation of negative internal features (i.e., microchannels) permitted improved transport toward the fabrication of larger scale constructs (**Figure 1.3c**). For example, ear-shaped scaffolds with encapsulated chondrocytes were printed and shown to form neocartilage after 5 weeks of chondrogenic culture *in vitro* and 2 months after subcutaneous implantation in athymic mice.⁴⁶ Alginate bioinks for cartilage bioprinting have similarly been reinforced via the inclusion of submicron polylactide fibers, which increased hydrogel Young's modulus three-fold.⁶⁶

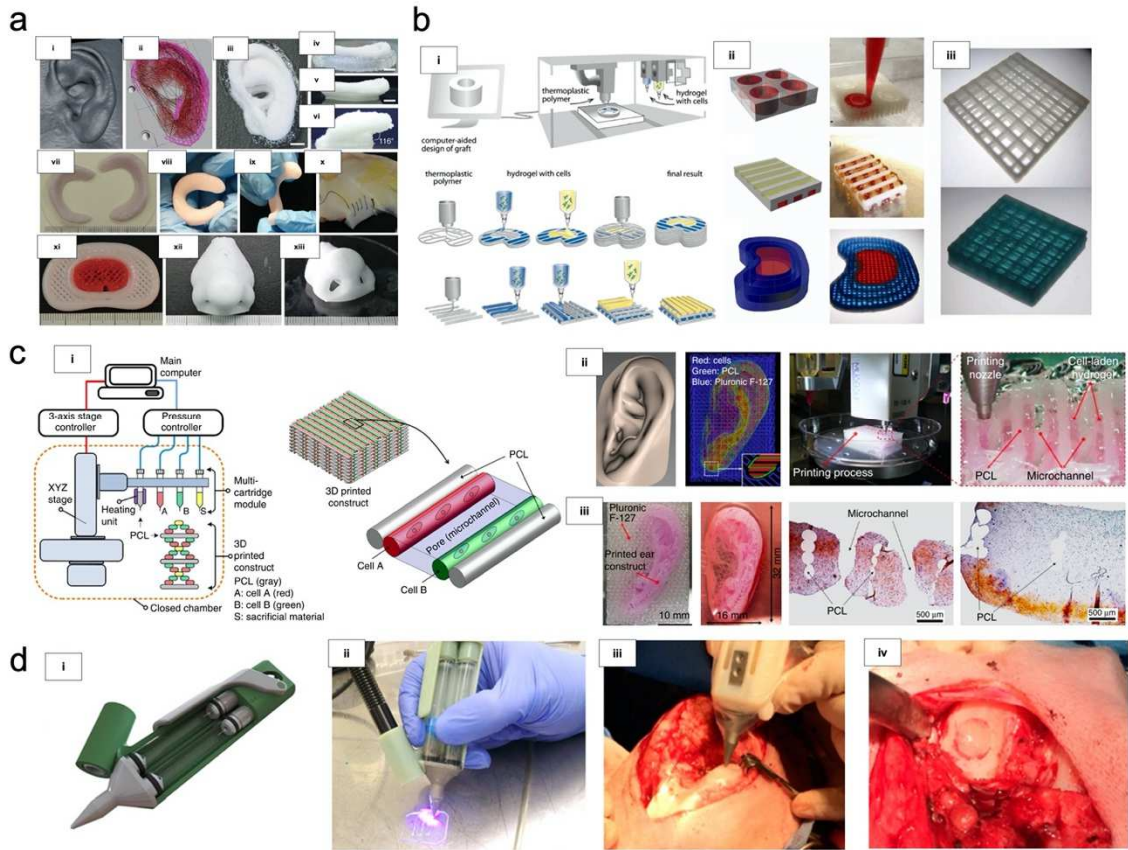


Figure 1.3: Extrusion printing for the formation of cartilage. a) Representative examples of extrusion 3D printing for the fabrication of gellan/alginate/ECM-based scaffolds with anatomical geometries, including in the shape of (i-iv) a model ear, (vii-x) model menisci, (xi) a model intervertebral disc, and (xii-xiii) a model nose. Schematics and images adapted from ⁵² b) (i) Schematic overview of co-printing of thermoplastic polymers and hydrogels (ii) to create complex, multi-material constructs and (iii) to reinforce soft hydrogels. Schematics and images adapted from ⁶³. c) (i, left) Schematic of the multi-material extrusion printer employed to fabricate PCL-reinforced hydrogels. A 3-axis stage controller enables the controlled deposition of filaments onto an underlying stage, while a pneumatic pressure controller regulates the flow of multiple inks from distinct cartridge modules. The entire system is enclosed within an acrylic chamber containing a temperature regulator and humidifier to enable the extrusion of thermoplastic PCL. (ii, right) A representative schematic detailing how PCL may be co-printed with multiple bioinks (i.e., red and green filaments, containing distinct cell populations “A” and “B”) to yield heterogeneous constructs. (ii) (From left to right) 3D CAD of a model ear, the print path employed to deposit cell-laden filaments (red), PCL (green), and fugitive ink (i.e., Pluronic F-127, blue) to support overhanging geometries, and representative images of the printing process. (iii) (From left to right) Representative images of the printed ear before and after removal of Pluronic F-127 via washing, and Safranin O staining of constructs with and without microchannels after 5 weeks culture in chondrogenic medium *in vitro*. Schematics and images adapted from ⁴⁶. d) (i) Schematic and (ii) representative image of the handheld biopen device, which permits (iii-iv) intraoperative extrusion bioprinting of cell-laden hydrogels within a focal articular cartilage defect. Schematic and images adapted from ⁶⁹ and ⁷⁰.

In a final representative example of PCL-hydrogel composites, MeHA was added to thermally sensitive triblock copolymers (i.e., methacrylated poly[N-(2-hydroxypropyl) methacrylamide mono/dilactate] (pHPMA-lac)/polyethylene glycol (PEG)) toward printing chondrocyte-laden constructs with defined mechanical properties and internal architectures. As previously discussed, these hydrogels were also mechanically reinforced via co-printing with PCL. ECM formation by chondrocytes exhibited a dose-dependent dependence on HA, with intermediate concentrations resulting in increased glycosaminoglycan and collagen contents when compared to inks without HA, while too much HA resulted in tissue more closely resembling fibrocartilage. Importantly, optimal formulations identified in the performed *in vitro* studies were combined with PCL to yield constructs with Young's moduli similar to native cartilage (3.5-4.6 MPa).⁶⁷

Toward translating extrusion printing into the clinic in a feasible manner, new intraoperative approaches have been developed (**Figure 1.3d**). The biopen is a handheld coaxial extrusion device that permits deposition of cultured cells and inks directly into cartilage defect sites.⁶⁸⁻⁷⁰ When evaluated in a large ovine model of full-thickness cartilage defects, MeHA/GelMA inks containing adipose-derived MSCs and printed with the biopen facilitated the formation of repair cartilage. Interestingly, these constructs exhibited superior gross and histological scoring over other investigated groups (empty defects, constructs printed a priori, and defects treated with microfracture).⁶⁹ The biopen has also demonstrated the ability to fabricate human articular cartilage through the chondrogenesis of human adipose derived MSCs.⁷¹

1.3.2 Incorporation of Fibrous Materials into 3D Printing

In addition to fused-deposition modeling (e.g., **Figure 1.3b**), PCL has also been fabricated into microfiber networks via melt electrowriting, a biofabrication approach that

permits the controlled deposition of micron-scale fibers in a layer-by-layer manner.⁷²⁻⁷⁴ These scaffolds can then be combined with cell-laden hydrogels to reinforce their mechanical properties.⁷⁵⁻⁷⁷ Moreover, MEW may be readily combined with extrusion bioprinting of MSCs, which may enable the fabrication of composites with more complex fiber architectures (i.e., out-of-plane fibers if co-printed with fugitive inks), heterogeneously patterned cell-laden hydrogels, or additional tissue phases (i.e., bioceramic inks for bone tissue engineering) toward fabricating osteochondral implants.^{78,79} It is expected that with the continued development of numerical and FE models, MEW architectures and composite properties can be further modulated toward achieving target mechanical properties that fully recapitulate each of the respective zones of cartilage.⁸⁰⁻⁸²

Besides MEW, alternative fabrication approaches have been employed to create nanofibrous scaffolds with architectures that mimic native ECM. For example, 3D printing of PLLA was combined with thermally-induced phase separation to create filaments with nanofibrous topography, which improved cell adhesion, protein adsorption, and MSC chondrogenesis over smooth filament controls.⁸³ PCL fiber scaffolds with microscale features have also been woven into fibrous scaffolds using a custom-built weaving loom that interlocks layers of fibers oriented in all three planes. These scaffolds were combined with agarose gels containing encapsulated chondrocytes toward the formation of a cell-laden implant with anisotropic features and mechanical properties ($H_A \sim 0.14-0.2$ MPa) that approach native tissue levels ($H_A \sim 0.1-2.0$ MPa).⁸⁴ Dual electrospinning of multiple fiber populations has been leveraged to create microfiber scaffolds with dispersed nanofibers, the inclusion of which improved GAG deposition by seeded hMSCs,⁸⁵ while gas foaming techniques have been employed to convert 2D electrospun fiber mats into 3D fiber scaffolds suitable for 3D culture of chondrocytes.⁸⁶ It is expected that combinations of

fibrous scaffolds or nanofibers with extrusion printing of bioinks may facilitate additional control over printed cellular behaviors (**Figure 1.4**).⁸⁷

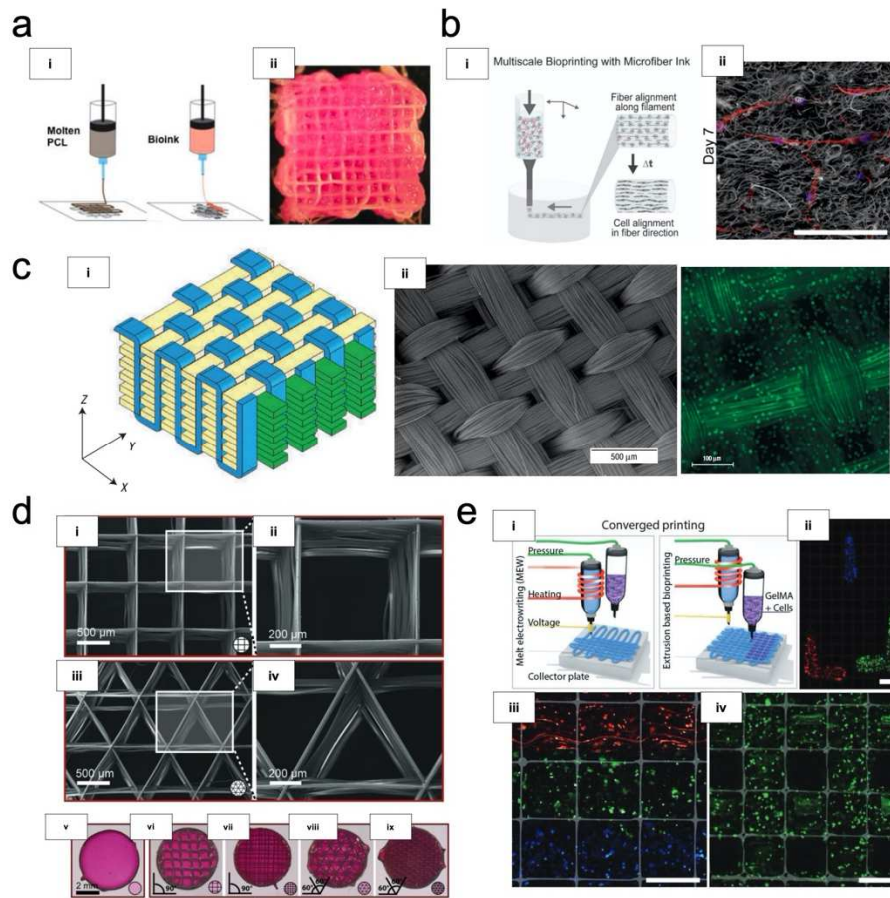


Figure 1.4: Incorporation of fibrous materials into 3D printing and biofabrication. a) (i) Representative schematic of the hybrid co-printing approach that involves the incorporation of melt-extruded PCL filaments within 3D printed bioinks. (ii) Printed lattice structure fabricated via hybrid co-printing of PCL and ECM/alginate hydrogels. Schematic and image adapted from ⁵³. b) (i) Multiscale bioprinting is achieved via the inclusion of fragmented electrospun nanofibers within an HA-based bioink. The fiber-laden bioink may be readily processed via embedded extrusion printing, such that shear forces generated during the extrusion process align the incorporated fibers. (ii) After 7 days of culture, cells align along the direction of aligned fibers within bioinks, demonstrating how these composite bioinks may be leveraged to direct cell behavior. Schematic and image adapted from ³⁷. c) (i) Schematic and (ii) representative images of composite PCL-agarose hydrogel scaffolds fabricated via the 3D weaving of fibrous PCL scaffolds using a custom-built weaving loom. Hydrogels containing encapsulated porcine articular chondrocytes (green, calcein AM) were then infilled into PCL scaffolds via vacuum-assisted infusion, but could be incorporated in future approaches using 3D printing. Schematic and images adapted from ⁸⁴. d) (i-iv) Melt electrowriting (MEW) of PCL scaffolds composed of microscale fibers organized into scaffolds with various mesh geometries. (v-ix) Reinforcement of soft hydrogels with fibrous PCL meshes of varied geometries and fabricated via MEW. Images adapted from ⁷⁶. e) Schematic overview of a co-printing approach that involves concurrent melt electrowriting and extrusion bioprinting. Representative prints of MEW mesh-hydrogel composites containing (ii-iv) heterogeneously patterned bioinks and scaffolds with the requisite porosity for 3D culture of encapsulated cells. Schematic and images adapted from ⁷⁸.

1.3.3 Inkjet Bioprinting and Biofabrication

Inkjet printing involves the controlled deposition of inks of cells and/or materials onto an underlying substrate in the form of droplets. In contrast to conventional extrusion printing, continuous inkjet printing involves the continuous flow of droplets out of a printhead. The inks employed are electrically conductive such that formed droplets can be deposited in a desired location via application of an electric or magnetic field. Alternatively, droplet-on demand inkjet printing involves the use of transient pressure pulses to form droplets from the ink and to deposit them onto the substrate.⁸⁸ In one approach, PEGDMA hydrogels with human articular chondrocytes were processed via an inkjet printer, and the transient presentation of growth factors FGF-2 and TGF-B1 improved both cell proliferation and chondrogenic differentiation over time within printed gels (**Figure 1.5a**).⁸⁹

One of the significant advantages of inkjet bioprinting is its amenability to multi-material printing, which can be readily achieved by using varied ink cartridges. For example, Daly and coworkers leveraged inkjet bioprinting to deposit cocultures of chondrocytes and MSCs within microarrays of PCL (**Figure 1.5b**), as cocultures of MSCs and chondrocytes have been previously shown to improve MSC chondrogenesis when compared to culture of MSCs alone.^{90,91} Cell suspensions were patterned within PCL templates to form spheroids that could then readily fuse and assemble into *de novo* cartilage with zonally stratified properties.⁹¹ Importantly, these scaffolds could be integrated with an underlying printed endochondral bone scaffold for applications in osteochondral tissue engineering (OCTE). Alternatively, a hybrid inkjet printing/electrospinning system was previously developed such that PCL fibrous scaffolds could be fabricated while fibrin-collagen gels containing chondrocytes were deposited in

an alternating manner, permitting fabrication of 1 mm thick constructs that supported the formation of neocartilage (**Figure 1.5c**).⁹²

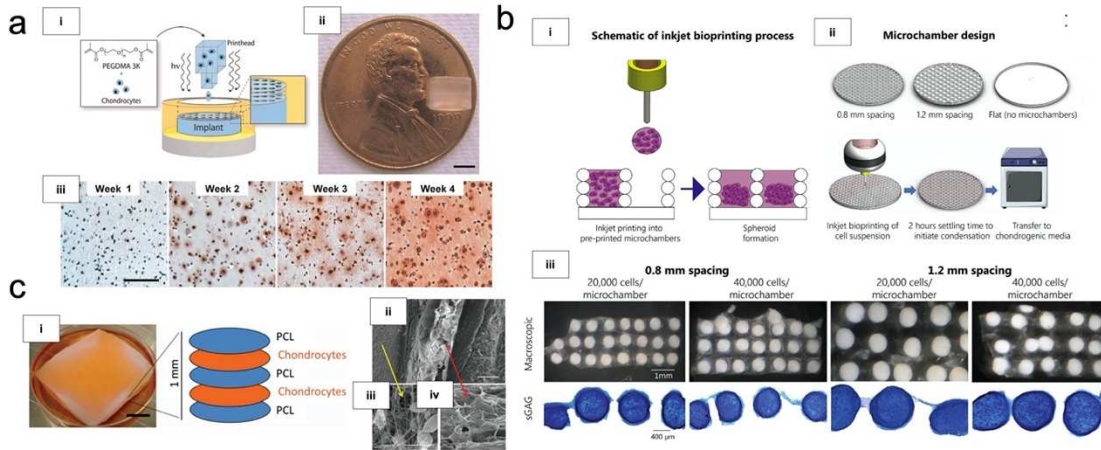


Figure 1.5 Inkjet bioprinting for the formation of articular cartilage. a) (i) Schematic overview of the inkjet bioprinting of human articular chondrocytes within PEG-based hydrogels. (ii) Representative image of a printed, chondrocyte-laden hydrogel. (iii) Safranin O staining of printed constructs treated with the growth factors FGF-2 and TGF-B1 indicated proteoglycan formation and neocartilage maturation over culture time. Schematic and images adapted from ⁸⁹. b) (i) Schematic on inkjet bioprinting process, which involves the deposition of droplets containing cell suspensions of MSCs and chondrocytes (3:1 ratio coculture of MSCs:chondrocytes) into pre-printed microchambers composed of PCL. (ii) Overview of microchamber designs and the employed cell seeding process. After deposition into microchambers, cell suspensions undergo condensation and spheroid formation. (iii) Macroscopic images and Alcian Blue staining of constructs fabricated with varied microchamber spacing (0.8 mm and 1.2 mm) and cell densities (20,000 cells/microchamber and 40,000 cells/microchamber) after 4 weeks of culture in chondrogenic media. The intense Alcian Blue staining indicates the presence of sulfated glycosaminoglycans (sGAG) in the formed tissue. Schematics and images adapted from ⁹¹. c) (i) Electrospinning and inkjet bioprinting were combined to fabricate 5-layered composite constructs composed of PCL and chondrocyte-laden hydrogels composed of fibrin and collagen. (ii-iv) SEM images demonstrate the presence of distinct (iii) PCL and (iv) hydrogel phases. Schematic and images adapted from ⁹².

1.3.4 Lithography-Based Bioprinting and Biofabrication

Lithography-based techniques have been previously reported as one of the most versatile 3D printing methods, providing the highest accuracy and precision to spatially

pattern 3D constructs.⁹³ This technology is dependent on photocrosslinking, as the working principle is based on spatial control of light-exposure to solidify a liquid photocrosslinkable resin. Using either a computer-controlled laser beam (projection stereolithography, SLA)⁹⁴ or a digital light projector (digital light processing, DLP),⁹⁵ the liquid resin can be photocrosslinked onto a computer-driven build stage or basement, which moves stepwise in the z-direction (vertically) to allow fabrication of a 3D construct in a layer-by-layer fashion.^{96,97} Lithography-based 3D biofabrication technologies allow significantly greater spatial resolutions to be achieved (25–50 μm),^{41,95,96} as well as enable the fabrication of free-form lattice and patterned structures that cannot be produced with conventional extrusion-based 3D printing approaches.

SLA has progressed greatly in recent years, with numerous examples where cells are included within resins (i.e., bioresin).^{98,99} For instance, PEGDA hydrogels were constructed via SLA with encapsulated adipose-derived stem cells, which retained high viabilities (>90%) through one week of culture.⁹⁷ Similarly, methacrylated [poly-D,L-lactic acid/polyethylene glycol/poly-D,L-lactic acid (PDLLA-PEG)] and MeHA hydrogels were fabricated via SLA with encapsulated human adipose-derived stem cells, which underwent chondrogenesis after culture for 28 days in the presence of TGF-B3.¹⁰⁰ In another study, mannan derived from yeast was methacrylated and printed via SLA, with cytocompatibility, biocompatibility, and neocartilage formation (i.e., histological observation of collagen, glycosaminoglycans) demonstrated *in vivo* in nude mice (**Figure 1.6a**).¹⁰¹ To this end, since bioresins typically form improved neocartilage in the presence of growth factors, composite resins have been developed to enable sustained delivery of factors to encapsulated cells. Zhu and coworkers showed that GelMA (10%) could be combined with PEGDA and TGF-B1 embedded nanospheres (fabricated via core-shell electrospraying) to yield a bioresin suitable for SLA-based 3D printing. Viable MSCs were readily printed

and increasing PEGDA concentrations improved the attainable print resolution (**Figure 1.6b**). The inclusion of nanospheres in formulations that supported optimal MSC viability (10%/5% GelMA/PEGDA) increased chondrogenic gene expression and the formation of nascent cartilage ECM.¹⁰²

DLP has similarly supported the fabrication of cell-laden scaffolds through the employment of natural, synthetic, and hybrid bioresins. In one approach, silk fibroin was methacrylated via reaction with glycidyl methacrylate and printed via DLP with UV-mediated photocrosslinking into model ear and trachea scaffolds. Importantly, printed constructs demonstrated cytocompatibility with chondrocytes and the ability to support nascent matrix formation after 4 weeks of culture in chondrogenic media.¹⁰³ Alternatively, PVA-Ma/Gel-MA bioresins have been processed via DLP with visible light photocrosslinking to bioprint articular cartilage derived progenitor cells toward the formation of cartilage.⁹⁵

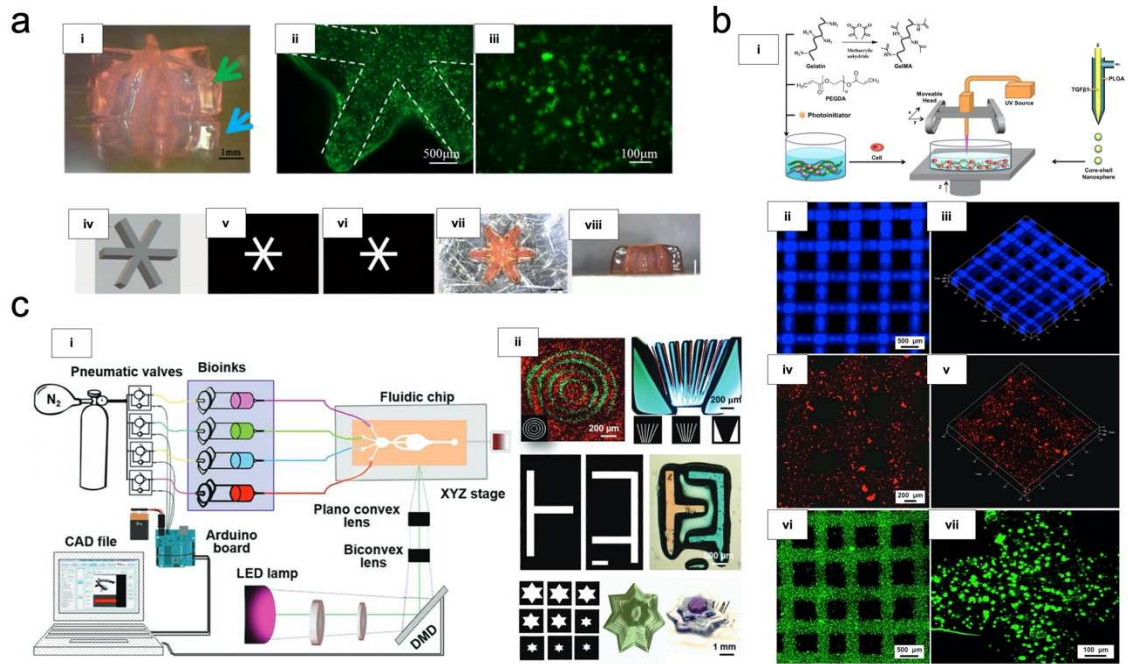


Figure 1.6: Stereolithography (SLA) and digital light processing (DLP) for the formation of articular cartilage. a) (i) Representative images of an asterisk symbol composed of modified-mannan hydrogel that was fabricated via SLA (ii-iii) with viable chondrocytes. (iv-vi) CAD geometry, (v-vi) geometry slices at the top and bottom, respectively, and (vii, viii) representative images of the printed asterisk symbol. Images adapted from ¹⁰¹. b) Schematic of the stereolithography (SLA) approach used to 3D print PEG/gelatin-based hydrogels with incorporated PLGA nanospheres for the delivery of TGF-B1 to encapsulated cells. Representative images of (ii, iii) printed hydrogels (blue), (iv, v) nanospheres (red), and (vi, vii) cells (green) within fabricated constructs. Schematic and images adapted from ¹⁰². c) Schematic overview of how pneumatically controlled microfluidics may be combined with DLP to achieve multi-material printing of heterogeneous constructs. Briefly, 365 nm light was reflected by digital micromirror devices (DMDs) and projected through a lens onto a build plate, which was in contact with a vat of photosensitive bioresin (i.e., PEGDA or GelMA) (ii) Representative images of printed hydrogels fabricated with complex, heterogeneous structures using this multi-material DLP approach. Schematic and images adapted from ¹⁰⁶.

While ongoing work within the field is focused on the continued development of bioresins, past studies have demonstrated that DLP of synthetic polymers can be combined with ECM molecules post-printing for cartilage tissue engineering. For example, Shie and colleagues developed a slow degrading resin for DLP that is composed of a water-soluble and photosensitive polyurethane. MSCs were seeded on these scaffolds, and HA could then be incorporated into the resin to help facilitate MSC chondrogenesis.¹⁰⁴ PCL-gelatin scaffolds have also been developed through an indirect 3D printing technique,

which involves casting of the blended materials within a fugitive negative mold fabricated via DLP. Once PCL/gelatin blends are crosslinked via glutaraldehyde, the mold composed of an alkali-soluble photoresin can be removed via washing with NaOH solution, and the scaffolds can be seeded with cells.¹⁰⁵ It is expected that the ability to achieve multimaterial printing via DLP through the employment of microfluidics will increase the prevalence of approaches that leverage composite or hybrid materials (**Figure 1.6c**).¹⁰⁶

To increase the overall throughput of lithography-based 3D printing, innovative printing technologies have been developed. In continuous liquid interphase polymerization (CLIP), an oxygen permeable window results in the formation of a dead zone in which oxygen inhibition impedes free radical crosslinking; as a result, a liquid resin interface can be maintained despite consistent irradiation with light. Thus, monolithic constructs can be fabricated as the build plate continuously moves up in the z-direction, permitting the fabrication of constructs at rates of hundreds of millimeters per hour. This is in stark contrast to conventional SLA or DLP, which requires that resin flow under the build plate and be replenished in between curing of each successive layer.¹⁰⁷ However, one of the disadvantages of CLIP is that it is limited to materials that undergo free radical crosslinking; as will be discussed in Chapter 3, a range of other photochemistries are becoming increasingly prevalent in light-based biofabrication.

In an alternative approach to improve print speed, volumetric bioprinting involves the curing of photosensitive resins via tomographic light projection through a rotating 3D volume (i.e., computed axial lithography, CAL).^{108,109} Through this novel technique, complex geometries can be readily fabricated, including free-form and free-floating architectures that cannot be formed via conventional layer-by-layer approaches. In addition, volumetric printing permits the formation of centimeter-scale constructs in a rapid manner (on the order of seconds), vastly improving on the print times associated with

extrusion printing and SLA/DLP. Volumetric printing of GelMA supported the encapsulation of viable cells (>85%) and the formation of menisci-shaped constructs that were cultured for fibrocartilage formation that possessed extensive amounts of glycosaminoglycans and type I collagen.¹⁰⁸

1.3.5 Scaffold-Free Biofabrication and Bioassembly

In addition to bioprinting, bioassembly approaches exploit the ability of cell-containing building units such as cell suspensions, spheroids/aggregates, organoids, and/or microtissues to self-organize into functional tissue units. These include approaches that facilitate the automated assembly of cell-containing building blocks such as micromolding, microfluidics and 3D plotting.²⁴ For example, micromolding via additive manufacturing techniques such as inkjet printing and selective laser sintering has been leveraged to scale the formation of spheroids for tissue engineering.¹¹⁰

Scaffold-free fabrication approaches have also been employed to engineer cartilage *in vitro*, including with the kenzan 3D printing method.¹¹¹⁻¹¹³ Briefly, cell spheroids are deposited onto microneedle arrays in user-configured, three-dimensional shapes via an automated handling system. Spheroids are then cultured on the microarray until spheroid fusion and ECM production results in the formation of stable, self-standing tissue constructs. For example, iPSC derived neural crest cells were formed into spheroids, bioprinted via the kenzan method, and differentiated into neocartilage (**Figure 1.7a,b**). Printed tissue constructs possessed high collagen contents, approaching native tissue mechanical properties after 5 weeks of culture (0.88 MPa). Moreover, this approach allows for the formation of large tissue constructs that mimic the articular surface of the femoral condyles and the trochlea.¹¹²

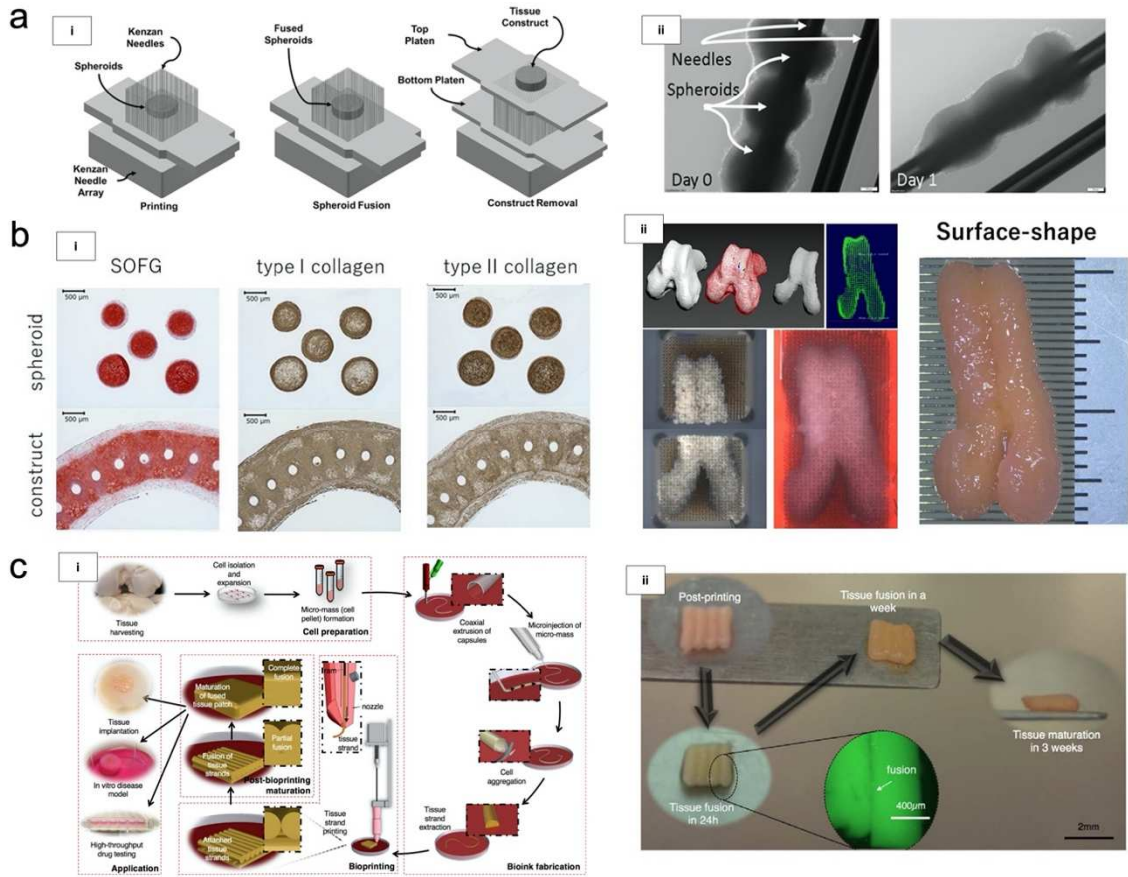


Figure 1.7: Scaffold-free fabrication approaches for articular cartilage formation. a) (i) Schematic of the kenzan bioprinting method and (ii) representative images from the printing process before (Day 0) and after (Day 1) spheroid fusion. Spheroids are first positioned onto a microneedle array into a pattern of interest. Spheroids are then cultured within a bioreactor until spheroid fusion occurs, which results in the formation of a stable, continuous tissue construct that can be removed from the needle array. Schematic and images adapted from ¹¹³. b) (i) MSCs sourced from iPSC-derived neural crest cells (iNCCs) through MSC induction (iNCMSCs) were bioprinted as individual spheroids (initially cultured for 10 days) or as ring constructs and subsequently cultured for 21 days in chondrogenic media. Representative images of Safranin O/Fast Green (SOFG), TUNEL, type I collagen, and type II collagen staining for ring constructs indicate the elaboration of nascent matrix containing both proteoglycans and collagens. However, elevated TUNEL staining around the holes created by Kenzan needles suggests that appreciable cell damage is caused by the fixation of spheroids on the needle arrays. Scale bars=500 μm . (ii) CAD model and design (top) of a minipig distal femoral condyle and trochlear groove (i.e., articular surface-shaped construct) and gross images of the printed construct on two kenzan arrays immediately after printing (left) and 3 days after bioreactor culture (right). (iii) Gross image of the bioprinted articular surface-shaped construct after removal from the kenzan needle array (day 15 of bioreactor culture). Images adapted from ¹¹². c) Schematic overview detailing the fabrication of bioinks from pre-formed microtissues. Cell aggregation is promoted via microinjection of cells within fabricated tubular alginate capsules. Thereafter, tissue strands are extracted and used (ii) for subsequent processing via extrusion bioprinting. The fusion of individual tissue strands with culture gives rise to the maturation of fabricated tissue constructs. Schematic and image adapted from ¹²⁰.

Spheroids hold promise as a clinical cell-based therapy for articular cartilage regeneration,¹¹⁴ with ongoing work focused on exploring how MSCs and chondrocytes in spheroid form can be utilized to improve ACI approaches. Lindberg and colleagues demonstrated that human MSCs (hMSCs), human articular chondrocytes (hACs), and mixtures of these cells can be processed as spheroids and precisely patterned within PCL scaffolds to direct spheroid fusion, either with or without the presence of a biomaterial to modulate the local microenvironment and presence of signaling factors at early timepoints. Importantly, this platform system may enhance our ability to study cell-cell interactions and differentiation capacity across length scales. For example preliminary studies demonstrated that hMSCs are more migratory than hACs when processed as spheroids, and mixed spheroid formulations (i.e., spheroids composed of both hMSCs and hACs) resulted in improved neocartilage formation over the co-culture of discrete hMSC and hAC spheroids.¹¹⁵

Several techniques have also been developed to improve the control over cellular phenotypes during spheroid formation or the culture of cells in pellet form. In one instance, globlet-shaped microwells were fabricated to improve the dynamic presentation of signaling factors during spheroid culture toward improving differentiation of stem cells into chondrocytes.¹¹⁶ Cellular pellets of MSCs can also be employed as modular building units due to their ability to promote mesenchymal condensation, a process known to be involved in cartilage development. However, challenges remain with regards to presenting a homogenous microenvironment to formed pellets, since transport limitations arise in conventional centrifugation or molding methods. To this end, Lee and coworkers fabricated a perichondrium-inspired permeable nanofibrous tube (PINaT) via electrospinning nanofibrous PCL to permit oxygen exchange and growth factor presentation to pellets, accelerating chondrogenic differentiation of iPSCs toward a

hyaline-like phenotype. PINaT pellets exhibited improved formation of repair cartilage over control pellets (formed in conical tubes) when evaluated in an osteochondral defect rat model (i.e., increased Alcian blue, safranin O, and type II collagen staining).¹¹⁷

A range of other building units such as articular cartilage sheets, which are fabricated via layering of decellularized cartilage matrix,¹¹⁸ and microtissues enable the assembly of tissue constructs from mature and functional matrix components in lieu of spheroids or cell pellets. For example, Mekhileri and coworkers developed an automated bioassembly platform that permits controlled localization of microtissues or chondrocyte-laden GelMA microspheres within a 3D plotted PEGT/PBT (poly(ethylene glycol)-terephthalate- poly(butylene terephthalate) block copolymer) scaffold. Microtissues were generated in 96-well plates, thereafter patterned within scaffolds, and cultured, resulting in tissue fusion and long-term formation of ECM proteins consistent with hyaline cartilage.¹¹⁹ In another scaffold-free approach, 8 cm-long tissue strands were implemented as a bioink, exhibiting rapid fusion with the ability to readily self-assemble into large tissue constructs. To create the inks, chondrocyte pellets were first formed, followed by aggregation within alginate tubular capsules to form tissue strands composed of aggregated cells. These strands were then extruded through a print head and cultured, such that over time layers of strands fused together (**Figure 1.7c**).¹²⁰

While these recent advances in bioassembly and scaffold-free biofabrication for cartilage formation are promising, it is expected that the convergence of these approaches with previously discussed biofabrication techniques will further improve our ability to emulate native cartilage. For example, the ability to integrate building units such as spheroids and microtissues, which may be assembled *a priori*, with bioprinting techniques may enable the biomaterial-mediated assembly of tissue constructs significantly larger than those formed by bioinks (i.e., cell suspensions) alone.

1.3.6 Biofabrication for Osteochondral Tissue Engineering

In addition to articular cartilage engineering, the biofabrication approaches herein discussed have also been leveraged for the fabrication of biphasic scaffolds toward osteochondral defect repair,^{121,122} since scaffolds suitable for repairing both articular cartilage and subchondral bone are required for osteochondral tissue engineering (OCTE). For example, microfluidic extrusion print heads can be utilized to bioprint multiple cell-laden hydrogels with varied populations of cells (i.e., MSCs and or chondrocytes), biomaterials, and/or signaling factors to direct differential tissue formation throughout target cartilage and bone zones (**Figure 1.8a**).¹²³ Fused deposition modeling has also been employed to create molds with stratified and graded pore distributions towards mimicking the differences observed in full thickness osteochondral units.¹²⁴ However, one significant advantage of printing biphasic scaffolds for OCTE in lieu of alternative fabrication approaches such as micromolding is the ability to create gradients of ink components to recapitulate gradients of different cells or ECM found in the native osteochondral unit. The inclusion of osteogenic factors such as β -tricalcium phosphate (β -TCP) and hydroxyapatite within bioinks has also been exploited to form calcified cartilage toward engineering the osteochondral interface, an important consideration to achieve tissue integration in full-thickness cartilage defects.^{125,126}

In one study the influence of type I collagen and HA on osteoblast and chondrocyte proliferation, differentiation, and migration were explored, where it was found that each cell type exhibited improved performance when cultured within gels that better mimicked their native ECM (i.e., chondrocytes in HA, osteoblasts in type I collagen). PCL structures were 3D printed with distinct cartilage and bone phases using these defined bioinks to fabricate an osteochondral unit.¹²⁷ Many other studies have adapted this generalizable approach to incorporate chondrogenic and osteogenic signaling factors or varied cell

populations within discrete zones of heterogeneous printed scaffold templates.^{128–130} For example, Wang and coworkers fabricated biphasic scaffolds composed of a peptide/ β -tricalcium phosphate/poly(lactic-co-glycolic acid) bone phase and a poly(D,L-lactic acid-co-trimethylene carbonate) cartilage phase via cryogenic 3D printing; the cartilage frame of composites could then be readily infilled with bMSC-laden collagen I hydrogels to form nascent cartilage (**Figure 1.8b**).¹³¹ PCL/PLGA scaffolds have also been fabricated via extrusion printing for OCTE, with chondroitin sulphate and β -TCP included in the cartilage and bone phases to induce the chondrogenesis or osteogenesis, respectively, of seeded adipose-derived MSCs.¹³²

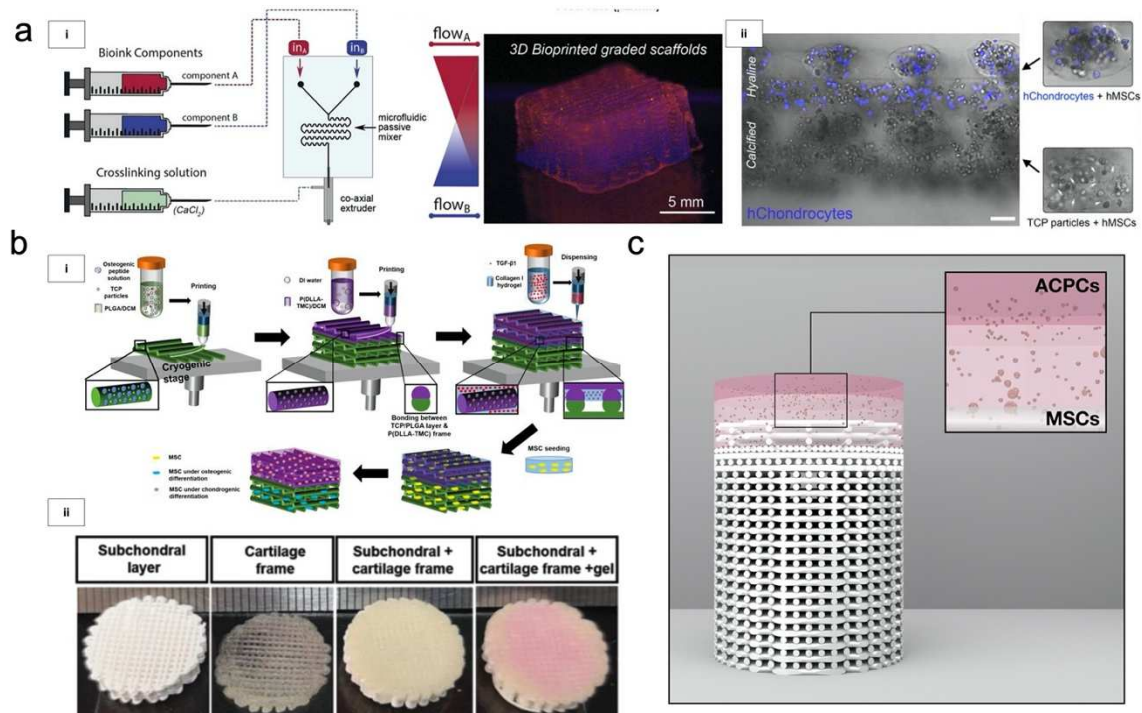


Figure 1.8: Biofabrication of biphasic, cell-laden scaffolds for the repair of full-thickness osteochondral defects. a) (i) Multi-material extrusion bioprinting of human chondrocytes and mesenchymal stromal cells within ECM-based bioinks was leveraged to fabricate graded scaffolds. (ii) Distinct hyaline and calcified zones containing co-culture of cells or β-tricalcium phosphate particles, respectively, were achieved towards engineering osteochondral tissue. Schematic and images adapted from ¹²³. b) (i) Schematic overview of the extrusion 3D printing of an osteogenic peptide/β-tricalcium phosphate/poly(lactic-co-glycolic acid) subchondral phase, a poly(D,L-lactic acid-co-trimethylene carbonate) cartilage frame, and MSC-laden collagen hydrogel for the formation of biphasic scaffolds. (ii) Representative images of the fabricated scaffold frames. Schematic and images adapted from ¹³¹. c) Cell-laden hydrogels (i.e., HA-SH/P(AGE-co-G)) were casted on top of 3D printed PCL osteochondral scaffolds. To engineer zonal constructs, the first layer of the scaffold's chondral phase was seeded with equine MSCs, while the second layer was seeded with chondroprogenitor cells (ACPCs). Schematic adapted from ¹³⁴.

Importantly, a number of biphasic scaffolds fabricated via 3D printing have been evaluated in large animal models of osteochondral damage.^{130,133,134} Critchley and colleagues investigated a range of fiber-reinforced hydrogel composites for their ability to support MSC chondrogenesis *in vitro* and facilitate osteochondral repair *in vivo*.¹³⁰ Fat-pad derived stromal cells were co-cultured with chondrocytes to form neocartilage in the top phase of biphasic scaffolds (with MSCs retained in the bone phase of the scaffold)

prior to implantation. Scaffolds supported the formation of endochondral bone with overlaying cartilage when implanted subcutaneously in rats, as well as the formation of hyaline-like cartilage after 6 months implantation in caprine osteochondral defects.¹³⁰

In a similar approach, PCL bone anchors were 3D printed with protruding, reinforcing fibers to support a chondral phase composed of HA/poly(glycidol) hybrid hydrogel (HA-SH/P(AGE-co-G)) and two distinct zones (**Figure 1.8c**).¹³⁴ Articular cartilage progenitor cells (ACPCs) were encapsulated in the top chondral part of the scaffold, while MSCs were encapsulated below this top phase to mimic the native tidemark (i.e., the cartilage-bone interface). Significant bone growth into the anchor was observed 6 months after implantation in an equine model, while only limited cartilage formation occurred in both zonal constructs and non-zonal controls. Although no differences were observed histologically, zonal constructs resulted in repair cartilage with higher compressive moduli. The authors speculate that inappropriate degradation rates and/or early loss of implanted cells could be responsible for the lack of significant cartilage repair in this system.¹³⁴

In an alternative approach to OCTE, composite scaffolds containing a PLGA/PLA cartilage zone and a PLGA/TCP bone zone were fabricated via the TheriForm process to create osteochondral implants with gradient porosities, mechanical properties, and composition. Briefly, this microfabrication process selectively binds powder-based materials together using a liquid binder to form three-dimensional constructs in a layer-by-layer manner. While chondrocytes preferentially attached to the top phase and formed neocartilage over 6 weeks of in vitro culture, the bottom phase ($E \sim 200$ MPa) approached tensile properties that were comparable to native cancellous bone ($E \sim 700-1000$ MPa).¹³⁵

Selective laser sintering is a similar additive manufacturing technique that involves the use of a laser to mediate the sintering or compaction of powdered materials in 3D space to fabricate a construct. Hydroxyapatite and PCL microspheres were previously

fabricated into multi-layered scaffolds via SLS (with gradients of hydroxyapatite concentration increasing toward the bone phase) and evaluated in a rabbit model of osteochondral defects.¹³⁶ Implantation of these scaffolds into rabbit defects resulted in the formation of repair articular cartilage due to the scaffolds ability to induce subchondral bone regeneration.¹³⁶ Similarly, SLS has been employed to fabricate PCL scaffolds with pores of varied shapes and sizes, which could then be readily combined with chondrocyte-seeded collagen gels.¹³⁷

1.4 CONCLUSIONS

Articular cartilage is critical to the healthy function of joints, but when it is damaged due to an acute or chronic injury, it unfortunately does not undergo self-repair.¹⁰ Surgical interventions are therefore required to mediate the restoration of the damaged articular surface; otherwise, cartilage defects that are left untreated may lead to the progression of osteoarthritis and/or other connective tissue injuries within the joint. While several strategies are clinically employed to treat focal cartilage defects, including microfracture and MACI, often these approaches yield repair tissue that does not fully capture the mechanical properties of healthy cartilage.

To this end, there is a demand for the development of biomaterials that may help facilitate improved neocartilage formation via the presentation of signaling cues to cells. HA hydrogels are of special interest for cartilage tissue engineering since HA is involved in a multitude of biological processes associated with tissue homeostasis, including but not limited to cell signaling via interactions with cell-surface receptors and ECM molecules, organization of the ECM, regulation of tissue hydration and solute transport within the milieu of the ECM, morphogenesis, and wound healing.¹³⁸ Moreover, the material properties of HA hydrogels can be readily tuned so that they may be processed via the additive manufacturing technologies herein discussed. Importantly, this enables the

creation of advanced tissue engineering scaffolds that better recapitulate important features of cartilage such as the anisotropic organization of ECM molecule, which contributes to the impressive mechanical properties of cartilage.

The different biofabrication technologies and representative studies highlighted throughout this chapter emphasize the general additive manufacturing approaches that have been employed for the repair of cartilage to date. In addition, the implementation of hydrogels for different biofabrication techniques is detailed to emphasize the importance of hydrogel design on the manufacturing process of constructs, as well as their resultant properties. However, several comprehensive reviews further describe the use of additive manufacturing technologies for the repair of damaged cartilage. This dissertation builds upon these established paradigms through the continued development of new bioprinting techniques, the rational design of implants for cartilage repair, and the characterization of novel biomaterial inks.

1.5 REFERENCES

1. Mansour, J. M. Biomechanics of Cartilage. *Kinesiol. Mech. pathomechanics Hum. Mov.* 66–79 (2009). doi:10.1002/art.23548
2. Nguyen, T. P. T. *et al.* Cell-laden injectable microgels: Current status and future prospects for cartilage regeneration. *Biomaterials* (2021). doi:10.1016/j.biomaterials.2021.121214
3. Mow, V. C., Holmes, M. H. & Michael Lai, W. Fluid transport and mechanical properties of articular cartilage: A review. *J. Biomech.* **17**, 377–394 (1984).
4. Müller, C. *et al.* Quantitative proteomics at different depths in human articular cartilage reveals unique patterns of protein distribution. *Matrix Biol.* **40**, 34–45 (2014).
5. Huang, C.-Y., Mow, V. C. & Ateshian, G. A. The Role of Flow-Independent Viscoelasticity in the Biphasic Tensile and Compressive Responses of Articular Cartilage. *J. Biomech. Eng.* **123**, 410–417 (2001).
6. Tiku, M. L. & Sabaawy, H. E. Cartilage regeneration for treatment of osteoarthritis: a paradigm for nonsurgical intervention. *Ther. Adv. Musculoskelet. Dis.* **7**, 76–87 (2015).
7. Klein, T. J., Malda, J., Sah, R. L. & Huttmacher, D. W. Tissue Engineering of Articular Cartilage with Biomimetic Zones. *Tissue Eng Part B Rev* **15**, 143–157 (2009).
8. Felson, D. T. An update on the pathogenesis and epidemiology of osteoarthritis. *Radiol. Clin.* **42**, 1–9 (2004).
9. Fisher, M. B. *et al.* Cartilage Repair and Subchondral Bone Remodeling in Response to Focal Lesions in a Mini-Pig Model : **21**, 850–860 (2015).
10. Sadtler, K. *et al.* Design, clinical translation and immunological response of

- biomaterials in regenerative medicine. *Nat. Rev. Mater.* **1**, 16040 (2016).
11. Heir, S. *et al.* Focal cartilage defects in the knee impair quality of life as much as severe osteoarthritis: a comparison of knee injury and osteoarthritis outcome score in 4 patient categories scheduled for knee surgery. *Am. J. Sports Med.* **38**, 231–237 (2010).
 12. Smith, G. D., Knutsen, G. & Richardson, J. B. A clinical review of cartilage repair techniques. *J. Bone Joint Surg. Br.* **87-B**, 445–449 (2005).
 13. Carey, J. L. Fibrocartilage Following Microfracture Is Not as Robust as Native Articular Cartilage. *J. Bone Jt. Surg. Am.* **94**, e80 (2012).
 14. Kalson, N. S., Gikas, P. D. & Briggs, T. W. R. Current strategies for knee cartilage repair. *Int. J. Clin. Pract.* **64**, 1444–1452 (2010).
 15. Chung, C. & Burdick, J. A. Engineering cartilage tissue. *Adv. Drug Deliv. Rev.* **60**, 243–262 (2008).
 16. Devitt, B. M., Bell, S. W., Webster, K. E., Feller, J. A. & Whitehead, T. S. Surgical treatments of cartilage defects of the knee: Systematic review of randomised controlled trials. *Knee* **24**, 508–517 (2017).
 17. Martín, A. R., Patel, J. M., Zlotnick, H. M., Carey, J. L. & Mauck, R. L. Emerging therapies for cartilage regeneration in currently excluded ‘red knee’ populations. *npj Regen. Med.* **4**, (2019).
 18. Makris, E. A., Gomoll, A. H., Malizos, K. N., Hu, J. C. & Athanasiou, K. A. Repair and tissue engineering techniques for articular cartilage. *Nat. Rev. Rheumatol.* **11**, 21–34 (2015).
 19. Kim, I. L., Mauck, R. L. & Burdick, J. A. Hydrogel design for cartilage tissue engineering : A case study with hyaluronic acid. *Biomaterials* **32**, 8771–8782 (2011).

20. Erickson, I. E. *et al.* Macromer density influences mesenchymal stem cell chondrogenesis and maturation in photocrosslinked hyaluronic acid hydrogels. *Osteoarthr. Cartil.* **17**, 1639–1648 (2009).
21. Cosgrove, B. D. *et al.* N-cadherin adhesive interactions modulate matrix mechanosensing and fate commitment of mesenchymal stem cells. *Nat. Mater.* **15**, 1297–1306 (2016).
22. Vega, S. L. *et al.* Combinatorial hydrogels with biochemical gradients for screening 3D cellular microenvironments. *Nat. Commun.* **9**, 614 (2018).
23. Malda, J. *et al.* 25th anniversary article: Engineering hydrogels for biofabrication. *Advanced Materials* **25**, 5011–5028 (2013).
24. Groll, J. *et al.* Biofabrication: Reappraising the definition of an evolving field. *Biofabrication* **8**, (2016).
25. Cui, H., Nowicki, M., Fisher, J. P. & Zhang, L. G. 3D Bioprinting for Organ Regeneration. *Adv. Healthc. Mater.* **6**, 1601118 (2017).
26. Woodfield, T. B. F. *et al.* Biofabrication in Tissue Engineering. in *Comprehensive Biomaterials II* (ed. Paul, M.) (Elsevier, 2017).
27. Chartrain, N. A., Williams, C. B. & Whittington, A. R. A review on fabricating tissue scaffolds using vat photopolymerization. *Acta Biomater.* **74**, 90–111 (2018).
28. Prendergast, M. E. & Burdick, J. A. Recent Advances in Enabling Technologies in 3D Printing for Precision Medicine. *Adv. Mater.* **32**, 1–14 (2020).
29. Kyle, S., Jessop, Z. M., Al-Sabah, A. & Whitaker, I. S. ‘Printability’ of Candidate Biomaterials for Extrusion Based 3D Printing: State-of-the-Art’. *Adv. Healthc. Mater.* **6**, 2017 (2017).
30. Groll, J. *et al.* A definition of bioinks and their distinction from biomaterial inks. *Biofabrication* **11**, 013001 (2019).

31. Groen, W. M., Diloksumpan, P., van Weeren, P. R., Levato, R. & Malda, J. From intricate to integrated: Biofabrication of articulating joints. *J. Orthop. Res.* **35**, 2089–2097 (2017).
32. Feinberg, A. W. & Miller, J. S. Progress in three-dimensional bioprinting. *MRS Bull.* **42**, 557–562 (2017).
33. Decante, G. *et al.* Engineering bioinks for 3D bioprinting. *Biofabrication* **13**, (2021).
34. Diamantides, N., Dugopolski, C., Blahut, E., Kennedy, S. & Bonassar, L. J. High density cell seeding affects the rheology and printability of collagen bioinks. *Biofabrication* **11**, (2019).
35. Blaeser, A. *et al.* Controlling Shear Stress in 3D Bioprinting is a Key Factor to Balance Printing Resolution and Stem Cell Integrity. *Adv. Healthc. Mater.* **5**, 326–333 (2016).
36. Müller, M., Öztürk, E., Arlov, Ø., Gatenholm, P. & Zenobi-Wong, M. Alginate Sulfate–Nanocellulose Bioinks for Cartilage Bioprinting Applications. *Ann. Biomed. Eng.* **45**, 210–223 (2017).
37. Prendergast, M. E., Davidson, M. D. & Burdick, J. A. A biofabrication method to align cells within bioprinted photocrosslinkable and cell-degradable hydrogel constructs via embedded fibers. *Biofabrication* **13**, 044108 (2021).
38. Malda, J. *et al.* 25th anniversary article: Engineering hydrogels for biofabrication. *Adv. Mater.* **25**, 5011–5028 (2013).
39. Costantini, M. *et al.* 3D bioprinting of BM-MSCs-loaded ECM biomimetic hydrogels for in vitro neocartilage formation. *Biofabrication* **8**, (2016).
40. Chu, Y. *et al.* Long-term stability, high strength, and 3D printable alginate hydrogel for cartilage tissue engineering application. *Biomed. Mater.* **16**, 064102 (2021).

41. Bertlein, S. *et al.* Thiol–Ene Clickable Gelatin: A Platform Bioink for Multiple 3D Biofabrication Technologies. *Adv. Mater.* **29**, (2017).
42. Ren, X. *et al.* Engineering zonal cartilage through bioprinting collagen type II hydrogel constructs with biomimetic chondrocyte density gradient. *BMC Musculoskelet. Disord.* **17**, 301 (2016).
43. Mouser, V. H. M. *et al.* Yield stress determines bioprintability of hydrogels based on gelatin-methacryloyl and gellan gum for cartilage bioprinting. *Biofabrication* **8**, 1–13 (2016).
44. Pan, J. F. *et al.* Evaluation of synovium-derived mesenchymal stem cells and 3D printed nanocomposite scaffolds for tissue engineering. *Sci. Technol. Adv. Mater.* **16**, (2015).
45. Wu, H. *et al.* Preparation and characterization of a novel galactomannan based bioink for 3D bioprinting. *J. Phys. Conf. Ser.* **1948**, (2021).
46. Kang, H. W. *et al.* A 3D bioprinting system to produce human-scale tissue constructs with structural integrity. *Nat. Biotechnol.* **34**, 312–319 (2016).
47. Daly, A. C., Critchley, S. E., Rencsok, E. M. & Kelly, D. J. A comparison of different bioinks for 3D bioprinting of fibrocartilage and hyaline cartilage. *Biofabrication* **8**, (2016).
48. Petta, D. *et al.* Hyaluronic acid as a bioink for extrusion-based 3D printing. *Biofabrication* **12**, (2020).
49. Müller, M., Becher, J., Schnabelrauch, M. & Zenobi-Wong, M. Nanostructured Pluronic hydrogels as bioinks for 3D bioprinting. *Biofabrication* **7**, (2015).
50. Stichler, S. *et al.* Double printing of hyaluronic acid/poly(glycidol) hybrid hydrogels with poly(ϵ -caprolactone) for MSC chondrogenesis. *Biofabrication* **9**, (2017).
51. Irmak, G. & Gümüşderelioglu, M. Photo-activated platelet-rich plasma (PRP) -

- based patient-specific bio-ink for cartilage tissue engineering. *Biomed. Mater.* **15**, (2020).
52. Kesti, M. *et al.* Bioprinting Complex Cartilaginous Structures with Clinically-Compliant Biomaterials. *Adv. Funct. Mater.* **25**, 7406–7417 (2015).
 53. Rathan, S. *et al.* Fiber Reinforced Cartilage ECM Functionalized Bioinks for Functional Cartilage Tissue Engineering. *Adv. Healthc. Mater.* **8**, 1–11 (2019).
 54. Kim, B. S., Kim, H., Gao, G., Jang, J. & Cho, D. W. Decellularized extracellular matrix: A step towards the next generation source for bioink manufacturing. *Biofabrication* **9**, (2017).
 55. Abbadessa, A. *et al.* A Synthetic Thermosensitive Hydrogel for Cartilage Bioprinting and Its Biofunctionalization with Polysaccharides. *Biomacromolecules* **17**, 2137–2147 (2016).
 56. Yang, F., Tadepalli, V. & Wiley, B. J. 3D Printing of a Double Network Hydrogel with a Compression Strength and Elastic Modulus Greater than those of Cartilage. *ACS Biomater. Sci. Eng.* **3**, 863–869 (2017).
 57. Markstedt, K. *et al.* 3D bioprinting human chondrocytes with nanocellulose-alginate bioink for cartilage tissue engineering applications. *Biomacromolecules* **16**, 1489–1496 (2015).
 58. Lee, M., Bae, K., Levinson, C. & Zenobi-Wong, M. Nanocomposite bioink exploits dynamic covalent bonds between nanoparticles and polysaccharides for precision bioprinting. *Biofabrication* **12**, (2020).
 59. Visser, J. *et al.* Biofabrication of multi-material anatomically shaped tissue constructs. *Biofabrication* **5**, (2013).
 60. Serex, L., Bertsch, A. & Renaud, P. Microfluidics: A New Layer of Control for Extrusion-Based 3D Printing. *Micromachines* **9**, 86 (2018).

61. Liu, W. *et al.* Rapid Continuous Multimaterial Extrusion Bioprinting. *Adv. Mater.* **29**, 1604630 (2017).
62. Skylar-Scott, M. A., Mueller, J., Visser, C. W. & Lewis, J. A. Voxeled soft matter via multimaterial multinozzle 3D printing. *Nature* **575**, 330–335 (2019).
63. Schuurman, W. *et al.* Bioprinting of hybrid tissue constructs with tailorable mechanical properties. *Biofabrication* **3**, (2011).
64. Kundu, J., Shim, J.-H., Jang, J., Kim, S.-W. & Cho, D.-W. An additive manufacturing-based PCL–alginate–chondrocyte bioprinted scaffold for cartilage tissue engineering. *J Tissue Eng Regen Med* **9**, 1286–1297 (2015).
65. Olubamiji, A. D. *et al.* Modulating mechanical behaviour of 3D-printed cartilage-mimetic PCL scaffolds: Influence of molecular weight and pore geometry. *Biofabrication* **8**, (2016).
66. Kosik-Kozioł, A. *et al.* PLA short sub-micron fiber reinforcement of 3D bioprinted alginate constructs for cartilage regeneration. *Biofabrication* **9**, (2017).
67. Mouser, V. H. M. *et al.* Development of a thermosensitive HAMA-containing bio-ink for the fabrication of composite cartilage repair constructs. *Biofabrication* **9**, (2017).
68. Duchi, S. *et al.* Handheld Co-Axial Bioprinting: Application to in situ surgical cartilage repair. *Sci. Rep.* **7**, 5837 (2017).
69. Di Bella, C. *et al.* In situ handheld three-dimensional bioprinting for cartilage regeneration. *J. Tissue Eng. Regen. Med.* **12**, 611–621 (2018).
70. O’Connell, C. D. *et al.* Development of the Biopen: A handheld device for surgical printing of adipose stem cells at a chondral wound site. *Biofabrication* **8**, 015019 (2016).
71. Onofrillo, C. *et al.* Biofabrication of human articular cartilage: A path towards the

- development of a clinical treatment. *Biofabrication* **10**, (2018).
72. Robinson, T. M., Hutmacher, D. W. & Dalton, P. D. The Next Frontier in Melt Electrospinning : Taming the Jet. *Adv. Funct. Mater.* **29**, 1904664 (2019).
 73. Wunner, F. M. *et al.* Melt Electrospinning Writing of Three-dimensional Poly(ϵ -caprolactone) Scaffolds with Controllable Morphologies for Tissue Engineering Applications. *J. Vis. Exp.* (2017). doi:10.3791/56289
 74. Hochleitner, G. *et al.* Additive manufacturing of scaffolds with sub-micron filaments via melt electrospinning writing. *Biofabrication* **7**, 035002 (2015).
 75. Visser, J. *et al.* Reinforcement of hydrogels using three-dimensionally printed microfibrils. *Nat. Commun.* **6**, 6933 (2015).
 76. Bas, O. *et al.* Enhancing structural integrity of hydrogels by using highly organised melt electrospun fibre constructs. *Eur. Polym. J.* **72**, 451–463 (2015).
 77. Bas, O. *et al.* Biofabricated soft network composites for cartilage tissue engineering. *Biofabrication* **9**, 025014 (2017).
 78. de Ruijter, M., Ribeiro, A., Dokter, I., Castilho, M. & Malda, J. Simultaneous Micropatterning of Fibrous Meshes and Bioinks for the Fabrication of Living Tissue Constructs. *Adv. Healthc. Mater.* **8**, 1800418 (2019).
 79. Diloksumpan, P. *et al.* Combining multi-scale 3D printing technologies to engineer reinforced hydrogel-ceramic interfaces. *Biofabrication* **12**, (2020).
 80. Castilho, M., Mouser, V., Chen, M., Malda, J. & Ito, K. Bi-layered micro-fibre reinforced hydrogels for articular cartilage regeneration. *Acta Biomater.* **95**, 297–306 (2019).
 81. Bas, O. *et al.* Rational design and fabrication of multiphasic soft network composites for tissue engineering articular cartilage: A numerical model-based approach. *Chem. Eng. J.* **340**, 15–23 (2018).

82. Castilho, M. *et al.* Mechanical behavior of a soft hydrogel reinforced with three-dimensional printed microfibre scaffolds. *Sci. Rep.* **8**, 1245 (2018).
83. Prasopthum, A., Shakesheff, K. M. & Yang, J. Direct three-dimensional printing of polymeric scaffolds with nanofibrous topography. *Biofabrication* **10**, (2018).
84. Moutos, F. T., Freed, L. E. & Guilak, F. A biomimetic three-dimensional woven composite scaffold for functional tissue engineering of cartilage. *Nat. Mater.* **6**, 162–167 (2007).
85. Levorson, E. J. *et al.* Fabrication and characterization of multiscale electrospun scaffolds for cartilage regeneration. *Biomed. Mater.* **8**, (2013).
86. Jia, Z. *et al.* Gas-foaming three-dimensional electrospun nanofiber scaffold improved three-dimensional cartilage regeneration. *Mater. Res. Express* **8**, (2021).
87. Prendergast, M. E., Davidson, M. D. & Burdick, J. A. A biofabrication method to align cells within bioprinted photocrosslinkable and cell-degradable hydrogel constructs via embedded fibers. *Biofabrication* **13**, (2021).
88. Gupta, S. & Bit, A., 3D bioprinting in tissue engineering and regenerative medicine. *Flow Dyn. Tissue Eng. Blood Vessel.* (2020). doi:10.1088/978-0-7503-2088-7ch3
89. Cui, X., Breitenkamp, K., Lotz, M. & D’Lima, D. Synergistic action of fibroblast growth factor-2 and transforming growth factor-beta1 enhances bioprinted human neocartilage formation. *Biotechnol. Bioeng.* **109**, 2357–2368 (2012).
90. Kim, M., Steinberg, D. R., Burdick, J. A. & Mauck, R. L. Extracellular vesicles mediate improved functional outcomes in engineered cartilage produced from MSC/chondrocyte cocultures. *Proc. Natl. Acad. Sci. U. S. A.* **116**, 1569–1578 (2019).

91. Daly, A. C. & Kelly, D. J. Biofabrication of spatially organised tissues by directing the growth of cellular spheroids within 3D printed polymeric microchambers. *Biomaterials* **197**, 194–206 (2019).
92. Xu, T. *et al.* Hybrid printing of mechanically and biologically improved constructs for cartilage tissue engineering applications. *Biofabrication* **5**, (2013).
93. Melchels, F. P. W., Feijen, J. & Grijpma, D. W. A review on stereolithography and its applications in biomedical engineering. *Biomaterials* **31**, 6121–6130 (2010).
94. Arcaute, K., Mann, B. & Wicker, R. Stereolithography of spatially controlled multi-material bioactive poly(ethylene glycol) scaffolds. *Acta Biomater.* **6**, 1047–1054 (2010).
95. Lim, K. S. *et al.* Bio-resin for high resolution lithography-based biofabrication of complex cell-laden constructs. *Biofabrication* **10**, 034101 (2018).
96. Melchels, F. P. W., Feijen, J. & Grijpma, D. W. A poly(D,L-lactide) resin for the preparation of tissue engineering scaffolds by stereolithography. *Biomaterials* **30**, 3801–3809 (2009).
97. Lin, H. *et al.* Application of Visible Light-based Projection Stereolithography for Live Cell-Scaffold Fabrication with Designed Architecture. *Biomaterials* **34**, 331–339 (2013).
98. Ng, W. L. *et al.* Vat polymerization-based bioprinting - process, materials, applications and regulatory challenges. *Biofabrication* **12**, (2020).
99. Mačiulaitis, J. *et al.* Preclinical study of SZ2080 material 3D microstructured scaffolds for cartilage tissue engineering made by femtosecond direct laser writing lithography. *Biofabrication* **7**, (2015).
100. Sun, A. X., Lin, H., Beck, A. M., Kilroy, E. J. & Tuan, R. S. Projection Stereolithographic Fabrication of Human Adipose Stem Cell-incorporated

- Biodegradable Scaffolds for Cartilage Tissue Engineering. *Front. Bioeng. Biotechnol.* **3**, 1–9 (2015).
101. Huang, Y. *et al.* Modified mannan for 3D bioprinting: A potential novel bioink for tissue engineering. *Biomed. Mater.* **16**, (2021).
 102. Zhu, W. *et al.* 3D bioprinting mesenchymal stem cell-laden construct with core-shell nanospheres for cartilage tissue engineering. *Nanotechnology* **29**, (2018).
 103. Kim, S. H. *et al.* Precisely printable and biocompatible silk fibroin bioink for digital light processing 3D printing. *Nat. Commun.* **9**, 1–14 (2018).
 104. Shie, M. Y. *et al.* 3D printing of cytocompatible water-based light-cured polyurethane with hyaluronic acid for cartilage tissue engineering applications. *Materials (Basel)*. **10**, (2017).
 105. Jung, J. W. *et al.* A new method of fabricating a blend scaffold using an indirect three-dimensional printing technique. *Biofabrication* **7**, (2015).
 106. Miri, A. K. *et al.* Microfluidics-Enabled Multimaterial Maskless Stereolithographic Bioprinting. *Adv. Mater.* **30**, (2018).
 107. Tumbleston, J. R. *et al.* Continuous liquid interface production of 3D objects. *Science (80-.)*. **347**, 1349–1352 (2015).
 108. Bernal, P. N. *et al.* Volumetric Bioprinting of Complex Living-Tissue Constructs within Seconds. *Adv. Mater.* **31**, 1904209 (2019).
 109. Kelly, B. E., Bhattacharya, I., Heidari, H. & Shusteff, M. Volumetric additive manufacturing via tomographic reconstruction. *Science (80-.)*. 1075–1079 (2019).
 110. Decarli, M. C. *et al.* Cell spheroids as a versatile research platform: Formation mechanisms, high throughput production, characterization and applications. *Biofabrication* **13**, (2021).
 111. Moldovan, N. I., Hibino, N. & Nakayama, K. Principles of the kenzan method for

- robotic cell spheroid-based three-dimensional bioprinting. *Tissue Eng. - Part B Rev.* **23**, 237–244 (2017).
112. Nakamura, A. *et al.* Bio-3D printing iPSC-derived human chondrocytes for articular cartilage regeneration. *Biofabrication* **13**, (2021).
 113. Aguilar, I. N. *et al.* Scaffold-free bioprinting of mesenchymal stem cells with the regenova printer: Optimization of printing parameters. *Bioprinting* **15**, e00048 (2019).
 114. Negoro, T., Takagaki, Y., Okura, H. & Matsuyama, A. Trends in clinical trials for articular cartilage repair by cell therapy. *npj Regen. Med.* **3**, (2018).
 115. Lindberg, G. C. J. *et al.* Probing Multicellular Tissue Fusion of Cocultured Spheroids — A 3D-Bioassembly Model. *Adv. Sci.* **2103320**, 1–14 (2021).
 116. Udomluck, N., Kim, S. H., Cho, H., Park, J. Y. & Park, H. Three-dimensional cartilage tissue regeneration system harnessing goblet-shaped microwells containing biocompatible hydrogel. *Biofabrication* **12**, (2020).
 117. Lee, S. J. *et al.* Perichondrium-inspired permeable nanofibrous tube well promoting differentiation of hiPSC-derived pellet toward hyaline-like cartilage pellet. *Biofabrication* **13**, (2021).
 118. Xue, J. *et al.* Repair of articular cartilage defects with acellular cartilage sheets in a swine model. *Biomed. Mater.* **13**, (2018).
 119. Mekhileri, N. V. *et al.* Automated 3D bioassembly of micro-tissues for biofabrication of hybrid tissue engineered constructs. *Biofabrication* **10**, (2018).
 120. Yu, Y. *et al.* Three-dimensional bioprinting using self-Assembling scalable scaffold-free ‘tissue strands’ as a new bioink. *Sci. Rep.* **6**, 1–11 (2016).
 121. Li, X., Ding, J., Wang, J., Zhuang, X. & Chen, X. Biomimetic biphasic scaffolds for osteochondral defect repair. *Regen. Biomater.* **2**, 221–228 (2015).

122. Daly, A. C. *et al.* 3D Bioprinting for Cartilage and Osteochondral Tissue Engineering. *Adv. Healthc. Mater.* **1700298**, 1700298 (2017).
123. Idaszek, J. *et al.* 3D bioprinting of hydrogel constructs with cell and material gradients for the regeneration of full-thickness chondral defect using a microfluidic printing head. *Biofabrication* **11**, (2019).
124. Nowicki, M. A., Castro, N. J., Plesniak, M. W. & Zhang, L. G. 3D printing of novel osteochondral scaffolds with graded microstructure. *Nanotechnology* **27**, (2016).
125. Kosik-Kozioł, A. *et al.* 3D bioprinted hydrogel model incorporating β -tricalcium phosphate for calcified cartilage tissue engineering. *Biofabrication* **11**, (2019).
126. You, F., Chen, X., Cooper, D. M. L., Chang, T. & Eames, B. F. Homogeneous hydroxyapatite/alginate composite hydrogel promotes calcified cartilage matrix deposition with potential for three-dimensional bioprinting. *Biofabrication* **11**, (2019).
127. Park, J. Y. *et al.* A comparative study on collagen type i and hyaluronic acid dependent cell behavior for osteochondral tissue bioprinting. *Biofabrication* **6**, (2014).
128. Shim, J. H. *et al.* Three-dimensional bioprinting of multilayered constructs containing human mesenchymal stromal cells for osteochondral tissue regeneration in the rabbit knee joint. *Biofabrication* **8**, (2016).
129. Shim, J. H., Lee, J. S., Kim, J. Y. & Cho, D. W. Bioprinting of a mechanically enhanced three-dimensional dual cell-laden construct for osteochondral tissue engineering using a multi-head tissue/organ building system. *J. Micromechanics Microengineering* **22**, (2012).
130. Critchley, S. *et al.* 3D printing of fibre-reinforced cartilaginous templates for the regeneration of osteochondral defects. *Acta Biomater.* **113**, 130–143 (2020).

131. Wang, C. *et al.* Cryogenic 3D printing of heterogeneous scaffolds with gradient mechanical strengths and spatial delivery of osteogenic peptide/TGF- β 1 for osteochondral tissue regeneration. *Biofabrication* **12**, (2020).
132. Natarajan, A., Sivadas, V. P. & Nair, P. D. 3D-printed biphasic scaffolds for the simultaneous regeneration of osteochondral tissues. *Biomed. Mater.* **16**, (2021).
133. Zhang, T. *et al.* Biomimetic design and fabrication of multilayered osteochondral scaffolds by low-temperature deposition manufacturing and thermal-induced phase-separation techniques. *Biofabrication* **9**, (2017).
134. Mancini, I. A. D. *et al.* A composite hydrogel-3D printed thermoplast osteochondral anchor as example for a zonal approach to cartilage repair: In vivo performance in a long-term equine model. *Biofabrication* **12**, (2020).
135. Sherwood, J. K. *et al.* A three-dimensional osteochondral composite scaffold for articular cartilage repair. *Biomaterials* **23**, 4739–4751 (2002).
136. Du, Y. *et al.* Selective laser sintering scaffold with hierarchical architecture and gradient composition for osteochondral repair in rabbits. *Biomaterials* **137**, 37–48 (2017).
137. Chen, C. H., Shyu, V. B. H., Chen, J. P. & Lee, M. Y. Selective laser sintered poly- ϵ -caprolactone scaffold hybridized with collagen hydrogel for cartilage tissue engineering. *Biofabrication* **6**, (2014).
138. Dicker, K. T. *et al.* Hyaluronan: A simple polysaccharide with diverse biological functions. *Acta Biomater.* **10**, 1558–1570 (2014).

CHAPTER 2: RESEARCH OVERVIEW

2.1 SPECIFIC AIMS

The overall goal of this dissertation work was to develop light-based biofabrication techniques to process hyaluronic acid (HA) hydrogels into useful structures for the repair of cartilage tissue. The completion of these specific aims has improved our understanding of how hydrogels can be designed in combination with biofabrication techniques towards the translation of clinically-relevant constructs for cartilage tissue engineering.

Specific Aim 1: Employ an *in situ* crosslinking bioprinting technique to fabricate MSC-laden HA constructs for the formation of cartilage.

Hypothesis: Norbornene-modified HA (NorHA) hydrogels can be processed with in situ crosslinking through control over the thiol-ene crosslinking kinetics and printing parameters into structures with defined shapes that support mesenchymal stromal cell (MSC) chondrogenesis and cartilage formation.

A limitation of current clinical approaches to cartilage repair is that they often do not account for variabilities in defect size and shape, which can lead to repair tissues that do not fully integrate with peripheral tissue.¹ 3D bioprinting enables the fabrication of cell-laden hydrogels with patient-specific geometries and controlled presentation of physicochemical cues, potentially improving prospects for defect filling and repair tissue integration.²⁻⁵ A range of bioinks, or biomaterials that may be processed with cells via automated biofabrication technologies,⁶ have been used to create constructs with precisely defined architectures;² however, many hydrogels do not exhibit suitable rheological properties for extrusion-bioprinting.⁷⁸⁻¹⁶ This limits the

advancement of hydrogels for cartilage tissue engineering, as desirable materials exist that cannot be processed using these biofabrication methods.^{8–16}

To address this, we previously developed a technique, termed *in situ* crosslinking, where non-viscous and photocrosslinkable materials are cured with light as they pass through a transparent capillary during printing.¹⁷ Here, we implemented this *in situ* crosslinking method and visible light to print NorHA hydrogels (~6 kPa) suitable for MSC chondrogenesis and tissue formation, where NorHA hydrogels are crosslinked from non-viscous solutions and would not have been printable with extrusion-bioprinting.¹⁷ NorHA hydrogels crosslink through a controlled thiol-ene reaction and are largely based on HA, which has been shown to be a promising component of hydrogels to support MSC chondrogenesis.¹⁸ Printing parameters were varied and combined with an understanding of gelation behavior to fabricate printed constructs. Once printed, MSC chondrogenesis and neocartilage formation within MSC-laden constructs were investigated.

Specific Aim 2: Fabricate composites of soft hydrogels with supporting melt electrowritten polycaprolactone and evaluate their potential for neocartilage formation.

Hypothesis: NorHA hydrogels with lower crosslink densities will exhibit enhanced matrix distribution and the formation of functional tissue properties when compared to hydrogels with increased crosslinking. Moreover, loosely crosslinked hydrogels can be mechanically reinforced with melt-electrowritten polycaprolactone meshes to improve bulk construct properties while retaining their ability to support tissue formation.

Within the field of cartilage tissue engineering, hydrogels have been employed to encapsulate MSCs and support their chondrogenesis and cartilage formation;

however, there are many biochemical and biophysical properties that may influence their success. For example, NorHA hydrogels are crosslinked in the presence of light and a di-thiol crosslinker, which allows for easy tuning of crosslink density. To investigate the influence of crosslink density on MSC chondrogenesis and tissue formation, NorHA hydrogels were fabricated with moduli ranging from ~2-60 kPa and cultured for up to 8 weeks. Bovine MSC chondrogenesis and cartilage tissue properties (gene expression, mechanical properties, ECM distribution) were then assessed to elucidate how the production and organization of extracellular matrix in NorHA hydrogels varies as a function of crosslink density.

While NorHA hydrogels may support the chondrogenesis of encapsulated MSCs and neocartilage formation, their low initial mechanics may restrict translation into the clinic. The employment of additive manufacturing techniques may address this concern and expand upon material combinations that meet the demands of *in vivo* loading environments. Melt electrowriting is a biofabrication process that permits the fabrication of polycaprolactone (PCL) meshes with unparalleled precision, such that composites of PCL and NorHA hydrogels can be readily prepared. Hydrogels that supported promising MSC chondrogenesis and neocartilage formation were reinforced with PCL meshes fabricated via melt electrowriting to create composites with enhanced initial mechanics. Composite constructs were then evaluated over 8 weeks for cartilage tissue formation *in vitro* (gene expression, mechanical properties, ECM distribution). Further, the ability of composites to integrate with cartilage was evaluated with *ex vivo* chondral plugs via pushout testing, MicroCT analyses, and histology/immunohistochemistry.

Specific Aim 3: Evaluate implantation of MEW-NorHA composites to facilitate cartilage repair in a porcine model of articular cartilage damage.

Hypothesis: MEW-NorHA composites will be readily secured within focal articular cartilage defects through two different fixation methods (bioresorbable polylactic acid (PLA) pins, fibrin glue) to support cartilage tissue repair.

Although *in vitro* cultures are important in the development of cartilage tissue engineering approaches, ultimately it is important to assess implantable constructs in cartilage defect models. A wide range of models have been developed to assess tissue engineered cartilage, ranging from small animals (mouse, rat) to intermediate-sized animals (rabbit) to large animals (porcine, goat). Each of these models are not without their limitations related to clinically-relevant sizes, natural regeneration, or difficulty in implementation. Despite their challenges, we chose a porcine model as a first step to investigate our composites. Porcine models were used, as larger animal models better recapitulate the loading environments of human joints and permit treatment of clinically relevant defect sizes;¹⁹ further, porcine models are commonly used in cartilage repair studies due to porcine cartilage thickness resembling human cartilage and operative access.^{19,20}

First, after validating the ability of composites containing bovine MSCs to support neocartilage formation and integration with native tissue in an *ex vivo* model, an *in vitro* culture study was performed to ensure that adult porcine MSCs across multiple donors and encapsulated in composites also form neocartilage. Composites were then implanted into 4-mm chondral defects formed in porcine models to assess their ability to form functional repair tissue *in vivo* 12 weeks after implantation. Outcomes included macroscopic and histologic analysis, mechanical testing, and MicroCT.

Specific Aim 4: Engineer hydrolytically degradable, thiol-ene step growth hydrogels amenable to digital light processing (DLP) for cartilage repair applications.

Hypothesis: Hydrogels composed of macromers with hydrolytically labile, pendant norbornene groups can be fabricated into macroporous constructs via DLP and engineered with user-defined degradability for future implementation in autologous matrix-induced chondrogenesis (AMIC)-based therapies for cartilage damage.

Alternative approaches to cartilage repair involve the use of acellular scaffolds to promote repair via presentation of signaling cues to endogenous cells. Specifically, implantation of an acellular, porous scaffold into a cartilage defect combined with microfracture allows for potential: (i) stabilization of the clot within the defect, (ii) infiltration of MSCs into the implanted scaffold, and (iii) delivery of factors that can stimulate chondrogenesis. Through AMIC-based approaches, these cells may then promote the formation and organization of improved repair cartilage within the scaffold. However, the success of this approach is predicated on the scaffold's ability to degrade as cells form and distribute nascent tissue throughout the scaffold, as well as the ability of scaffolds to exhibit controlled porosity. The work in this Aim represents a step towards improvement of this approach, although the work is limited to material development and characterization.

Enzymatically degradable hydrogels have been previously explored for this use, but these systems rely heavily on the dynamic *in vivo* environment, which may exhibit variable enzyme concentrations prior to and after scaffold implantation, resulting in unpredictable degradation behaviors. Thus, we implemented the design of hydrolytically degradable hydrogels with user-defined degradation rates, such that the hydrogel degradation behavior is more controlled and predictable. Carbic anhydride

was reacted with HA to create a novel resin (NorHA_{CA}) that is suitable for DLP, and the mechanical properties and degradability were investigated experimentally. A Monte Carlo stochastic model was also developed using empirical hydrogel swelling properties to characterize and predict the degradation behavior of NorHA_{CA} hydrogels, including those with mixed degradable/non-degradable macromer formulations. Lastly, proof-of-concept processing of NorHA_{CA} hydrogels was performed toward creating resins with degradation rates that may match the rate of neocartilage formation in future cartilage repair applications.

2.2 CHAPTER OUTLINE

Chapter 1 highlights the clinical demand that exists for innovations in articular cartilage repair and the ways in which biofabrication approaches have been leveraged towards improving repair cartilage for future therapies. Chapter 3 details how the fundamentals of common photocrosslinking chemistries inform the design and implementation of bioinks and biomaterials in light-based biofabrication techniques. Thereafter, Chapter 4 discusses the work proposed in Specific Aim 1 on the use of *in situ* crosslinking for the formation of large cartilage constructs with controlled shapes. Chapter 5 focuses on work proposed throughout Specific Aim 2, which details the influence of crosslink density on cartilage formation, the fabrication process and characterization of MEW mesh-NorHA hydrogel composites, and the functional utility of these composites in *ex vivo* models. Chapter 6 describes the evaluation of composite implantation and their ability to repair cartilage in a porcine model of cartilage damage. In Chapter 7, the synthesis and design of hydrolytically degradable HA hydrogels described in Specific Aim 4 is detailed. In addition to their characterization, this chapter also describes preliminary studies on how these hydrogels may be tuned to yield variable degradation timescales and printing via DLP. Finally, Chapter 8 discusses the conclusions, limitations, and future directions of this

dissertation work, reviewing how these findings may inform future therapies for cartilage repair.

2.3 REFERENCES

1. Chung, C. & Burdick, J. A. Engineering cartilage tissue. *Adv. Drug Deliv. Rev.* **60**, 243–262 (2008).
2. Malda, J. *et al.* 25th anniversary article: Engineering hydrogels for biofabrication. *Advanced Materials* **25**, 5011–5028 (2013).
3. Cui, H., Nowicki, M., Fisher, J. P. & Zhang, L. G. 3D Bioprinting for Organ Regeneration. *Adv. Healthc. Mater.* **6**, 1601118 (2017).
4. Groll, J. *et al.* Biofabrication: Reappraising the definition of an evolving field. *Biofabrication* **8**, (2016).
5. Woodfield, T. B. F. *et al.* Biofabrication in Tissue Engineering. in *Comprehensive Biomaterials II* (ed. Paul, M.) (Elsevier, 2017).
6. Groll, J. *et al.* A definition of bioinks and their distinction from biomaterial inks. *Biofabrication* **11**, 013001 (2019).
7. Kyle, S., Jessop, Z. M., Al-Sabah, A. & Whitaker, I. S. ‘Printability’ of Candidate Biomaterials for Extrusion Based 3D Printing: State-of-the-Art’. *Adv. Healthc. Mater.* **6**, 2017 (2017).
8. Xavier, J. R. *et al.* Bioactive nanoengineered hydrogels for bone tissue engineering: A growth-factor-free approach. *ACS Nano* **9**, 3109–3118 (2015).
9. Hong, S. *et al.* 3D Printing of Highly Stretchable and Tough Hydrogels into Complex, Cellularized Structures. *Adv. Mater.* **27**, 4035–4040 (2015).
10. Yang, F., Tadepalli, V. & Wiley, B. J. 3D Printing of a Double Network Hydrogel with a Compression Strength and Elastic Modulus Greater than those of Cartilage. *ACS Biomater. Sci. Eng.* **3**, 863–869 (2017).

11. Markstedt, K. *et al.* 3D bioprinting human chondrocytes with nanocellulose-alginate bioink for cartilage tissue engineering applications. *Biomacromolecules* **16**, 1489–1496 (2015).
12. Müller, M., Öztürk, E., Arlov, Ø., Gatenholm, P. & Zenobi-Wong, M. Alginate Sulfate–Nanocellulose Bioinks for Cartilage Bioprinting Applications. *Ann. Biomed. Eng.* **45**, 210–223 (2017).
13. Hinton, T. J. *et al.* Three-dimensional printing of complex biological structures by freeform reversible embedding of suspended hydrogels. *Sci. Adv.* **1**, e1500758 (2015).
14. Sawyer, W. G. *et al.* Writing in the granular gel medium. *Sci. Adv.* **1**, e1500655 (2015).
15. Shi, L. *et al.* Dynamic Coordination Chemistry Enables Free Directional Printing of Biopolymer Hydrogel. *Chem. Mater.* acs.chemmater.7b00128 (2017). doi:10.1021/acs.chemmater.7b00128
16. Highley, C. B., Rodell, C. B. & Burdick, J. A. Direct 3D Printing of Shear-Thinning Hydrogels into Self-Healing Hydrogels. *Adv. Mater.* **27**, 5075–5079 (2015).
17. Ouyang, L., Highley, C. B., Sun, W. & Burdick, J. A. A Generalizable Strategy for the 3D Bioprinting of Hydrogels from Nonviscous Photo-crosslinkable Inks. *Adv. Mater.* **29**, (2017).
18. Kim, I. L., Mauck, R. L. & Burdick, J. A. Hydrogel design for cartilage tissue engineering: A case study with hyaluronic acid. *Biomaterials* **32**, 8771–8782 (2011).
19. Chu, C. R., Szczodry, M. & Bruno, S. Animal models for cartilage regeneration and repair. *Tissue Eng Part B Rev* **16**, 105–115 (2010).

20. Pfeifer, C. G., Fisher, M. B., Carey, J. L. & Mauck, R. L. Impact of guidance documents on translational large animal studies of cartilage repair. *Sci. Transl. Med.* **7**, 1–9 (2015).

CHAPTER 3: FUNDAMENTALS OF PHOTOCROSSLINKING IN BIOPRINTING

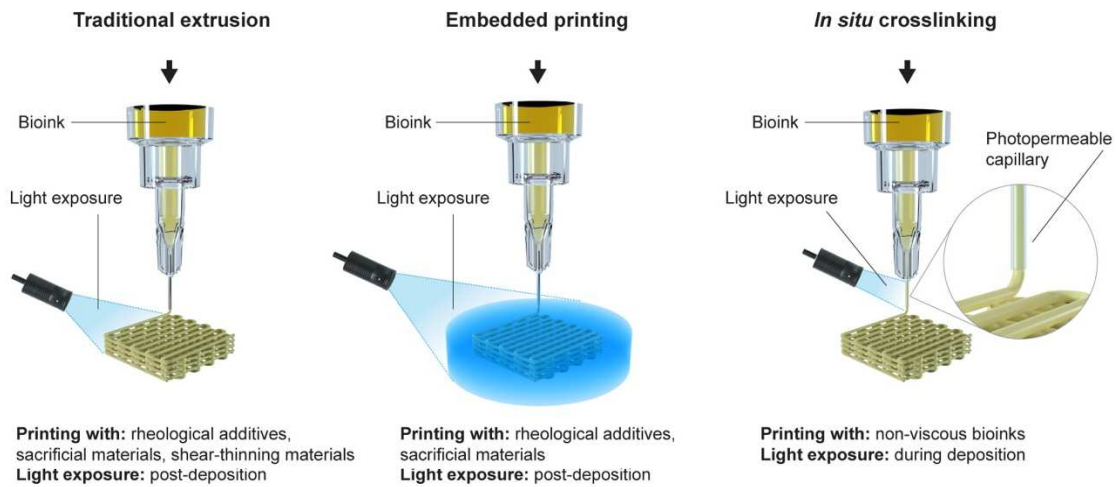
The following chapter is adapted from:

Lim, K.S.[†], Galarraga, J.H.[†], Cui, X, Lindberg, G.C. J, Burdick, J.A., Woodfield, T.B.F. *Chemical Reviews* 2020 120 (19), 10662-10694.

3.1 INTRODUCTION

Despite significant research attention and developments in photocrosslinking approaches and techniques in biofabrication for regenerative medicine and *in vitro* 3D tissue models, in combination with a number of existing reviews focusing primarily only on polymerization of hydrogels,^{1,2} there is limited information available that reviews the key fundamentals of photocrosslinking and necessary compositional and processing criteria for the successful design and implementation of photocrosslinked bioinks and bioresins. The aim of this review is to provide a detailed overview of the various widely adopted 3D bioprinting methods that utilize light (**Figure 3.1**).

Extrusion



Lithography

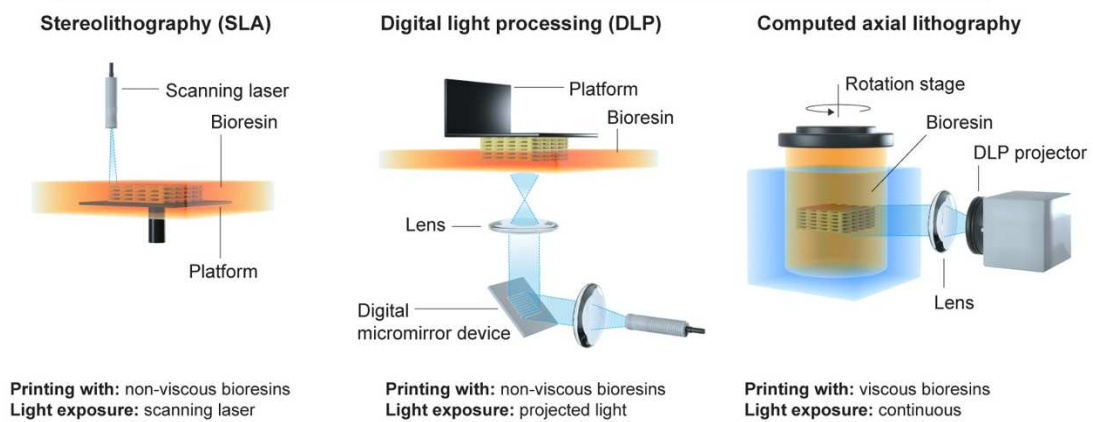


Figure 3.1: Light-based bioprinting techniques. Schematic illustrating (top) extrusion-based bioprinting and (bottom) lithography-based bioprinting techniques that use light to control the spatial organization of materials, cell-instructive factors, and cells towards the engineering of tissues.

First, an overview of the fundamental mechanisms associated with photocrosslinking reactions (e.g., free-radical chain polymerization, thiol-ene, redox) that are used with light-based bioprinting techniques towards the processing of natural and synthetic materials are discussed. The critical design criteria required for successful bioink and bioresin development including: the selection of polymers, modification of functional groups that permit photocrosslinking of these polymers, and optimal

photoinitiator and light source selection, are then detailed. Thereafter, the specific bioink or bioresin properties that must be achieved to ensure successful printability are described. Significant progress will be made as these light-based techniques are further advanced and this review – by introducing the relevant fundamentals in photochemistry combined with a description of the unique bioink design criteria that must be implemented for individual extrusion-based and lithography-based bioprinting technologies – motivates future opportunities within the landscape of light-based bioprinting.

3.2 OVERVIEW OF PHOTOCROSSLINKING REACTIONS

Bioinks and bioresins used in both extrusion-based and lithography-based bioprinting are most commonly fabricated as water-swollen polymer networks (i.e., hydrogels). Hydrogels are of interest, as they can be designed with a range of chemical, mechanical, and biological properties and support the encapsulation of cells. These networks can be fabricated through a number of techniques, such as enzymatic activity,^{3,4} redox reactions,⁵⁻⁷ or exogenous stimuli such as temperature or light.¹ The application of light-based methods for hydrogel formation is especially useful in additive manufacturing and 3D printing due to the inherent spatiotemporal control over photocrosslinking reactions, which can be used to optimize the printing process and to build up materials into desired 3D structures. Traditionally, three different photocrosslinking reactions have been utilized in bioprinting to induce the conversion of precursor bioinks and bioresins into solid materials at various stages of the bioprinting process (**Figure 3.1**) – these include free-radical chain polymerization, thiol-ene photocrosslinking, and photo-mediated redox crosslinking. Each respective photocrosslinking approach exhibits distinct advantages and disadvantages, but all have been leveraged to fabricate 3D printed constructs. This section will be used to provide a basic background on each of these techniques to better inform the design of bioprinting processes.

3.2.1 Free-Radical Chain Polymerization

Materials crosslinked via free-radical chain polymerization generally undergo three reaction stages: initiation, propagation, and termination. Each reaction stage contains its own associated kinetics, which may individually change the microscopic and macroscopic characteristics of formed networks. For a free-radical chain polymerization to occur, a radical species must first be generated. During initiation, the first stage of a free-radical chain polymerization, photoinitiators are transformed into reactive radical species through photolysis, or light-induced cleavage (**Figure 3.2a**). The rate of formation of these initial radical species varies as a function of: i) incident light intensity, ii) efficiency of the photoinitiator, iii) photoinitiator concentration, iv) quantum yield, and v) the number of effective radicals generated per photolysis event (typically, homolytic photolysis yields two reactive radical species).¹

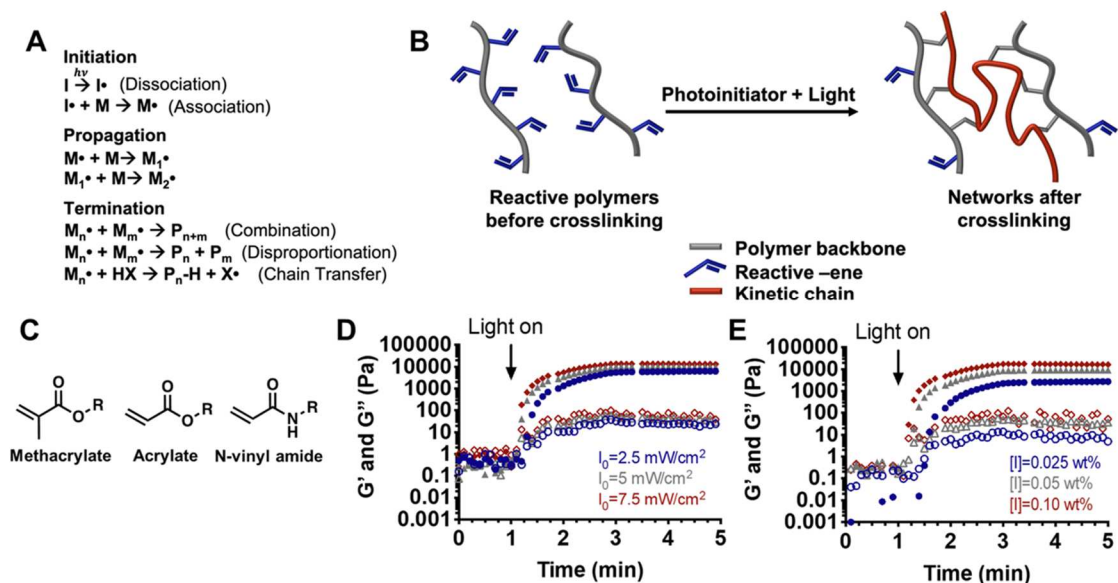


Figure 3.2: Overview of free-radical chain polymerization. A) General mechanism for the free-radical chain polymerization of bioinks and bioresins, including initiation, propagation, and termination. B) Schematic of polymer chains containing reactive groups crosslinking through free-radical chain polymerization, where kinetic chains form to crosslink polymers together. C) Common functional groups employed in free-radical chain polymerization in bioprinting. D) Change in storage (G' , closed) and loss (G'' , open) moduli measured via oscillatory shear rheology (1 Hz, 0.5% strain, 25°C) during the free-radical chain polymerization of hyaluronic acid modified with methacrylate groups (MeHA, 30% modification, 3 wt%) in the presence of photoinitiator Irgacure 2959 (0.05 wt%) at variable UV light intensities (320-390 nm; $I_0 = 2.5 \text{ mW/cm}^2$, 5 mW/cm^2 , 7.5 mW/cm^2). E) Change in storage (G' , closed) and loss (G'' , open) moduli measured via oscillatory shear rheology (1 Hz, 0.5% strain, 25°C) during the free-radical chain polymerization of MeHA (30% modification, 3 wt%) in the presence of UV light (320-390 nm, $I_0 = 5 \text{ mW/cm}^2$) with variable concentrations of Irgacure 2959 (0.025 wt%, 0.05 wt%, 0.10 wt%).

After successful initiation, free radicals can then react with specific functional groups on polymer chains, effectively forming new covalent bonds and reactive radical intermediates. These reactive intermediates may then proceed to react with subsequent reactive groups, resulting in the propagation of radical species and the formation of a kinetic chain (**Figure 3.2a,b**). Specifically, radicals propagate through unreacted double bonds (e.g., methacrylates, acrylates, acrylamides) (**Figure 3.2c**). Since the reaction between growing polymer chains and unreacted groups largely occurs during the

propagation phase, the consumption of double bonds may be approximated as a second order reaction.¹

This process of propagation is ultimately concluded when termination occurs, which can encompass the quenching of reactive radical species via radical coupling (two chain ends combine to form one continuous chain), disproportionation (two chain ends terminate, one with a saturated terminal group and one with a non-saturated terminal group), or the transfer of radicals away from propagating polymer chains via a chain transfer event (**Figure 3.2a**). If the total radical species concentration is assumed to be at pseudo-steady state (i.e., rate of initiation is equal to the rate of termination) and the photoinitiator yields two reactive radical species upon photolysis, the rate of polymerization (R_p) may then be described by Equation 3.1:

$$(3.1) \quad R_p = k_p \left(\frac{\phi \epsilon I_0}{k_t} \right)^{\frac{1}{2}} [M][I]^{\frac{1}{2}}$$

where k_p is the polymerization rate constant, ϕ is the quantum yield, ϵ is the molar extinction coefficient of the photoinitiator, I_0 is the intensity of incident light, k_t is the termination rate constant, $[M]$ is the concentration of unreacted monomer, and $[I]$ is the concentration of photoinitiator.

The kinetics of free-radical chain polymerization for common reactive functional groups such as acrylate and methacrylate derivatives have been extensively studied via pulsed-laser polymerization and size exclusion chromatography (PLP-SEC).⁸⁻¹⁵ For example, it is well-established that acrylates homo-polymerize appreciably faster than methacrylates.¹⁴ In addition, the reactivity of different functional groups can be readily modulated. Typically, acrylates and methacrylates with adjacent groups that withdraw

electrons react faster because these adjacent groups impart stability to intermediate radical species. Thus, reactivity increases with larger alkyl chains on acrylates and methacrylates.^{10,12}

Monitoring of hydrogel mechanics is also commonly used to characterize reaction behavior and the transition of a hydrogel precursor (i.e., bioink, bioresin) into a solid hydrogel. Specifically, oscillatory shear rheology can be performed to track the evolution of mechanics in real time, where the storage modulus (G') and loss modulus (G'') correlate to the elastic and viscous character of a material, respectively. As an example, a methacrylated hyaluronic acid (MeHA) was cured in the presence of the photoinitiator Irgacure 2959 and ultraviolet light (note: additional discussion on polymers and photoinitiators is provided in a later section) (**Figure 3.2d,e**). The rate of polymerization increased in the representative crosslinking of MeHA as both the light intensity and photoinitiator concentration increased, highlighting parameters that can be used to tailor the reaction kinetics of bioinks and bioresins. The optimization of reaction kinetics is required for any given bioprinting technique and even the specific bioprinter used, but generally can occur very rapidly.

While the rapid nature of free-radical chain polymerization allows the fast crosslinking of bioinks and bioresins, these reactions do exhibit complex kinetics; specifically, the propensity for peroxy radicals to form (via chain transfer) can result in oxygen inhibition.¹⁶ This is very important in the context of bioprinting, where the presence of ambient oxygen – which is normally always the case for bioprinting of cell-laden bioinks and bioresins – may impede complete crosslinking of precursor materials during the fabrication process. Incomplete crosslinking negatively impacts print fidelity and downstream maintenance of shape fidelity, which are both critical criteria for successful

3D bioprinting of complex constructs and tissues.¹⁷ The intensity of light and total number of radical species generated should be minimized, as both have been shown to exhibit cytotoxicity to cells.¹⁷

Further, the structure and crosslink density of photocrosslinked networks formed via free-radical chain polymerization may be tuned via changes in initiator concentration, reactive group concentration, and light intensity. Typically, higher degrees of crosslinking within polymer networks yield higher mechanical properties and slower degradation times in the case of degradable materials.^{1,18} The distribution of propagating kinetic chain lengths achieved also introduces heterogeneity to local network structures. This heterogeneity may be attributed to the rapid formation of concentration gradients and diffusion limitations as kinetic chains rapidly form, resulting in auto-acceleration of propagation and diffusion-controlled termination.^{24,25} Specifically, as polymer networks begin to evolve during polymerization, steric hindrance limits the ability for radicals to terminate, thus effectively increasing the total radical concentration. As a result, the rate of polymerization increases, leading to auto-acceleration. Towards the end of polymerization, auto-deceleration occurs, as the consumption of radicals is diffusion-limited and termination predominantly occurs through disproportionation. Due to the heterogeneous reaction behavior that arises from these phenomena, intramolecular chain transfer events may also occur, in which mid-chain radical species result in the branching and cyclization of polymer backbones, as well as the formation of non-idealities within networks.

3.2.2 Thiol-ene Photocrosslinking

Thiol-ene reactions have garnered appreciable attention throughout the biofabrication community due to the control over the crosslinking approach, particularly in

comparison to free-radical chain polymerization, while still leveraging the benefits of light. Thiol-ene reactions give rise to polymer networks with less heterogeneity, as the network's crosslink density, mesh size, and mechanics may be tuned as a function of crosslinker functionality, length, and concentration.¹⁹⁻²¹ Furthermore, radical-mediated thiol-ene polymerizations are insensitive to oxygen and exhibit less network relaxation or stress accumulation after crosslinking.²⁰

When radicals are generated via initiation, sulfide groups within thiol-containing molecules are converted into reactive thiyl radicals. These intermediate thiyl radicals may then form thioether bonds with secondary molecules containing electron-rich or strained -enes (**Figure 3.3a**).

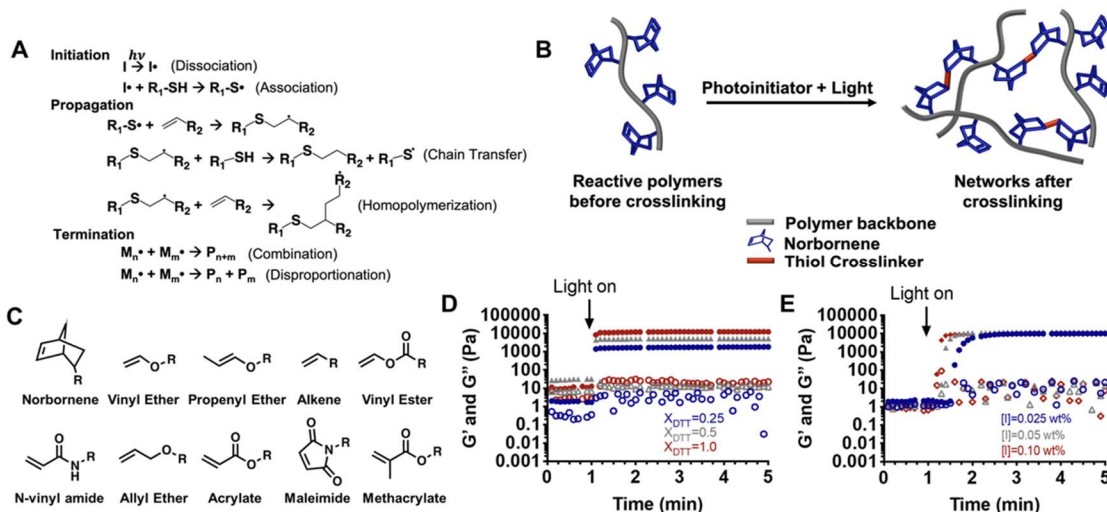


Figure 3.3: Overview of thiol-ene photocrosslinking. A) General mechanism for radical-mediated thiol-ene photocrosslinking. After initiation, reactive thiyl radicals form thioether bonds with molecules containing reactive -enes. Thereafter, propagation may proceed via step growth polymerization (chain transfer events) or kinetic chain growth (homopolymerization). Termination occurs when all of the monomer is consumed, disulfide formation depletes the total number of radicals, or radicals are quenched through disproportionation. B) Schematic of polymer chains containing reactive groups crosslinking through radical-mediated thiol-ene reactions. C) Common -ene groups employed in radical-mediated thiol-ene reactions. Functional groups are listed in descending order of reactivity (left to right, top to bottom), although reactivity of -enes will vary with different thiols.^{22–25} D-E) Change in storage (G' , closed) and loss (G'' , open) moduli measured via oscillatory shear rheology (1 Hz, 0.5% strain, 25°C) during the thiol-ene crosslinking of hyaluronic acid modified with norbornene groups (NorHA, 20% modification, 3 wt% in PBS) in the presence of either D) UV light (320-390 nm, $I_0 = 10 \text{ mW/cm}^2$), 0.05 wt% Irgacure 2959, and variable stoichiometric amounts of dithiothreitol (DTT) crosslinker ($X_{\text{DTT}} = 0.25, 0.5, 1.0$) or E) visible light (400-500 nm, $I_0 = 10 \text{ mW/cm}^2$), constant DTT crosslinker ($X_{\text{DTT}} = 1.0$), and variable amounts of lithium phenyl-2,4,6-trimethylbenzoylphosphinate (LAP) photoinitiator (0.025-0.1 wt% LAP).

Although it is possible for chain growth to occur in thiol-ene reactions, polymer chains are predominantly crosslinked via a step growth mechanism. Step growth reactions involve the sequential conjugation of macromers or polymers, resulting in a gradual increase in polymer molecular weight. When crosslinkers have a functionality of at least two (thiol or -ene moieties), the addition of crosslinkers to polymer chains results in the formation of a network. In bioinks and bioresins, the reaction most commonly occurs through the reaction of a reactive polymer with a multi-functional thiolated crosslinker for network formation (Figure 3.3b).

While these step growth reactions typically proceed without the presence of chain growth reactions (i.e., homopolymerization of a single reactive group), it is important to note that some thiol-ene reactions can occur concurrently with free radical chain polymerization, in what is termed mixed-mode polymerization.²⁰ It has previously been shown that the use of functional groups associated with both thiol-ene photocrosslinking and free radical chain polymerization in a single material system permits copolymerization, such that crosslinking occurs via both mechanisms.²⁰ For example, a multifunctional thiol may react with acrylates or methacrylates to form crosslinks in a step growth manner, while the same acrylates or methacrylates can independently form crosslinks via the propagation of kinetic chains. Alternatively, more complex, ternary systems comprising a thiol, an acrylate or methacrylate, and an alkene that does not undergo free radical chain polymerization can be employed to effectively tune the extent of crosslinking achieved via each respective mechanism. Mixed-mode polymerizations may be of interest and provide further advantages in tailoring bioink properties, such as, to mitigate oxygen-inhibition associated with conventional free radical chain polymerizations and/or to modulate the kinetics of a thiol-ene reaction. However, the resultant kinetics of these polymerizations are complex, and formed networks may potentially exhibit phase separation between networks crosslinked via different mechanisms.²⁰

The reactivity of –ene groups is determined by their electron density, stability of intermediate carbon-centered radicals, and steric hindrance. Terminal -ene groups with larger electron densities are typically more reactive than internal –enes or –ene groups with less electron density (**Figure 3.3c**).²² Conversion alone does not reflect the inherent kinetics of different thiol-ene reactions, as the propensity for homopolymerization between -enes and effects such as auto-acceleration and diffusion-controlled termination that arise from high crosslinking can lead to similar stoichiometric conversions in systems with

different reaction kinetics. However, thiol-ene reactions allow for enhanced control over reactive group consumption relative to free-radical chain polymerization, since the degree of crosslinking is modulated by the concentration of crosslinker used rather than the concentration of reactive groups. Thus, it is possible for multiple crosslinking events to be induced in a sequential manner. Furthermore, the use of thiol-ene chemistry permits the incorporation of signaling ligands important for tissue engineering into the networks.

Similar to free-radical chain polymerization, there are numerous parameters that can influence the rate of polymerization and the final network properties. In general, reactions can be quite rapid, with crosslinking on the order of seconds, and the final network properties achieved can be modulated through the extent of crosslinking. As described above, oscillatory shear rheology can be performed to track the evolution of mechanics in real time, where the storage modulus (G') and loss modulus (G'') correlate to the elastic and viscous character of a material, respectively. As an example, the crosslinking of norbornene-modified hyaluronic acid (NorHA) in the presence of a crosslinker (dithiothreitol, DTT), ultraviolet light, and the Irgacure 2959 photoinitiator was monitored (note: additional discussion on polymers and photoinitiators is provided in a later section) (**Figure 3.3d**). The crosslinker amount did not greatly change the rate of the reaction but did modulate the final material properties. As an additional example, the reaction behavior was monitored with variations in the concentration of lithium phenyl-2,4,6-trimethylbenzoylphosphinate (LAP) photoinitiator used in the presence of visible light and photocrosslinking was more rapid with increased photoinitiator concentration (**Figure 3.3e**). Overall, thiol-ene photocrosslinking is a highly tunable approach in the processing of bioinks and bioresins in bioprinting applications.

3.2.3 Photo-mediated Redox Crosslinking

Finally, photo-mediated redox reactions have been employed to photocrosslink bioinks; specifically, polymers modified with phenyl groups may be photocrosslinked in the presence of a photosensitizer via photooxidation and subsequent radical coupling between reactive groups (**Figure 3.4a-c**).^{26,27}

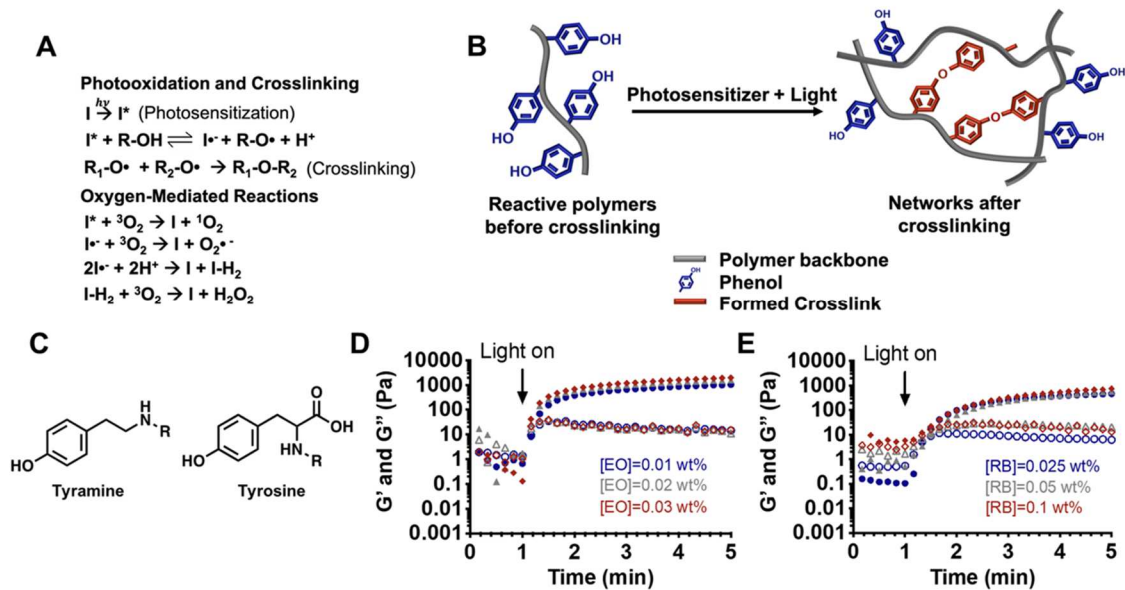


Figure 3.4: Overview of photo-mediated redox crosslinking. A) General mechanism for photo-mediated redox reactions. After a photosensitizer excites oxygen to its singlet state, generated radicals will form intermolecular bonds between paired reactive groups. Termination occurs when all the reactive groups are consumed and/or all of the photosensitizer is deactivated. B) Schematic of polymer chains containing reactive groups crosslinking through photo-mediated redox reactions. C) Common functional groups employed in photo-mediated redox reactions in bioprinting. D-E) Change in storage (G' , closed) and loss (G'' , open) moduli measured via oscillatory shear rheology (1 rad/s, 1% strain, 20°C) during the photo-mediated redox crosslinking of hyaluronic acid modified with tyramine groups (HA-Tyr, 7.8% modification, 3.5 wt% in PBS) in the presence of visible light (350-700 nm, $I_0 = 134 \text{ mW/cm}^2$) with variable amounts of D) eosin Y (0.01-0.03 wt%) and E) rose bengal (0.025-0.1 wt%) photosensitizers.

Photosensitizers here are defined as dyes or additives that can absorb light and undergo transition into excited states, rendering them capable of oxidizing reactive groups

of interest. It is important that a photosensitizer exhibit a high absorption coefficient within the spectra of incident light used, a high quantum yield, and sufficient stability to catalyze photooxidation.²⁸ If each of these criteria are met, then sensitizers may generate free radicals via electron transfer or hydrogen-atom abstraction with a substrate.

It is important to note that in the presence of oxygen, photosensitizers undergo additional side reactions, leading to the generation of singlet oxygen, superoxides, and potentially hydrogen peroxide.²⁸ All of these side reactions result in the regeneration of ground state photosensitizers and the consumption of photosensitizer radicals, with the advantage of further increasing the overall rate of photooxidation and reactive group crosslinking. The first type of side reaction involves energy transfer via collision between an excited photosensitizer (i.e., triplet state) and oxygen in its ground state. This reaction yields excited singlet oxygen species, that can readily oxidize hydroxyl, sulfide, and amine groups due to their high electrophilicity. Alternatively, after photosensitizers undergo electron transfer or abstract a hydrogen from a substrate, their radical derivatives may undergo a different side reaction with triplet oxygen to form reactive oxygen species such as superoxides. If photosensitizer intermediate radical species undergo coupling, they may then react with ground state oxygen to produce hydrogen peroxide.

It has previously been shown that under anaerobic conditions, appreciable photocrosslinking does not proceed.²⁶ Therefore, although singlet oxygen may not be directly involved in reacting with functional groups, oxygen is required to mediate the photo-oxidation and crosslinking of hydroxyphenyls. As a result, it is also important that photosensitizers exhibit the ability to readily transfer energy to triplet oxygen. This is in stark contrast to conventional free radical chain polymerization, where the presence of oxygen inhibits photocrosslinking.

Photosensitizers such as rose bengal, eosin Y, and flavin mononucleotide are examples that have been used to catalyze photooxidation of tyrosine and tyramine functional groups applied to photocrosslinking.^{26–29} As examples, hyaluronic acid with a tyramine modification was photocrosslinked in the presence of various concentrations of rose bengal and eosin Y (note: additional discussion on polymers and photoinitiators is provided in a later section) (**Figure 3.4d,e**). The reactions occurred within minutes with modest changes based on the initiator concentration and initiator type. For further discussion on the selection and use of photosensitizers to generate reactive singlet oxygen, an extensive review has been performed on the photo-physical properties of previously used photosensitizers.²⁸ Prior to use in bioprinting, however, consideration should be given to the cytotoxicity of photosensitizers, as well as the generation of reactive oxygen species during photocrosslinking. These adverse effects may be mitigated using low photosensitizer concentrations, so long as favorable crosslinking kinetics are conserved.

3.3 LIGHT-BASED BIOPRINTING METHODS

As aforementioned, light is a powerful tool in bioprinting given that it permits spatiotemporal control over the reaction behavior of bioinks and bioresins, using the range of photocrosslinking reactions that were just described. In this section, we detail more specifically how light may be utilized to process bioinks and bioresins and highlight the critical design specifications associated with extrusion-based and lithography-based bioprinting.

3.3.1 Extrusion-Based Bioprinting

3.3.1.1 Traditional Fabrication Window

One of the most significant considerations when engineering a bioink for extrusion-based bioprinting is its printability, or ability to be readily extruded and deposited with high shape fidelity to directly replicate the CAD designed 3D geometry of interest. To successfully 3D print a bioink via extrusion printing, the initial bioink formulation residing in the print head reservoir or syringe must exhibit suitable rheological properties so that it can flow through a small diameter print head nozzle (generally 100-800 μm) to dispense a filament. Due to the nozzle constriction, bioinks that have a lower viscosity are typically easier to initially extrude and deposit in a layer-by-layer manner due to the high shear stress experienced in the nozzle. However, after initial extrusion and deposition of a bioink, the printed construct must also have sufficient mechanical integrity to maintain shape fidelity and structure to withstand external forces (e.g., gravity). Typically, the printability of bioinks is validated via oscillatory shear rheology experiments and the assessment of filament stability post extrusion via washing, imaging and/or mechanical testing;³⁰ these criteria for bioink printability have been extensively reviewed to identify materials that are amenable to extrusion-based bioprinting.³¹

With these criteria in mind, bioink formulations comprised of high viscosity materials or high polymer contents often yield printed constructs with higher resolution and shape fidelity than those of low viscosity materials.³⁰ However, a balance must be achieved so that embedded cell viability and cell function such as migration, spreading, and extracellular matrix formation are supported after crosslinking. Traditionally, the need to design bioinks with the requisite printability and functionality for cell culture has led to

the identification of a *biofabrication window*, within which materials possess the critical properties required to achieve both high shape fidelity and bioactivity.³² A number of techniques have been developed to 3D print photocrosslinkable bioinks within this *biofabrication window* or to circumvent the traditional design criteria for bioink printability for low viscosity bioinks.

With regards to photocrosslinkable bioinks, light can be applied simultaneously during the entire printing process, after the entire construct is printed, or with multiple photocrosslinking steps after the deposition of each printed layer. This depends on the stability of the material after extrusion and how quickly further stabilization is needed. For example, Trachtenberg, *et al.* extruded up to ten alternating layers of perpendicular fibers with a subsequent UV crosslinking step after the printing of each layer.³³ The resulting scaffold was then exposed to additional UV light during a post-processing step to ensure complete crosslinking of the bioink.³³ While this printing approach results in an even amount of light exposure within a single layer, there is the potential to overexpose the initially deposited layers due to multiple light exposures. Therefore, there has been a gradual shift towards using visible light photoinitiators to avoid continuous UV exposure.^{17,34}

As an alternative, multi-step crosslinking can be used to improve the processing of hydrogel bioinks. For example, tyramine-modified hyaluronic acid (HA) was first enzymatically crosslinked to enable cell encapsulation and extrusion capability in the form of a soft gel. Subsequently, photo-redox crosslinking was utilized to stabilize deposited filaments via green-light irradiation in the presence of the photoinitiator eosin-Y.³⁵ These approaches exploit the control that is possible over the material photocrosslinking to achieve the appropriate material processing to build desired structures.

3.3.1.2 Rheological Additives and Sacrificial Materials

Another very common strategy to manipulate a bioink's rheological properties for extrusion bioprinting is to introduce additives that impart non-Newtonian flow properties. These additives support rapid switching between low viscosity nozzle flow and high viscosity gelation upon exiting the nozzle. A range of materials have been utilized to introduce non-Newtonian shear-thinning properties to a bioink of interest, thereby allowing for a rapid reduction in viscosity with applied stress.³² Bioinks with these additives then exhibit the ability to recover their properties upon removal of shear stress so that they retain shape fidelity post-extrusion. With light-based bioprinting techniques, it is important that rheological additives are transparent to the light used to avoid any light attenuation in thicker constructs.

Nanosilicates and nanocellulose have been employed to impart shear-thinning behavior to bioinks.³⁶⁻³⁹ For example, Xavier *et al.* demonstrated that the nanosilicate Laponite could be incorporated into a photocrosslinkable bioink, rendering it amenable for layer-by-layer extrusion printing. This was attributed to the zwitterionic character of the Laponite nanosilicate, which enables electrostatic interactions between both the nanosilicates themselves and between nanosilicates and the polymer. As a result, physically crosslinked networks with shear-thinning properties were formed.⁴⁰ Importantly, these nanosilicates exhibit optical transparency in solution, allowing for orthogonal, photocrosslinking of bioinks after printing.

In addition to these rheological additives, other materials that may be physically crosslinked are also often exploited to tune bioink printability and stability upon extrusion. Physical crosslinking refers to any type of reversible, non-covalent interaction that imparts structure through the formation of a polymer network. These types of crosslinking

chemistries include the self-assembly of peptides, ionic bonding, and supramolecular interactions.⁴¹ Oxidized alginate has been crosslinked via electrostatic interactions with calcium chloride to permit extrusion-based fabrication of biodegradable hydrogels.^{42,43} Colosi et al. showed that alginate could be utilized as a sacrificial material to render non-viscous polymers printable (**Figure 3.5a**).⁴⁴

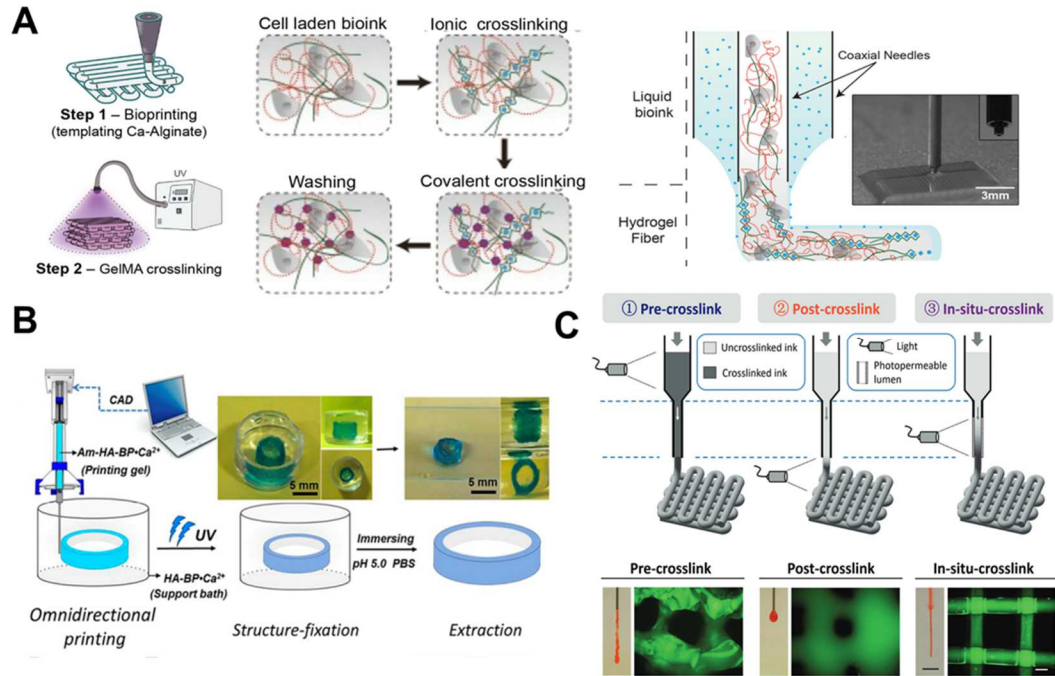


Figure 3.5: Overview of techniques commonly employed in extrusion-based bioprinting. A) Schematic of coaxial printing of GelMA-alginate blended bioink.⁴⁴ As the liquid bioink is deposited in the presence of calcium chloride, alginate undergoes ionic crosslinking. Afterwards, GelMA is photocrosslinked via UV irradiation to form a covalent network. Then, the sacrificial alginate network may be washed away to obtain the final print construct comprised of solely gelatin. B) Direct printing of acrylamide-modified HA-BP into a support bath.⁴⁶ With this approach, shear-thinning, photocrosslinkable inks were printed into support baths, cured and extracted to yield user-defined print structures. C) Schematic of pre-crosslinking, post-crosslinking, and *in situ* crosslinking techniques.⁴⁷ *In situ* crosslinking involves the photocrosslinking of bioink as it transits through a photopermeable lumen. In this representative example, methacrylated-HA is printed with light exposure before (pre-crosslink), after (post-crosslink) or during (*in situ* crosslink) bioink extrusion. Unlike pre-crosslinking and post-crosslinking techniques, *in situ* crosslinking results in the formation of overlaying filaments that do not flow and exhibit high print fidelity. Images adapted from ^{44,47,48}.

A coaxial extrusion system was utilized such that an alginate-gelatin ink blend was extruded through an internal needle, while calcium chloride was extruded through an

external needle. At the terminus of the coaxial needle, alginate would then crosslink in the presence of calcium, allowing for the deposition of the alginate-gelatin polymer blend. Thereafter, gelatin was photocrosslinked and the ionically crosslinked alginate was subsequently washed away. Materials that exhibit sol-gel transitions that are temperature dependent have also been printed with photocrosslinkable polymers as sacrificial materials. For example, poly(N-isopropylacrylamide) (pNIPAM) has been conjugated to hyaluronic acid to impart thermal sensitivity to a desired ink; HA-pNIPAM was co-printed with methacrylated hyaluronic acid (MeHA) onto a heated stage at 37 °C. Thereafter, printed constructs were photocrosslinked with UV light, so that HA-pNIPAM could be subsequently removed via cooling below the lower critical solution temperature.⁴⁵

HA-based hydrogels modified with guest-host moieties and methacrylate groups have similarly been synthesized to permit shear-thinning and recovery of bioinks during extrusion-based bioprinting and stabilization via post-print UV crosslinking.³⁵ Dynamic covalent chemistries have also been employed to impart non-Newtonian flow properties to a bioink of interest.⁴⁹ Importantly, photocrosslinkable polymers can be readily incorporated within these inks to enable the formation of light-induced interpenetrating networks.⁴⁹ While physically crosslinked networks exhibit rapid crosslinking, their transient nature and propensity to undergo dissolution often limit their utility as individual networks. However, double network hydrogels have been engineered with both covalently and physically crosslinked networks that coexist in an interpenetrating manner. The ability for physical crosslinks to reform spontaneously may be leveraged in these systems to impart enhanced mechanics via load dissipation and subsequent network recovery, with photocrosslinking used to introduce covalent networks.^{50,51}

3.3.1.3 *Embedded Printing and Granular Media*

Conventionally, extrusion-based bioprinting has been utilized to fabricate constructs in a layer-by-layer manner through the continuous deposition of overlaying filaments. However, more complex structures, such as architectures found in native vasculature (e.g., branching networks or bifurcations) require modifications to traditional approaches. Therefore, alternative techniques that enable omnidirectional printing of a bioink are of growing interest. For example, support baths have been developed as a method of depositing a bioink of interest anywhere in arbitrary 3D space, using embedded printing techniques.^{46,52-56} These materials exhibit the ability to confine an ink wherever it is deposited, but are equally able to yield and recover as a needle or printer nozzle translates through them. Thus, hydrogels can be readily suspended within a contained volume prior to photocrosslinking for stabilization and subsequent release from the support material. This approach allows for biofabrication of bioinks independent of their viscosity or viscoelasticity, such as with very low viscosity bioinks that do not meet the traditional, requisite properties for extrusion-based bioprinting.

The reversible nature of physically crosslinked hydrogels makes them suitable as support inks for embedded printing of constructs with high aspect ratios. For example, HA hydrogels modified with supramolecular moieties have been previously employed for the printing of non-viscous hydrogels into a support bath.⁵⁶ HA was modified with cyclodextrin (CD-HA) and adamantane (Ad-HA) moieties that spontaneously interact with one another. These functional groups allow for the rapid association and dissociation of supramolecular bonds, such that a needle can readily transit through the support bath while concomitantly depositing ink. To this end, CD-HA and Ad-HA have also been adorned with photosensitive methacrylates, so that the support bath may be photocrosslinked upon

deposition of an interstitial, sacrificial material. This approach has been utilized to print negative features within a support bath to fabricate open-lumen structures that recapitulate native vasculature.^{56,57} Alternatively, photocrosslinkable inks can be deposited into support baths to fabricate complex geometries normally not possible with conventional layer-by-layer extrusion bioprinting.^{46,56} For example, Shi *et al.* modified HA with bisphosphonate (HA-BP) so that it formed dynamic metal-ligand coordination bonds with calcium ions, creating a support bath that enabled direct printing of inks and bioactive ligands into a self-healing hydrogel (**Figure 3.5b**).⁴⁶

Gelatin microparticle slurries are often employed as support baths, as they enable facile deposition of bioink and can be readily melted away at 37 °C.^{52,53} Similarly, polyacrylic acid (PAA)-based granular media have been utilized to fabricate complex geometries within a support bath.^{55,58} Electrostatic interactions between PAA microparticles result in the formation of a stable support bath with shear-thinning and self-healing capabilities. An important consideration when printing photosensitive bioinks into support baths is the degree to which the support bath itself may potentially attenuate light. Furthermore, attention must be given to the mechanism employed to remove printed constructs from support baths, as this may prove difficult for highly porous and/or soft bioinks.

In addition to their use as support baths, granular media may also be utilized as bioinks themselves in extrusion-based bioprinting.^{59,60} Photocrosslinking is used frequently to make hydrogel particles from emulsion batches, through microfluidics, or through photolithography approaches.⁶¹ When microgels are jammed into close proximity, they are immobilized, giving rise to elastic properties. The application of shear allows for the transient disruption of these physical interactions, such that jammed microgels can be readily printed as shear-thinning bioinks.⁵⁹ Photocrosslinking can then be used to

introduce inter-particle crosslinks to stabilize the printed structures. Highley *et al.* and Xin *et al.* have used this approach to print HA and PEG-based hydrogel microparticles, respectively, via thiol-ene photocrosslinking.^{59,60}

3.3.1.4 *In Situ Crosslinking Technique*

To address the need for both bioink fluidity and mechanics, additional methods of crosslinking bioinks have been employed to optimize printed construct shape fidelity and properties. Ouyang *et al.* demonstrated that *in situ* crosslinking of hydrogels during extrusion with light can appreciably improve the resolution of printed constructs relative to those fabricated via pre-crosslinking or post-crosslinking bioinks (**Figure 3.5c**).⁴⁷ As opposed to crosslinking precursor macromer before or after extrusion, *in situ* crosslinking involves the fabrication of filaments via irradiation of bioink as it transits through a photopermeable capillary or lumen. Unlike some of the other approaches described above, *in situ* crosslinking permits extrusion printing of non-viscous bioinks without the addition of additives or post-processing steps. Moreover, complex structures such as core-shell structures may also be readily fabricated using this *in situ* crosslinking technique. Galarraga *et al.* described the steps needed to apply this *in situ* crosslinking technique towards the bioprinting of a specific non-viscous bioink, including the assessment of photorheology during bioink curing, light attenuation across the capillary, and design specifications (e.g., capillary width and length, bioink flowrate, light intensity).⁶²

3.3.2 Lithography-Based Bioprinting

3.3.2.1 Engineering Printability in Lithographic Techniques

SLA and DLP techniques utilize similar concepts for processing. In SLA (developed in the 1980s), a concentrated laser spot is swept across a vat of liquid resin following a specified design, inducing spatial polymerization wherever the laser has travelled.^{63,64} In a typical setting, instead of shining the laser directly into the resin, the laser is often localized to a designated point through deflection off a rapidly moving mirror galvanometer.⁶⁵ After photocrosslinking of the first layer, the platform is moved away from the surface to be recoated with a fresh liquid resin for photocrosslinking of the second layer. To this end, multi-layered constructs with precise features can be achieved (**Figure 3.6a**).

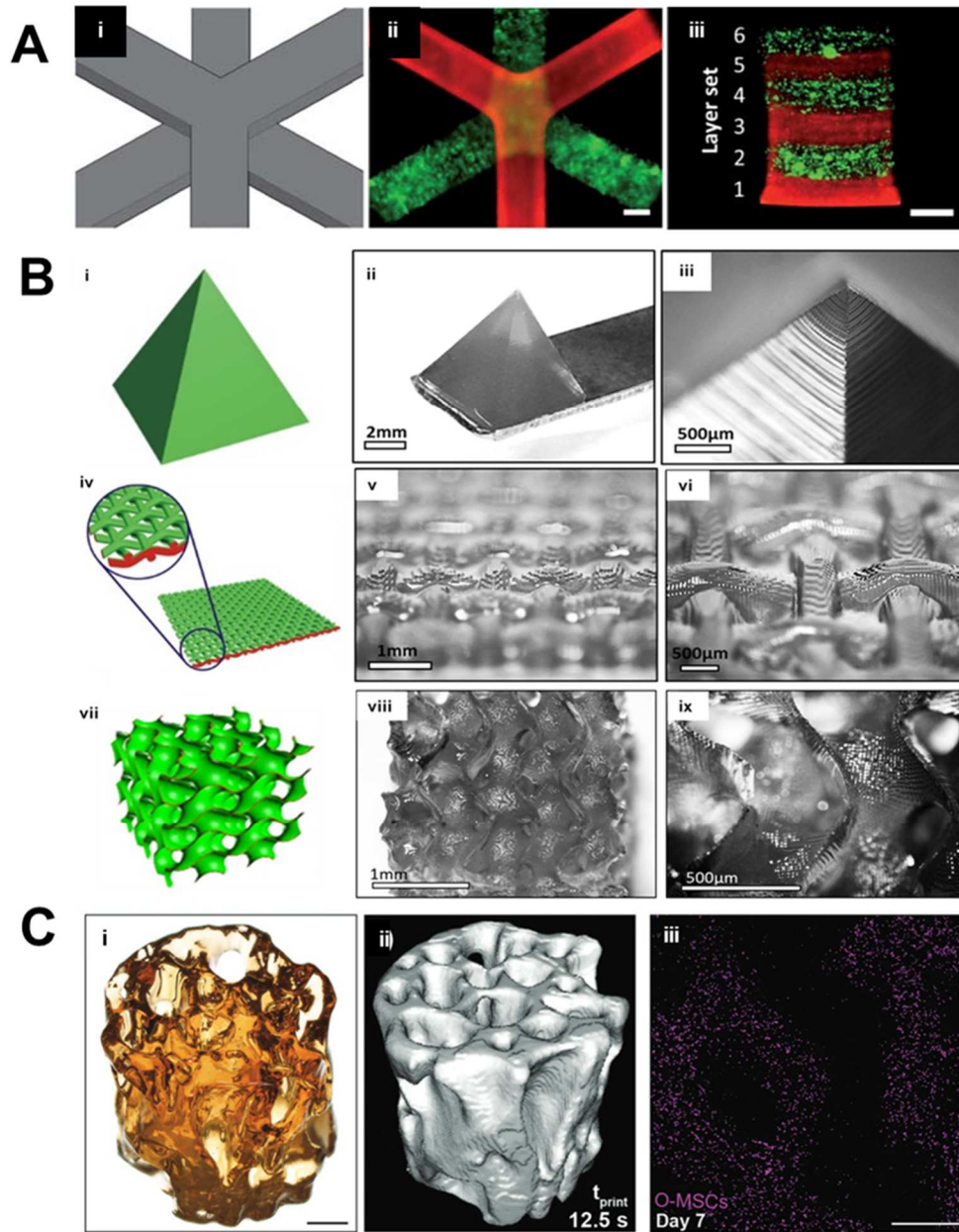


Figure 3.6: Representative examples of constructs fabricated with lithography-based bioprinting technologies. A) SLA printing of poly(ethylene glycol)-based hydrogels to create multi-layered, heterogeneous constructs comprised of multiple materials. Scale bar = 1mm. B) DLP printing of a poly(vinyl alcohol)-based bioresin into user-defined shapes, including i-iii) pyramids, iv-vi) woven mat, and vii-iv) gyroidal structure with 25µm petals and 500µm pore size.⁶⁷ Scale bars = (ii) 2mm, (iii) 500µm, (v) 1mm, (vi) 500µm, (viii) 1mm, (ix) 500µm. Images reproduced with permission from ref 11. Copyright 2018 IOP Publishing. C) CAL allows for the rapid fabrication of complex geometries, including a i) trabecular bone with high porosity, ii) validated via µCT, and iii) containing MSCs.⁶⁸ Scale bars=1mm.

In contrast, DLP operates by using a digital mirror device (DMD), an array of up to several millions of mirrors, to mask the light that passes through. The photocrosslinking of the resin takes place through projection of the light through this digital mask, photocrosslinking an entire layer in a single exposure. Given that no scanning of the resin is required as in SLA, DLP offers a faster total build time, as each layer only depends on the set layer thickness and required exposure time, and is independent of the layer geometry complexity (size in x-y plane). However, conserved across both of these light-based bioprinting approaches are the requisite bioresin properties for printability. A bioresin must be readily photocrosslinked via irradiation (i.e., rapid curing kinetics) and be able to flow, such that uncured resin continuously interfaces with previously cured layers on the computer-driven build stage. If a bioresin is too viscous, then it will be incapable of recoating the build stage with precursor material in between layers, rendering it impossible to build up a 3D structure.⁶⁶

A typical resin consists of a mixture of photocrosslinkable components, photoinitiators, reactive diluents, and inhibitors.^{63,69} Currently, the photocrosslinkable components are mostly oligomers, elastomers, monomers or macromers grafted with unsaturated vinyl moieties such as acrylamides,⁶³ vinyl esters,^{70,71} vinyl carbonates,⁷⁰ acrylates,^{72,73} and methacrylates.^{72,74} In SLA and DLP, the control of the thickness of each layer that is cured is essential. For most resins, the cure depth is determined by the depth/thickness of the cured layer during photocrosslinking and is dependent on the light energy and photoinitiator concentration in the resin.⁷⁵ This energy can be controlled by adjusting the power of the light source, and the scanning speed (for SLA), or the exposure time (for DLP). Although theoretically the photocrosslinking mechanism with the different stages of the reaction (e.g., initiation, propagation, termination) is well documented and modeled, the kinetics of the crosslinking reaction remains quite complex. Specifically,

most commercial resins consist of mixed multi-functional monomers and macromers, complicating the reactions.⁷⁶ For most resins used in SLA and DLP, it is important to first determine the working curve, which can be extrapolated from Equation 3.2 below, and is absolutely fundamental to not only understand this technology, but also to determine the correct settings for the fabrication process.^{67,75–77}

$$(3.2) \quad C_d = D_p \ln \left(\frac{E}{E_c} \right)$$

Where C_d = cure depth, D_p = penetration depth into the resin, E = applied irradiation dosage per area, and E_c = critical irradiation dosage to reach the gel point. This empirical equation is an adapted form of the Beer-Lambert equation, which relates the attenuation of the intensity of light as it passes through a medium in which it is absorbed. In photocrosslinking reactions, the time required to reach the gel point depends linearly on the intensity of the light at that specific location. Therefore, C_d increases logarithmically with the total applied irradiation dosage. Specifically, for lithography-based approaches, the reactivity and printability of the resin are characterized by both E_c and D_p , where the total applied light irradiation dosage has to exceed the E_c to allow solidification of the initial layer on the build plate. The penetration of light into the resin is further characterized by D_p and has been previously reported to not only be dependent on the resin properties that influence light attenuation, but also the photoinitiator concentration.⁷⁵ Although it is often implied that increasing photoinitiator concentration increases C_d by facilitating more double-bond conversion of the monomer/macromer in the resin, Lee *et al.* reported that a higher photoinitiator concentration in fact decreases the C_d .⁷⁵ As the photoinitiator concentration increases, the penetration depth of the photons decreases, where the free-radical initiation is thus localized closer to the surface. Lin *et al.* also reported that increasing the photoinitiator concentration decreases print resolution due to excess radical

production and diffusion.⁶⁹ Hence, besides controlling the irradiation dosage, an optimal photoinitiator concentration has to be determined for most resins to be successfully applied to SLA or DLP printing.

Furthermore, conversion at the interface between the layers should be targeted to be slightly higher than the gel point to ensure adequate chemical and mechanical bonding between the layers during printing. This overexposure may result in overcuring into the preceding layer, which can be particularly problematic when preparing porous constructs or objects with open channels. A high extinction coefficient of the resin corresponds to a low D_p and allows more accurate control of the polymerization process and minimal overcure. The penetration depth can be decreased by either increasing the photoinitiator concentration or by including a photoabsorber in the resin that competes with the photoinitiator in absorbing light. For example, a study by Lim *et al.* demonstrated that addition of 1wt% Ponceau 4R (red food coloring) was required to reduce the D_p of a poly(vinyl alcohol)-methacrylate based bioresin, allowing improved control over print resolution.⁶⁷ With the incorporation of Ponceau 4R into bioresins, complex geometries could be readily printed (**Figure 3.6b**). Similarly, Grigoryan *et al.* examined a number of additives such as tartrazine (yellow food coloring), curcumin (from turmeric), anthocyanin (from blueberries) and inorganic gold nanoparticles, as effective photoabsorbers to increase the resolution of DLP-printed perfusable poly(ethylene glycol)-diacrylate (PEGDA) hydrogels.⁷⁸ Other photoabsorbers such as Phenol Red and Orasol Orange G have also been used in DLP bioprinting.^{69,79}

3.3.2.2 Computed Axial Lithography Bioprinting

A recent breakthrough from Kelly *et al.* addressed the limitations of the aforementioned but relatively slow processes of 3D printing by projecting a series of 2D patterned optical light fields to fabricate a 3D object within a rotating liquid resin volume.⁸⁰ This new computed axial lithography (CAL) technology adopted from computed tomography produces an optical 3D dose distribution of light by combining 2D light patterns to photocrosslink a material.^{80,81} Each image projection propagates through the material from a different angle, where the superposition of exposures from multiple angles results in a sufficient 3D energy dose to facilitate solidification. The printing technique is also dependent on oxygen inhibition. Free radicals are generated by light activation and then rapidly quenched and deactivated by oxygen during the initial, inhibition phase of printing. For the material to photocrosslink at a given position within the volume, sufficient depletion of oxygen at the local focal point is required, where the non-linear oxygen inhibition process sets the critical dose threshold.

Another major parameter in CAL is the rotation rate of the uncured polymer which must be time-sequenced with respect to the projection intensity. As such, the resins used are either highly viscous or solid (thermal gelled) precursor materials to minimize relative motion between the printed object and the precursor. After exposure, solvent rinsing is used to remove uncured material, combined with moderate heating or further curing using light to enhance material properties. For materials that are not susceptible to oxygen inhibition, other inhibiting molecules (photoabsorbers) such as food dyes can be utilized where the CAL requires penetration of the curing wavelength through the printing volume, but dye can be added to block other wavelengths and tune component opacity. The CAL approach has several advantages over conventional layer-based printing methods,

particularly the ability to print large volumes several orders of magnitude faster. Bernal *et al.* further showed that large, free-form cell-laden structures, could be fabricated using this volumetric CAL technology, with a print speed much faster (within seconds) than conventional bioprinting methods with high cell viability (**Figure 3.6c**).⁸¹

3.3.2.3 Other Lithographic-Based Printing Techniques

Given that both SLA and DLP crosslink bioresins in a layer-by-layer manner, then, depending on the exposure time of each layer, the fabrication process has often been considered slow. Most resins or bioresins adopted for SLA/DLP are crosslinked using free-radical chain polymerization which is prone to oxygen inhibition. Typically, oxygen inhibition occurs when oxygen rapidly scavenges the radicals required for the radical polymerization, or create peroxides by combining with the free radical from the photoinitiator, causing incomplete crosslinking of the resins.^{82,83} In most conventional lithography techniques, the photocrosslinking occurs at an air-resin interface, where an adequate irradiation dosage (intensity and exposure time) is required to overcome the effect of oxygen inhibition, further restricting the print speed to a few millimeters per hour.^{67,84} Tumblestone *et al.* conducted DLP above an oxygen-permeable build window, termed continuous liquid interface production (CLIP), to utilize the oxygen-containing “dead zone” for rapid replenishing of resin during printing. By taking advantage of the oxygen-inhibited dead zone, the print speed is greatly enhanced, allowing fabrication of constructs of 5 cm in less than 10 minutes.⁸⁵ While the CLIP process has not been applied to bioresins, it does possess the potential to rapidly fabricate cell-laden constructs, at a much faster speed than SLA or DLP processes.

Another biofabrication technology that is also highly specific to light-curable materials is two-photon polymerization (2PP). 2PP adopts two-photon optics, which

leverages the two-photon absorption of near-infrared (NIR) radiation and multiphoton polymerization, allowing fabrication of constructs with features on the submicron to nano-scale.^{29,86} The most simple 2PP setup consists of a laser source, a focusing objective, a translational stage, a laser power control system, and a shutter. Most 2PP resins have been adopted from established lithography-based technologies, and also require relatively longer fabrication speeds due to the nano-scale precision.⁸⁷ However, unlike conventional lithography techniques, 2PP involves extremely high laser irradiation dosage/intensities, mostly on the order of terawatts per cm². Moreover, in conventional 2PP processes, the height of the printed structure is limited by the working distance of the microscope objective used for focusing laser pulses into the photosensitive material.⁸⁸

While the technologies reviewed thus far have focused on the building up of materials through additive manufacturing technologies, it may also be of interest to employ photodegradation (i.e., subtractive manufacturing) to fabricate constructs with desired 3D structures. For example, it has been previously shown that the incorporation of ortho-nitrobenzyl (o-NB) moieties in hydrogel crosslinks can render hydrogels degradable via near-UV irradiation (365 nm), allowing spatiotemporal control over hydrogel degradation, including with two-photon techniques.⁸⁹⁻⁹¹ For example, Lunzer *et al.* reported on the controlled erosion of PEG-HA hydrogels via two-photon photopatterning, including with the incorporation of photosensitizers to increase the efficiency of o-NB degradation and under cytocompatible conditions.⁹¹ Coumarin-fluorophores have also been previously incorporated into PEG hydrogels containing o-NB moieties to enhance the efficiency of two-photon-mediated photolysis.⁹²

Beyond o-NB moieties, alternative photodegradation chemistries susceptible to variable wavelengths of light have been developed. For example, coumarin-derivatives

have been incorporated into both PEG⁹³ and PVA⁹⁴ hydrogels for degradation under either visible or UV light. Rapp *et al.* developed photodegradable crosslinkers that are sensitive to visible light (400-540 nm) through the incorporation of ruthenium-based crosslinkers (i.e. Ru-aldehyde, $[\text{Ru}(\text{bpy})_2(3\text{-pyridinaldehyde})_2]\text{Cl}_2$) into HA hydrogels.⁹⁵ Similar ruthenium-based complexes have also been used to induce the degradation of supramolecular hydrogels via two-photon optics.⁹⁶ Advances in two-photon optics, photosensitizers, and photodegradation chemistries will enable the continued development and fabrication of complex, negative features within bioresins via subtractive manufacturing.

3.4 OVERVIEW OF MATERIALS IN LIGHT-BASED BIOPRINTING

With the implementation of each of the aforementioned light-based bioprinting techniques, there are a range of photocrosslinkable materials, photoinitiators, and photosensitizers that have been utilized to offer a library of possible bioink formulations and crosslinking conditions. This section describes the various materials that have been developed or applied to bioprinting that utilize photocrosslinking during fabrication.

3.4.1 Reactive Polymers used for Photocrosslinkable Bioinks and Bioresins

Hydrogels are water-swollen polymer networks comprised of natural and/or synthetic materials, and are of special interest in the development of bioinks for bioprinting because they can be rationally designed and crosslinked to emulate features and organization of native tissues for applications in tissue engineering. At the most simple level, the highly hydrated environment (i.e. > 90 wt% water content) of hydrogels recapitulates the aqueous environment of *in vivo* tissue systems and permits additional complexity via the encapsulation of cells, bioactive molecules, and peptides.¹⁸ Printable hydrogel platforms are also used in 3D bioassembly to encapsulate and fabricate complex

cellular aggregates or modular components, such as tissue spheroids and cell-laden microcarriers.^{97,98} Furthermore, hydrogels are generally biodegradable and can be readily engineered to capture a range of physiochemical properties.¹ For example, the degree of crosslinking achieved in hydrogels can be directly tuned to yield scaffolds with well-defined mesh sizes.⁹⁹ Networks that support diffusivity are necessary in printed hydrogels to ensure that encapsulated or seeded cells distributed throughout constructs receive nutrients, metabolites, and oxygen,⁹⁹ and to allow cells to secrete extracellular matrix and/or undergo vascularization.^{100,101} Crosslink density also directly influences the bulk mechanics of hydrogels and may be controlled to yield scaffolds with viscoelasticity and stiffness comparable to native tissues. Finally, engineered hydrogels can be functionalized with bioactive molecules and peptides to direct signaling, adhesion, migration, proliferation, and differentiation of encapsulated cells.¹⁰² Each of these respective characteristics make hydrogels appealing as biomaterials for the repair of diseased tissues. However, hydrogels previously implemented in bioprinting have been very diverse in both their composition and crosslinking chemistry. Here, we provide an overview on the types of natural, synthetic, and hybrid hydrogel materials that have been used as bioinks and bioresins in bioprinting applications (**Table 3.1**).

Table 3.1: Representative hydrogels used in bioprinting, including the polymer, introduced reactive group, crosslinking chemistry, and bioprinting technique employed.

Polymer	Reactive Group Modification	Crosslinking Chemistry	Bioprinting Technique
Gelatin	Methacryloyl	Free-Radical Chain Polymerization	Extrusion, ^{31,111–126} DLP, ^{84,106,119–121} CAL ^{80,81}
	Methacrylamide	Free-Radical Chain Polymerization	Extrusion ¹²²
	Allyl glycidyl ether	Thiol-ene	DLP, ¹²³ Extrusion ¹²³
	Norbornene	Thiol-ene	2PP ^{124,125}
	Thiol	Thiol-ene	Extrusion ¹²⁶
Hyaluronic Acid (HA)	Methacrylate	Free-Radical Chain Polymerization	Extrusion ^{45,127–134}
	Norbornene	Thiol-ene	Extrusion ⁴⁷
	Tyramine	Photo-Redox	Extrusion ³⁵
	Thiol	Thiol-ene	Extrusion ^{126,135,136}
	Acrylamide	Free-Radical Chain Polymerization	Extrusion ⁴⁶
	Glycidyl methacrylate	Free-Radical Chain Polymerization	DLP ^{106,137}
Silk Fibroin	Glycidyl methacrylate	Free-Radical Chain Polymerization	DLP ¹³⁸
Decellularized ECM	Innate proteins	Photo-Redox	Extrusion ¹³⁹
Collagen	Methacrylate	Free-Radical Chain Polymerization, Thiol-ene	Extrusion ¹³⁶
Chondroitin Sulfate (CS)	Glycidyl methacrylate	Free-Radical Chain Polymerization	Extrusion ¹⁴⁰
Dextran	Hydroxyethyl methacrylate	Free-Radical Chain Polymerization	Extrusion ¹⁴¹

Poly(ethylene glycol) (PEG)	Acrylate	Free-Radical Chain Polymerization	Extrusion, ^{108,126,135,142-144} SLA ^{145,146} , DLP ⁸⁴
	Methacrylate	Free-Radical Chain Polymerization	Extrusion, ^{130,147,148} SLA, ^{145,149} DLP ⁶⁹
	Thiol	Thiol-ene	Extrusion ^{60,112}
	Norbornene	Thiol-ene	Extrusion ^{60,112}
	Alkyne	Thiol-yne	Extrusion ¹³⁵
Poly(ethylene oxide) (PEO)	Methacrylate	Free-Radical Chain Polymerization	SLA ¹⁴⁹
Poly(glycidol)	Allyl glycidyl ether	Thiol-ene	Extrusion ^{150,151}
	Thiol	Thiol-ene	Extrusion ^{150,151}
PEG-co-depsipeptide	Methacrylate	Free-Radical Chain Polymerization	DLP ⁶⁴
Poly(vinyl alcohol) (PVA)	Methacrylate	Free-Radical Chain Polymerization	DLP ⁶⁷

3.4.1.1 Natural Materials

Natural materials are often used as the primary component for many bioinks and bioresins since they typically exhibit high biocompatibility, biodegradability, and bioactivity. For example, gelatin, which is derived from denatured collagen, contains innate adhesive peptide sequences (i.e., RGD) that allows embedded cells to attach and spread along its matrix. Furthermore, gelatin contains peptide sequences that are sensitive to endogenous enzymes (matrix metalloproteinases), imparting responsive degradability. To engineer gelatin so that it can photocrosslink via free radical chain polymerization, gelatin is most commonly modified with methacryloyl groups via esterification with methacrylic anhydride. In lieu of methacryloyl groups, gelatin can also be modified with reactive groups that are amenable to thiol-ene polymerizations. For example, gelatin has been previously modified with both allyl groups and norbornenes. To obtain allyl-modified gelatin, allyl glycidyl ether

is reacted with gelatin at 65 °C under alkaline conditions.¹²³ To modify gelatin with norbornene, 5-norbornene-2-carboxylic acid can be reacted with primary amines in gelatin via traditional carbodiimide/N-hydroxysuccinimide (EDC/NHS) coupling.¹⁵² Both of these gelatin derivatives are capable of reacting with multifunctional-thiol crosslinkers to form hydrogels. However, gelatin may also be modified with pendant thiol groups, offering an additional functional handle that can be leveraged to incorporate desired biomolecules or crosslinks into a designed hydrogel. To thiolate gelatin, dithiobis(propanoic dihydrazide) (DTP) or dithiobis(butyric dihydrazide) (DTB) is first coupled to the backbone of gelatin again using EDC/NHS chemistry. Thereafter, disulfides contained within DTP or DTB can be reduced in the presence of excess dithiothreitol (DTT), giving rise to thiol-modified gelatin.¹⁵³

Hyaluronic acid (HA) is a non-sulfated glycosaminoglycan that is found in many connective tissues and is involved in a number of biological processes such as wound healing, development and normal tissue homeostasis.¹⁵⁴ HA is attractive for photocrosslinkable bioinks because it may be readily cleared by the body via hyaluronidases and oxidative species, and it contains many pendant groups that can be readily modified. For example, HA has been modified with methacrylates via esterification with methacrylic anhydride or reaction with glycidyl methacrylate in the presence of triethylamine.^{127,137} Carbodiimide chemistry has also been utilized to modify HA with photocrosslinkable acrylamide groups.⁴⁶ Similar to gelatin, HA may also be modified with norbornenes via di-tert-butyl-dicarbonate (Boc₂O) coupling of 5-norbornene-2-carboxylic acid to its primary alcohol or benzotriazole-1-yloxytris(dimethylamino)phosphonium hexafluorophosphate (BOP) coupling of 5-norbornene-2-methylamine to the carboxylic acid group.^{155,156} Similar approaches have been used as previously described to thiolate HA (i.e., via conjugation of DTP or DTB, followed by reduction with DTT),¹⁵⁷ but it is also

possible to react methacrylated-HA in the presence of excess DTT to obtain pendant thiols, albeit in a less controlled manner. However, it has been previously shown that modification of the carboxylic acid group within HA can attenuate its ability to interact with cell-binding sites such as CD44.¹⁵⁸ Therefore, alternative strategies have been developed to modify the primary alcohol of HA with cysteines via an ether bond.¹⁵⁹ HA has also been modified with maleimide groups via BOP coupling of N-(2-aminoethyl)maleimide trifluoroacetate.¹⁶⁰ To render HA amenable to photo-mediated redox polymerization, tyramine groups have been conjugated to the carboxylic acid of HA via 4-(4,6-dimethoxy-1,3,5-triazin-2-yl)-4-methyl-morpholinium chloride (DMTMM) amide-coupling.²⁹ All of these derivatives of HA provide a multitude of possible crosslinking timescales and network architectures, effectively expanding upon the range of scaffold properties that can be engineered in HA hydrogels.

Chondroitin sulfate (CS) is a proteoglycan found in connective tissues such as cartilage that may be enzymatically degraded and modified with glycidyl methacrylate. To achieve methacrylation, chondroitin sulfate is first converted into its tetrabutylammonium salt and then undergoes esterification with glycidyl methacrylate in the presence of dimethylaminopyridine (DMAP).¹⁴⁰ Other naturally derived materials that may be used for photocrosslinkable bioinks and bioresins include dextran,¹⁴¹ silk fibroin,¹³⁸ collagen,¹⁶¹ decellularized ECM,¹³⁹ alginate,¹⁶² κ -carrageenan,¹⁶³ and chitosan.¹⁶⁴ All of these biopolymers can similarly be modified with reactive functional groups that are suitable for photocrosslinking. While dextran has been reacted with methacrylic anhydride as previously described to achieve methacrylate modification,¹⁴¹ silk fibroin has been methacrylated via reaction with glycidyl methacrylate in lithium bromide at 60 °C.¹³⁸ To methacrylate chitosan for use as a biomaterial ink, carbonyldiimidazole was used to

activate hydroxyethyl methacrylate (HEMA), allowing for HEMA conjugation to the alcohols of chitosan.¹⁶⁴

The advantage to using all these natural materials over synthetic materials when designing a bioink or bioresin is that they contain either native adhesive surfaces for cells, signaling cues that impart bioactivity, innate degradability, minimal immunogenicity, and/or pendant groups that can be easily modified. However, one major limitation of naturally derived polymers is that they may exhibit unpredictable composition (e.g., dispersity) and batch-to-batch variations, such that their mechanical properties and degradation rates are not always easy to control.

3.4.1.2 Synthetic Materials

Generally, synthetic hydrogels offer high batch-to-batch uniformity with more controllable and reproducible scaffold structures, gelation kinetics, degradation rates, and mechanical properties when compared to naturally-derived materials. Poly(ethylene glycol) (PEG) is one of the most commonly utilized synthetic polymers in bioprinting, as it can be easily modified with a range of functional reactive groups and exhibits high hydrophilicity, attenuating protein adsorption in culture and *in vivo*.¹ PEG has been reacted with acryloyl chloride and methacryloyl chloride in the presence of triethylamine to achieve pendant acrylate and methacrylate moieties that can be photocrosslinked via free radical chain polymerization.¹ To allow for hydrolytic degradation of PEG networks, α -hydroxy acids have been incorporated between these photosensitive end-groups and the PEG backbone.¹⁶⁵ PEG can also be modified with pendant thiol or norbornene groups so that it may be photocrosslinked via thiol-ene reactions.^{60,112} Poly(vinyl alcohol) (PVA) has also found use as a bioink due to its hydrophilicity and readily modified alcohol groups.⁶⁷ Similar to the abovementioned naturally-derived polymers, polyvinyl alcohol can be methacrylated

via esterification with methacrylic anhydride.⁶⁷ PVA has also been modified with tyramine groups by carboxylation via succinic anhydride and subsequent coupling via carbodiimide chemistry, allowing it to be crosslinked via photo-mediated redox polymerization.¹⁶⁶

Although synthetic materials permit a high level of tunability and control, unmodified synthetic hydrogels (e.g., PEG, PVA) commonly lack suitable binding sites for cells to adhere. Furthermore, these hydrogels are also limited in their ability to support cell differentiation. Therefore, modifications that have been applied to enhance cell-instructive capacity include incorporation of adhesive sequences (e.g., RGD) or heparin-binding sites.^{102,167} The incorporation of MMP-sensitive crosslinkers has also been used to enable cell-mediated degradation and remodeling of synthetic matrices.¹⁶⁸ Since synthetic materials often fail to incorporate the bioactivity of naturally derived materials, some bioinks combine both natural and synthetic materials to achieve the advantages each class of materials offers in the form of hybrid bioinks and bioresins.^{67,120,142,169}

3.4.2 Photoinitiators and light sources used for bioinks and bioresins

Despite the vast application of photocrosslinking in 3D bioprinting, the conditions (e.g., light source, light intensity, exposure time, irradiation wavelength and photoinitiator concentration) in which this occurs varies greatly across laboratories. This makes it challenging to compare results between different studies, even when identical compositions and photoinitiators are used. As most photocrosslinking processes are dependent on free radicals, understanding the effects of these radicals on cells is important, given that free radicals can react with cell membranes, proteins, DNA, potentially causing cellular damage.¹⁷⁰⁻¹⁷⁴ Moreover, in the context of applying photocrosslinking to bioprinting, understanding the fundamental reaction mechanism is even more important to ensure that the targeted shape fidelity and resolution are not

jeopardized, while preserving overall cell viability and functionality. This section will cover various photoinitiators and light sources used during the photocrosslinking reactions within bioprinting.

3.4.2.1 Free-Radical Photoinitiators

Free-radical photoinitiators are the most commonly employed type of photoinitiator in bioprinting, as their reaction mechanisms are well studied and established. In general, these photoinitiators use light to dissociate into radicals, which then facilitate photocrosslinking. Photoinitiators can be further classified into Type I or Type II, where the former is usually a single component photoinitiator, while the latter requires two components, usually a photoinitiator in combination with a co-initiator.

Type I Photoinitiators

When incident light is absorbed by type I photoinitiators, a homolytic cleavage process starts once the molecules reach the excited singlet or triplet state.^{175,176} This photochemical cleavage creates free radicals, mostly from Norrish type I reactions, which can subsequently induce the polymerization process. Cleavage can occur at any weak bond, but usually takes place at the α -position of the carbonyl group (α -cleavage). Bryant *et al.* previously conducted a comprehensive and systematic cytocompatibility comparison between a range of type I photoinitiators, 2,2-dimethoxy-2-phenylacetophenone (Irgacure 651), 1-hydroxycyclohexyl phenyl ketone (Irgacure 184), 2-methyl-1-[4-(methylthio)phenyl]-2-(4-morpholinyl)-1-propanone (Irgacure 907), and 2-hydroxy-1-[4-(hydroxyethoxy)phenyl]-2-methyl-1-propanone (Irgacure 2959), which concluded that Irgacure 2959 promoted the best cell viability of chondrocytes encapsulated within acrylated PVA hydrogels.¹⁷⁰ One of the advantages of Irgacure 2959 is that it possesses a p-hydroxyethoxy group, which gives it a hydrophilic nature with slight water solubility of

0.7w/v%.¹⁷⁰ This water solubility is an important feature, as it allows cells to be encapsulated in hydrogels without the presence of any toxic organic solvents. Another benefit of Irgacure 2959 is that it does not produce cytotoxic benzaldehyde as a by-product of the photo-cleavage reaction.¹⁷⁷ To this end, Irgacure 2959 has been extensively used to fabricate cell-laden hydrogel constructs in the last two decades.

For efficient polymerization, understanding the absorption spectrum of the selected photoinitiator is important. Irgacure 2959 absorbs within the UV range (200-370 nm), where upon absorption of a UV photon, the excited singlet state converts to a triplet state via inter-system crossing, and this triplet state dissociates to form benzoyl and ketyl radicals.^{177,178} In most cases, the benzoyl radicals then react with unsaturated double bonds, facilitating free-radical chain polymerization or thiol-ene photocrosslinking.¹⁷⁹⁻¹⁸¹ However, the use of light at the lower wavelength UV range (<300 nm) has been associated with phototoxicity and mutagenicity,^{171,182,183} which is impractical for cell encapsulation purposes. As such, most research groups have been using Irgacure 2959 with a light source of 365 nm, which is closer to the visible light range to minimize cytotoxicity and genotoxicity.¹⁸⁴ Using Irgacure 2959 at higher wavelength comes with a cost of low reaction efficiency, since the molar extinction coefficient of Irgacure 2959 at 365 nm is very low (only $4 \text{ M}^{-1}\text{cm}^{-1}$) (**Figure 3.7**).¹⁸⁵

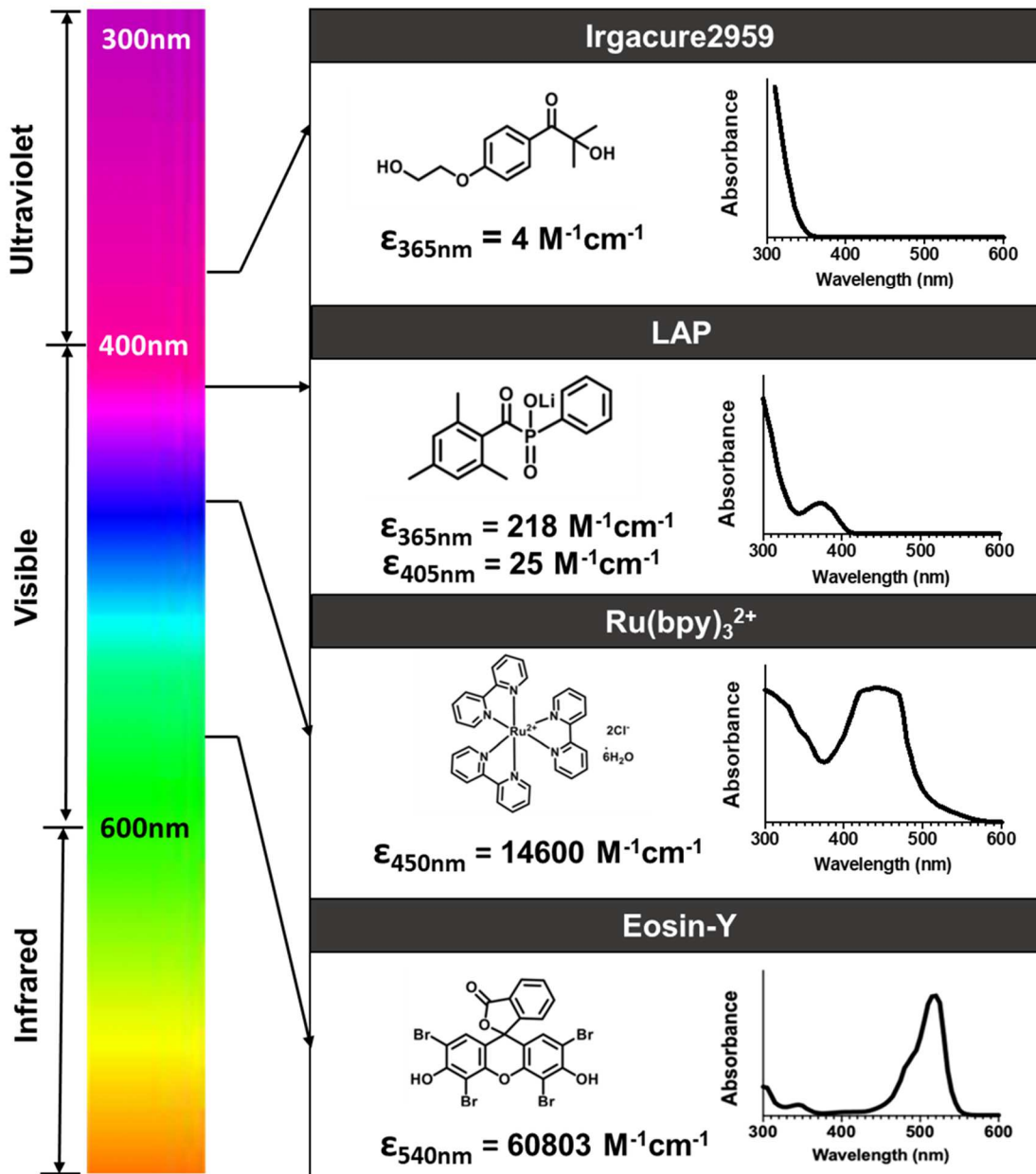


Figure 3.7: Absorption spectra and molar extinction coefficients of commonly used photoinitiators for light-based bioprinting.

Therefore, most studies have either used much higher light intensity, longer exposure times or higher photoinitiator concentrations (**Table 3.2**) to circumvent the low polymerization efficiency of Irgacure 2959 at 365 nm. Bioinks containing Irgacure 2959 have been used for both extrusion and lithography-based bioprinting.

Table 3.2: Photocrosslinking parameters used for various photoinitiators during light-based bioprinting.

Photoinitiator	Concentration	Intensity, Wavelength	Duration	Bioprinting Technique
Irgacure 2959	0.2 wt%	4-6 mW/cm ² , 365 nm	< 30 sec	Extrusion ⁴⁴
	0.5 wt%	6.9 mW/cm ² , 360-480 nm	60 sec	Extrusion ¹¹⁰
	0.05 wt%	30 mW/cm ² , 365 nm	3 min	Extrusion ¹²³
	0.5 wt%	Intensity not reported, 250-365 nm	Not reported	Extrusion ¹¹⁷
	0.1 wt%	1.2 mW/cm ² , 365 nm	5 min	Extrusion ¹³¹
	0.2 wt%	500 mW/cm ² , 290-320 nm	2 min	Extrusion ¹⁰⁷
	0.1 wt%	150 mW/cm ² , 365 nm	100-230 sec	Extrusion ¹¹⁸
	0.05 wt%	6 mW/cm ² , 365 nm	10 min	Extrusion ¹⁴⁷
	0.05 wt%	103 mW/cm ² , 300-600 nm	69 sec	Extrusion ^{130,140,148}
	0.05 wt%	10-15 mW/cm ² , 320-390 nm	2 min	Extrusion ¹²⁷
	0.1 w/v%	3-240 mW/cm ² , 365 nm	10 sec - 5 min	Extrusion ¹¹⁶
	0.1 w/v%	2.6 mW/cm ² , 365 nm	30 min immersed in Irgacure 2959 bath	Extrusion ¹¹¹
	0.5 wt%	10 mW/cm ² , 365 nm	5 min	Extrusion ¹⁸⁶
	0.05 wt%	130 mW/cm ² , 365 nm	2 sec/layer, total of 20 layers	Extrusion ^{150,151}
	0.5 wt%	3.95 W/cm ² , 365 nm	30 sec	Extrusion ¹⁸⁷
	0.5 w/v%	850 mW/cm ² , 365 nm	15 sec	Extrusion ¹⁰⁵
	0.01 w/v%	1.3 mW/cm ² , 365 nm	5 min	Extrusion ¹⁴²
	0.1 w/v%	Not reported	10 sec	Extrusion ¹³⁶
	0.1 w/v%	20 mW/cm ² , 365 nm	Continuous during printing	Extrusion ¹¹⁴
	0.3-2 wt%	Not reported	1-5 min	Extrusion ¹⁰⁴
	1 wt%	1.3 mW/cm ² , 365 nm	5 min	Extrusion ¹⁴³
	0.05 wt%	Not reported	45 sec/layer	Extrusion ¹³²
	0.5 wt%	65-78 mW/cm ² , 325 nm	2-10 sec/layer	SLA ^{145,188}
	0.4 w/v%	Power=36 W, Wavelength not reported	10 min	Extrusion ⁴⁸
	0.05 wt%	10 mW/cm ² , 320-390 nm	Continuous during printing	Extrusion ⁴⁷
	0.3 wt%	5 mW/cm ² , Wavelength not reported	60 sec	Extrusion ¹⁰³
	0.1 w/v%	3 mW/cm ² , 365 nm	10 min	Extrusion ¹²⁸
0.2 w/v%	5 mW cm ² , Wavelength not reported	5 sec/layer, 6 min after printing	Extrusion ¹¹²	
1 w/v%	20 mW cm ² , 350-450 nm	5 min	Extrusion ¹⁴¹	
0.05-0.1 w/v%	18 w/cm ² , 365 nm	2-4 sec	Extrusion ¹³⁵	
Not reported	14-16 mW/cm ² , 365nm	2-3 min/layer	SLA ¹⁴⁹	
LAP	0.037 wt%	Power = 6.4 W, 405 nm	23 sec	CAL ⁸¹
	0.5 wt%	0.5 – 2 mW/cm ² , 365 nm	Throughout printing	Extrusion ¹⁸⁶
	0.05 wt%	2 W/cm ² , 365 nm	120 sec	Extrusion ¹⁸⁹
	0.1 wt%	700 mW/cm ² , 365 nm	10 sec	Extrusion ¹³³
	0.1 wt%	Intensity not reported, 400-410 nm	5 min	Extrusion ¹⁰⁸
	0.5 w/v%	7 mW/cm ² , 405 nm	2 min	Extrusion ¹¹³
	4.46 mM	5 mW/cm ² , 365 nm	Continuous during printing	Extrusion ¹¹⁴
0.5 w/v%	0.5 W/cm ² , 365 nm	30 sec	Extrusion, ¹²¹ DLP ¹²¹	

	0.15-0.3 w/v%	88 mW/cm ² , 365 nm	Not reported	DLP ¹⁰⁶
	0.2 w/v%	30 mW/cm ² , 365 nm	4 sec/layer	DLP ¹³⁸
	0.6 w/v%	Intensity not reported, 365 nm	Not reported	DLP ¹²⁰
	0.2-0.6 wt%	Intensity not reported, 400-450 nm	Not reported	DLP ^{69,79}
	0.2 w/v%	5 mW cm ² , Wavelength not reported	5 sec/layer, 6 min after printing	Extrusion ¹¹²
	34 mM	16.4 mW/cm ² , 405 nm	Not reported	DLP ⁸⁴
	0.05 w/v%	6.09 mW/cm ² , 365 nm	10 sec	Extrusion ¹⁹⁰
	0.05 wt%	15 mW/cm ² , 400-500 nm	Continuous during printing	Extrusion ⁴⁷
	0.05 wt%	5-15 mW/cm ² , 400-500 nm	Continuous during printing	Extrusion ⁶²
	Not reported	60 mW/cm ² , 365 nm	3 min	Extrusion ⁶⁰
0.15-0.22 w/v%	88 mW/cm ² , 365 nm	Not reported	DLP ¹¹⁹	
0.25 w/v%	Not reported	100, 120, or 160 sec/layer	DLP ⁶⁴	
VA086	1.1 w/v%	1.2 mw/cm ² , 365 nm	5 min	Extrusion ¹⁴⁴
	0.5 wt%	130 mW/cm ² , 365 nm	60 sec	Extrusion ¹³⁴
	0.5-5 wt%	Not reported	1-5 min	Extrusion ¹⁰⁴
	20 mol%	4 mW/cm ² , 365 nm	7.5 min	Extrusion ¹²²
Eosin-Y	0.01 w/v%	80 mW/cm ² , 505 nm	Throughout printing	Extrusion ³⁵
	0.1 mM	Intensity not reported, 514 nm	2 min/layer	SLA ¹⁴⁶
Ru/SPS	1/10 mM	30 mW/cm ² , 400-450 nm	3 min	Extrusion, ^{123,191} DLP ¹²³
	1/10 mM	50 mW/cm ² , 400-450 nm	15 min	Extrusion ¹⁷
	0.2/2 mM	7.25 mW/cm ² , 400-450 nm	10 sec/layer	DLP ⁶⁷
	1/10 mM	3 mW/cm ² , 400-450 nm	5 min	Extrusion ¹⁹²
	0.5/5 mM	30 mW/cm ² . 400-450 nm	3 min	Extrusion ²⁷

Another commonly adopted type I photoinitiator is lithium phenyl-2,4,6-trimethylbenzoylphosphinate (LAP), which was initially synthesized by Majima *et al.* and reported to be water-soluble up to 8.5w/v%. Fairbanks *et al.* then conducted a comparative study between Irgacure 2959 and LAP, and reported that LAP has a much higher molar extinction coefficient (218 M⁻¹cm⁻¹) at 365 nm, hence allowing much more light to be absorbed at this wavelength.¹⁸⁵ This higher light absorption leads to more rapid gelation (using PEGDA hydrogel) due to a higher initiation rate and subsequent polymerization rate.¹⁸⁵ Another interesting feature of LAP is that it also absorbs mildly in the visible light range (405 nm), with a molar extinction coefficient of 25 M⁻¹cm⁻¹. Therefore, LAP has been widely used in the biofabrication community at either 365 nm or 405 nm, with varying concentrations and irradiation conditions. Similar to Irgacure 2959, LAP has been applied

to a range of bioinks and bioresins that undergo either free-radical chain polymerization or thiol-ene photocrosslinking, and also for both extrusion-based and lithography-based bioprinting. In recent years, 2, 2'-azobis[2-methyl-n-(2-hydroxyethyl) propionamide] (VA-086) has also been exploited for use in extrusion or lithography bioprinting applications. VA-086 is water soluble and absorbs at 375nm with a molar absorption coefficient of $30 \text{ M}^{-1}\text{cm}^{-1}$, which is 7-times higher than Irgacure 2959. It was shown that the generated radicals as a product of the photo-dissociation of VA-086 are less cytotoxic to cells when compared to Irgacure 2959.^{162,193} To date, VA-086 has only been applied to free-radical chain polymerization, mainly methacrylates and methacrylamides.^{122,194,195} One drawback of VA-086 is the generation of N_2 gas as a product of the azo-bond (N=N) dissociation of the photoinitiator, resulting in cloudy or opaque hydrogels.^{146,194}

Type II Photoinitiators

In contrast to type I photoinitiators, type II photoinitiators often have a more complex initiating mechanism, where following photon absorption, the excited initiator abstracts a hydrogen atom from a co-initiator, forming H-donor radicals that initiate the photocrosslinking process.¹⁹⁶ One of the most widely used type II photoinitiators is 2,3-bornanedione, also known as camphorquinone, which has a long-standing history in photocuring dental composites. Although camphorquinone has been successfully used to encapsulate cells within hydrogels with adequate cell viability,¹⁷⁰ its poor water solubility poses an additional practical challenge for most bioprinting applications. Alternatively, the organic dye eosin-Y has been used as a photoinitiator for tissue engineering due to its high water solubility.^{197,198} Eosin-Y absorbs green light, with a molar extinction coefficient of $60803 \text{ M}^{-1}\text{cm}^{-1}$ at 539 nm.¹⁹⁹ Upon excitation, eosin-Y undergoes rapid intersystem crossing to the lowest energy triplet state, which has a life time of 24 μs .²⁰⁰ Subsequently, the photo-excited eosin-Y extracts hydrogen atoms from an amine-functionalized co-

initiator, such as triethanolamine.^{197,201} The deprotonated radical then serves as the main component to facilitate photocrosslinking.¹⁹⁸ However, this reaction is often slow and requires additional accelerants such as N-vinylpyrrolidone or N-vinylcaprolactam.^{146,175,198} The need for additional co-initiators and accelerant species has become a practical drawback for the use of eosin-Y in bioprinting applications, as it is often more challenging to optimize the concentrations of a set of initiators as opposed to just a single component such as type I photoinitiators. It is also important to ensure that each of the components are applied within a non-cytotoxic concentration threshold and that the combination of all three components do not produce toxic by-products that can cause cell death. In addition to the free-radical chain polymerization and thiol-ene photocrosslinking mechanisms, eosin-Y has also been reported to facilitate photo-mediated redox reactions, without the need of a co-initiator or accelerant. Loebel *et al.* showed the successful fabrication of HA-Tyr hydrogels through di-tyramine crosslinking using eosin-Y and 2PP.²⁰²

In recent years, another photo-initiating system of interest is tris(2,2-bipyridyl) dichlororuthenium (II) hexahydrate (Ru), which is based on a transition metal complex. Ru has been previously characterized to be highly absorptive in the visible light range, with a molar extinction coefficient of $14600 \text{ M}^{-1}\text{cm}^{-1}$ in the visible light range (450 nm).^{17,203} When irradiated with visible light, the ground state Ru^{2+} gets photo-excited and then oxidizes into Ru^{3+} through donating electrons to a co-initiator such as sodium persulfate (SPS). After accepting electrons, SPS dissociates into sulfate anions and sulfate radicals, where the newly generated sulfate radicals can either trigger free-radical chain polymerization or thiol-ene photocrosslinking. Interestingly, the photo-excited Ru^{3+} can also facilitate photo-mediated redox reactions by oxidizing aromatic residues such as tyrosine.^{203,204} These oxidized tyrosine groups are further converted into tyrosyl radicals, which are then

subsequently quenched by forming di-tyrosine bonds with other nearby tyrosine groups.^{205,206}

3.4.2.2 Light Sources used for Bioprinting and Light Attenuation

Photoinitiators are activated through their absorption of specific wavelengths; thus, the light source used must be compatible with the photoinitiator used. One source that has been used in bioprinting is light emitting diodes (LEDs), which have a number of advantages such as low heat generation, low energy consumption, low operating costs, less maintenance, portability, compact design, and easy and safe handling. LED light sources have already been integrated in the dentistry space for the past few decades and are also used in 3D printing technologies such as digital inkjet printing. Commercial LEDs can be obtained at 365, 385, 395, 405, 455 or 477 nm. Interestingly for bioprinting, most type I photoinitiators absorb in the UV range, whereas type II photoinitiators are often irradiated in the visible light range. The intensity of the light used and its compatibility with the selected initiator combine towards alterations in the kinetics of bioink gelation.

An important design criterion when engineering a bioink or bioresin is the degree to which they may attenuate light, including all components (e.g., rheological additives). In the case of curing large constructs, it is possible that over long length scales (i.e., many millimeters), the intensity of light will decrease. Decreased light intensities may give rise to differential reaction kinetics and degrees of crosslinking throughout a photocrosslinked construct, resulting in heterogeneous network properties. To understand this, quantitative Beer-Lambert law calculations are often performed to understand how much light attenuation occurs due to absorbing species within a bioink. Specifically, the intensity drop across a length scale of interest, L , due to a single absorbing species may generally be described by Equation 3.3:

$$(3.3) \quad I = I_0 e^{-\epsilon L C}$$

where I_0 is the initial light intensity, ϵ is the molar extinction coefficient for the absorbing species (i.e., photoinitiator), C is the concentration of the absorbing species, and I is the final intensity. If there are multiple components within a bioink that significantly attenuate light, the Beer-Lambert Law may be further updated. Obstacles introduced by significant light attenuation may be overcome through the implementation of dual initiator systems or photobleaching initiators.¹

3.5 CELLULAR CONSIDERATIONS IN LIGHT-BASED BIOPRINTING

One of the main components of bioinks and bioresins are cells. Although there has been much success with bioprinting of cell-laden constructs, considerations must be made to ensure the viability and function of the cells. This was highlighted above by the selection of the appropriate material to be included within the bioink or bioresin. However, the printing process itself must also inform bioink or bioresin formulation design. For example, features such as the potential for shear forces on cells during the printing process, the exposure of the cells to light and radicals during photocrosslinking, and the settling of cells throughout potentially extended print times elicit important consideration. Furthermore, in most reports, bioink and bioresin properties are characterized in the absence of cells. It should be noted that the presence of cells may indeed change a number of bioink or bioresin properties (e.g., light attenuation, rheological properties, crosslinking efficiency) depending on the cell concentration used. To this end, the incorporation of cells and the cell density within a bioink or bioresin may require changes or optimization of either the ink formulation or the printing process. In this section, we discuss various printing

parameters in the context of cells and how each can be tuned through the design of the bioink or bioresin and their processing to maximize cell viability and functionality.

3.5.1 Shear forces

To achieve optimal cell cytocompatibility and functionality, it is important to ensure that cells within the bioinks or bioresins survive the printing process. In terms of extrusion bioprinting, the influence of external forces such as shear stress on cell viability should be first evaluated. For example, in scenarios where bioprinted constructs are subjected to light irradiation post extrusion, the initial cell damage due to the shear stress during flow through the print head nozzle must be considered, as the mechanically disrupted cells could be more vulnerable to oxidative damage arising from photocrosslinking reactions. Shear stress is the specific sum of forces that impose a deformation on a material in a plane parallel to the direction of the force. For instance, gelatin and HA based bioinks often exhibit a shear-thinning behavior, where the viscosity of the bioink formulation decreases by shear force.^{127,207} However, during extrusion, the shear field that is present within the syringe nozzle might also contribute to mechanical disruption of the cell membrane, leading to cell damage or cell death. During bioink extrusion from a syringe nozzle, mechanical cell disruption is a direct consequence of shear, where fluid at the nozzle walls undergo shear-thinning behavior while remaining in laminar flow.

Hydrogel bioinks have been previously reported to be cell-protective, where cells extruded in a hydrogel experience plug-flow rather than the detrimental Poiseuille flow experienced when cells are simply extruded in solution.^{108,208,209} Blaeser *et al.* used fibroblast-laden alginate hydrogel bioinks to model the effect of shear forces on cell viability, and showed a significant reduction in cell viability when shear forces >10kPa were exerted.²¹⁰ It was also reported that the shear stress increased with the viscosity of

the alginate bioink. Billiet *et al.* further showed that the shapes of the needles also play an important role in controlling the shear stress exerted onto cells within the bioink. For example, a high cell viability was obtained by flow through a conically shaped needle instead of cylindrical needles. Interestingly, although higher shear stresses were obtained for the conical needle type, the shear stress built-up was only observed close to the fluid outlet (1 mm). On the other hand, flow through a cylindrical needle type resulted in lower peak shear stresses that were exerted for an increased passage length (>16 mm). This result suggests that generally, short exposure to higher shear stresses is instead favorable, where extended exposure to lower shear stresses results in the accumulation of mechanical damage to cells.

In contrast to extrusion-based bioprinting, in lithography-based bioprinting technologies, cells are generally exposed to lower shear stresses. Shear forces would include when the resin bath is filling with the bioresin from the surrounding vat. Overall, the printing process and material may both play a role on the shear forces generated on cells.

3.5.2 Photoirradiation conditions

The selection of photoinitiator is important for most light-based bioprinting technologies, as the efficiency and reactivity of the photoinitiators influence the irradiation conditions (light intensity and exposure time) needed. As summarized in **Table 3.2**, a wide variety of photoinitiator concentrations, light intensities, and exposure times have been used during light-based bioprinting. Taking Irgacure 2959, the most commonly used photoinitiator, as an example, the employed concentrations ranged over at least 20-fold from 0.05 to 1wt%, and the light intensity varied from 1.2 to 850 mW/cm². Although Irgacure 2959 exhibits a low molar absorptivity at 365nm, most research groups have still

chosen to utilize the photoinitiator at this wavelength to mitigate the use of low-wavelength UV irradiation (200-300 nm), which is well documented to be cytotoxic and genotoxic.^{183,211} However, the low reactivity of Irgacure 2959 might compromise the hydrogel crosslinking efficiency, leading to the need for higher UV irradiation dosages or higher Irgacure 2959 concentrations. For example, Lim *et al.* showed that GelMA constructs bioprinted via free-radical chain polymerization were susceptible to oxygen inhibition when irradiated in normoxic environment, causing the constructs to collapse due to incomplete crosslinking.¹⁷ This oxygen inhibitory effect can be circumvented by using higher photoinitiator concentration or irradiation dosage. However, when using Irgacure 2959, increasing its concentration from 0.05 to 0.5wt% or light intensity from 3 to 100 mW/cm² significantly reduced the cell viability. This was improved with the use of an alternative Ru/SPS and visible light system. Similarly, Colosi *et al.* reported that increased UV exposure time reduced cell viability.⁴⁴ Billiet *et al.* also showed that increasing irradiation doses of UV (365nm) from 1350 mJcm⁻² to 5400 mJcm⁻² significantly reduced the viability of Hep-G2 cells from 90% to 56% in extruded GelMA constructs.¹²² Tigner *et al.* demonstrated that due to a higher molar absorptivity than Irgacure 2959 at 365 nm, LAP resulted in faster photocrosslinking of gelatin bioinks.

However, it remains unclear as to whether the observed cytotoxicity is due solely to UV exposure. Mironi-Harpaz *et al.* previously reported that short exposure of cells to UV irradiation at 365nm within PEGDA hydrogels is not cytotoxic.²¹² Furthermore, a recent study by Rustkowitz *et al.* showed that exposing fibroblasts and MSCs to a low-dose of 365nm light (10 minutes, 1 to 20 mWcm⁻²) did not affect cellular proliferation rates, induce apoptosis of the cells, or change their proteome.²¹³ These studies suggest that perhaps the radical species following photo-cleavage of photoinitiators is responsible for the reported cytotoxicity. A comparative study between Irgacure 2959 and VA-086 revealed

that at a similar photoinitiator concentration and UV (365nm) irradiation dosage, HepG2 cells encapsulated in GelMA using VA-086 exhibited much higher cell viability.¹²² This is in agreement with a study conducted by Rouillard *et al.* where radicals generated via photo-dissociation of Irgacure 2959 are said to be the cause of the cytotoxicity effect observed.¹⁶² Therefore, bioinks may generally be printed using UV light if the total dosage of light used is mitigated.²¹³ However, since the cytotoxic effects of radicals may appreciably impede cell behaviors, it is imperative that cell-laden printed constructs be washed after light exposure whenever possible to remove any potentially harmful radical species.

3.5.3 Cell Settling

One challenge to the incorporation of cells into bioinks and bioresins is the settling of cells during printing. While extrusion bioprinting is amenable to the fabrication of large constructs and is highly modular, printing times may take on the order of hours for completion. Additionally, lithography-based bioprinting techniques are typically used to achieve print features with higher resolution (25 – 50 μ m), however, printing can be slow. For example, for a 5mm x 5mm x 5mm cube, a typical DLP process can take up to 1.5 hours.^{67,111,214} The time that it takes to print the desired construct, as well as the viscosity of the bioink or bioresin determine whether the settling of cells is a concern to obtain uniform cell distributions throughout a printed construct.

Chan *et al.* previously reported that in a typical top-down SLA approach, cells mixed within the bioresin settled to the bottom of the resin reservoir during the printing process, causing inhomogeneous cell distribution within the printed construct. In addition, Lin *et al.* showed that 37.5 (v/v%) of Percoll was required as an additive in a PEGDA bioresin to match the buoyant density of the cells to prevent cell settling.^{69,73} It is therefore

desirable for any bioresin to have rheological properties that limit potential cell settling within the resin bath during fabrication, so as not to yield inhomogeneous cell distributions throughout prints. For extrusion bioprinting, cell settling is usually not observed when viscous bioinks are utilized. However, for the cases of non-viscous inks, it is possible that cells within a loaded syringe may settle prior to deposition, resulting in printing of inhomogeneous features. These challenges may be circumvented through the employment of microfluidic printing or viscosity modulators.^{116,207,215,216}

An advantage of CAL bioprinting over these techniques is the low print times required, which ensures that cells are rapidly encapsulated within the bioresin of interest upon photocrosslinking.⁸¹ Furthermore, bioresins employed in CAL printing are typically more viscous, mitigating the potential for cell settling during the printing process.⁸⁰ In general, cell settling can be mitigated either through the printing technique adopted, and/or through the control over light exposure, as this will control the properties of the bioink or bioresin and resulting cell settling.

3.6 CONCLUSIONS

The fundamental understanding and application of photocrosslinking techniques have been important in the design of a range of bioinks and bioresins tailored for multiple biofabrication technologies, including the most widely adopted extrusion bioprinting approaches to control pre-, in-situ-, and post-crosslinking of bioinks, as well as rapidly advancing lithography bioprinting approaches of photopolymerizable bioresins. As outlined in this review, understanding the fundamentals of photocrosslinking and their application in advanced biofabrication is critical to future developments. The rapid uptake and breakthroughs achieved via photocrosslinking in bioprinting described herein are largely due to the flexible and tunable photocrosslinking methods that have allowed for

hydrogel bioink and bioresin designs to be realized and exploited, specifically targeting unique bioprinting techniques and fabrication technologies (e.g., shear-thinning bioinks for extrusion bioprinting). Critical considerations in these approaches remain the appropriate selection of bioink and bioresin materials, including the polymers used within precursors, the photoinitiator and its inter-related action on cell function, and the optimal light source and light intensity.

The concept of 4D printing – where materials change over time - has been embraced within the biofabrication community as a method of probing fundamental biological questions. One method through which different physiochemical cues can be spatiotemporally presented to cells within printed constructs is through photopatterning, which has potential to converge with existing bioprinting approaches to achieve even greater flexibility and control.^{217,218} Further, a growing area of interest within bioprinting is the development of technologies that allow for the design and fabrication of constructs with heterogeneous materials and cells. As most organs and tissues are composed of multiple cell types with hierarchical structures, there is a need to create printing processes through which we can better capture these features. Thus, added complexity will likely be incorporated into bioprinted constructs in the future as technologies advance.

One major challenge commonly encountered in bioprinting of large constructs for applications in tissue engineering and regenerative medicine is the need for nutrient transport and metabolite exchange. The role of photocrosslinking in further improving the resolution of perfusable and stable prevascularized structures or tissues (e.g., via DLP lithography-based bioprinting) is likely to grow, offering important solutions to the problem of fabricating clinically-relevant sized tissues for regenerative medicine. This can be achieved through the added spatial control of photocrosslinking techniques or through the

implementation of light-based degradation methods, where photosensitive materials are eroded in 3D throughout hydrogel constructs.^{89,219–221} This control of both building and eroding materials will enhance the formation of hierarchical structures, including vascular components.

Novel photocrosslinking chemistries and approaches such as *in situ* crosslinking and multi-step redox and photoredox approaches are further providing novel strategies to expand the existing *biofabrication window*, allowing greater flexibility for processing a wider range of printable low viscosity bioinks. This will enhance our ability to harness cell functionality through changes in bioink or bioresin stiffness, chemical variations with multi-material bioinks,²²² and gradients in cell-instructive cues through precise control of light exposure to facilitate improved tissue formation and function.^{223,224} This is further evidenced by exciting developments in new bioprinting approaches such as CAL bioprinting,^{80,81} where again our understanding and control of photocrosslinking mechanisms of hydrogel bioinks is leveraged to drive rapid gelation of projected light for the formation of large centimeter-scale, complex cell-laden constructs within seconds. Our advancing knowledge of photocrosslinkable, biocompatible hydrogel bioinks supports the rapid development of such new bioprinting technologies towards clinical translation given the speed advantages offered to fabricate clinically relevant sized, centimeter-scale constructs with patient specific and anatomical shapes.

As progress in bioprinting continues to enable the fabrication of more precise constructs, future work will aim to further improve *in vitro* models and to elucidate how biofabrication can be employed to understand fundamental biological questions surrounding development and disease. To this end, innovations towards the fabrication of multimaterial constructs, recapitulating dynamic cellular and signaling events via

photopatterning, and engineering larger vascularized constructs will continue to advance the field.

3.7 REFERENCES

1. Ifkovits, J. L. & Burdick, J. A. Review: Photopolymerizable and Degradable Biomaterials for Tissue Engineering Applications. *Tissue Eng.* **13**, 2369–2385 (2007).
2. Caliani, S. R. & Burdick, J. A. A practical guide to hydrogels for cell culture. *Nat. Methods* **13**, 405–414 (2016).
3. Roberts, J. J., Naudiyal, P., Lim, K. S., Poole-Warren, L. A. & Martens, P. J. A comparative study of enzyme initiators for crosslinking phenol-functionalized hydrogels for cell encapsulation. *Biomater. Res.* **20**, 30 (2016).
4. Das, S. *et al.* Bioprintable, cell-laden silk fibroin-gelatin hydrogel supporting multilineage differentiation of stem cells for fabrication of three-dimensional tissue constructs. *Acta Biomater.* **11**, 233–246 (2015).
5. Yang, C., Tibbitt, M. W., Basta, L. & Anseth, K. S. Mechanical memory and dosing influence stem cell fate. *Nat. Mater.* **13**, 645–652 (2014).
6. Hao, Y., Fowler, E. W. & Jia, X. Chemical synthesis of biomimetic hydrogels for tissue engineering. *Polym. Int.* (2017). doi:10.1002/pi.5407
7. Zhu, J. Bioactive modification of poly(ethylene glycol) hydrogels for tissue engineering. *Biomaterials* **31**, 4639–4656 (2010).
8. Barner-kowollik, C. *et al.* Critically evaluated termination rate coefficients for free-radical polymerization : Experimental methods. *Prog. Polym. Sci.* **30**, 605–643 (2005).
9. Buback, M., Gilbert, R. G., Driscoll, K. F. O., Russello, G. T. & Schweerg, J. Critically evaluated rate coefficients for free-radical, Propagation rate coefficient for styrene. *Macromol. Chem. Phys.* **3280**, 3267–3280 (1995).
10. Beuermann, S., Paquet, D. A., Mcminn, J. H. & Hutchinson, R. A. Determination of Free-Radical Propagation Rate Coefficients of Butyl, 2-Ethylhexyl, and Dodecyl Acrylates by Pulsed-Laser Polymerization. *Macromolecules* 4206–4215 (1996).
11. Beuermann, S. *et al.* Critically evaluated rate coefficients for free-radical Propagation rate coefficients for methyl methacrylate. *Macromol. Chem. Phys.* **1560**, 1545–1560 (1997).
12. Beuermann, S. *et al.* Critically evaluated rate coefficients for free-radical polymerization, Propagation rate coefficients for alkyl methacrylates. *Macromol. Chem. Phys.* **1364**, 1355–1364 (2000).
13. Gilbert, R. G. & Hutchinson, R. A. Critically Evaluated Rate Coefficients for Free-Radical Polymerization, Propagation Rate Coefficients for Methacrylates with Cyclic Ester Groups. *Macromol. Chem. Phys.* 1338–1350 (2003).
14. Asua, M. *et al.* Critically Evaluated Rate Coefficients for Free-Radical Polymerization, Propagation Rate Coefficient for Butyl Acrylate. *Macromol. Chem. Phys.* 2151–2160 (2004). doi:10.1002/macp.200400355

15. Beurmann, S. *et al.* Critically Evaluated Rate Coefficients For Free-Radical Polymerization Part 6: Propagation Rate Coefficient Of Methacrylic Acid In Aqueous Solution. *Pure Appl. Chem.* **79**, 1463–1469 (2007).
16. Ligon, S., Husár, B., Wutzel, H., Holman, R. & Liska, R. Strategies to reduce oxygen inhibition in photoinduced polymerization. *Chem. Rev.* **114**, 557–589 (2014).
17. Lim, K. S. *et al.* New Visible-Light Photoinitiating System for Improved Print Fidelity in Gelatin-Based Bioinks. *ACS Biomater. Sci. Eng.* **2**, 1752–1762 (2016).
18. Caliari, S. R. & Burdick, J. A. A practical guide to hydrogels for cell culture. *Nat. Methods* **13**, 405–414 (2016).
19. Kolb, H. C., Finn, M. G. & Sharpless, K. B. Click Chemistry: Diverse Chemical Function from a Few Good Reactions. *Angew. Chemie - Int. Ed.* **40**, 2004–2021 (2001).
20. Hoyle, C. E. & Bowman, C. N. Thiol-ene click chemistry. *Angew. Chemie - Int. Ed.* **49**, 1540–1573 (2010).
21. Hoyle, C. E., Lowe, A. B. & Bowman, C. N. Thiol-click chemistry: a multifaceted toolbox for small molecule and polymer synthesis. *Chem. Soc. Rev.* **39**, 1355 (2010).
22. Lowe, A. B. Thiol-ene “click” reactions and recent applications in polymer and materials synthesis. *Polym. Chem.* **1**, 17–36 (2010).
23. Hoyle, C. E., Lee, T. A. I. Y. & Roper, T. Thiol – Enes : Chemistry of the Past with Promise for the Future. *J. Polym. Sci. Part A Polym. Chem.* **42**, 5301–5338 (2004).
24. Morgan, C. R., Magnotta, F. & Ketley, A. D. Thiol / Ene Photocurable Polymers *. *J. Polym. Sci. Polym. Chem. Ed.* **15**, 627–645 (1977).
25. Cramer, N. B., Reddy, S. K., Brien, A. K. O. & Bowman, C. N. Thiol - Ene Photopolymerization Mechanism and Rate Limiting Step Changes for Various Vinyl Functional Group Chemistries. *Macromolecules* **36**, 7964–7969 (2003).
26. Spikes, J. D., Shen, H., Kopekovd, P. & Kopecew, J. Photodynamic Crosslinking of Proteins. Kinetics of the FMN- and Rose Bengal-sensitized Photooxidation and Intermolecular Crosslinking of Model Tyrosine-containing N-(2-Hydroxypropyl)methacrylamide Copolymers. *Photochem. Photobiology* **70**, 130–137 (1999).
27. Cui, X. *et al.* Rapid Photocrosslinking of Silk Hydrogels with High Cell Density and Enhanced Shape Fidelity. *Adv. Healthc. Mater.* **9**, 1901667 (2020).
28. Derosa, M. C. & Crutchley, R. J. Photosensitized singlet oxygen and its applications. *Coord. Chem. Rev.* **234**, 351–371 (2002).
29. Loebel, C., Broguiere, N., Alini, M., Zenobi-wong, M. & Eglin, D. Microfabrication of Photo-Cross-Linked Hyaluronan Hydrogels by Single- and Two-Photon Tyramine Oxidation. (2015). doi:10.1021/acs.biomac.5b00363
30. Kyle, S., Jessop, Z. M., Al-Sabah, A. & Whitaker, I. S. ‘Printability’ of Candidate

- Biomaterials for Extrusion Based 3D Printing: State-of-the-Art'. *Adv. Healthc. Mater.* **6**, 2017 (2017).
31. Levato, R. *et al.* From Shape to Function: The Next Step in Bioprinting. *Adv. Mater.* **32**, 1906423 (2020).
 32. Malda, J. *et al.* 25th anniversary article: Engineering hydrogels for biofabrication. *Advanced Materials* **25**, 5011–5028 (2013).
 33. Trachtenberg, J. E. *et al.* Extrusion-Based 3D Printing of Poly(propylene fumarate) in a Full-Factorial Design. *ACS Biomater. Sci. Eng.* **2**, 1771–1780 (2016).
 34. Lim, K. S. *et al.* Visible Light Cross-Linking of Gelatin Hydrogels Offers an Enhanced Cell Microenvironment with Improved Light Penetration Depth. *Macromol. Biosci.* **19**, (2019).
 35. Petta, D. *et al.* 3D bioprinting of a hyaluronan bioink through enzymatic- and visible light-crosslinking. (2018).
 36. Hong, S. *et al.* 3D Printing of Highly Stretchable and Tough Hydrogels into Complex, Cellularized Structures. *Adv. Mater.* **27**, 4034 (2015).
 37. Yang, F., Tadepalli, V. & Wiley, B. J. 3D Printing of a Double Network Hydrogel with a Compression Strength and Elastic Modulus Greater than those of Cartilage. *ACS Biomater. Sci. Eng.* **3**, 863–869 (2017).
 38. Markstedt, K., Mantas, A., Tournier, I., Ha, D. & Gatenholm, P. 3D Bioprinting Human Chondrocytes with Nanocellulose – Alginate Bioink for Cartilage Tissue Engineering Applications. *Biomacromolecules* **16**, 1489–1496 (2015).
 39. Müller, M., Öztürk, E., Arlov, Ø., Gatenholm, P. & Zenobi-Wong, M. Alginate Sulfate--Nanocellulose Bioinks for Cartilage Bioprinting Applications. *Ann. Biomed. Eng.* **45**, 210–223 (2017).
 40. Xavier, J. R. *et al.* Bioactive nanoengineered hydrogels for bone tissue engineering: A growth-factor-free approach. *ACS Nano* **9**, 3109–3118 (2015).
 41. Uman, S., Dhand, A. & Burdick, J. A. Recent advances in shear-thinning and self-healing hydrogels for biomedical applications. **48668**, 1–20 (2019).
 42. Jia, J. *et al.* Engineering alginate as bioink for bioprinting. *Acta Biomater.* **10**, 4323–4331 (2014).
 43. Bouhadir, K. H. *et al.* Degradation of Partially Oxidized Alginate and Its Potential Application for Tissue Engineering. *Biotechnol. Prog.* **17**, 945–950 (2001).
 44. Colosi, C. *et al.* Microfluidic Bioprinting of Heterogeneous 3D Tissue Constructs Using Low-Viscosity Bioink. *Adv. Mater.* **28**, 677-684a (2016).
 45. Kesti, M. *et al.* A versatile bioink for three-dimensional printing of cellular scaffolds based on thermally and photo-triggered tandem gelation. *Acta Biomater.* **11**, 162–172 (2015).
 46. Shi, L. *et al.* Dynamic Coordination Chemistry Enables Free Directional Printing of Biopolymer Hydrogel. *Chem. Mater.* [acs.chemmater.7b00128](https://doi.org/10.1021/acs.chemmater.7b00128) (2017).

doi:10.1021/acs.chemmater.7b00128

47. Ouyang, L., Highley, C. B., Sun, W. & Burdick, J. A. A Generalizable Strategy for the 3D Bioprinting of Hydrogels from Nonviscous Photo-crosslinkable Inks. *Adv. Mater.* **29**, (2017).
48. Shi, L. *et al.* Dynamic Coordination Chemistry Enables Free Directional Printing of Biopolymer Hydrogel. *Chem. Mater.* **29**, 5816–5823 (2017).
49. Wang, L. L. *et al.* Three-dimensional extrusion bioprinting of single- and double-network hydrogels containing dynamic covalent crosslinks. *J. Biomed. Mater. Res. - Part A* **106**, 865–875 (2018).
50. Yan, Y. *et al.* Construction of Injectable Double-Network Hydrogels for Cell Delivery. *Biomacromolecules* **18**, 2128–2138 (2017).
51. Rodell, C. B., Dusaj, N. N., Highley, C. B. & Burdick, J. A. Injectable and Cytocompatible Tough Double-Network Hydrogels through Tandem Supramolecular and Covalent Crosslinking. 8419–8424 (2016). doi:10.1002/adma.201602268
52. Lee, A. *et al.* 3D bioprinting of collagen to rebuild components of the human heart. **365**, 482–487 (2019).
53. Hinton, T. J. *et al.* Three-dimensional printing of complex biological structures by freeform reversible embedding of suspended hydrogels. *Sci. Adv.* **1**, e1500758–e1500758 (2015).
54. Bhattacharjee, T. *et al.* Liquid-like Solids Support Cells in 3D. *ACS Biomater. Sci. Eng.* (2016). doi:10.1021/acsbiomaterials.6b00218
55. Bhattacharjee, T. *et al.* Writing in the granular gel medium. *Sci. Adv.* **1**, e1500655–e1500655 (2015).
56. Highley, C. B., Rodell, C. B. & Burdick, J. A. Direct 3D Printing of Shear-Thinning Hydrogels into Self-Healing Hydrogels. *Adv. Mater.* **27**, 5075–5079 (2015).
57. Song, K. H., Highley, C. B., Rouff, A. & Burdick, J. A. Complex 3D-Printed Microchannels within Cell-Degradable Hydrogels. *Adv. Funct. Mater.* **28**, 1801331 (2018).
58. Bryan, C. S. O. *et al.* Self-assembled micro-organogels for 3D printing silicone structures. *Sci. Adv.* **3**, e1602800 (2017).
59. Highley, C. B., Song, K. H., Daly, A. C. & Burdick, J. A. Jammed Microgel Inks for 3D Printing Applications. *Adv. Sci.* **6**, (2019).
60. Xin, S., Alge, D. L., Chimene, D., Garza, J. E. & Gaharwar, A. K. Clickable PEG hydrogel microspheres as building blocks for 3D bioprinting. *Biomater. Sci.* 1179–1187 (2019). doi:10.1039/c8bm01286e
61. Daly, A. C., Riley, L. & Segura, T. Hydrogel microparticles for biomedical applications. *Nat. Rev. Mater.* doi:10.1038/s41578-019-0148-6
62. Galarraga, J. H., Kwon, M. Y. & Burdick, J. A. 3D bioprinting via an in situ crosslinking technique towards engineering cartilage tissue. *Sci. Rep.* **9**, 19987

(2019).

63. Zorlutuna, P., Jeong, J. H., Kong, H. & Bashir, R. Stereolithography-Based Hydrogel Microenvironments to Examine Cellular Interactions. *Adv. Funct. Mater.* **21**, 3642–3651 (2011).
64. Elomaa, L., Pan, C., Shanjani, Y. & Malkovskiy, A. Three-dimensional fabrication of cell-laden biodegradable poly(ethylene glycol-co-depsipeptide) hydrogels by visible light stereolithography. *J. Mater. Chem. B* **3**, 8348–8358 (2015).
65. Wang, W. *et al.* Computer-stereolithography-based laser rapid prototyping & manufacturing system. *IFAC Proc. Vol.* **32**, 61–66 (1999).
66. Chartrain, N. A., Williams, C. B. & Whittington, A. R. A review on fabricating tissue scaffolds using vat photopolymerization. *Acta Biomater.* **74**, 90–111 (2018).
67. Lim, K. S. *et al.* Bio-resin for high resolution lithography-based biofabrication of complex cell-laden constructs. *Biofabrication* **10**, 034101 (2018).
68. Bernal, P. N. *et al.* Volumetric Bioprinting of Complex Living-Tissue Constructs within Seconds. *Adv. Mater.* **31**, 1904209 (2019).
69. Lin, H. *et al.* Application of Visible Light-based Projection Stereolithography for Live Cell-Scaffold Fabrication with Designed Architecture. *Biomaterials* **34**, 331–339 (2013).
70. Russmueller, G. *et al.* 3D Printable Biophotopolymers for in Vivo Bone Regeneration. *Materials (Basel)*. **8**, 3685–3700 (2015).
71. Heller, C. *et al.* Vinyl esters: Low cytotoxicity monomers for the fabrication of biocompatible 3D scaffolds by lithography based additive manufacturing. *J. Polym. Sci. Part A Polym. Chem.* **47**, 6941–6954 (2009).
72. Liska, R. *et al.* Photopolymers for rapid prototyping. *J. Coatings Technol. Res.* **4**, 505–510 (2007).
73. Chan, V., Zorlutuna, P., Jeong, J. H., Kong, H. & Bashir, R. Three-dimensional photopatterning of hydrogels using stereolithography for long-term cell encapsulation. *Lab Chip* **10**, 2062–2070 (2010).
74. Soman, P., Chung, P. H., Zhang, A. & Chen, S. Digital microfabrication of user-defined 3D microstructures in cell-laden hydrogels. *Biotechnol. Bioeng.* **110**, 3038–3047 (2013).
75. Lee, J. H., Prud'homme, R. K. & Aksay, I. A. Cure depth in photopolymerization: Experiments and theory. *J. Mater. Res.* **16**, 3536–3544 (2001).
76. Melchels, F. P. W., Feijen, J. & Grijpma, D. W. A review on stereolithography and its applications in biomedical engineering. *Biomaterials* **31**, 6121–6130 (2010).
77. Jacobs, P. F. Fundamentals of stereolithography. in *1992 International Solid Freeform Fabrication Symposium* (1992).
78. Grigoryan, B. *et al.* Multivascular networks and functional intravascular topologies within biocompatible hydrogels. *Science (80-)*. **364**, 458–464 (2019).

79. Sun, A. X., Lin, H., Beck, A. M., Kilroy, E. J. & Tuan, R. S. Projection Stereolithographic Fabrication of Human Adipose Stem Cell-incorporated Biodegradable Scaffolds for Cartilage Tissue Engineering. *Front. Bioeng. Biotechnol.* **3**, 1–9 (2015).
80. Kelly, B. E., Bhattacharya, I., Heidari, H. & Shusteff, M. Volumetric additive manufacturing via tomographic reconstruction. *Science (80-.)*. 1075–1079 (2019).
81. Bernal, P. N. *et al.* Volumetric Bioprinting of Complex Living-Tissue Constructs within Seconds. *Adv. Mater.* **1904209**, (2019).
82. Studer, K., Decker, C., Beck, E. & Schwalm, R. Overcoming oxygen inhibition in UV-curing of acrylate coatings by carbon dioxide inerting, Part I. *Prog. Org. Coatings* **48**, 92–100 (2003).
83. Decker, C. & Jenkins, A. D. Kinetic approach of oxygen inhibition in ultraviolet- and laser-induced polymerizations. *Macromolecules* **18**, 1241–1244 (1985).
84. Grigoryan, B. *et al.* Multivascular networks and functional intravascular topologies within biocompatible hydrogels. *Science (80-.)*. **364**, 458 LP – 464 (2019).
85. Tumbleston, J. R. *et al.* Continuous liquid interface production of 3D objects. *Science (80-.)*. **347**, 1349–1352 (2015).
86. Nguyen, A. K. & Narayan, R. J. Two-photon polymerization for biological applications. *Mater. Today* **20**, 314–322 (2017).
87. Maruo, S., Nakamura, O. & Kawata, S. Three-dimensional microfabrication with two-photon-absorbed photopolymerization. *Opt. Lett.* **22**, 132–134 (1997).
88. Obata, K., El-Tamer, A., Koch, L., Hinze, U. & Chichkov, B. N. High-aspect 3D two-photon polymerization structuring with widened objective working range (WOW-2PP). *Light Sci. Appl.* **2**, e116–e116 (2013).
89. Deforest, C. A. & Anseth, K. S. Cytocompatible click-based hydrogels with dynamically tunable properties through orthogonal photoconjugation and photocleavage reactions. *Nat. Chem.* **3**, 925–931 (2011).
90. Kloxin, A. M., Kasko, A. M., Salinas, C. N. & Anseth, K. S. Photodegradable hydrogels for dynamic tuning of physical and chemical properties. *Science (80-.)*. **324**, 59–63 (2009).
91. Lunzer, M. *et al.* A Modular Approach to Sensitized Two-Photon Patterning of Photodegradable Hydrogels. *Angew. Chemie Int. Ed.* **57**, 15122–15127 (2018).
92. Wong, D. Y., Griffin, D. R., Reed, J. & Kasko, A. M. Photodegradable Hydrogels to Generate Positive and Negative Features over Multiple Length Scales. *Macromolecules* **43**, 2824–2831 (2010).
93. Azagarsamy, M. A., McKinnon, D. D., Alge, D. L. & Anseth, K. S. Coumarin-Based Photodegradable Hydrogel: Design, Synthesis, Gelation, and Degradation Kinetics. *ACS Macro Lett.* **3**, 515–519 (2014).
94. Lee, M. S. & Kim, J.-C. Photodependent release from poly(vinyl alcohol)/epoxypropoxy coumarin hydrogels. *J. Appl. Polym. Sci.* **124**, 4339–4345

(2012).

95. Rapp, T. L., Highley, C. B., Manor, B. C., Burdick, J. A. & Dmochowski, I. J. Ruthenium-Crosslinked Hydrogels with Rapid, Visible-Light Degradation. *Chem. – A Eur. J.* **24**, 2328–2333 (2018).
96. Theis, S. *et al.* Metallo-Supramolecular Gels that are Photocleavable with Visible and Near-Infrared Irradiation. *Angew. Chemie Int. Ed.* **56**, 15857–15860 (2017).
97. Williams, S. K., Touroo, J. S., Church, K. H. & Hoying, J. B. Encapsulation of Adipose Stromal Vascular Fraction Cells in Alginate Hydrogel Spheroids Using a Direct-Write Three-Dimensional Printing System. *Biores. Open Access* **2**, 448–454 (2013).
98. Levato, R. *et al.* Biofabrication of tissue constructs by 3D bioprinting of cell-laden microcarriers. *Biofabrication* **6**, 035020 (2014).
99. Annabi, N. *et al.* Controlling the Porosity and Microarchitecture of Hydrogels for Tissue Engineering. *Tissue Eng. Part B Rev.* **16**, 371–383 (2010).
100. Lien, S.-M., Ko, L.-Y. & Huang, T.-J. Effect of pore size on ECM secretion and cell growth in gelatin scaffold for articular cartilage tissue engineering. *Acta Biomater.* **5**, 670–679 (2009).
101. Chiu, Y.-C. *et al.* The role of pore size on vascularization and tissue remodeling in PEG hydrogels. *Biomaterials* **32**, 6045–6051 (2011).
102. Murphy, W. L., McDevitt, T. C. & Engler, A. J. Materials as stem cell regulators. *Nat. Mater.* **13**, 547–557 (2014).
103. Kolesky, D. B. *et al.* 3D Bioprinting of Vascularized , Heterogeneous Cell-Laden Tissue Constructs. *Adv. Mater.* 3124–3130 (2014). doi:10.1002/adma.201305506
104. Belleghem, S. Van *et al.* Hybrid 3D Printing of Synthetic and Cell-Laden Bioinks for Shape Retaining Soft Tissue Grafts. **1907145**, 1–10 (2019).
105. Koti, P., Muselimyan, N., Mirdamadi, E., Asfour, H. & Sarvazyan, N. A. Use of GelMA for 3D printing of cardiac myocytes and fibroblasts. *J. 3D Print. Med.* **3**, 11–22 (2019).
106. Tigner, T. J., Rajput, S., Gaharwar, A. K. & Alge, D. L. Comparison of Photocrosslinkable Gelatin Derivatives and Initiators for Three-Dimensional Extrusion Bioprinting. *Biomacromolecules* **21**, 454–463 (2020).
107. Mouser, V. H. M. *et al.* Yield stress determines bioprintability of hydrogels based on gelatin-methacryloyl and gellan gum for cartilage bioprinting. *Biofabrication* **8**, 1–13 (2016).
108. Levato, R. *et al.* The bio in the ink: cartilage regeneration with bioprintable hydrogels and articular cartilage-derived progenitor cells. *Acta Biomater.* **61**, 41–53 (2017).
109. Gao, Q. *et al.* 3D printing of complex GelMA-based scaffolds with nanoclay. *Biofabrication* **11**, 35006 (2019).
110. Zhuang, P., Ng, W. L., An, J., Chua, C. K. & Tan, L. P. Layer-by-layer ultraviolet

- assisted extrusion-based (UAE) bioprinting of hydrogel constructs with high aspect ratio for soft tissue engineering applications. *PLoS One* **14**, e0216776 (2019).
111. Du, M. *et al.* 3D bioprinting of BMSC-laden methacrylamide gelatin scaffolds with CBD-BMP2-collagen microfibers. *Biofabrication* **7**, 44104 (2015).
 112. Bhise, N. S. *et al.* A liver-on-a-chip platform with bioprinted hepatic spheroids. *Biofabrication* **8**, 14101 (2016).
 113. Zhu, W. *et al.* Direct 3D bioprinting of prevascularized tissue constructs with complex microarchitecture. *Biomaterials* **124**, 106–115 (2017).
 114. Suntornnond, R., Tan, E. Y. S., An, J. & Chua, C. K. A highly printable and biocompatible hydrogel composite for direct printing of soft and perfusable vasculature-like structures. *Sci. Rep.* **7**, 16902 (2017).
 115. Dubbin, K., Tabet, A. & Heilshorn, S. C. Quantitative criteria to benchmark new and existing bio-inks for cell compatibility. *Biofabrication* **9**, 44102 (2017).
 116. Yin, J., Yan, M., Wang, Y., Fu, J. & Suo, H. 3D Bioprinting of Low-Concentration Cell-Laden Gelatin Methacrylate (GelMA) Bioinks with a Two-Step Cross-linking Strategy. *ACS Appl. Mater. Interfaces* **10**, 6849–6857 (2018).
 117. Bertassoni, L. E. *et al.* Direct-write bioprinting of cell-laden methacrylated gelatin hydrogels. *Biofabrication* **6**, 24105 (2014).
 118. Melchels, F. P. W., Dhert, W. J. A., Hutmacher, D. W. & Malda, J. Development and characterisation of a new bioink for additive tissue manufacturing. *J. Mater. Chem. B* **2**, 2282 (2014).
 119. Ma, X. *et al.* Deterministically patterned biomimetic human iPSC- derived hepatic model via rapid 3D bioprinting. *Proc. Natl. Acad. Sci.* **113**, 2206–2211 (2016).
 120. Ma, X. *et al.* Rapid 3D bioprinting of decellularized extracellular matrix with regionally varied mechanical properties and biomimetic microarchitecture. *Biomaterials* **185**, 310–321 (2018).
 121. Ying, G.-L. *et al.* Aqueous Two-Phase Emulsion Bioink-Enabled 3D Bioprinting of Porous Hydrogels. *Adv. Mater.* **30**, 1805460 (2018).
 122. Billiet, T., Gevaert, E., De Schryver, T., Cornelissen, M. & Dubruel, P. The 3D printing of gelatin methacrylamide cell-laden tissue-engineered constructs with high cell viability. *Biomaterials* **35**, 49–62 (2014).
 123. Bertlein, S. *et al.* Thiol–Ene Clickable Gelatin: A Platform Bioink for Multiple 3D Biofabrication Technologies. *Adv. Mater.* **29**, (2017).
 124. Dobos, A. *et al.* Thiol – Gelatin – Norbornene Bioink for Laser-Based High-Definition Bioprinting. *Adv. Healthc. Mater.* **1900752**, 1–9 (2019).
 125. Tigner, T. J., Rajput, S., Gaharwar, A. K. & Alge, D. L. Comparison of Photocrosslinkable Gelatin Derivatives and Initiators for Three-Dimensional Extrusion Bioprinting. *Biomacromolecules* (2019).
doi:10.1021/acs.biomac.9b01204

126. Skardal, A., Zhang, J. & Prestwich, G. D. Bioprinting vessel-like constructs using hyaluronan hydrogels crosslinked with tetrahedral polyethylene glycol tetracrylates. *Biomaterials* **31**, 6173–6181 (2010).
127. Ouyang, L., Highley, C. B., Rodell, C. B., Sun, W. & Burdick, J. A. 3D Printing of Shear-Thinning Hyaluronic Acid Hydrogels with Secondary Cross-Linking. *ACS Biomater. Sci. Eng.* **2**, 1743–1751 (2016).
128. Poldervaart, M. T. *et al.* 3D bioprinting of methacrylated hyaluronic acid (MeHA) hydrogel with intrinsic osteogenicity. *PLoS One* **12**, e0177628 (2017).
129. Mouser, V. H. M. *et al.* Development of a thermosensitive HAMA-containing bio-ink for the fabrication of composite cartilage repair constructs. *Biofabrication* **9**, 015026 (2017).
130. Abbadessa, A. *et al.* A Synthetic Thermosensitive Hydrogel for Cartilage Bioprinting and Its Biofunctionalization with Polysaccharides. *Biomacromolecules* **17**, 2137–2147 (2016).
131. Mouser, V. H. M. *et al.* Bio-ink development for three-dimensional bioprinting of hetero-cellular cartilage constructs. *Connect. Tissue Res.* **00**, 1–15 (2018).
132. Wang, Y. *et al.* 3D Bioprinting of Breast Cancer Models for Drug Resistance Study. *ACS Biomater. Sci. Eng.* **4**, 4401–4411 (2018).
133. Duchi, S. *et al.* Handheld Co-Axial Bioprinting: Application to in situ surgical cartilage repair. *Sci. Rep.* **7**, 5837 (2017).
134. O'Connell, C. D. *et al.* Development of the Biopen: a handheld device for surgical printing of adipose stem cells at a chondral wound site. *Biofabrication* **8**, 15019 (2016).
135. Skardal, A. *et al.* A hydrogel bioink toolkit for mimicking native tissue biochemical and mechanical properties in bioprinted tissue constructs. *Acta Biomater.* **25**, 24–34 (2015).
136. Mazzocchi, A., Devarasetty, M., Huntwork, R., Soker, S. & Skardal, A. Optimization of collagen type I-hyaluronan hybrid bioink for 3D bioprinted liver microenvironments. *Biofabrication* **11**, 15003 (2018).
137. Ma, X. *et al.* Deterministically patterned biomimetic human iPSC- derived hepatic model via rapid 3D bioprinting. **113**, 3–8 (2016).
138. Kim, S. H. *et al.* Precisely printable and biocompatible silk fibroin bioink for digital light processing 3D printing. *Nat. Commun.* **9**, 1–14 (2018).
139. Jang, J. *et al.* Tailoring mechanical properties of decellularized extracellular matrix bioink by vitamin B2-induced photo-crosslinking. *Acta Biomater.* **33**, 88–95 (2016).
140. Abbadessa, A. *et al.* A thermo-responsive and photo-polymerizable chondroitin sulfate-based hydrogel for 3D printing applications. *Carbohydr. Polym.* **149**, 163–174 (2016).
141. Pescosolido, L. *et al.* Hyaluronic Acid and Dextran-Based Semi-IPN Hydrogels as Biomaterials for Bioprinting. *Biomacromolecules* **12**, 1831–1838 (2011).

142. Maiullari, F. *et al.* A multi-cellular 3D bioprinting approach for vascularized heart tissue engineering based on HUVECs and iPSC-derived cardiomyocytes. *Sci. Rep.* **8**, 13532 (2018).
143. Costantini, M. *et al.* Microfluidic-enhanced 3D bioprinting of aligned myoblast-laden hydrogels leads to functionally organized myofibers in vitro and in vivo. *Biomaterials* **131**, 98–110 (2017).
144. Kang, L. H. *et al.* Optimizing Photo-Encapsulation Viability of Heart Valve Cell Types in 3D Printable Composite Hydrogels. *Ann. Biomed. Eng.* **45**, 360–377 (2017).
145. Arcaute, K., Mann, B. K. & Wicker, R. B. Stereolithography of Three-Dimensional Bioactive Poly(Ethylene Glycol) Constructs with Encapsulated Cells. *Ann. Biomed. Eng.* **34**, 1429–1441 (2006).
146. Wang, Z., Abdulla, R., Parker, B. & Samanipour, R. A simple and high-resolution stereolithography-based 3D bioprinting system using visible light crosslinkable bioinks. *Biofabrication* **7**, 1–29 (2015).
147. Censi, R. *et al.* A Printable Photopolymerizable Thermosensitive p(HPMAm-lactate)-PEG Hydrogel for Tissue Engineering. *Adv. Funct. Mater.* **21**, 1833–1842 (2011).
148. Mouser, V. H. M. *et al.* Development of a thermosensitive HAMA-containing bio-ink for the fabrication of composite cartilage repair constructs. *Biofabrication* **9**, 015026 (2017).
149. Dhariwala, B., Hunt, E. & Boland, T. Rapid prototyping of tissue-engineering constructs, using photopolymerizable hydrogels and stereolithography. *Tissue Eng.* **10**, 1316–1322 (2004).
150. Stichler, S. *et al.* Thiol-ene Clickable Poly(glycidol) Hydrogels for Biofabrication. *Ann. Biomed. Eng.* **45**, 273–285 (2017).
151. Stichler, S., Bertlein, S., Tessmar, J., Jüngst, T. & Groll, J. Thiol-ene Cross-Linkable Hydrogels as Bioinks for Biofabrication. *Macromol. Symp.* **372**, 102–107 (2017).
152. Van Hoorick, J. *et al.* Highly Reactive Thiol-Norbornene Photo-Click Hydrogels : Toward Improved Processability. *Macromol. Rapid Commun.* **1800181**, 1–7 (2018).
153. Shu Zheng, X., Liu, Y., Palumbo, F. & Prestwich, G. D. Disulfide-crosslinked hyaluronan-gelatin hydrogel films : a covalent mimic of the extracellular matrix for in vitro cell growth. *Biomaterials* **24**, 3825–3834 (2003).
154. Highley, C. B., Prestwich, G. D. & Burdick, J. A. Recent advances in hyaluronic acid hydrogels for biomedical applications. *Curr. Opin. Biotechnol.* **40**, 35–40 (2016).
155. Gramlich, W. M., Kim, I. L. & Burdick, J. A. Synthesis and orthogonal photopatterning of hyaluronic acid hydrogels with thiol-norbornene chemistry. *Biomaterials* **34**, 9803–9811 (2013).

156. Vega, S. L. *et al.* Combinatorial hydrogels with biochemical gradients for screening 3D cellular microenvironments. *Nat. Commun.* **9**, 614 (2018).
157. Shu, X. Z., Liu, Y., Luo, Y., Roberts, M. C. & Prestwich, G. D. Disulfide cross-linked hyaluronan hydrogels. *Biomacromolecules* **3**, 1304–1311 (2002).
158. Kwon, M. Y. *et al.* Influence of hyaluronic acid modification on CD44 binding towards the design of hydrogel biomaterials. *Biomaterials* **222**, (2019).
159. Zhang, X., Sun, P., Huangshan, L., Hu, B. & Messersmith, P. B. Improved method for synthesis of cysteine modified hyaluronic acid for in situ hydrogel. *Chem. Commun.* **51**, 9662–9665 (2015).
160. Wade, R. J., Bassin, E. J., Rodell, C. B. & Burdick, J. A. Protease-degradable electrospun fibrous hydrogels. *Nat. Commun.* **6**, 6639 (2015).
161. Drzewiecki, K. E. *et al.* Methacrylation Induces Rapid, Temperature-Dependent, Reversible Self-Assembly of Type - I Collagen. *Langmuir* **30**, 11204–11211 (2014).
162. Rouillard, A. D. *et al.* Methods for Photocrosslinking Alginate Hydrogel Scaffolds with High Cell Viability. **17**, (2011).
163. Thakur, A., Jaiswal, M. K., Peak, C. W. & Carrow, J. K. Injectable shear-thinning nanoengineered hydrogels for stem cell delivery. *Nanoscale* 12362–12372 (2016). doi:10.1039/c6nr02299e
164. Cebe, T. *et al.* Novel 3D-printed methacrylated chitosan-laponite nanosilicate composite scaffolds enhance cell growth and biomineral formation in MC3T3 pre-osteoblasts. *J. Mater. Res.* 1–18 (2018). doi:10.1557/jmr.2018.260
165. Li, Q. *et al.* Biodegradable and photocrosslinkable polyphosphoester hydrogel. *Biomaterials* **27**, 1027–1034 (2006).
166. Lim, K. S., Alves, M. H., Poole-Warren, L. A. & Martens, P. J. Covalent incorporation of non-chemically modified gelatin into degradable PVA-tyramine hydrogels. *Biomaterials* **34**, 7097–7105 (2013).
167. Hern, D. L. & Hubbell, J. A. Incorporation of adhesion peptides into nonadhesive hydrogels useful for tissue resurfacing. *J. Biomed. Mater. Res.* **39**, 266–276 (1998).
168. Lutolf, M. P. *et al.* Synthetic matrix metalloproteinase-sensitive hydrogels for the conduction of tissue regeneration: Engineering cell-invasion characteristics. *Proc. Natl. Acad. Sci. U. S. A.* **100**, 5413–5418 (2003).
169. Ma, X. *et al.* 3D bioprinting of functional tissue models for personalized drug screening and in vitro disease modeling. *Adv. Drug Deliv. Rev.* **132**, 235–251 (2018).
170. Bryant, S. J., Nuttelman, C. R. & Anseth, K. S. Cytocompatibility of UV and visible light photoinitiating systems on cultured NIH/3T3 fibroblasts in vitro. *J. Biomater. Sci. Polym. Ed.* **11**, 439–457 (2000).
171. Lavker, R. & Kaidbey, K. The Spectral Dependence for UVA-Induced Cumulative

- Damage in Human Skin. *J. Invest. Dermatol.* **108**, 17–21 (1997).
172. Cooke, M. S., Evans, M. D., Dizdaroglu, M. & Lunec, J. Oxidative DNA damage: mechanisms, mutation, and disease. *FASEB J.* **17**, 1195–1214 (2003).
 173. Machlin, L. J. & Bendich, A. Free radical tissue damage: protective role of antioxidant nutrients. *FASEB J* **1**, 441–445 (1987).
 174. Lim, K. S. *et al.* Visible Light Cross-Linking of Gelatin Hydrogels Offers an Enhanced Cell Microenvironment with Improved Light Penetration Depth. *Macromol. Biosci.* **19**, 1900098 (2019).
 175. Kaastrup, K. & Sikes, H. D. Using photo-initiated polymerization reactions to detect molecular recognition. *Chem. Soc. Rev.* **45**, 532–545 (2016).
 176. Santini, A., Gallegos, I. T. & Felix, C. M. Photoinitiators in Dentistry: A Review. *Prim. Dent. J.* **2**, 30–33 (2013).
 177. Liu, M., Li, M.-D., Xue, J. & Phillips, D. L. Time-resolved spectroscopic and density functional theory study of the photochemistry of Irgacure-2959 in an aqueous solution. *J. Phys. Chem. A* **118**, 8701–8707 (2014).
 178. O'Connell, C. D. *et al.* Tailoring the mechanical properties of gelatin methacryloyl hydrogels through manipulation of the photocrosslinking conditions. *Soft Matter* **14**, 2142–2151 (2018).
 179. Andrzejewska, E. Photopolymerization kinetics of multifunctional monomers. *Prog. Polym. Sci.* **26**, 605–665 (2001).
 180. Martens, P. & Anseth, K. S. Characterization of hydrogels formed from acrylate modified poly(vinyl alcohol) macromers. *Polymer (Guildf)*. **41**, 7715–7722 (2000).
 181. Burdick, J. A., Chung, C., Jia, X., Randolph, M. A. & Langer, R. Controlled degradation and mechanical behavior of photopolymerized hyaluronic acid networks. *Biomacromolecules* **6**, 386–391 (2005).
 182. Urushibara, A., Kodama, S. & Yokoya, A. Induction of genetic instability by transfer of a UV-A-irradiated chromosome. *Mutat. Res. Toxicol. Environ. Mutagen.* **766**, 29–34 (2014).
 183. Dahle, J., Kvam, E. & Stokke, T. Bystander effects in UV-induced genomic instability: antioxidants inhibit delayed mutagenesis induced by ultraviolet A and B radiation. *J. Carcinog.* **4**, 11 (2005).
 184. Fedorovich, N. E. *et al.* The effect of photopolymerization on stem cells embedded in hydrogels. *Biomaterials* **30**, 344–353 (2009).
 185. Fairbanks, B. D., Schwartz, M. P., Bowman, C. N. & Anseth, K. S. Photoinitiated polymerization of PEG-diacrylate with lithium phenyl-2,4,6-trimethylbenzoylphosphinate: polymerization rate and cytocompatibility. *Biomaterials* **30**, 6702–6707 (2009).
 186. Xu, W. *et al.* On Low-Concentration Inks Formulated by Nanocellulose Assisted with Gelatin Methacrylate (GelMA) for 3D Printing toward Wound Healing Application. *ACS Appl. Mater. Interfaces* **11**, 8838–8848 (2019).

187. Liu, W. *et al.* Extrusion Bioprinting of Shear-Thinning Gelatin Methacryloyl Bioinks. *Adv. Healthc. Mater.* **1601451**, 1601451 (2017).
188. Arcaute, K., Mann, B. & Wicker, R. Stereolithography of spatially controlled multi-material bioactive poly(ethylene glycol) scaffolds. *Acta Biomater.* **6**, 1047–1054 (2010).
189. Liu, J. *et al.* 3D printing of biomimetic multi-layered GelMA/nHA scaffold for osteochondral defect repair. *Mater. Des.* **171**, 107708 (2019).
190. Kesti, M. *et al.* A versatile bioink for three-dimensional printing of cellular scaffolds based on thermally and photo-triggered tandem gelation. *Acta Biomater.* **11**, 162–172 (2015).
191. Alcalá-Orozco, C. R. *et al.* Design and characterisation of multi-functional strontium-gelatin nanocomposite bioinks with improved print fidelity and osteogenic capacity. *Bioprinting* **18**, e00073 (2020).
192. Cidonio, G. *et al.* Osteogenic and angiogenic tissue formation in high fidelity nanocomposite Laponite-gelatin bioinks. *Biofabrication* **11**, 035027 (2019).
193. Chandler, E. M. *et al.* Stiffness of photocrosslinked RGD-alginate gels regulates adipose progenitor cell behavior. *Biotechnol. Bioeng.* **108**, 1683–1692 (2011).
194. Occhetta, P. *et al.* Fabrication of 3D cell-laden hydrogel microstructures through photo-mold patterning. *Biofabrication* **5**, 35002 (2013).
195. Occhetta, P. *et al.* VA-086 methacrylate gelatine photopolymerizable hydrogels: A parametric study for highly biocompatible 3D cell embedding. *J. Biomed. Mater. Res. A* **103**, 2109–2117 (2015).
196. Qin, X. H., Ovsianikov, A., Stampfl, J. & Liska, R. Additive manufacturing of photosensitive hydrogels for tissue engineering applications. *BioNanoMaterials* **15**, 49 (2014).
197. Cruise, G. M., Hegre, O. D., Scharp, D. S. & Hubbell, J. A. A sensitivity study of the key parameters in the interfacial photopolymerization of poly(ethylene glycol) diacrylate upon porcine islets. *Biotechnol. Bioeng.* **57**, 655–665 (1998).
198. Noshadi, I. *et al.* In vitro and in vivo analysis of visible light crosslinkable gelatin methacryloyl (GelMA) hydrogels. *Biomater. Sci.* **5**, 2093–2105 (2017).
199. Srivastava, V. & Singh, P. P. Eosin Y catalysed photoredox synthesis: a review. *RSC Adv.* **7**, 31377–31392 (2017).
200. Penzkofer, A., Beidoun, A. & Speiser, S. Singlet excited-state absorption of eosin Y. *Chem. Phys.* **170**, 139–148 (1993).
201. Pathak, C. P., Sawhney, A. S. & Hubbell, J. A. Rapid photopolymerization of immunoprotective gels in contact with cells and tissue. *J. Am. Chem. Soc.* **114**, 8311–8312 (1992).
202. Loebel, C., Broguiere, N., Alini, M., Zenobi-wong, M. & Eglin, D. Microfabrication of Photo-Cross-Linked Hyaluronan Hydrogels by Single- and Two-Photon Tyramine Oxidation. *Biomacromolecules* **16**, 2624–2630 (2015).

203. Fancy, D. A. & Kodadek, T. Chemistry for the analysis of protein–protein interactions: rapid and efficient cross-linking triggered by long wavelength light. *Proc Natl Acad Sci U S A* **96**, 6020–6024 (1999).
204. Fancy, D. A. *et al.* Scope, limitations and mechanistic aspects of the photo-induced cross-linking of proteins by water-soluble metal complexes. *Chem. Biol.* **7**, 697–708 (2000).
205. Elvin, C. M. *et al.* Evaluation of photo-crosslinked fibrinogen as a rapid and strong tissue adhesive. *J Biomed Mater Res A* **93**, 687–695 (2010).
206. Elvin, C. M. *et al.* A highly elastic tissue sealant based on photopolymerised gelatin. *Biomaterials* **31**, 8323–8331 (2010).
207. Schuurman, W. *et al.* Gelatin-Methacrylamide Hydrogels as Potential Biomaterials for Fabrication of Tissue-Engineered Cartilage Constructs. *Macromol. Biosci.* **13**, 551–561 (2013).
208. Suzanne, M. & Steller, H. Shaping organisms with apoptosis. *Cell Death Differ.* **20**, 669–675 (2013).
209. Aguado, B. A., Mulyasmita, W., Su, J., Lampe, K. J. & Heilshorn, S. C. Improving viability of stem cells during syringe needle flow through the design of hydrogel cell carriers. *Tissue Eng. Part A* **18**, 806–815 (2012).
210. Blaeser, A. *et al.* Controlling Shear Stress in 3D Bioprinting is a Key Factor to Balance Printing Resolution and Stem Cell Integrity. *Adv. Healthc. Mater.* **5**, 326–333 (2016).
211. Bahney, C. S. *et al.* Visible Light Photoinitiation of Mesenchymal Stem Cell-laden Bioreponsive Hydrogels. *Eur. Cells Mater.* **22**, 43–55 (2011).
212. Mironi-Harpaz, I., Wang, D. Y., Venkatraman, S. & Seliktar, D. Photopolymerization of cell-encapsulating hydrogels: Crosslinking efficiency versus cytotoxicity. *Acta Biomater.* **8**, 1838–1848 (2012).
213. Ruskowitz, E. R. & Deforest, C. A. Proteome-wide Analysis of Cellular Response to Ultraviolet Light for Biomaterial Synthesis and Modification. *ACS Biomater. Sci. Eng.* **5**, 2111–2116 (2019).
214. Schuurman, W. *et al.* Bioprinting of hybrid tissue constructs with tailorable mechanical properties. *Biofabrication* **3**, (2011).
215. Klotz, B. J., Gawlitta, D., Rosenberg, A. J. W. P., Malda, J. & Melchels, F. P. W. Gelatin-Methacryloyl Hydrogels: Towards Biofabrication-Based Tissue Repair. *Trends Biotechnol.* **34**, 394–407 (2016).
216. Serex, L., Bertsch, A. & Renaud, P. Microfluidics: A New Layer of Control for Extrusion-Based 3D Printing. *Micromachines* **9**, 86 (2018).
217. Shadish, J. A., Strange, A. C. & DeForest, C. A. Genetically Encoded Photocleavable Linkers for Patterned Protein Release from Biomaterials. *J. Am. Chem. Soc.* **141**, 15619–15625 (2019).
218. Shadish, J. A., Benuska, G. M. & DeForest, C. A. Bioactive Site-Specifically

- Modified Proteins for 4D Patterning of Gel Biomaterials. *Nat. Mater.* (2019).
219. Burdick, J. A. & Murphy, W. L. Moving from static to dynamic complexity in hydrogel design. *Nat. Commun.* **3**, 1–8 (2012).
 220. Kloxin, A. M., Kasko, A. M., Salinas, C. N. & Anseth, K. S. Photodegradable Hydrogels for Dynamic Tuning of Physical and Chemical Properties. *Science* (80-). **324**, 59–63 (2009).
 221. Khetan, S. & Burdick, J. A. Patterning hydrogels in three dimensions towards controlling cellular interactions. *Soft Matter* **7**, 830–838 (2011).
 222. Liu, W. *et al.* Rapid Continuous Multimaterial Extrusion Bioprinting. *Adv. Mater.* **29**, 1604630 (2017).
 223. Hardin, J. O., Ober, T. J., Valentine, A. D. & Lewis, J. A. Microfluidic Printheads for Multimaterial 3D Printing of Viscoelastic Inks. *Adv. Mater.* **27**, 3279–3284 (2015).
 224. Skylar-Scott, M. A., Mueller, J., Visser, C. W. & Lewis, J. A. Voxelated soft matter via multimaterial multinozzle 3D printing. *Nature* **575**, 330–335 (2019).

CHAPTER 4: 3D BIOPRINTING VIA AN IN SITU CROSSLINKING TECHNIQUE TOWARDS ENGINEERING CARTILAGE

The following chapter is adapted from:

Galarraga, J.H., Kwon, M.Y., Burdick, J.A. 3D bioprinting via an *in situ* crosslinking technique towards engineering cartilage tissue. *Sci Rep* 9, 19987 (2019).

4.1 INTRODUCTION

Cartilage is a load-bearing connective tissue found in articulating joints that permits movement between bones with minimal friction. When articular cartilage is damaged due to disease or traumatic injury, loss of cartilage throughout the joint surface may occur, resulting in reduced joint mobility and eventually osteoarthritis.¹ Since native cartilage does not possess any regenerative capacity, surgical interventions are often required to mitigate the progression of cartilage degeneration in afflicted patients. Procedures such as microfracture aim to stimulate cells (e.g., mesenchymal stromal cells, MSCs) in the underlying bone marrow, while cell-based therapies such as matrix-assisted autologous chondrocyte implantation (MACI) focus on scaffolds to elicit tissue formation from donor cells.² Despite their clinical use, these approaches have only exhibited limited success, as they fail to fully restore the function of healthy cartilage. These findings have motivated the use of tissue engineering to improve the quality of repair cartilage for clinical applications.

Within the field of tissue engineering, 3D bioprinting enables the fabrication of cell-laden hydrogel scaffolds with anatomically relevant structures and patient-specific geometries, improving the prospects for repair tissue integration.³ For example, poly(ethylene glycol) (PEG)-based hydrogel implants with embedded chondrocytes have been fabricated via extrusion-based printing and shown to integrate with peripheral

cartilage tissue in *ex vivo* osteochondral plugs.⁴ Unlike alternative fabrication approaches such as micromolding, 3D bioprinting permits the modular and scalable design of precise scaffold features that better recapitulate properties of native tissue. Specifically, 3D bioprinting allows for unparalleled spatial control over materials^{5,6} or cell types⁷ in 3D space, which has been used to mimic the zonal stratification of properties found in cartilage or osteochondral units.⁸ Daly et al. used the inkjet printing of cell spheroids into 3D printed polycaprolactone (PCL)-based microchambers for guidance of spheroid growth and fusion, permitting the formation of neotissues with depth-dependent collagen architectures.⁹ PCL has also been utilized to increase the mechanics of printed hydrogels (e.g., fibrin-collagen, alginate, agarose, PEG) with embedded chondrocytes or MSCs towards cartilage formation,^{10–13} including through the combination of melt electrowriting of PCL with extrusion-based printing of gelatin-methacryloyl (GelMA).¹⁴ Other hydrogel inks that have been previously used for engineering cartilage include hyaluronic acid (HA),⁷ decellularized extracellular matrix (ECM),¹⁵ and gellan gum.^{7,16}

Bioinks, which are typically comprised of a hydrogel precursor solution containing cells,¹⁷ must exhibit a number of requisite design specifications to be printable with traditional printing technologies. For example, in extrusion-based 3D bioprinting, bioinks must first have suitable rheological properties such that they can readily flow through a printer head. If a candidate bioink is too viscous, appreciable shear forces will be exerted on encapsulated cells, reducing cell viability and long-term functional properties of printed constructs. Beyond flow, bioinks must also possess sufficient mechanical integrity upon deposition so that extruded filaments are stable and can be deposited in a layer-by-layer manner. A number of bioinks have been designed with these specific criteria in mind, such as with guest-host supramolecular hydrogels that are shear-thinning and self-healing and can be stabilized via secondary covalent crosslinking.¹⁸ However, if a bioink is non-

viscous, it will flow rapidly upon deposition due to gravity, limiting printed filament resolution.

While many advances have been made in the design and implementation of bioinks, including towards cartilage tissue engineering, it is of interest to expand on the possible properties available with printable bioinks rather than only using inks that meet current printing criteria. As described by Malda et al, the traditional window for bioprinting is often not optimal for maintaining desired cell behavior, including cell viability.¹⁹ Further, it may be of interest to harness diverse bioink properties, as it is now well known that biochemical and biophysical properties of hydrogels influence encapsulated cells - for example, the presentation of signaling cues such as ECM ligands and mechanics are known to regulate cell differentiation, proliferation and migration.²⁰ Thus, generalizable techniques that allow the printing of a wider range of bioinks are of interest for tissue engineering to introduce optimal cellular environments.

To overcome the challenges of printing bioinks that do not meet traditional criteria, several strategies have been pursued. One approach involves the introduction of rheological additives, such as silicates²¹⁻²³ or nanocellulose^{24,25} into bioinks to impart desired rheological properties for extrusion-based printing. Support hydrogels have also been developed, where hydrogels can be printed in any arbitrary space, allowing for embedded printing of geometries not feasible by traditional layer-by-layer fabrication. For example, hydrogels have been printed into self-healing, supramolecular guest-host hydrogels²⁶ and into granular support baths comprised of either a gelatin slurry²⁷ or Carbopol microgels.²⁸ Sacrificial materials have also been utilized, where polymers such as alginate can be introduced into an ink for stabilization (e.g., via calcium through a coaxial needle) and then later washed away after the desired ink material is stabilized, such as with photocrosslinking.²⁹ Lastly, jammed microgels have recently been used for

printing, as many materials can be formed into microgels and jammed to meet printing requirements, including with encapsulated cells.³⁰ While each of these approaches expands upon the number of candidate bioinks available, the need for additives or post-processing steps could impede or compromise the design of target cellular microenvironments.

In the context of photocrosslinkable bioinks, we recently developed an approach to print non-viscous polymers, where light exposure occurs prior to bioink deposition as it passes through a photopermeable capillary (Figure 4.1).³¹

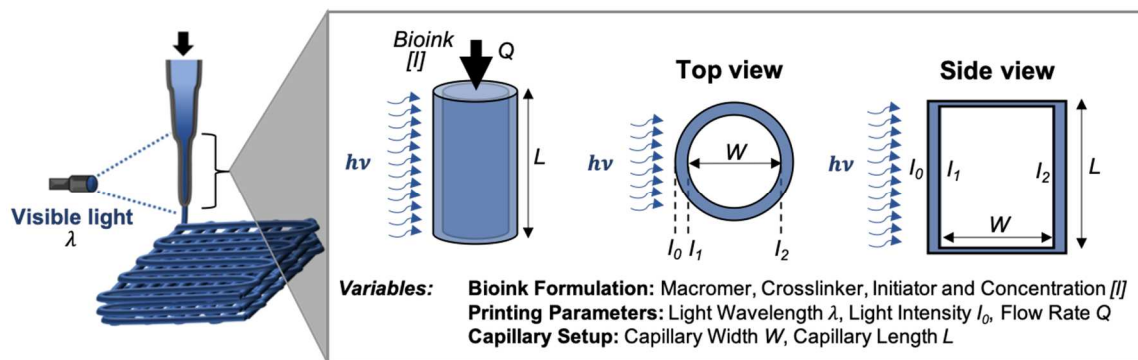


Figure 4.1: Schematic of *in situ* crosslinking approach for 3D printing. Bioinks are loaded into a syringe and irradiated with light through a photopermeable capillary during extrusion, resulting in the plug flow of filaments through the end of the capillary. There are numerous variables within the printing approach, including the bioink formulation, the printing parameters, and the capillary setup, all of which can influence printing success. These should be balanced to regulate the residence time of the bioink within the light path (Q , L , W), as well as the reaction kinetics of crosslinking ($[I]$, I_0). The intensity of light across the capillary lumen varies as a function of light attenuation due to the capillary walls and absorbing species within the designed bioink.

With this *in situ* crosslinking approach, stable hydrogel filaments are readily extruded across many hydrogel types, while the shear forces generated on cells are attenuated so that high cell viability is conserved. Furthermore, this printing approach does not require post-processing steps or the use of rheological additives, allowing for one-step 3D printing of bioactive materials. Here, we selected one potential bioink of interest for the 3D bioprinting of cartilage tissue, based on norbornene-modified hyaluronic acid

(NorHA)³² that can be crosslinked via a thiol-ene reaction in the presence of visible light and a water-soluble photoinitiator.³³ HA is a promising biomaterial in cartilage tissue engineering, particularly towards influencing MSC chondrogenesis;^{34–36} however, the NorHA bioink is non-viscous and does not meet traditional printing requirements. In this study, we explain the various steps used to implement *in situ* crosslinking with this NorHA bioink and illustrate its utility in engineering cartilage with encapsulated MSCs.

4.2 METHODS

4.2.1 Materials

Sodium hyaluronic acid (HA, MW=74 kDa) was purchased from Lifecore Biomedical (Chaska, MN) and lithium phenyl-2,4,6-trimethylbenzoylphosphinate (LAP) was purchased from Colorado Photopolymer Solutions (Boulder, CO). All other reagents were purchased from Sigma-Aldrich (St. Louis, MO) unless specified otherwise.

4.2.2 NorHA Synthesis and Characterization

Sodium HA was converted into its tetrabutylammonium salt (HA-TBA) and then modified with norbornene functional groups via benzotriazole-1-yl-oxy-tris-(dimethylamino)-phosphonium hexafluorophosphate (BOP) coupling as previously described.⁴⁹ Upon dissolving HA in distilled H₂O, Dowex 50Wx200 resin was added to the solution in a 3:1 mass ratio. After mixing for 30 minutes, the Dowex resin was filtered via vacuum filtration, and the filtrate was titrated with tetrabutylammonium hydroxide solution to a pH of 7.02-7.05. The HA-TBA solution was then frozen and lyophilized. Thereafter, 5-norbornene-2-methylamine was added to lyophilized HA-TBA and dissolved in anhydrous DMSO under inert nitrogen. BOP was then added via cannulation to the reaction round bottom flask, and the reaction was allowed to proceed for 2 hours at room temperature. The reaction was quenched with the addition of cold DI H₂O (4°C) and

dialyzed for 5 days at room temperature. Then, the crude product solution was filtered to remove precipitates and dialyzed for an additional 3-5 days. Finally, the product was frozen and lyophilized. All synthesized polymers were stored under inert nitrogen at -20°C and the extent of modification of HA with norbornene was quantified via $^1\text{H-NMR}$ (Bruker 360 MHz, **Figure 4.2**). To ensure the same level of norbornene modification ($\sim 40\%$) was achieved across different synthesis reactions (i.e. batches), $^1\text{H-NMR}$ was performed after every reaction; further, all experiments with a specific outcome were performed using the same batch of NorHA.

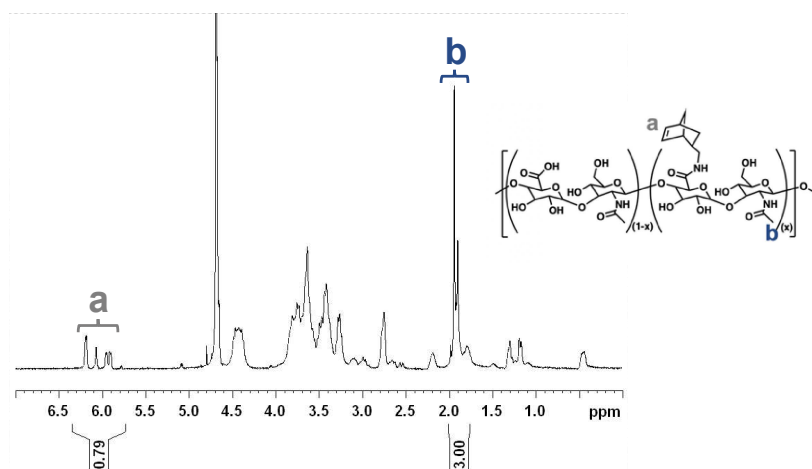


Figure 4.2: $^1\text{H NMR}$ characterization of NorHA in D_2O . Norbornene modification was determined by integrating the a) vinyl protons of norbornene (2H , $\delta \sim 5.8\text{-}6.3$ ppm) relative to the b) methyl group of HA (3H , $\delta \sim 1.8\text{-}2.0$ ppm) to obtain a relative norbornene modification of $\sim 40\%$ of the disaccharide repeat units of HA.

4.2.3 Hydrogel Formation and Rheological Characterization

One bioink formulation was investigated: 2 wt% NorHA, 0.05 wt% LAP, and 0.08 wt% DL-dithiothreitol (DTT). The absorbances of bioink components were determined using a Tecan Infinite M200 spectrometer and cuvettes with a pathlength of 1 cm. Rheological measurements were performed using an AR2000 stress-controlled rheometer

(TA Instruments) fitted with a 20 mm diameter cone and plate geometry, 59 min 42 s cone angle, and 27 μm gap. The bioink formulation was placed on the rheometer and rheological properties were examined by time sweeps (1.0 Hz, 0.5% strain) in the presence of visible light (Exfo Omnicure S1500 lamp, 400–500 nm filter) applied at variable light intensities (I_2 , expected light intensity after attenuation through the capillary and bioink). Gelation profiles obtained from oscillatory shear time sweeps are reported as the percent of the maximum storage modulus (G') observed after 10 minutes of irradiation with visible light.

4.2.4 3D Printing of NorHA

Constructs were printed using a custom-modified 3D FDM printer (Velleman K8200) and *in situ* crosslinking at variable capillary lengths ($L=15\text{-}60$ mm, Masterflex 96410-13), volumetric flow rates ($Q=0.8\text{-}3.2$ mL/h) and light intensities of ($I_1=5\text{-}15\text{mW/cm}^2$, $\lambda=400\text{-}500$ nm). Upon loading inks (acellular or cellular) into a 1 mL BD syringe, Repetier software was used to slice computer-aided design (CAD) models and control the ink deposition. An Exfo Omnicure S1500 lamp with a collimating lens was used to irradiate the photopermeable capillary during material extrusion (**Figure 4.3**).

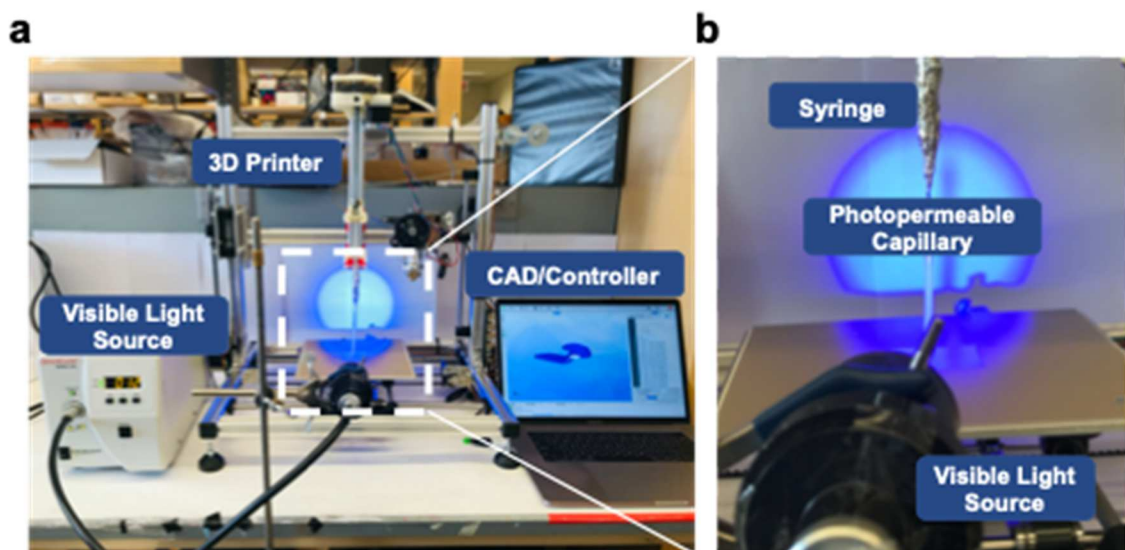


Figure 4.3: *In situ* crosslinking technique setup. a) Image of the 3D printing setup employed to print NorHA bioinks via *in situ* crosslinking. b) Zoomed image of collimated, visible blue light irradiation through a photopermeable capillary. NorHA bioink is extruded through a syringe, such that stable filaments are formed and deposited via CAD/controller

4.2.5 Cell Encapsulation and Viability

All macromers were sterilized under germicidal irradiation prior to use. Primary juvenile mesenchymal stromal cells were isolated from the bone marrow of bovine femora and tibiae (Research 87, Boylston, MA) as previously described.³⁵ Thereafter, MSCs (P1) expanded in Dulbecco's modified eagle medium (+10% fetal bovine serum +1% penicillin/streptomycin) were washed, trypsinized (0.05%), centrifuged, and resuspended (20×10^6 cells/mL) in NorHA dissolved in phosphate buffered saline (PBS) and manually transferred to a 1 mL BD syringe. Following 3D printing, constructs were cultured in chondrogenic media ($2.50 \mu\text{g mL}^{-1}$ amphotericin B, 1×10^{-3} M sodium pyruvate, $40 \mu\text{g mL}^{-1}$ L-proline, 1×10^{-7} M dexamethasone, $50 \mu\text{g mL}^{-1}$ ascorbic acid 2-phosphate, 1% ITS+, and 5 ng mL^{-1} TGF-B3). For cell viability analyses, printed hydrogels were stained with calcein AM/ethidium homodimer (0, 3, 7 days) according to manufacturer's instructions (Invitrogen). Confocal images (Leica SP5) of stained, cell-laden constructs

were analyzed using Image J software to assess both the cell viability and cell density of the top, middle, and bottom thirds of printed constructs. Cell viability was calculated as the number of live cells per total cells within a single image ($n \geq 3$ gels, 9 images per group). Cell density was calculated by counting the total number of cells within randomly placed $600 \times 600 \mu\text{m}^2$ image frames ($n \geq 3$ gels, 9 images per group).

4.2.6 Gene Expression Analysis

PCR was performed for MSCs encapsulated in printed discs as previously described.⁵⁵ After 3 days of culture, samples were mechanically agitated using a handheld tissue homogenizer so that RNA could be isolated via Trizol (Invitrogen). Isolated RNA was reverse transcribed to cDNA, and PCR was then conducted on an Applied Biosystems 7300 Real-Time PCR system. Type II-collagen (COLII), aggrecan (ACAN), type I-collagen (COL I) and SOX9 were selected as targets, with glyceraldehyde 3-phosphate dehydrogenase (GAPDH) used as a housekeeping gene. Gene expression relative to MSCs expanded on tissue culture plastic was determined using the $\Delta\Delta\text{CT}$ method, where the fold difference is found by $2^{-\Delta\Delta\text{C}}$.

4.2.7 Construct Mechanical and Biochemical Characterization

Upon printing of hydrogel bioinks (2 wt% NorHA, 0.05 wt% LAP, 5.2 mM DTT), mechanical testing was performed (TA Instruments, DMA Q800) to determine the compressive moduli of samples. Hydrogels were secured within a fluid cup via a 0.01 N pre-load, compressed until failure at a rate of 0.5 N min^{-1} , and the moduli calculated as the slope from 10-20% strain. After culture for 0, 28, and 56 days, constructs were fixed in 10% buffered formalin for 2 hours at room temperature and then washed three times with PBS. Constructs were cut into halves for either biochemical or histological analysis. Towards quantifying the biochemical content of constructs, samples were first digested

via papain (0.56 U mL⁻¹ in a mixture of 0.1 M sodium acetate, 10 M cysteine hydrochloric acid, and 0.05 M ethylenediaminetetraacetic acid, pH 6.0, ~1 mL/construct) at 60 °C overnight. Dimethylmethylene Blue (DMMB), PicoGreen, and hydroxyproline assays (Abcam Hydroxyproline Assay Kit, ab222941) were subsequently performed to quantify sulfated glycosaminoglycan (GAG), DNA, and collagen (COL) contents, respectively.⁵⁶

4.2.8 Construct Histological Characterization

To histologically analyze samples, constructs were first embedded in paraffin and incubated for 24 hours at 4°C. Thereafter, embedded samples were sectioned (5 µm) and stained with alcian blue (1%, pH 1.0, Newcomer Supply), anti-collagen type I (COL I, mouse monoclonal anticollagen type 1, Millipore Sigma), or anti-collagen type II (COL II, mouse monoclonal anticollagen type II, Developmental Studies Hybridoma Bank) antibodies to observe GAG, COL I, and COL II, respectively. Native tissue samples were isolated from the femoral condyle of a juvenile bovine joint and processed in the same manner. To quantify staining, images were first converted to 8-bit and then inverted as previously described.⁵⁵ For each section, mean intensities for three distinct and randomly selected frames were measured in Image J.

4.2.9 Statistical Analysis

All data are reported as mean ± standard deviation and n≥3 unless specified otherwise, and all statistics were performed using GraphPad Prism 7 software. For comparisons between two groups, Student t-tests were performed with two-tailed criteria and significance determined at p<0.05. For comparisons between more than two groups, one-way analysis of variance (ANOVA) was performed with *post hoc* testing and significance determined at p<0.05. Holm-Sidak correction was used for multiple comparisons with $\alpha=0.05$.

4.3 RESULTS AND DISCUSSION

4.3.1 Design of *In Situ* Crosslinking Approach Based on Bioink Formulation

HA was modified with pendant norbornene functional groups, such that approximately 40% of disaccharide repeat units contained norbornene (NorHA), as determined by quantitative ^1H NMR (Figure 4.2). Bioinks were formulated from 2 wt% NorHA, 0.05 wt% LAP, and 0.08 wt% DTT (Figure 4.4a). To assess how much light each ink component attenuates, the absorption spectra of NorHA, LAP and DTT were measured from 300-500 nm (Figure 4.4b).

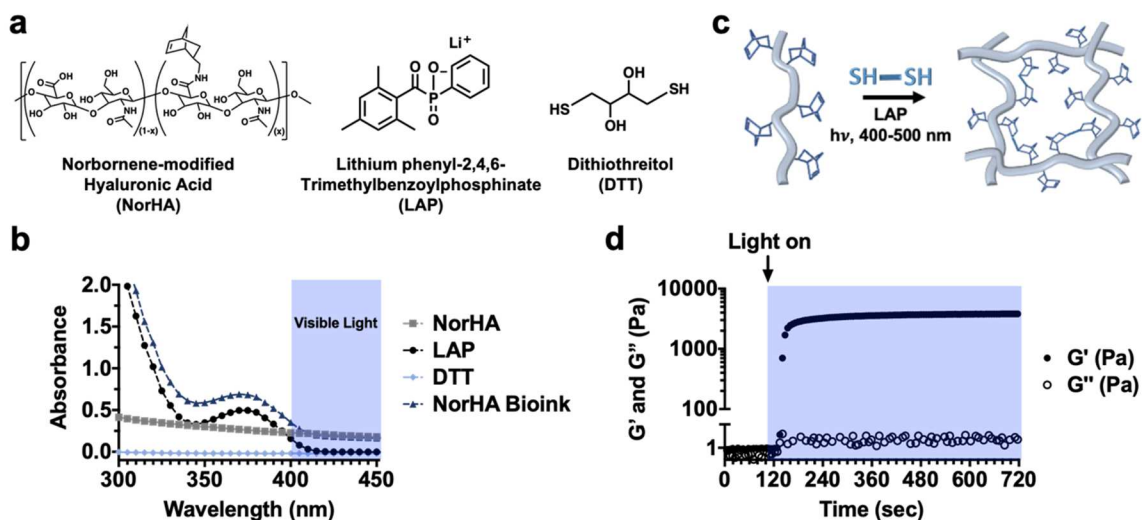


Figure 4.4: NorHA bioink composition and crosslinking. a) Chemical structures of components incorporated into NorHA bioinks and their b) absorption spectra, including for NorHA (2wt%, square), LAP (0.05 wt%, circle), DTT (0.08 wt%, diamond), and their combination into a single bioink formulation (triangle). c) Schematic of thiol-ene reaction employed to crosslink the NorHA bioink in the presence of visible light and LAP photoinitiator. d) Representative photorheology time sweep (1 Hz, 0.5% strain) during the photocrosslinking of the NorHA bioink with visible light (400-500 nm) at $I_T=10$ mW/cm 2 , illustrating increases in storage (G' , closed circles) and loss (G'' , open circles) moduli over time.

After elucidating each of these respective absorption spectra, the molar extinction coefficients (ϵ) of ink components were determined using Beer-Lambert Law (Equation 4.1), which states that the absorption of a species of interest is proportional to the

pathlength of light (W), the concentration of the species (c), and the degree to which the species absorbs that specific wavelength of light (ϵ).

$$(4.1) A = \epsilon W c$$

As shown in these spectra, the degree of light attenuation due to DTT within the bioink is negligible, whereas both NorHA and LAP absorb light up to ~420 nm. To better understand the potential for light attenuation through the printer's photopermeable capillary, the maximum amount of attenuation possible, which occurs at 400 nm, was quantified. Since the molar extinction can be determined using equation (1) and absorbance measurements of NorHA and LAP samples with known concentrations, the molar extinction coefficient for LAP at 400 nm was determined to be ~0.078 cm⁻¹mM⁻¹, while the coefficient for NorHA was ~855 cm⁻¹mM⁻¹. The light attenuation (of 400 nm light) due to multiple absorbing species can then be quantified via an alternative form of Beer-Lambert law, given by Equation 4.2.

$$(4.2) I = I_0 e^{-W(\epsilon_I[I] + \epsilon_{NorHA}[NorHA])}$$

Thus, the drop in light intensity across the capillary lumen ($W=800 \mu\text{m}$) due to the bioink used in our printing setup was negligible (**Figure 4.3**), as the initial intensity within the capillary (I_1) only decreases ~3% across the width of the capillary (I_2); however, larger decreases in light intensity could be expected if a higher concentration of initiator ($[I]$), wider tubing (increased W), or different wavelength (λ) of light were employed (**Figure 4.5**).

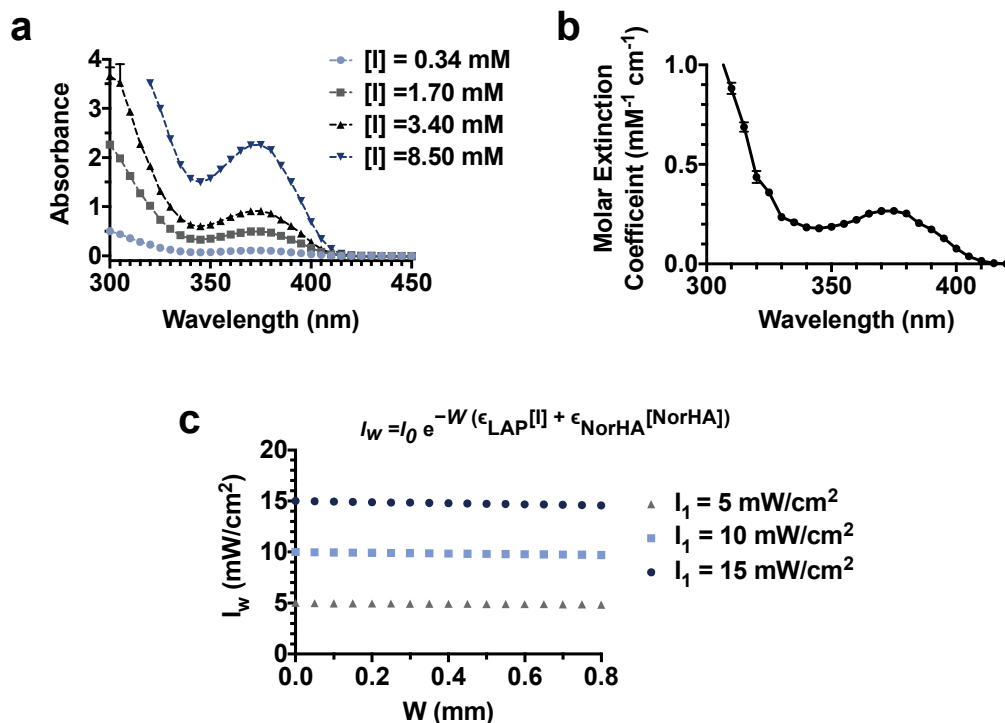


Figure 4.5: Influence of light absorbance on printability. a) Absorbance measurements and b) quantified molar extinction coefficients of the LAP photoinitiator at variable concentrations ($[I]$) and light wavelengths (λ). c) Quantification of light attenuation across the width of the capillary (I_w), due to absorbing species within the NorHA bioink (1.70 mM LAP), where $I_w = I_2$ for $W = 800 \mu\text{m}$ (experimental parameter in this study). Drops in light intensity: $I_1 = 5.00 \text{ mW/cm}^2$ to $I_2 = 4.86 \text{ mW/cm}^2$ (triangle); $I_1 = 10.0 \text{ mW/cm}^2$ to $I_2 = 9.72 \text{ mW/cm}^2$ (square); $I_1 = 15.0 \text{ mW/cm}^2$ to $I_2 = 14.6 \text{ mW/cm}^2$ (circle).

Finally, to target a specific I_1 within the photopermeable capillary, experimental relationships of light attenuation due to the capillary walls themselves were developed (Figure 4.6).

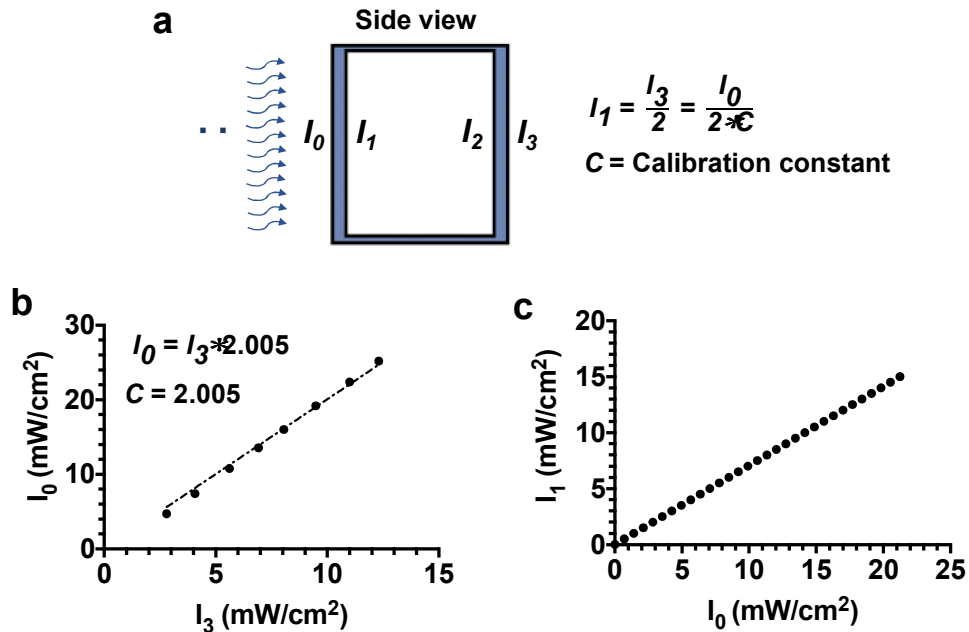


Figure 4.6: Light attenuation through the capillary. a) Schematic illustrating the various light intensities during *in situ* crosslinking, including directly from the light guide (I_0), at the inner edge of the capillary lumen (I_1), after passing through the capillary lumen (I_2), and at the opposite side of the capillary (I_3). An equation describing this relationship is shown to account for light attenuation by the capillary itself. b) Experimental measurements of the incident light intensity (I_0) compared to the light intensity at the opposite end of the capillary from the light source (I_3). c) Calculated calibration curve to determine the required I_0 to achieve a desired I_1 to cure the bioink.

4.3.2 Photorheology to Identify Permissible Printing Regimes

The NorHA within the bioink undergoes a thiol-ene reaction for crosslinking (**Figure 4.4c**), which can be monitored experimentally with photorheology to assess the kinetics of gelation for our distinct ink formulation (**Figure 4.4d**). Photoreology time sweeps were performed at $I_2 \sim 4.86, 9.72$ and 14.6 mW/cm^2 (corresponding to $I_1 = 5, 10$ and 15 mW/cm^2 , respectively) towards creating gelation profiles that could predict permissible printing regimes (**Figures 4.4, 4.7**).

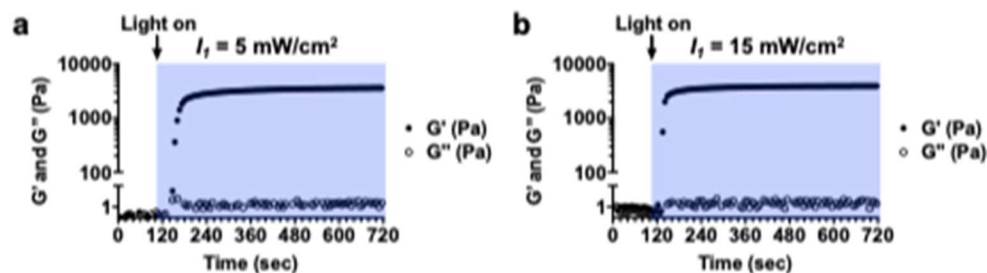


Figure 4.7: Rheological properties of bioinks across various light intensities. Representative photorheology time sweeps (1 Hz, 0.5% strain) during the photocrosslinking of the NorHA bioink with visible light (400-500 nm) at either a) $I_l=5$ mW/cm² or b) $I_l=15$ mW/cm², illustrating increases in storage (G' , closed circles) and loss (G'' , open circles) moduli over time.

When NorHA inks were initially subjected to shear at 1 Hz and 0.5% strain, the storage (G') and loss moduli (G'') were on the order of 1-10 Pa, consistent with a non-viscous material. It was not possible to measure the viscosity of the initial bioink formulation. However, upon irradiation with visible light, a rapid evolution of mechanics was observed (increasing G'), indicating NorHA crosslinking into an elastic hydrogel.

These photorheological time sweeps were normalized to their maximum value to develop a heuristic for the time required for G' to plateau; it has previously been shown that the percent of maximum storage G' correlates with the conversion of crosslinker in thiol-ene reactions.³⁷ This metric was therefore used to quantitatively estimate the extent of reaction as a function of time. Since the capillary length, bioink volumetric flow rate, and incident light intensity are all user-defined parameters for *in situ* crosslinking, we aimed to elucidate how each of these variables can be tuned in conjunction with these normalized gelation profiles to enhance ink printability.

First, an analysis was performed on the influence of capillary lengths on ink printability, while setting the light intensity and flow rate at constant values ($I_l=10$ mW/cm², $Q=0.8$ mL/h). If the time of light exposure (**Figure 4.4d**; x-axis) is multiplied by the ink velocity (which is set by the flow rate and the width of the capillary lumen), then a

relationship between the percent of maximum G' versus capillary length can be generated (Figure 4.8a). By experimentally printing the bioink under various conditions, it is clear that the quality of printed filaments is dependent on the capillary length. Here, a capillary length of 60 mm was needed for good print resolution, whereas capillary lengths of 15 mm and 30 mm resulted in irregular and spread filaments, indicating that the curing was not complete.

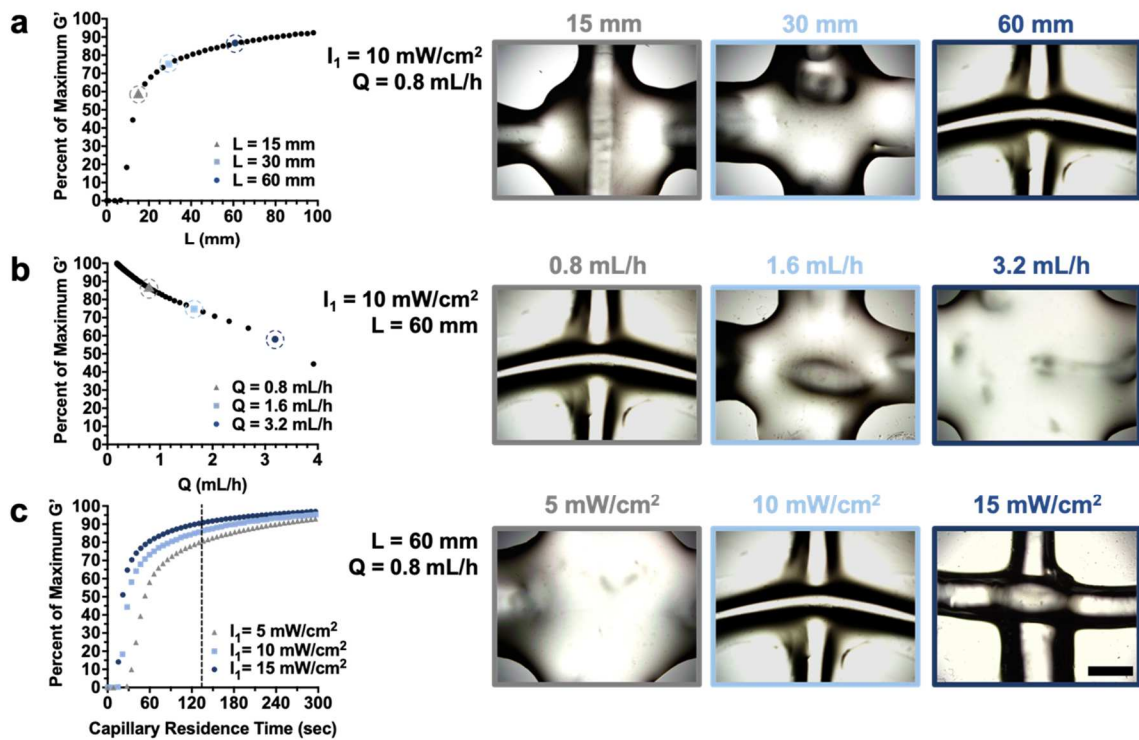


Figure 4.8: Identification of permissible printing conditions via photorheology. a) Left: Percent of maximum G' as a function of variable capillary lengths and Right: representative images of overlaying filaments, with $I_1=10$ mW/cm², $Q=0.8$ mL/h and variable capillary lengths ($L=15, 30, 60$ mm). b) Left: Percent of maximum G' as a function of variable flow rates and Right: representative images of overlaying filaments, with $L=60$ mm, $I_1=10$ mW/cm² and variable flow rates ($Q=0.8, 1.6, 3.2$ mL/h). c) Left: Percent of maximum G' as a function of capillary residence time across variable light intensities (dashed line indicates the fixed residence time of 135 seconds) and Right: representative images of overlaying filaments, with $L=60$ mm, $Q=0.8$ mL/h and variable light intensities ($I_1= 5, 10, 15$ mW/cm²). Scale bar = 1 mm. Note: the same representative image was used for the printing parameters used subsequently in this study ($L=60$ mm, $Q=0.8$ mL/h, $I_1=10$ mW/cm²).

Similarly, these gelation profiles can be employed towards understanding how bioink flow rate influences the *in situ* crosslinking process, while setting the light intensity

and capillary length at constant values ($I_1=10 \text{ mW/cm}^2$, $L=60 \text{ mm}$). A relationship between the percent of maximum G' versus bioink flow rate was obtained (**Figure 4.8b**) by converting the time of light exposure (Figure 2d; x-axis) into volumetric flow rate using Equation 4.3 below, where $W=0.8 \text{ mm}$ for this experiment and t is time.

$$(4.3) \quad Q = \frac{\pi * L * W^2}{4 * t}$$

Again, the NorHA bioink was printed with varied bioink flow rates to observe the influence of printing conditions on filament quality (**Figure 4.8b**). Here a flow rate as slow as 0.8 mL/h was needed for high resolution filaments, as faster flow rates did not permit sufficient times for bioink curing under this *in situ* crosslinking setup and resulted in spread filaments.

Finally, the influence of light intensity on crosslinking was explored, where increased light intensities led to more rapid curing (**Figure 4.8c**). While selecting a common ink residence time of 135 seconds (**Figure 4.8c**; $L=60 \text{ mm}$, $Q=0.8 \text{ mL/h}$), it was clear that at least 10 mW/cm^2 light intensity was needed for filament curing, whereas lower light intensities were not sufficient for crosslinking under the specific *in situ* crosslinking setup. Overall, the most consistently printable and stable filaments were achieved when printing conditions resulted in NorHA bioinks reaching $>85\%$ of their maximum G' . It should be noted that the maximum G' achieved after 10 minutes of irradiation may decrease appreciably if the reaction kinetics are slow (i.e., significantly lower light intensities); therefore, the predictive power of these gelation profiles is only valid if a plateau in storage modulus is observed in the photorheology studies.

Through the implementation of this approach, a set of optimal printing conditions was determined ($L=60 \text{ min}$, $Q=0.8 \text{ mL/h}$, $I_1=10 \text{ mW/cm}^2$) and utilized to print larger, multilayered constructs. Specifically, *in situ* crosslinking was employed to create large

constructs with anatomically relevant features, such as a femoral condyle (**Figure 4.9a**). In addition, discs (~1.5 mm thickness, ~6.5 mm diameter) were printed (**Figure 4.9b**) and shown to retain their structure after immersion in PBS for one week (**Figure 4.10**).

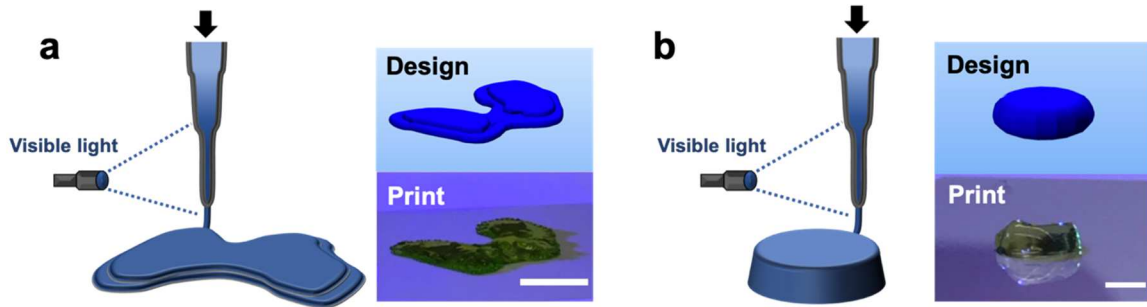


Figure 4.9: Representative multi-layered constructs printed via *in situ* crosslinking. Left: Schematic of *in situ* crosslinking method and Right: CAD design and representative image of a printed construct (labeled with food coloring) for designs of a) a model femoral condyle or b) a disc (~1.5 mm thickness, ~6.5 mm diameter). Scale bars = 1 cm (a) and 5 mm (b).

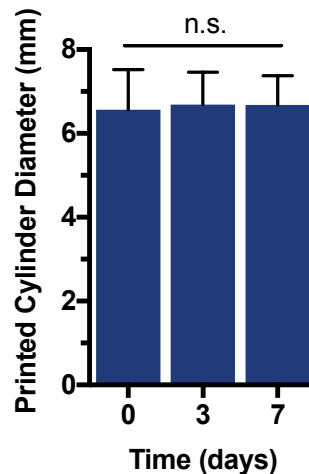


Figure 4.10: Stability of discs printed via *in situ* crosslinking technique. Printed discs were immersed in PBS for 0, 3, or 7 days and imaged to quantify any changes in the disc diameter over time. $n \geq 3$, n.s. = not significant.

To demonstrate the reproducibility of this printing approach, we quantified the percent error between the targeted and observed dimensions of printed filaments and discs, which both exhibited on average ~3% error (**Figure 4.11**).

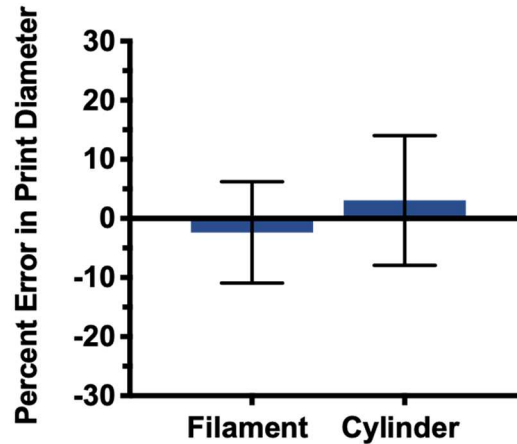


Figure 4.11: Quantification of printing error associated with in situ crosslinking technique. Percent errors between target dimensions and observed dimensions are reported for both printed filaments (target dimension: 800 μm diameter) and printed discs (target dimension: 6.3 mm diameter). $n \geq 7$ constructs.

To ensure the viability of this printing approach towards fabricating constructs for long-term culture and neocartilage formation, we also validated that the printing process does not alter the swelling behavior or the mechanics of NorHA hydrogels (**Figure 4.12**). Specifically, the volumetric swelling ratios and compressive moduli of both printed and casted discs incubated in PBS were determined at 0, 1, 3 and 7 days, and no differences were observed across these timepoints.

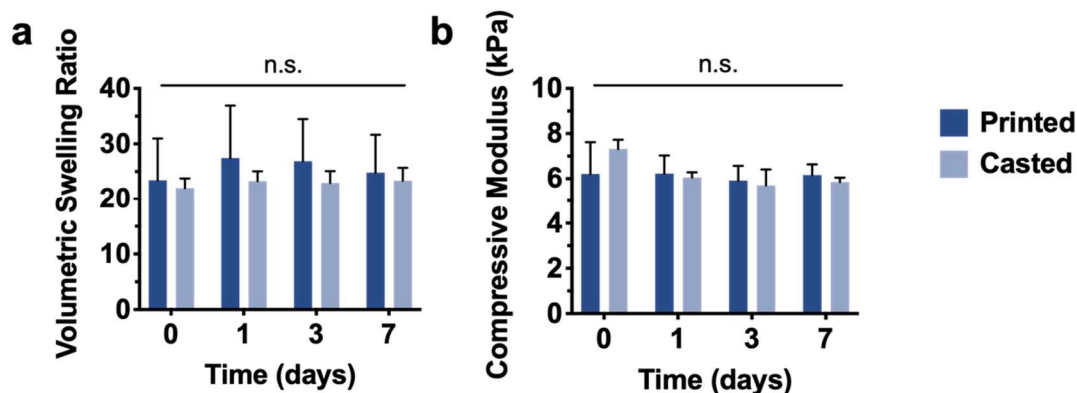


Figure 4.12: Swelling behavior and mechanics of printed versus casted NorHA discs. a) Volumetric swelling ratios are reported for printed and casted discs as the ratio between hydrogel wet weights and dry weights. Samples were incubated in PBS and analyzed at days 0, 1, 3 and 7. b) Compressive moduli for printed and casted discs at days 0, 1, 3 and 7. $n \geq 3$. n.s. = not significant.

4.3.3 *In Situ* Crosslinking of NorHA Bioink for MSC Encapsulation

To assess the cytocompatibility of the printing process, primary juvenile bovine MSCs were isolated, printed into discs, and cultured in chondrogenic media for up to one week. Confocal images of constructs stained with Live/Dead assays indicated that high cell viabilities (>85%) persisted through 7 days after printing, although small decreases in viability were observed from the initial time point (day 0) to 3 and 7 days. To ensure that the observed cytocompatibility was conserved throughout all depths of the printed constructs, confocal images for distinct thirds (top, middle, bottom) of each disc were analyzed (**Figure 4.13a,b**). At all timepoints (days 0, 3, 7), cell viabilities in distinct regions of the discs exhibited no significant differences, indicating that large constructs could be readily printed while retaining consistent cell viability throughout the duration of printing (**Figure 4.13c**).

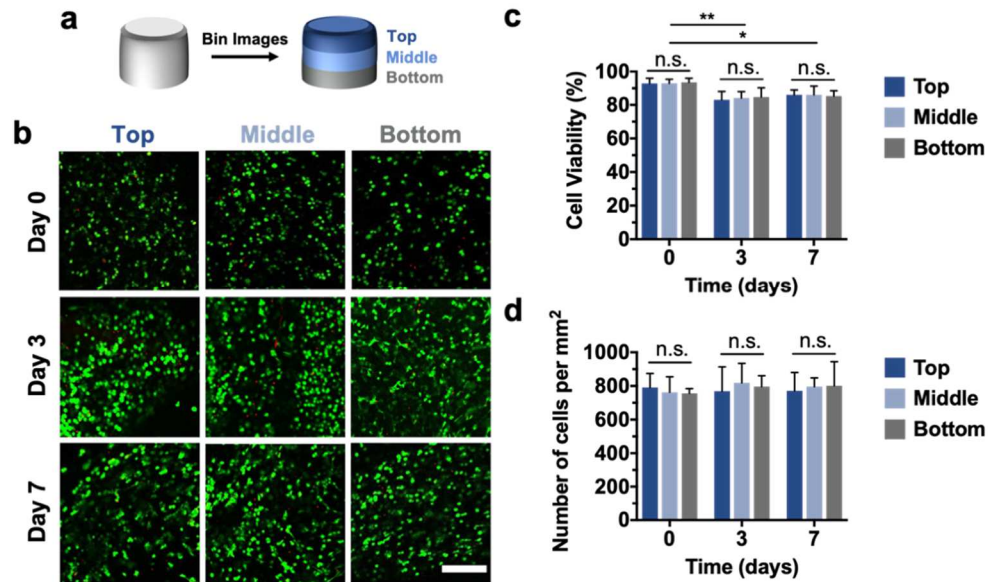


Figure 4.13: Cell viability and distribution in printed constructs. a) Schematic demonstrating the binning of acquired Live/Dead confocal images for analysis of the top, middle and bottom thirds of printed discs. b) Representative Live/Dead images (scale bar = 200 μm), c) quantification of cell viability, and d) quantification of cell density for the top, middle and bottom thirds of printed discs after 0, 3, and 7 days of culture. $n \geq 3$, * $p < 0.05$, ** $p < 0.01$, n.s. = not significant.

One challenge in the printing of bioinks is cell sedimentation and achieving a homogenous distribution of cells throughout a printed construct.³⁸ Thus, cell densities were also quantified throughout different depths of the printed discs to demonstrate that cell settling did not impact cell distribution at the print times employed with the *in situ* crosslinking technique. At each timepoint, the cell density was within the range of 750-820 cells/ mm^2 , with no significant differences existing between different depths of the constructs or across different timepoints (**Figure 4.13d**). Therefore, *in situ* crosslinking supported the fabrication of multi-layered constructs with viable and well-distributed MSCs.

4.3.4 Neocartilage Formation in 3D Printed NorHA Constructs

After validating the printability and cytocompatibility of NorHA hydrogels printed via *in situ* crosslinking, we next printed constructs for long-term culture to investigate neocartilage formation. Printed discs were cultured for up to 56 days in chondrogenic media; upon fixing, all samples were characterized to assess changes in biochemical content, mechanics, and matrix distribution over time. Initially, printed discs were analyzed after three days of culture via PCR to ensure that encapsulated MSCs would undergo chondrogenesis (**Figure 4.14**); the observed expression of chondrogenic markers such as type II-collagen (COLII), aggrecan (ACAN), and SOX9 indicated that printed constructs were conducive to neocartilage formation.

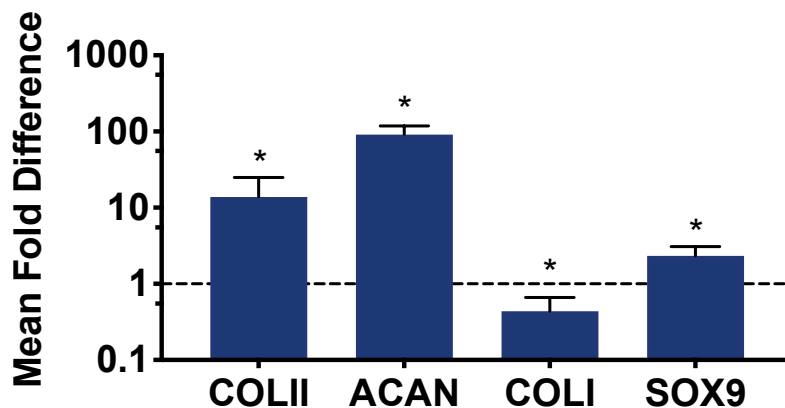


Figure 4.14: Relative gene expression of encapsulated MSCs in printed NorHA constructs. Mean fold difference of type II-collagen (COLII), aggrecan (ACAN), type I-collagen (COLI) and SOX 9 gene expression for printed discs cultured for 3 days relative to MSCs cultured on tissue culture plastic (i.e., day 0, 2D control). Dashed line represents expression level of control group, which are cells at the time of encapsulation. $n \geq 5$ printed discs, $*p < 0.05$.

After 56 days of culture, printed discs exhibited an increase in normalized DNA content, suggesting that viable cells proliferated and persisted throughout the duration of culture (**Figure 4.15a**). Further evidence of neocartilage formation is provided by metrics

of increased sulfated glycosaminoglycan (GAG) and collagen (COL) contents (**Figure 4.15b,c**).

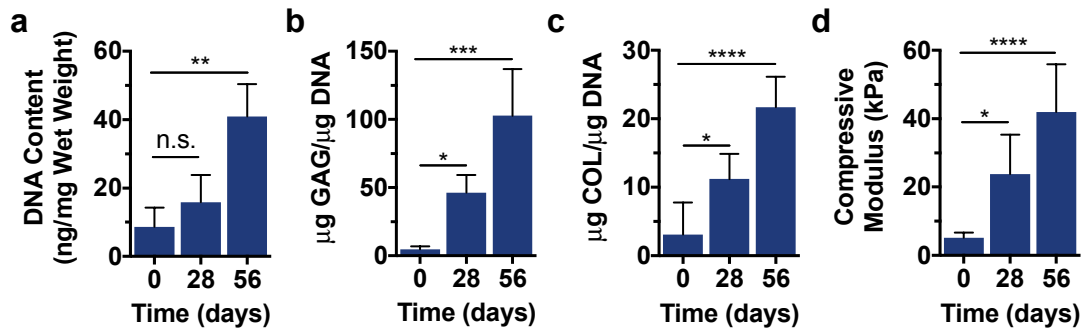


Figure 4.15: Mechanical characterization and biochemical analysis of printed constructs. a) DNA content, b) sulfated glycosaminoglycan (GAG) content, c) collagen (COL) content, and d) compressive moduli for printed constructs after 0, 28, and 56 days of culture. $n \geq 3$, * $p < 0.05$, ** $p < 0.01$, *** $p < 0.001$, **** $p < 0.0001$, n.s. = not significant.

Both of these extracellular matrix components are indicative of MSC chondrogenesis and tissue maturation, demonstrating that printed discs formed into neocartilage. Sulfated GAG content increased to over 100 $\mu\text{g}/\mu\text{g DNA}$ by 56 days, likely enhancing the mechanics of the printed constructs, as these polysaccharides impart osmotic swelling and high compressive properties to native tissue.³⁹ Collagen, the main ECM-protein found in cartilage, was also deposited by embedded cells, with collagen content increasing 7-fold from 0 to 56 days. These results were corroborated by dynamic mechanical analysis, which showed increases in the compressive moduli of printed discs from 5.2 ± 1.5 kPa initially to 42.0 ± 13.9 kPa after 56 days of culture (**Figure 4.15d**). Although these mechanics pale in comparison to those of native bovine articular cartilage, which has been shown to possess Young's moduli on the order of 0.3-0.6 MPa⁴⁰ and aggregate moduli ranging between 0.5 MPa and 1.0 MPa,⁴¹ the observed increases in compressive moduli demonstrate the evolution of functional tissue properties in printed constructs.

Histological analyses were subsequently performed to assess the distribution of ECM components within the printed discs. Alcian blue staining indicated that GAGs were homogeneously distributed by encapsulated MSCs by as early as 28 days, with staining intensities increasing over time and trending towards native tissue levels (**Figure 4.16a**).

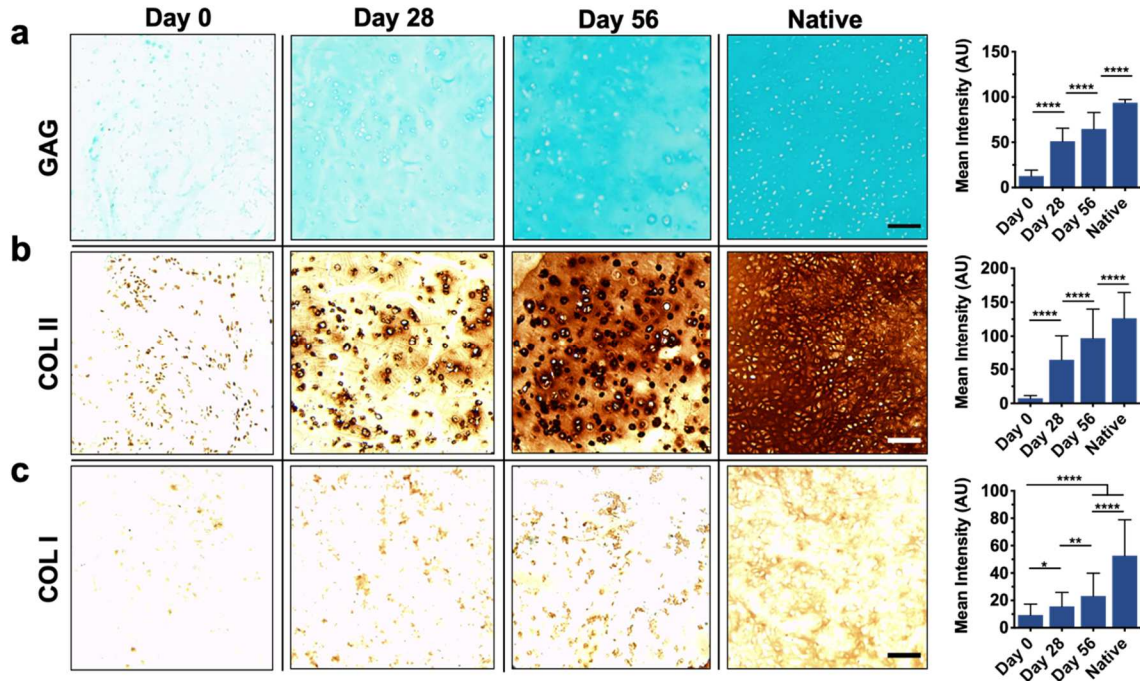


Figure 4.16: Histological evaluation of printed constructs. Left: Representative images and Right: staining quantification of a) alcian blue staining for glycosaminoglycans (GAG), b) immunohistochemistry for type II collagen (COL II), and c) immunohistochemistry for type I collagen (COL I) for printed constructs after 0, 28, and 56 days of culture or native bovine articular cartilage. Scale bars = 100 μ m, $n \geq 15$ sections, 45 images per group, * $p < 0.05$, ** $p < 0.01$, *** $p < 0.0001$.

Collagen II (COLII), one of the most abundant matrix proteins found in cartilage, was also detected in printed constructs, indicating that appreciable matrix was formed over long-term culture (**Figure 4.16b**). The observed increases in COL II staining intensity are of interest, as COLII imparts tensile strength to cartilage in native tissue.³⁹ Furthermore, the deposition of COLII in printed discs was disperse and well distributed, albeit less homogenous than the observed GAGs. Noticeably, COLII staining was most

intense at 56 days within the pericellular space of encapsulated cells. Finally, the distribution of collagen I (COL I), which is more prevalent in fibrocartilage, was measured to qualitatively assess the phenotype of the fabricated neocartilage (**Figure 4.16c**). While increases in COLI staining were observed from the initial timepoint to 56 days, there was appreciably less COL I than COLII in printed constructs, suggesting that the tissue formed more closely resembles hyaline cartilage over fibrocartilage.

It is noteworthy that this *in situ* crosslinking technique may also be leveraged towards the design and fabrication of neocartilage into more complex geometries. To this end, femoral condyles were printed and cultured for 56 days in a similar manner to printed discs (**Figure 4.17a**), resulting in the formation of larger tissue constructs.

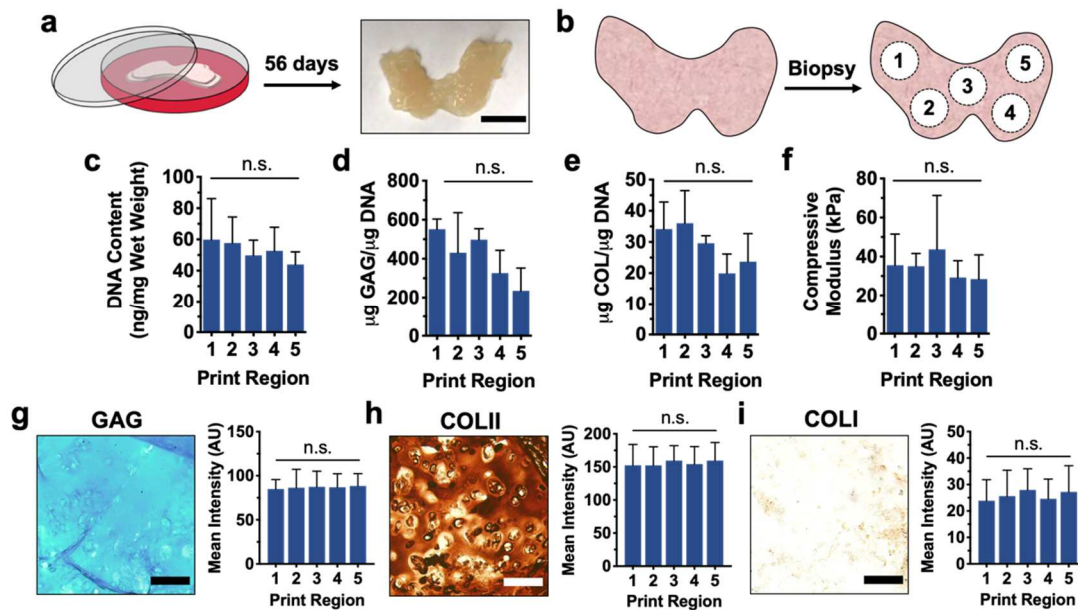


Figure 4.17: Culture and characterization of printed femoral condyles. a) Schematic of printed femoral condyle and image of printed construct after 56 days of culture. b) Schematic of five distinct print regions biopsied from printed femoral condyle models for analysis. c) DNA content, d) sulfated glycosaminoglycan (GAG) content, e) collagen (COL) content, and f) compressive moduli for construct biopsies after 56 days of culture. Left: Representative images and Right: staining quantification of g) alcian blue staining for glycosaminoglycans (GAG), h) immunohistochemistry for type II collagen (COL II), and i) immunohistochemistry for type I collagen (COL I) for construct biopsies after 56 days of culture. Scale bars = 1 cm (a) and 100 μm (g-i), $n=3$ printed constructs, $n\geq 15$ sections, 45 images per group, n.s.=not significant.

To assess the homogeneity and quality of neotissue formed in these constructs, condyles were biopsied such that 4mm discs were isolated from five distinct print regions (**Figure 4.17b**). As anticipated, each of these biopsies exhibited biochemical content associated with neocartilage, including elevated amounts of normalized DNA content (**Figure 4.17c**), sulfated GAG content (**Figure 4.17d**) and collagen content (**Figure 4.17e**). Tissue samples isolated from printed condyles also showed enhanced compressive properties relative to acellular constructs (**Figures 4.8, 4.17f**). It should be noted that any discrepancies observed between the moduli of biopsied tissue samples (i.e., from printed femoral condyles) and previously printed discs may be attributed to differences in sample topography, as the biopsied condyle samples possessed a convex surface. Interestingly, no significant differences in biochemical content or compressive moduli were observed across the five biopsied print regions of femoral condyles, suggesting that *in situ* photocrosslinking supports the fabrication of neocartilage in a controlled and scalable manner. Similarly, all five biopsied print regions displayed an appreciable amount of ECM deposition, as demonstrated by histological analysis (**Figure 4.17g-i**). Staining intensities for GAG, COLII and COLI did not vary significantly between distinct print regions, and the relative amounts of COLII and COLI observed suggest that femoral condyle models were successfully printed to form hyaline cartilage.

4.3.5 Evaluation of *In Situ* Crosslinking Approach

To engineer precise tissues for clinical medicine, the development of scaffolds with complex, hierarchical structures are of great interest, particularly with patient-specific defect geometries.⁴² 3D printing is a promising approach towards this, including for the repair of cartilage;^{3,43} however, the design of 3D printed scaffolds has been limited to only a small number of bioinks with the requisite properties for printability. This inherently limits 3D printing in tissue repair, as cells are responsive to their local environment and we would

like to print materials to guide cell behavior, rather than use materials only because they are printable. To address this, we recently developed an approach that permits the printing of non-viscous, photocrosslinkable bioinks without the use of additives or sacrificial materials.³¹

Our *in situ* crosslinking approach is simple - the non-viscous bioink is cured with light as it passes through a photopermeable capillary, prior to deposition onto a surface (**Figures 4.1, 4.2**). The design of the system includes many variables that can be balanced to ensure crosslinking as the hydrogel precursor transits through the capillary; thus, it is important to understand both the reaction kinetics of the specific bioink composition and the residence time of the material within the capillary. The steps to *in situ* crosslinking include: (i) selecting a desired bioink (macromer, crosslinker, initiator/concentration), (ii) characterizing the gelation behavior for this bioink using the light wavelength and intensity available for the printing setup, and (iii) designing the capillary (width/length) and bioink flow rate for crosslinking to occur prior to deposition. For example, as the bioink's residence time within the capillary increases (e.g., increased capillary length, lower volumetric flow rate), the light exposure time and time permitted for *in situ* crosslinking increases, resulting in elevated crosslinking until maximum conversions are reached. Similarly, increased reaction rates (e.g., increased initiator concentration or light intensity) increase the rate of gelation and support altered printing setups (e.g., lower capillary lengths). Attention should be given to the exposure of cells to any harmful components (radicals, shear forces), but the photoencapsulation of cells and extrusion of cells from needles has now been performed extensively, and any issues are mitigated by following general considerations of these prior studies.⁴⁴⁻⁴⁶ Too much curing during printing should also be considered, as it may lead to clogging of the capillary during the curing process.

HA-based hydrogels are of particular interest in cartilage repair since HA is a natural component of cartilage, biodegradable, non-toxic, and may be easily modified to form hydrogels with a range of properties; in addition, HA is already used in numerous clinical applications, such as in joint viscosupplements or tissue-fillers.⁴⁷ Therefore, NorHA was selected as a photocrosslinkable macromer to comprise our bioink for engineering cartilage. NorHA is crosslinked into hydrogels via a thiol-ene reaction, where radical species are first generated (e.g., light exposure of a photoinitiator) to subsequently form reactive thiyl radical intermediates in the presence of thiol-containing molecules; these intermediates may then undergo reactions with free norbornene groups.³³ Here, the photoinitiator LAP was selected since it is a water-soluble, visible light photoinitiator that has limited cytotoxicity and has been previously employed towards the formation of HA-based hydrogels.⁴⁸ Although visible light is used in this approach, macromer solutions were still stable under ambient light and the process can be used across a wide range of wavelengths with the appropriate initiator systems. Further, DTT was selected as the dithiol crosslinker due to previous use in cell encapsulation.⁴⁹

To implement this *in situ* crosslinking approach, careful consideration must first be given to the distinct components incorporated into the bioink (**Figure 4.4a**). NorHA was used at a relatively low concentration (2 wt%), as it has been previously shown that lower crosslink densities give rise to hydrogels with increased nutrient transport and ECM dispersion by encapsulated cells.³⁵ Similarly, the concentration of LAP (0.05 wt%) was selected to ensure appreciably quick gelation kinetics while mitigating any potential cytotoxic effects. Varying DTT concentration has been shown to modulate the mechanics of NorHA hydrogels, as the degree of crosslinking is dependent on the number of crosslinks formed;³² thus, 0.08 wt% DTT (ca. 5.2 mM) was used in the identified bioink to obtain gels with compressive moduli of approximately 6 kPa. The light absorbance of the

bioink is dependent upon the selection of these components and their concentrations; thus, we characterized absorbance to understand both radical generation and potential light transmittance across the capillary. Significant light attenuation can alter the uniformity of reaction across the capillary and should be minimized where possible to reduce filament heterogeneity. To address this, quantitative Beer-Lambert Law calculations were performed to determine how light intensity varies during printing as a function of light wavelength, ink formulation, and capillary width (**Figure 4.5**). These calculations were imperative for elucidating the reaction conditions experienced by NorHA bioinks during the *in situ* crosslinking process.

With these irradiation conditions determined, photorheology experiments were performed to identify how user-defined printing parameters (capillary length, bioink flow rate, and light intensity) influenced the *in situ* crosslinking printing process. Specifically, bioink gelation profiles were created to demonstrate how the extent of reaction within the photopermeable capillary affects bioink printability. Longer capillary lengths resulted in greater ink residence times within the capillary, effectively increasing the extent of thiol-ene reaction and degree of ink crosslinking. This phenomenon was demonstrated by representative prints fabricated at variable capillary lengths (**Figure 4.8a**). Under these printing conditions, both 15 mm and 30 mm capillaries did not permit sufficient time for stable overlaying filaments to form, resulting in unstable filament structures. While the final capillary length evaluated resulted in successful filaments (60 mm), it is important to note that if the capillary length is too long, inks may clog the capillary over time, compromising printability and giving rise to high shear forces. Clogging of the capillary could indicate interactions at the capillary interface with the hydrogel filament, which may be overcome through capillary selection or treatment of the lumen.

As expected, printing with faster bioink flow rates resulted in shorter ink residence times within the capillary and printing of unstable filaments, whereas printing with slower flow rates resulted in more precise filaments and sufficient time for the thiol-ene reaction to proceed (**Figure 4.8b**). Lower light intensities ($I_l=5$ mW/cm²) reduced the rate of polymerization within the capillary during printing, such that unstable filaments were formed; however, stable filaments were readily printed when $I_l=10$ mW/cm² and $I_l=15$ mW/cm² (**Figure 4.8c**). While suitable print resolution was obtained with these print conditions at $I_l=15$ mW/cm², capillary clogging commonly occurred, suggesting that an upper-limit of printability exists. Thus, there is a balance between appropriate curing conditions to obtain stable filaments and the potential for clogging of the capillary with extended residence times or too rapid of crosslinking (i.e., increased light intensity).

Upon identifying permissible printing conditions via photorheology time sweeps, NorHA bioinks were printed via *in situ* crosslinking to form multilayered constructs of various shapes, including condyles and simple discs that could be used for cell culture. The process was cytocompatible, as the *in situ* photocrosslinking of NorHA bioinks resulted in constructs with high cell viability (>85% at 7 days after printing) and homogeneously distributed MSCs. Variations in cell densities may be a concern with very long print times, but this was not an issue with the printing regimes used in the current study. There was no change in cell numbers over the first week of culture, likely due to encapsulation in the covalently crosslinked hydrogel and MSCs undergoing chondrogenesis. Further, these inks could be printed into constructs amenable to long-term culture and tissue formation. With 56 days of culture in chondrogenic media, printed constructs exhibited significant increases in compressive moduli and biochemical content associated with cartilaginous tissue. Histological analyses validated the production of both

GAG and COL by encapsulated MSCs, indicating the formation and maturation of neocartilage.

An important consideration in the design of hydrogels for cartilage tissue engineering is their ability to degrade, as it has been shown that hydrogels that can readily degrade enable improved tissue formation and matrix distribution by encapsulated cells.^{50,51} Since NorHA hydrogels were filled with extracellular matrix upon culture, we were unable to monitor NorHA degradation in the presence of cells; however, the elaboration of this matrix by encapsulated cells indicates that NorHA hydrogels support cartilage formation. Importantly, the degradability of NorHA hydrogels can be tuned if desired via the incorporation of degradable (e.g., matrix metalloproteinase-degradable) crosslinkers.³¹ The success of this study, including printed construct stability over time, cell viability, and tissue formation, validates the approach presented here to use *in situ* crosslinking to 3D print a selected bioink. Towards translating these printed tissue constructs in the future; it will be important to consider how neocartilage may be integrated into articular focal defects for the repair of diseased cartilage. It is expected that with the development of *ex vivo* osteochondral defect models⁵² and hydrogel adhesives,⁵³ constructs printed via *in situ* crosslinking may be amenable to implantation.

4.4 CONCLUSIONS

The example presented here with the visible light crosslinking of NorHA to encapsulate MSCs towards chondrogenesis and cartilage formation is only meant to be illustrative of this printing approach. The bioink composition can be greatly varied across macromers that undergo crosslinking through light exposure, including both radical polymerizations or thiol-ene reactions in the presence of photoinitiators.⁵⁴ For example, Vega et al. recently developed a screening platform to identify optimal cellular

environments within photocrosslinkable hydrogels.⁴⁹ Bioinks can then be readily designed from information from these types of screening platforms and implemented into the *in situ* crosslinking 3D printing approach. Further, the applications of printed constructs using this approach can be easily expanded depending on the cell types and tissue of interest, and include not only for clinical applications of tissue repair, but also for *in vitro* models to probe fundamental biological questions or for drug screening.

4.5 REFERENCES

1. Makris, E. A., Gomoll, A. H., Malizos, K. N., Hu, J. C. & Athanasiou, K. A. Repair and tissue engineering techniques for articular cartilage. *Nat. Rev. Rheumatol.* **11**, 21–34 (2015).
2. Hunziker, E. B., Lippuner, K., Keel, M. J. B. & Shintani, N. An educational review of cartilage repair: Precepts & practice - myths & misconceptions - progress & prospects. *Osteoarthr. Cartil.* **23**, 334–350 (2015).
3. Mouser, V. H. M. *et al.* Three-Dimensional Bioprinting and Its Potential in the Field of Articular Cartilage Regeneration. *Cartilage* **8**, 327–340 (2017).
4. Cui, X., Breitenkamp, K., Finn, M. G., Lotz, M. & D'Lima, D. D. Direct Human Cartilage Repair Using Three-Dimensional Bioprinting Technology. *Tissue Eng. Part A* **18**, 1304–1312 (2012).
5. Fedorovich, N. E. *et al.* Biofabrication of Osteochondral Tissue Equivalents by Printing Topologically Defined, Cell-Laden Hydrogel Scaffolds. *Tissue Eng. Part C Methods* **18**, 33–44 (2012).
6. Rhee, S., Puetzer, J. L., Mason, B. N., Reinhart-King, C. A. & Bonassar, L. J. 3D Bioprinting of Spatially Heterogeneous Collagen Constructs for Cartilage Tissue Engineering. *ACS Biomater. Sci. Eng.* **2**, 1800–1805 (2016).
7. Mouser, V. H. M. *et al.* Bio-ink development for three-dimensional bioprinting of

- hetero-cellular cartilage constructs. *Connect. Tissue Res.* (in press).
8. Tatman, P. D. *et al.* Multiscale Biofabrication of Articular Cartilage: Bioinspired and Biomimetic Approaches. *Tissue Eng. Part B Rev.* **21**, 543–559 (2015).
 9. Daly, A. C. & Kelly, D. J. Biofabrication of spatially organised tissues by directing the growth of cellular spheroids within 3D printed polymeric microchambers. *Biomaterials* **197**, 194–206 (2019).
 10. Daly, A. C., Critchley, S. E., Rencsok, E. M., & Kelly, D. J. A comparison of different bioinks for 3D bioprinting of fibrocartilage and hyaline cartilage. *Biofabrication* **8**, 45002 (2016).
 11. Xu, T. *et al.* Hybrid printing of mechanically and biologically improved constructs for cartilage tissue engineering applications. *Biofabrication* **5**, 015001 (2013).
 12. Kundu, J., Shim, J.-H., Jang, J., Kim, S.-W. & Cho, D.-W. An additive manufacturing-based PCL–alginate–chondrocyte bioprinted scaffold for cartilage tissue engineering. *J Tissue Eng Regen Med* **9**, 1286–1297 (2015).
 13. Lee, J. S. *et al.* 3D printing of composite tissue with complex shape applied to ear regeneration. *Biofabrication* **6**, 024103 (2014).
 14. de Ruijter, M., Ribeiro, A., Dokter, I., Castilho, M. & Malda, J. Simultaneous Micropatterning of Fibrous Meshes and Bioinks for the Fabrication of Living Tissue Constructs. *Adv. Healthc. Mater.* **8**, 1800418 (2019).
 15. Pati, F. *et al.* Printing three-dimensional tissue analogues with decellularized extracellular matrix bioink. *Nat. Commun.* **5**, 3935 (2014).
 16. Kesti, M. *et al.* Bioprinting Complex Cartilaginous Structures with Clinically Compliant Biomaterials. *Adv. Funct. Mater.* **25**, 7406–7417 (2015).
 17. Groll, J. *et al.* A definition of bioinks and their distinction from biomaterial inks. *Biofabrication* **11**, 013001 (2019).

18. Ouyang, L., Highley, C. B., Rodell, C. B., Sun, W. & Burdick, J. A. 3D Printing of Shear-Thinning Hyaluronic Acid Hydrogels with Secondary Cross-Linking. *ACS Biomater. Sci. Eng.* **2**, 1743–1751 (2016).
19. Malda, J. *et al.* 25th anniversary article: Engineering hydrogels for biofabrication. *Advanced Materials* **25**, 5011–5028 (2013).
20. Murphy, W. L., McDevitt, T. C. & Engler, A. J. Materials as stem cell regulators. *Nat. Mater.* **13**, 547–557 (2014).
21. Xavier, J. R. *et al.* Bioactive nanoengineered hydrogels for bone tissue engineering: A growth-factor-free approach. *ACS Nano* **9**, 3109–3118 (2015).
22. Hong, S. *et al.* 3D Printing: 3D Printing of Highly Stretchable and Tough Hydrogels into Complex, Cellularized Structures. *Adv. Mater.* **27**, 4034 (2015).
23. Yang, F., Tadepalli, V. & Wiley, B. J. 3D Printing of a Double Network Hydrogel with a Compression Strength and Elastic Modulus Greater than those of Cartilage. *ACS Biomater. Sci. Eng.* **3**, 863–869 (2017).
24. Markstedt, K. *et al.* 3D bioprinting human chondrocytes with nanocellulose-alginate bioink for cartilage tissue engineering applications. *Biomacromolecules* **16**, 1489–1496 (2015).
25. Müller, M., Öztürk, E., Arlov, Ø., Gatenholm, P. & Zenobi-Wong, M. Alginate Sulfate–Nanocellulose Bioinks for Cartilage Bioprinting Applications. *Ann. Biomed. Eng.* **45**, 210–223 (2017).
26. Highley, C. B., Rodell, C. B. & Burdick, J. A. Direct 3D Printing of Shear-Thinning Hydrogels into Self-Healing Hydrogels. *Adv. Mater.* **27**, 5075–5079 (2015).
27. Hinton, T. J. *et al.* Three-dimensional printing of complex biological structures by freeform reversible embedding of suspended hydrogels. *Sci. Adv.* **1**, e1500758 (2015).

28. Sawyer, W. G. *et al.* Writing in the granular gel medium. *Sci. Adv.* **1**, e1500655 (2015).
29. Colosi, C. *et al.* Microfluidic Bioprinting of Heterogeneous 3D Tissue Constructs Using Low-Viscosity Bioink. *Adv. Mater.* **28**, 677-684 (2016).
30. Highley, C. B., Song, K. H., Daly, A. C. & Burdick, J. A. Jammed Microgel Inks for 3D Printing Applications. *Adv. Sci.* **6**, 1801076 (2019).
31. Ouyang, L., Highley, C. B., Sun, W. & Burdick, J. A. A Generalizable Strategy for the 3D Bioprinting of Hydrogels from Nonviscous Photo-crosslinkable Inks. *Adv. Mater.* **29**, 1604983 (2017).
32. Gramlich, W. M., Kim, I. L. & Burdick, J. A. Synthesis and orthogonal photopatterning of hyaluronic acid hydrogels with thiol-norbornene chemistry. *Biomaterials* **34**, 9803–9811 (2013).
33. Cramer, N. B., Davies, T., O'Brien, A. K. & Bowman, C. N. Mechanism and modeling of a thiol-ene photopolymerization. *Macromolecules* **36**, 4631–4636 (2003).
34. Chung, C. & Burdick, J. A. Influence of Three-Dimensional Hyaluronic Acid Microenvironments on Mesenchymal Stem Cell Chondrogenesis. *Tissue Eng. Part A* **15**, 243–254 (2008).
35. Erickson, I. E. *et al.* Macromer density influences mesenchymal stem cell chondrogenesis and maturation in photocrosslinked hyaluronic acid hydrogels. *Osteoarthr. Cartil.* **17**, 1639–1648 (2009).
36. Erickson, I. E. *et al.* High mesenchymal stem cell seeding densities in hyaluronic acid hydrogels produce engineered cartilage with native tissue properties. *Acta Biomater.* **8**, 3027–3034 (2012).
37. Chiou, B.-S. & Khan, S. A. Real-Time FTIR and in Situ Rheological Studies on the

- UV Curing Kinetics of Thiol-ene Polymers. *Macromolecules* **30**, 7322–7328 (1997).
38. Dubbin, K., Hori, Y., Lewis, K. K. & Heilshorn, S. C. 3D Bioprinting: Dual-Stage Crosslinking of a Gel-Phase Bioink Improves Cell Viability and Homogeneity for 3D Bioprinting. *Adv. Healthc. Mater.* **5**, 2568–2568 (2016).
 39. Mow, V. C., Holmes, M. H. & Michael Lai, W. Fluid transport and mechanical properties of articular cartilage: A review. *J. Biomech.* **17**, 377–394 (1984).
 40. Korhonen, R. K. *et al.* Comparison of the equilibrium response of articular cartilage in unconfined compression, confined compression and indentation. *J. Biomech.* **35**, 903–909 (2002).
 41. Mow, V. C., Kuei, S. C., Lai, W. M. & Armstrong, C. G. Biphasic creep and stress relaxation of articular cartilage in compression: Theory and experiments. *J. Biomech. Eng.* **102**, 73–84 (1980).
 42. Aguado, B. A., Grim, J. C., Rosales, A. M., Watson-Capps, J. J., & Anseth, K. S. Engineering precision biomaterials for personalized medicine. *Sci. Transl. Med.* **10**, eaam8645 (2018).
 43. Moroni, L. *et al.* Biofabrication strategies for 3D in vitro models and regenerative medicine. *Nat. Rev. Mater.* **3**, 21–37 (2018).
 44. Ruskowitz, E. R. & Deforest, C. A. Proteome-wide Analysis of Cellular Response to Ultraviolet Light for Biomaterial Synthesis and Modification. *ACS Biomater. Sci. Eng.* **5**, 2111–2116 (2019).
 45. Burdick, J. A., Mauck, R. L. & Gerecht, S. To Serve and Protect: Hydrogels to Improve Stem Cell-Based Therapies. *Cell Stem Cell* **18**, 13–15 (2016).
 46. Li, M., Tian, X., Zhu, N., Schreyer, D. J. & Chen, X. Modeling Process-Induced Cell Damage. *Tissue Eng. Part C Methods* **16**, 533–542 (2010).

47. Highley, C. B., Prestwich, G. D. & Burdick, J. A. Recent advances in hyaluronic acid hydrogels for biomedical applications. *Curr. Opin. Biotechnol.* **40**, 35–40 (2016).
48. Caliari, S. R. *et al.* Stiffening hydrogels for investigating the dynamics of hepatic stellate cell mechanotransduction during myofibroblast activation. *Sci. Rep.* **6**, 21387 (2016).
49. Vega, S. L. *et al.* Combinatorial hydrogels with biochemical gradients for screening 3D cellular microenvironments. *Nat. Commun.* **9**, 614 (2018).
50. Chung, C. *et al.* The influence of degradation characteristics of hyaluronic acid hydrogels on in vitro neocartilage formation by mesenchymal stem cells. *Biomaterials.* **30**, 4287–4296 (2009).
51. Roberts, J. *et al.*, Degradation Improves Tissue Formation in (Un)Loaded Chondrocyte-laden Hydrogels, *Clin. Orthop. Relat. Res.*, **469**, 2725–2734 (2011).
52. Mouser, V. H. M. *et al.* Ex vivo model unravelling cell distribution effect in hydrogels for cartilage repair. *Altex* **35**, 65–76 (2018).
53. Sharma, B. *et al.* Human cartilage repair with a photoreactive adhesive-hydrogel composite. *Sci. Transl. Med.* **5**, 167ra6 (2013).
54. Lin, C. C. Recent advances in crosslinking chemistry of biomimetic poly(ethylene glycol) hydrogels. *RSC Adv.* **5**, 39844–39853 (2015).
55. Kwon, M. Y. *et al.* Dose and Timing of N-Cadherin Mimetic Peptides Regulate MSC Chondrogenesis within Hydrogels. *Adv. Healthc. Mater.* **7**, 1701199 (2018).
56. Kim, M., Erickson, I. E., Choudhury, M., Pleshko, N. & Mauck, R. L. Transient exposure to TGF- β 3 improves the functional chondrogenesis of MSC-laden hyaluronic acid hydrogels. *J. Mech. Behav. Biomed. Mater.* **11**, 92–101 (2012).

CHAPTER 5: FABRICATION OF MSC-LADEN COMPOSITES OF HYALURONIC ACID HYDROGELS REINFORCED WITH MEW SCAFFOLDS FOR CARTILAGE REPAIR

The following chapter is adapted from:

Galarraga, J.H., Locke, R.C., Witherel, C.W., Stoeckl, B.D., Castilho, M., Mauck, R.L., Malda, J., Levato, R., Burdick, J.A., Fabrication of MSC-laden composites of hyaluronic acid hydrogels reinforced with MEW scaffolds for cartilage repair. *Biofabrication* 14, 014106 (2021).

5.1 INTRODUCTION

Articular cartilage damage is a pervasive problem that significantly inhibits quality of life and joint mobility in afflicted patients ¹. Focal defects on the articulating surface of joints may form in patients due to trauma, sports injuries, or daily activities associated with joint function ². Native cartilage unfortunately does not possess significant regenerative capacity ³, and these defects may further progress if left untreated, resulting in significant pain and dysfunction ⁴. To this end, a number of clinical approaches have been developed for cartilage defect repair, including microfracture, mosaicplasty, and matrix-assisted chondrocyte implantation (MACI) ⁵. However, despite their promise, these surgical procedures often result in repair cartilage with inferior composition and mechanical properties when compared to healthy hyaline cartilage ^{1,6,7}. Thus, there is a continued and significant clinical need for the development of new approaches that support the restoration of functional cartilage.

Hydrogels have emerged as a promising approach for the encapsulation of cells that then synthesize and organize nascent cartilagenous extracellular matrix. A range of materials have been used for the formation of neocartilage from cell-laden hydrogels ⁸, and advancements in both hydrogel processing and our ability to incorporate physiochemical cues within hydrogels (e.g., patterning of signaling ligands, controlled

release of biochemical signals) have improved the quality of engineered cartilage *in vitro*⁹. Towards translating these hydrogels into the clinic, biofabrication approaches have enabled the fabrication of cell-laden hydrogels with patient-specific geometries and high porosity. For instance, the biopen is a handheld device that permits extrusion of bioinks into focal cartilage defects intraoperatively, such that cartilage repair can occur *in situ* within defects^{10,11}. Other extrusion-based bioprinting techniques have facilitated the expansion of candidate bioinks for cartilage tissue engineering¹², while lithographic and new tomographic bioprinting approaches have drastically improved the resolution and throughput with which cell-laden implants can be engineered^{13,14}. Despite these recent advances in bioprinting, one of the persistent challenges associated with engineering hydrogels for cartilage tissue engineering is the balance of two, opposing design criteria. Specifically, hydrogels with large mesh sizes are promising candidates given their ability to maintain cell viability and to promote the distribution of deposited matrix, but these hydrogels have much lower initial mechanical properties^{15,16}.

Hydrogels with tunable degradability have been engineered to address this challenge, such that higher initial mechanical properties can be achieved while cell-mediated enzymatic degradation ensures that the mesh size increases over time, permitting matrix distribution and cartilage maturation¹⁷. Similarly, hydrolytically degradable polyethylene glycol (PEG) and hyaluronic acid (HA) hydrogels were designed to improve matrix production and distribution by encapsulated chondrocytes and mesenchymal stromal cells (MSCs), respectively, when compared to non-degradable hydrogel controls^{18,19}. However, these approaches are generally still limited with regards to initial hydrogel mechanics due to cell viability concerns and they also require that the rate of hydrogel degradation be carefully balanced with the rate of tissue formation and maturation to maintain mechanical properties²⁰.

Alternatively, a range of strategies have been employed to enhance the mechanical properties of hydrogels for cartilage repair. Interpenetrating network (IPN) hydrogels, which are composed of multiple interdigitating networks, are one approach to engineering hydrogels with high toughness. By tuning the properties of combined brittle and ductile networks at the molecular scale, non-additive increases in hydrogel moduli can be achieved²¹. As an alternative, extruded polycaprolactone (PCL) may be incorporated within 3D printed hydrogels (e.g., fibrin-collagen, alginate, agarose, PEG) containing encapsulated chondrocytes or MSCs for cartilage formation^{22–26}. PCL is a well-established biomaterial with extended degradation profiles and significantly higher moduli than traditional hydrogels, such that its combination with hydrogels results in improved mechanical integrity. To this end, electrospun nanofibrous PCL scaffolds have also been incorporated into bioprinted hydrogels to improve both the shape fidelity and mechanical properties of fabricated construct.²⁷ In another approach, IPNs composed of alginate and methacryloyl-modified gelatin (GelMA) were reinforced with 3D printed PCL templates towards recapitulating the tension-compression non-linearity of native cartilage.^{28,29} A multi-head printing setup enabled fabrication of these composites with encapsulated MSCs and chondrocytes toward the formation of hyaline cartilage.²⁸ However, while IPNs or composite scaffolds containing PCL may improve the mechanical properties of cell-laden hydrogels, these approaches can also reduce the relative volume available for the formation of new tissue by embedded cells.³⁰

In response to this design limitation, reinforcement of printed gelatin-methacryloyl (GelMA) hydrogels with PCL microfibers has been achieved via melt-electrowriting (MEW).^{31,32} MEW is a biofabrication process that allows for the controlled deposition of electrically charged polymer melt fibers in a layer-by-layer manne.³³ Similar to conventional electrospinning, a voltage source is applied to a polymer to extract the

material from a spinneret onto a collector. However, unlike electrospinning, where large distances between the spinneret and collector typically lead to whipping instabilities and unpredictable flow behaviors, MEW permits control over a stable polymer jet. The high viscosity of the polymer melt, along with a reduced spinneret-to-collector distance and the applied voltage source helps to stabilize the flow of polymer melt so that it may be predictably and directly written onto a computer-controlled collector. After controlled deposition, the rapid cooling of the polymer melt gives rise to a stable, fiber structure. Thus, the advantage of MEW over electrospinning is its ability to finely control the organization of polymer melt fibers to fabricate user-defined geometries. Moreover, highly porous, microfiber meshes can be printed via MEW at even submicron resolutions that are not possible via traditional extrusion 3D printing.³⁴

Hyaluronic acid (HA)-based hydrogels are a specific class of hydrogels that have been shown to support the chondrogenesis of MSCs and chondrocytes, but exhibit the aforementioned limitations with significantly inferior mechanical properties when compared to native cartilage.³⁵ In consideration of advances in the biofabrication field, the overall aim of this study was to introduce MEW reinforcement into engineered HA hydrogels to meet desired design criteria for cartilage repair. To do this, we first screened formulations of norbornene-modified HA (NorHA) across varied crosslinking densities to identify a hydrogel formulation that would be most permissive to the formation of neocartilage. Next, MEW meshes were introduced into NorHA hydrogels to increase the initial mechanical properties and stability of these soft hydrogels.³¹ Last, composites of NorHA and MEW meshes were assessed for their integration potential with native cartilage rings. Acellular composites, cell-laden composites, and pre-cultured cell-laden composites were press-fit into cartilage rings, and their integration within rings was compared to autologous cartilage controls. These studies collectively demonstrate that

NorHA-MEW composites maximize the chondrogenesis of encapsulated MSCs while increasing the mechanical properties of hydrogels, both initially and over extended culture periods, suggesting that composites may improve *in vivo* integration and cartilage formation in future studies.

5.2 METHODS

5.2.1 Materials

Sodium HA was purchased from Lifecore Biomedical (Chaska, MN) and lithium phenyl-2,4,6-trimethylbenzoylphosphinate (LAP) was purchased from Colorado Photopolymer Solutions (Boulder, CO). Unless otherwise specified, all other reagents and materials were purchased from Sigma-Aldrich (St. Louis, MO).

5.2.2 Hydrogel Fabrication and Characterization

5.2.2.1 NorHA Synthesis

NorHA was synthesized as previously reported.³⁶ Briefly, sodium HA was first converted into its tetrabutylammonium salt form (HA-TBA) and then modified with norbornene functional groups via benzotriazole-1-yl-oxy-tris-(dimethylamino)-phosphonium hexafluorophosphate (BOP) coupling. After dissolving sodium HA in distilled water, Dowex 50Wx200 resin was added to the solution in a 3:1 mass ratio. The solution was then mixed for 30 minutes, and Dowex resin was subsequently removed via vacuum filtration. Thereafter, the filtrate was titrated with tetrabutylammonium hydroxide solution to a pH of 7.02–7.05, frozen, and lyophilized. The resulting lyophilized HA-TBA and 5-norbornene-2-methylamine were then dissolved in anhydrous dimethyl sulfoxide (DMSO) under inert nitrogen. BOP was then added to the reaction solution via cannulation and the reaction proceeded for 2 hours at room temperature. The reaction was quenched with the

addition of cold distilled water and subsequently dialyzed for 5 days. Any precipitates within the crude product solution were then removed via filtration and the solution was dialyzed for an additional 3-5 days. After freezing and lyophilizing the synthesized NorHA, the extent of norbornene modification was determined via $^1\text{H-NMR}$ to be $\sim 22\%$ of the disaccharide repeat units of HA (**Figure 5.1**).

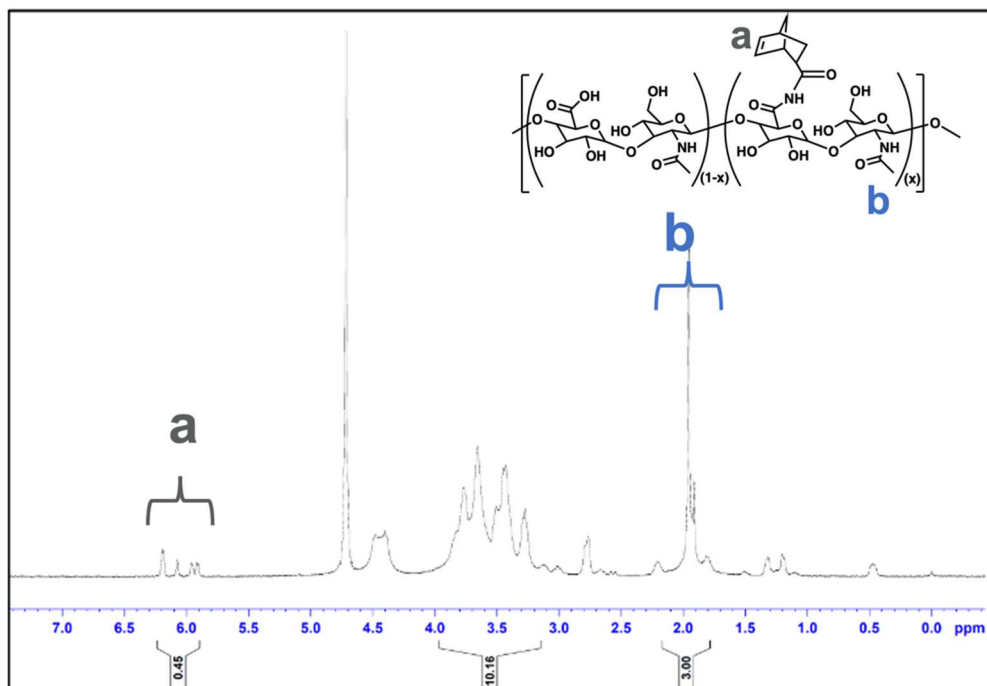


Figure 5.1: $^1\text{H-NMR}$ spectra of synthesized NorHA. To characterize the degree of norbornene modification on the backbone of HA, the vinyl protons of norbornene (2H, $\delta \sim 5.8$ -6.3 ppm) were integrated and compared to the integration value of the methyl group of HA (3H, $\delta \sim 1.8$ -2.0 ppm). $\sim 22\%$ of the disaccharide repeat units of HA were modified with norbornene groups.

5.2.2.2 Hydrogel Fabrication

Lyophilized NorHA macromer was dissolved in phosphate buffered saline (PBS) and LAP photoinitiator was added to a final concentration of 0.05%. DL-dithiothreitol (DTT) was subsequently added at concentrations of 0.54 mM, 2.17 mM, 5.71 mM, or 13.58 mM (to obtain compressive moduli of approximately 2, 6, 20, and 60 kPa, respectively). After

all precursor materials were thoroughly mixed, hydrogels were cast into molds (diameter ~4.8 mm) and irradiated with blue light (400-500 nm, Omnicure lamp with an affixed collimator, $I=10 \text{ mW/cm}^2$) for 5 minutes.

5.2.2.3 Compression Testing

To evaluate the compressive properties of hydrogels, samples were subjected to unconfined, uniaxial compressive testing with a constant loading rate of 0.2 N/min (Q800 DMA, TA Instruments). The compressive modulus was then quantified as the slope of the stress-strain curves between 10-20% strain.

5.2.3 Cell Culture and Characterization of MSC-Laden Constructs

5.2.3.1 Cell/tissue Isolation and Culture

Juvenile bovine knee joints were obtained (Research 87, Boylston, MA) and dissected under sterile conditions as previously described.¹⁶ Femoral bone marrow was extracted and MSCs were isolated via plastic adherence during culture in Dulbecco's modified eagle medium (DMEM) supplemented with 10% fetal bovine serum (FBS) and 1% penicillin/streptomycin (P/S). After expansion, MSCs were washed, trypsinized (0.05%), centrifuged, and resuspended in PBS for use. NorHA macromer solution with sterile filtered LAP and DTT was prepared as described above prior to the suspension and encapsulation of MSCs (P1, 20×10^6 cells/mL) with blue light exposure. Constructs were subsequently cultured in chondrogenic media (1% ITS+; 2.50 $\mu\text{g/mL}$ amphotericin B; 1×10^{-3} M sodium pyruvate; 50 $\mu\text{g/mL}$ ascorbic acid 2-phosphate; 40 $\mu\text{g/mL}$ L-proline; 1×10^{-7} M dexamethasone; 10 ng/mL TGF-B3) for up to 56 days.

5.2.3.2 Cell Viability

To evaluate the cytocompatibility of constructs, hydrogels were stained with calcein AM and ethidium homodimer (0, 3, 7 days) in accordance with manufacturer's instructions (Invitrogen). Cell viability was quantified via analysis of confocal images (Leica SP5) using Image J software. Viability was calculated as the number of live cells per total cells within an image ($n \geq 3$ hydrogels, 9 images per sample).

5.2.3.3 *Gene Expression Analysis and Biochemical Assays*

Each sample was immediately placed in 1 mL ice-cold TRIzol (Invitrogen) and stored at -80°C for later RNA isolation. Pre-processing of samples was performed by first homogenizing samples in TRIzol on ice, subsequently adding 0.2 mL of chloroform, vigorously shaking by hand for 15 seconds, and centrifuging for 15 minutes at 4°C . RNA was then isolated by collecting and mixing the aqueous layer with equal-parts 70% ethanol via pipetting and proceeding with the RNeasy Mini kit (QIAGEN) per manufacturer's instructions; isolated RNA concentrations were then quantified (NanoDrop 1000). RNA was processed with DNase to remove any DNA impurities and then reverse-transcribed into cDNA using the High Capacity cDNA Reverse Transcription kit (Applied Biosystems). qRT-PCR reactions were performed with 10ng cDNA and Taqman probes (Life Technologies, **Table 5.1**); type I collagen (Col1a1), type II collagen (Col2a1), aggrecan (ACAN), and SOX9 were selected as targets, with glyceraldehyde 3-phosphate dehydrogenase (GAPDH) used as a housekeeping gene. Relative gene expression of experimental samples was determined using the $\Delta\Delta\text{CT}$ method and MSCs expanded on tissue culture plastic as the control.³⁷

Table 5.1: qRT-PCR bovine Taqman primers.

Gene	Assay ID
GAPDH	Bt03210913_g1
COL1A1	Bt03225322_m1
COL2A1	Bt03251861_m1
ACAN	Bt03212186_m1
SOX9	Bt07108872_m1

To quantify the biochemical content of cell-laden constructs, samples were minced and digested via overnight incubation at 60°C in solution containing papain and hyaluronidase (0.56 U/mL papain and 750-3000 U/mL hyaluronidase were dissolved in buffer containing 0.1 M sodium acetate, 10 M cysteine hydrochloric acid, and 0.05 M ethylenediaminetetraacetic acid). The dimethylmethylene blue assay was utilized to quantify the sulfated glycosaminoglycan (sGAG) content, the hydroxyproline (OHP) assay was performed to determine collagen content (Abcam Hydroxyproline Assay Kit, ab222941), and the Picogreen dsDNA assay was performed to measure total DNA content within cultured constructs.³⁸

5.2.3.4 Histology and Immunohistochemistry

After culture, constructs were fixed in 10% formalin for two hours at room temperature and then washed in PBS. Samples were then dehydrated, embedded in paraffin, and sectioned (5 µm) prior to staining. Sulfated glycosaminoglycan (sGAG) deposition by embedded cells was visualized via Alcian blue staining (1%, pH 1.0, Newcomer Supply), while deposition of type I and type II collagen were visualized via

labeling with anti-collagen type I (COL I, mouse monoclonal anti-collagen type 1, Millipore Sigma) and anti-collagen type II (COL II, mouse monoclonal anti-collagen type II, Developmental Studies Hybridoma Bank) antibodies and staining with DAB chromogen (Millipore Sigma). To quantify staining intensity, acquired images were converted to 8-bit and then inverted.³⁹ For each sample section, the mean intensities for three separate and randomly selected frames were measured in Image J.

5.2.4 Composite fabrication and characterization

5.2.4.1 MEW of PCL Meshes

Box-structured meshes (4 x 4 cm²) composed of polycaprolactone (Purasorb PC 12, Corbion Inc., Gorinchem, Netherlands) were fabricated with 70 layers (1 mm height) of overlaying fibers (layered in orthogonal directions) as previously described.⁴⁰ A custom-built MEW device equipped with an electrical heating system (TR 400, HKEtec, Germany; heating temperature = 90 °C) was used to feed PCL polymer melt (feed pressure = 3 bar) through a 23G spinneret charged by a high voltage power supply (LNC 10000–5 pos, Heinzinger Electronic GmbH, Rosenheim, Germany). Processed PCL fibers were then collected on a computer-controlled collector plate (acceleration voltage=5.5 kV, spinning gap= 3.3 mm, E = 1.3 kV/mm). Each mesh was fabricated with a 90° lay-down pattern and the spacing between deposited fibers was 200µm, 400 µm or 800 µm. Disc-shaped mesh constructs were obtained from printed MEW meshes using a 4 mm biopsy punch.

5.2.4.2 Composite Fabrication

To create composites combining NorHA hydrogels and PCL meshes, lyophilized NorHA macromer and meshes (4 mm diameter, 1 mm height) were first sterilized via irradiation with a germicidal lamp in a laminar flow hood. Thereafter, NorHA (matching the formulation for 2 kPa hydrogels from above) was dissolved in PBS along with sterile filtered LAP and DTT. Juvenile bovine MSCs were then trypsinized (0.05%), counted, and suspended in the macromer solution (P1, 20×10^6 cells/mL). This solution was then carefully pipetted on top of MEW meshes and allowed to fill into the interstitial spaces of the box-structured scaffolds.⁴¹ Meshes were then flipped, so that additional macromer could be pipetted on the other side. Finally, macromer was crosslinked within the meshes via photocrosslinking with visible light irradiation as described above.

Cells and meshes within composites were visualized using CellTracker Red (Invitrogen) and fluorescein isothiocyanate-bovine serum albumin (FITC-BSA), respectively, and were imaged via confocal microscopy. The density of cells within the top 100 μm and bottom 100 μm of composites was calculated by counting the total number of cells within randomly placed $600 \times 600 \mu\text{m}^2$ image frames ($n \geq 3$ hydrogels, 9 images per group). Composites were cultured in chondrogenic media for up to 56 days and characterized for cell viability, gene expression, biochemical content, histology/immunohistochemistry, and biomechanics as described above and compared to hydrogels alone.

5.2.5 Assessment of ex vivo integration capacity

5.2.5.1 Fabrication of press-fit constructs in cartilage ring explants

Juvenile bovine joints were dissected in a similar fashion as previously described and osteochondral plugs were biopsied from the trochlear groove to obtain cartilage explants for *ex vivo* integration studies. After conditioning osteochondral plugs in serum-free expansion media for 1-2 days (DMEM; 1% P/S; 10mM HEPES, 0.1 mM non-essential amino acids; 2.50 µg/mL amphotericin B; 1×10^{-3} M sodium pyruvate; 50 µg/mL ascorbic acid 2-phosphate; 40 µg/mL L-proline),⁴² cartilage rings were isolated and prepared (8 mm outer diameter, 4 mm inner diameter, 1 mm thickness) such that acellular composites, cell-laden composites (i.e., composites immediately after MSC encapsulation), or cell-laden composites that were pre-cultured for 28 days in chondrogenic media (cell-laden+PC) could be press-fit into the inner cores of cartilage rings. As a control, biopsied autologous cartilage was press-fit back into the inner cores of rings. Each of these four different press-fit constructs (i.e., autologous cartilage control, acellular, cell-laden, cell-laden+PC) were then cultured within cartilage rings in chondrogenic media for 28 days.

5.2.5.2 Push-Out Testing

The integration strength (i.e., failure stress) of press-fit constructs cultured within explanted cartilage rings was determined via push-out testing as previously described.⁴³ Briefly, an indenter (3.8 mm) was affixed to an Instron 5848 testing device and used to push out the central core of the cartilage constructs (0.2 mm/s). The failure stress was calculated by dividing the load at failure by the lateral surface area of press-fit constructs (i.e., interfacial area).

5.2.5.3 *MicroCT and Interfacial Contact Area*

The integration strength (i.e., failure stress) of press-fit constructs cultured within explanted cartilage rings was determined via push-out testing as previously described³³. Briefly, an indenter (3.8 mm) was affixed to an Instron 5848 testing device and used to push out the central core of the cartilage constructs (0.2 mm/s). The failure stress was calculated by dividing the load at failure by the lateral surface area of press-fit constructs (i.e., interfacial area).

5.2.6 **Statistical Analysis**

All statistical analyses were performed using GraphPad Prism 9 software, data are reported as mean \pm standard deviation, and significance for all performed analyses was determined at $p < 0.05$. Two-way ANOVAs were performed with construct formulation and culture time set as independent variables, and multiple comparisons were performed with $\alpha = 0.05$ and Tukey's honestly significant difference (HSD) post-hoc test. Comparisons between just two groups were made via student t-tests with two-tailed criteria. For comparisons between more than two groups, one-way ANOVAs were performed, with Tukey's HSD post-hoc test; Kruskal–Wallis tests were performed for non-parametric comparisons (normality assessed via Shapiro-Wilk test, $\alpha = 0.05$), with multiple comparisons performed via Dunn's multiple comparison test.

5.3 **RESULTS AND DISCUSSION**

5.3.1 **Influence of Crosslink Density on Cartilage Formation in NorHA Hydrogels**

When designing hydrogels for cartilage tissue engineering, consideration must be given to the choice of material used as well as the crosslinking chemistry selected. Here

we chose HA, due to its native presence in cartilage and roles in development, wound healing, and natural extracellular matrix (ECM) organization and maintenance.⁴⁴ HA possesses innate bioactivity, can be readily degraded by hyaluronidases and oxidative species, and can be easily modified with pendant functional groups for crosslinking, all of which supports its use in tissue engineering applications.⁴⁵ In this work, we modified HA with norbornene groups for crosslinking via thiol-ene photocrosslinking (**Figure 5.2a**), which enables the crosslink density to be easily modulated by the crosslinker concentration used during the step-growth crosslinking reaction.⁴⁶

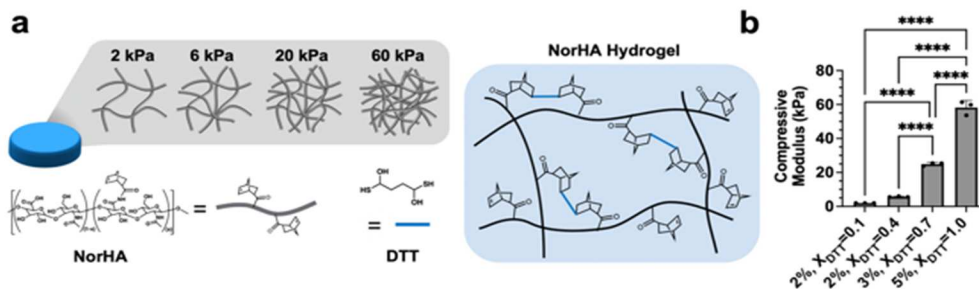


Figure 5.2: NorHA hydrogels with varied crosslink densities. (a) Hyaluronic acid modified with norbornene (NorHA) groups undergoes thiol-ene crosslinking in the presence of a dithiol crosslinker (DL-dithiothreitol, DTT), LAP photoinitiator, and visible light. (b) The crosslink density and compressive moduli of NorHA hydrogels are tuned (i.e., 2-60 kPa) via the polymer concentration (w/v%) and the extent of macromer crosslinking (thiol-to-norbornene ratio: X_{DTT}). ****p<0.0001, n=3.

Although other modifications are possible (e.g., methacrylation or MeHA), it is challenging to modify crosslinking due to the uncontrolled radical polymerization used for gelation.¹⁶ Further, the use of NorHA not only allows for more modular control of hydrogel crosslinking, but also enables photopatterning with signaling ligands (i.e., peptides) of interest.³⁶

By changing both the macromer concentration and crosslinker concentration, NorHA hydrogels ranging from ~2 to 60 kPa (**Figure 5.2b**) were fabricated and are hereafter referred to by their approximate initial compressive moduli (i.e., 2 kPa, 6 kPa,

20 kPa, 60 kPa). Since the crosslink density of hydrogels has been previously shown to influence both encapsulated cell viability and matrix distribution by encapsulated cells,¹⁵ we first aimed to identify which hydrogel formulation best supported the viability and chondrogenesis of encapsulated MSCs. While softer, more loosely crosslinked hydrogels (i.e., 2 kPa, 6 kPa) exhibited high cell viability after 7 days of culture (~90%), more densely crosslinked hydrogels (i.e., 20 kPa, 60 kPa) resulted in significant loss in cell viability over time (**Figure 5.3**).

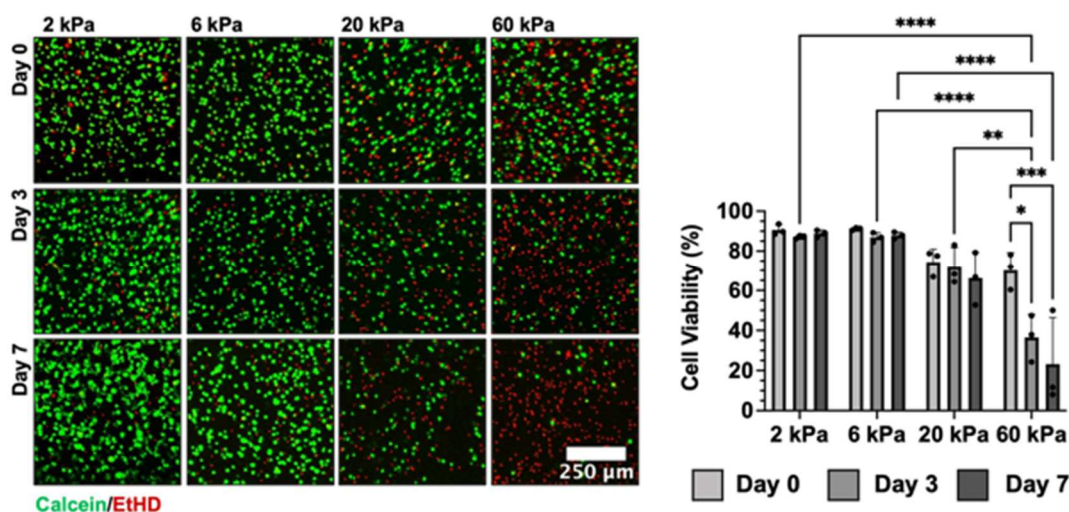


Figure 5.3: Viability of NorHA hydrogels with varied crosslink densities. Representative images (day 0, 3, and 7) and quantification of encapsulated MSC viability in NorHA hydrogels, where live cells (green) and dead cells (red) are stained with calcein AM and ethidium homodimer, respectively. * $p < 0.01$, ** $p < 0.005$, *** $p < 0.001$, **** $p < 0.0001$, $n = 3$.

Past fluorescent recovery after photobleaching (FRAP) studies in NorHA hydrogels suggest that the relative diffusivity of macromolecules within these networks decreases with increasing crosslink density, which may explain the observed differences in cell viability in these hydrogels.⁴⁷

To assess the ability of these hydrogel formulations to support MSC chondrogenesis and cartilage formation, cell-laden hydrogels were cultured for up to 56 days in chondrogenic media and characterized for gene expression, mechanical

properties, and biochemical content. All hydrogels exhibited increased expression of aggrecan and type II collagen over time, both of which are hallmark ECM components of hyaline cartilage and suggest that embedded MSCs underwent chondrogenesis (**Figure 5.4a**). Generally, expression of each of these genes increased the most within the first week of culture. Importantly, encapsulated MSCs also expressed SOX9, a marker of chondrogenesis,⁴⁸ at early culture times, and type I collagen expression was low and decreased over culture time for 2 kPa hydrogels (**Figure 5.5**).

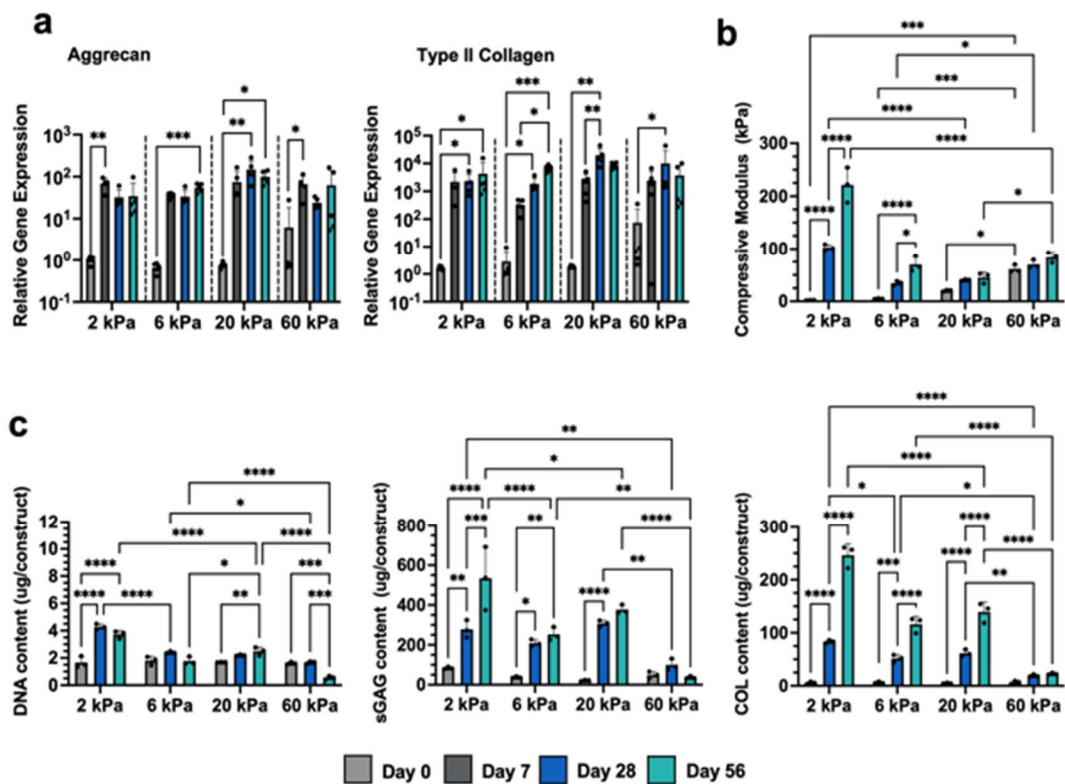


Figure 5.4: Influence of NorHA crosslink density on MSC chondrogenesis and neocartilage formation. Mesenchymal stromal cell (MSC)-laden hydrogels are cultured in chondrogenic media for up to 56 days and assessed for (a) chondrogenic gene expression (Aggrecan, Type II Collagen), (b) compressive moduli, and (c) biochemical content (DNA, sulfated glycosaminoglycan (sGAG), and collagen (COL)) after 0 (light gray), 7 (dark gray), 28 (blue), and 56 (teal) days of culture in chondrogenic media. * $p < 0.05$, ** $p < 0.01$, *** $p < 0.001$, **** $p < 0.0001$, $n \geq 3$, individual one-way ANOVAs (20 kPa) or Kruskal–Wallis tests (2,6,60 kPa) performed for each hydrogel formulation for qRT-PCR data.

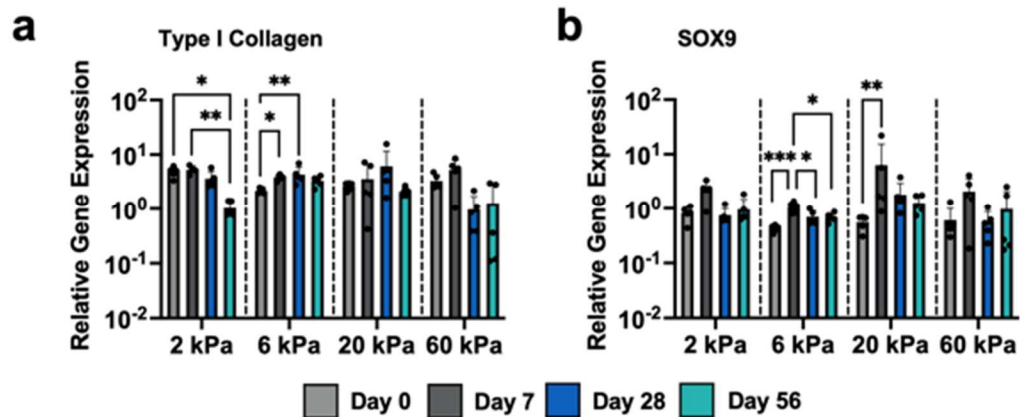


Figure 5.5: Influence of NorHA crosslink density on MSC gene expression. Relative gene expression of (a) type I collagen (COL1A1) and (b) SOX9 in NorHA hydrogels of varied moduli when cultured in chondrogenic media for up to 56 days. * $p < 0.05$, ** $p < 0.01$, *** $p < 0.001$, $n \geq 4$, with individual one-way ANOVAs or Kruskal–Wallis tests performed for each hydrogel formulation.

The appearance of each hydrogel formulation noticeably changed over 56 days of culture. While more loosely crosslinked hydrogels turned opaque, suggesting the elaboration of neotissue by embedded cells, 60 kPa hydrogels remained relatively translucent (**Figure 5.6**).

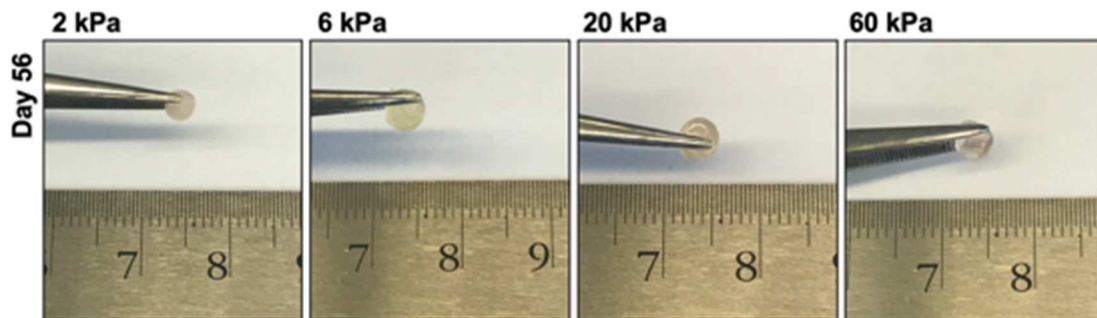


Figure 5.6: Representative gross images of MSC-laden NorHA hydrogels. After 56 days of culture in chondrogenic media, more loosely crosslinked hydrogels exhibited an opacity resembling neocartilage, while more densely crosslinked hydrogels (i.e., 60 kPa) remained translucent after culture.

All hydrogels also increased in compressive modulus with culture, although to varying extents based on initial crosslinking density (**Figure 5.4b**). 2 kPa NorHA hydrogels resulted in the formation of cartilage with the highest compressive properties, reaching a compressive modulus of 102.6 ± 5.4 kPa after 28 days and 221.4 ± 33.0 kPa after 56 days. No other group reached values higher than 100 kPa, even after 56 days of culture, and the 60 kPa NorHA hydrogels barely increased in modulus with culture. These observed differences in compressive moduli were supported by the relative differences in biochemical content across each hydrogel formulation (**Figure 5.4c**). 2 kPa hydrogels resulted in significant increases in DNA content with culture, likely due to some degree of cell proliferation, whereas the DNA content within 6 kPa hydrogels and higher were much more modest and did not significantly change throughout the duration of culture. 60 kPa hydrogels exhibited decreasing DNA content over time consistent with the observed reduction in cell viability (**Figure 5.3**). With regards to biochemical content, 2 kPa hydrogels exhibited the largest increases in sulfated glycosaminoglycan (sGAG) and collagen (COL) contents with culture. 6 kPa and 20 kPa hydrogels similarly showed significant increases in both sGAG and COL content over the course of 56 days of culture, albeit with lower total amounts produced when compared to the 2 kPa group. Minimal changes in sGAG or COL content were observed with the 60 kPa formulation.

These results indicate that softer NorHA hydrogels result in neocartilage with improved functional properties, and so we next aimed to elucidate the organization of nascent matrix within these hydrogels via histology for sGAG and immunohistochemistry for type I and type II collagen (**Figures 5.7-5.9**). Alcian blue staining for sGAG revealed that 2 kPa hydrogels support increased sGAG deposition and dispersion, as indicated by significant increases in staining intensity between 28 and 56 days of culture (**Figure 5.7**). Moreover, 2 kPa hydrogels stained much more intensely and uniformly than the other

investigated formulations, particularly at day 56. These results are consistent with past observations in MeHA hydrogels¹⁶ and recent studies that demonstrated that the extent of nascent matrix dispersion decreases with increasing NorHA crosslink density.⁴⁷

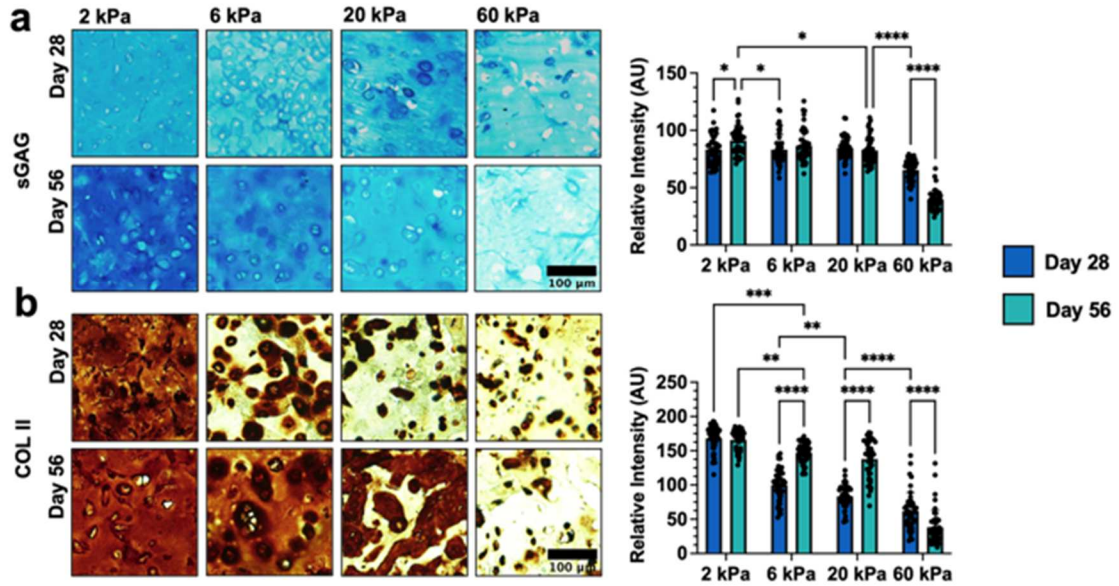


Figure 5.7: Influence of NorHA crosslink density on matrix production and distribution. Representative images and quantification of matrix distribution within NorHA hydrogels after 28 and 56 days of culture for (a) sulfated glycosaminoglycans (sGAG) via Alcian blue staining or (b) type II collagen (COLII) via immunohistochemistry. * $p < 0.05$, ** $p < 0.01$, *** $p < 0.001$, **** $p < 0.0001$, $n = 45$ images, 5 sections, 3 constructs.

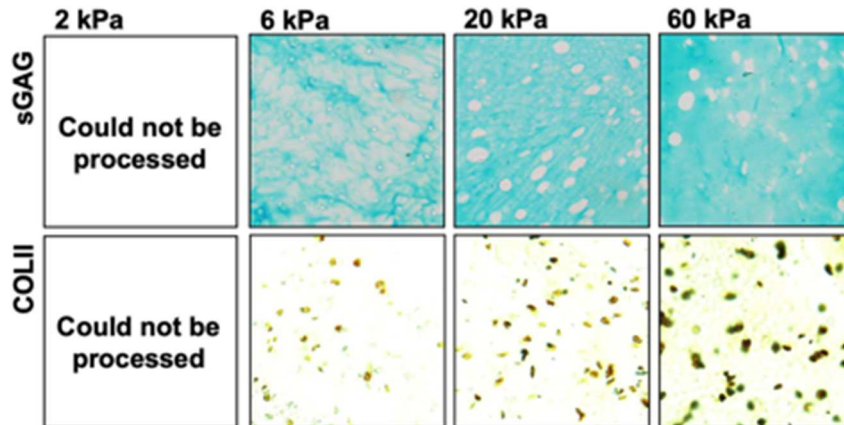


Figure 5.8: Alcian Blue and Collagen Immunohistochemistry. Representative images of Alcian blue staining and type II collagen immunohistochemistry for NorHA hydrogels at day 0 with varied crosslink densities.

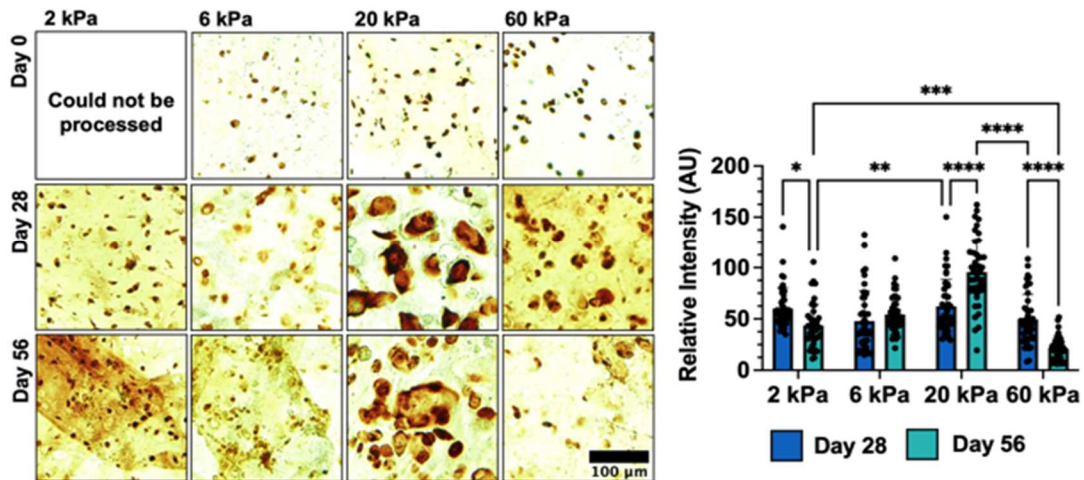


Figure 5.9: Influence of NorHA crosslink density on type I collagen elaboration and distribution. Representative images (days 0, 28, and 56) and quantification of type I collagen (COLI) distribution within NorHA hydrogels via type I collagen immunohistochemistry. * $p < 0.05$, ** $p < 0.01$, *** $p < 0.001$, **** $p < 0.0001$, $n = 45$ images, 5 sections, 3 constructs.

These observed differences can be attributed to the hydrogel network being more permissive to matrix dispersion due to its increased mesh size,⁴⁹ as well as the increased cell viability in less crosslinked formulations. Similar trends were observed for type II collagen staining, as 2 kPa hydrogels exhibited type II collagen that extended

beyond the pericellular space of embedded cells and that was more homogenous (**Figure 5.7b**). In contrast, dark staining localized around cells was observed in 6 kPa hydrogels after 56 days of culture, and both 20 kPa and 60 kPa hydrogels exhibited minimal type II collagen staining. Importantly, all hydrogels resulted in minimal type I collagen deposition over culture time, suggesting that hyaline-like cartilage formed within hydrogels as opposed to fibrocartilage, which is composed of more type I collagen (**Figure 5.9**). Taken together, these results indicate that 2 kPa NorHA hydrogels support the formation of neocartilage *in vitro*, likely due to an increased mesh size that allows for increased matrix distribution and increased viability. The greater than 100-fold increase in compressive modulus achieved in these hydrogels over the culture period is particularly promising; however, the application of these soft hydrogels for tissue engineering is still limited by their initial mechanical properties, especially in terms of handling and stability

5.3.2 Reinforcement of NorHA Hydrogels with MEW Meshes

To address the limitations of soft hydrogels, we reinforced the hydrogels with a secondary, microfiber mesh. Since MEW meshes can be readily incorporated within hydrogels to increase their compressive properties,^{31,50} we first demonstrated that composites composed of NorHA hydrogels and polycaprolactone (PCL) box-structured meshes could be formed by curing NorHA macromer within the interstitial spaces of MEW meshes (**Figure 5.10a**). The spacing between overlaying fibers within meshes was readily tuned between 200 μm and 800 μm to change the overall fiber density and porosity of the mesh (**Figure 5.10b**). Interestingly, combinations of NorHA hydrogel with PCL meshes led to synergistic increases in compressive moduli, including an ~ 50 -fold increase from the initial hydrogel modulus. The increase in mechanics is attributed to the ability of the hydrogel to mitigate MEW fiber buckling, which effectively increases the load-carrying

capacity of MEW meshes since the PCL fibers can resist deformation in the transverse direction when loaded in compression.⁴⁰ Similarly, the presence of PCL fibers surrounding the NorHA hydrogel decreases the rate of water efflux from the hydrogel (i.e., syneresis) upon loading, further increasing the mechanical properties of the entire composite. The observed increases in compressive moduli are also consistent with similar composite systems that have leveraged MEW meshes to reinforce alternative hydrogels (i.e., gelatin, alginate, PEG, fibrin).^{31,51,52}

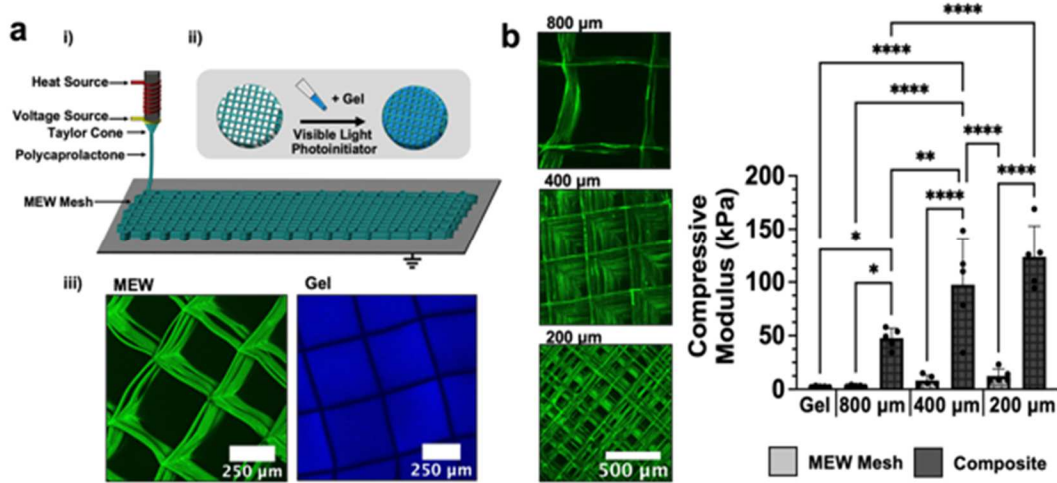


Figure 5.10: PCL meshes reinforce NorHA hydrogels. (a) (i) Schematic of the melt-electrowriting process (MEW) employed to fabricate fibrous PCL meshes. PCL is heated to form a polymer melt that can be readily extruded through a printhead with an attached voltage source to deposit PCL onto a grounded print bed. (ii) PCL meshes are then filled with NorHA macromer/crosslinker precursor and exposed to visible light in the presence of a photoinitiator to form composites. (iii) Images of composites containing PCL MEW meshes (green) and NorHA hydrogel (blue). (b) Representative images of MEW meshes of varied interfiber spacing (800 μm, 400 μm, 200 μm). Compressive moduli of NorHA hydrogel alone, PCL MEW meshes of varied interfiber spacing alone, and composites containing NorHA hydrogel infused into meshes with varied interfiber spacing. * $p < 0.05$, ** $p < 0.01$, **** $p < 0.0001$, $n = 5$.

Importantly, the PCL fibers embedded within composites only account for ~7% of the composite's volume fraction, such that constructs may be engineered largely with a cell-laden hydrogel conducive to neotissue formation.⁴⁰ As the interfiber spacing decreases, the total fiber density within composites increases, giving rise to elevated

compressive moduli (**Figures 5.10, 5.11**). However, decreasing the interfiber spacing also resulted in misalignment of overlaying fibers. As a result, composites composed of meshes with 400 μm spacing were selected and employed for all subsequent studies to maximize the compressive properties of formed composites while conserving mesh alignment for optimal filling of macromer within the interstitial spaces of the mesh. All subsequent studies were also performed with 2 kPa NorHA hydrogel formulations (i.e., 2% NorHA, $X_{\text{DTT}}=0.1$).

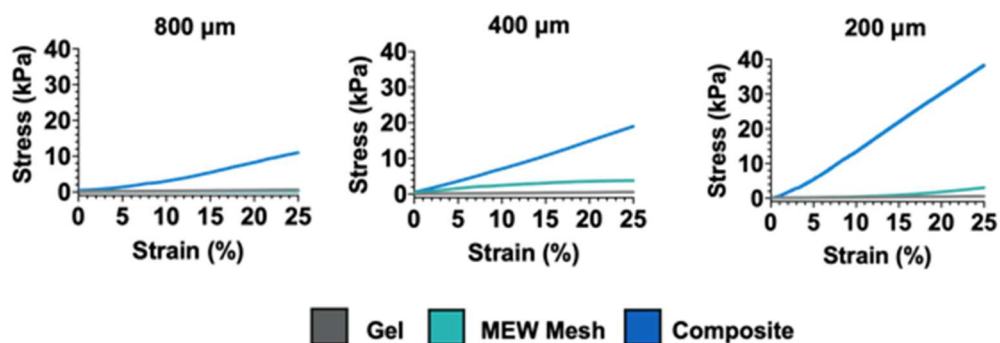


Figure 5.11: MEW Mesh dimensions influence composite mechanical properties. Representative stress-strain curves corresponding to 2 kPa hydrogels alone (Gel, gray), PCL meshes alone with varied interfiber spacing (MEW Mesh, teal), and composites (blue) composed of meshes with varied interfiber spacing.

5.3.3 Neocartilage Formation in MEW-Reinforced NorHA Hydrogels

Although the incorporation of MEW meshes within NorHA hydrogels significantly improved their compressive properties, it remained unclear how the inclusion of PCL would impact embedded MSC chondrogenesis and their ability to synthesize and distribute ECM. Thus, chondrogenesis and cartilage formation was evaluated in hydrogels alone (2 kPa NorHA) and compared to cell-laden composites containing the same hydrogel within PCL meshes (**Figure 5.12a**). Cell viability in composites was high ($92.0 \pm 2.7\%$) after one week of culture, and homogenous filling of the hydrogel within composites

was observed, as indicated by comparable cell densities near the top (716 ± 130 cells/mm²) and bottom (638 ± 77 cells/mm²) of composites (**Figure 5.13**).

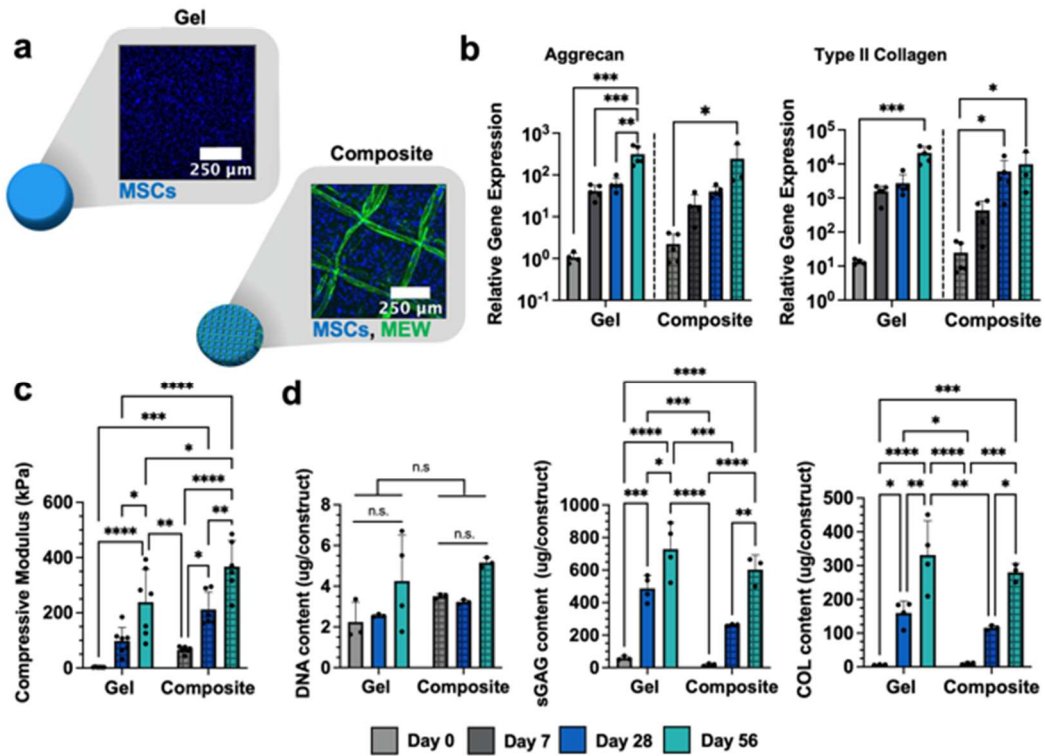


Figure 5.12: Influence of MEW meshes on MSC chondrogenesis and neocartilage formation. (a) Representative images of MSC-laden hydrogels and composites. Hydrogels and composites are cultured in chondrogenic media for up to 56 days and assessed for (b) chondrogenic gene expression (Aggrecan, Type II Collagen), (b) compressive moduli, and (c) biochemical content (DNA, sulfated glycosaminoglycan (sGAG), and collagen (COL)) after 0 (light gray), 7 (dark gray), 28 (blue), and 56 (teal) days of culture in chondrogenic media. *p<0.05, **p<0.01, ***p<0.001, ****p<0.0001, n.s. = not significant, n≥3, individual one-way ANOVAs (Aggrecan) or Kruskal–Wallis tests (Type II Collagen) performed for each formulation for qRT-PCR data.

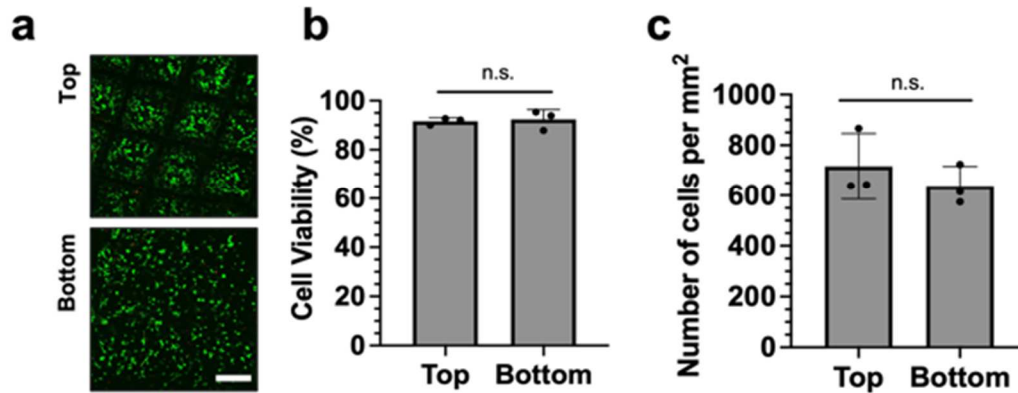


Figure 5.13: Viability within NorHA-MEW Composites. (a) Representative images (day 7) and (b) quantification of encapsulated MSC viability in the top and bottom 100 μm of composites at day 7, where live cells (green) and dead cells (red) are stained with calcein AM and ethidium homodimer, respectively. (c) Quantification of cell density in the top and bottom 100 μm of composites at day 7. n.s.= not significant, n=3.

While local heterogeneity within cell-laden hydrogels may improve neocartilage formation,⁵³ the observation of homogenous cell densities throughout constructs ensures that matrix deposition occurs throughout the full-thickness of composites. As expected, MSCs exhibited significant increases in aggrecan and type II collagen expression over 56 days of culture, consistent with chondrogenesis and similar to their differentiation in hydrogels alone (Figure 5.12b). Similarly, MSCs within both hydrogels alone and composites expressed SOX9 and decreasing amounts of type I collagen over culture time (Figure 5.14).

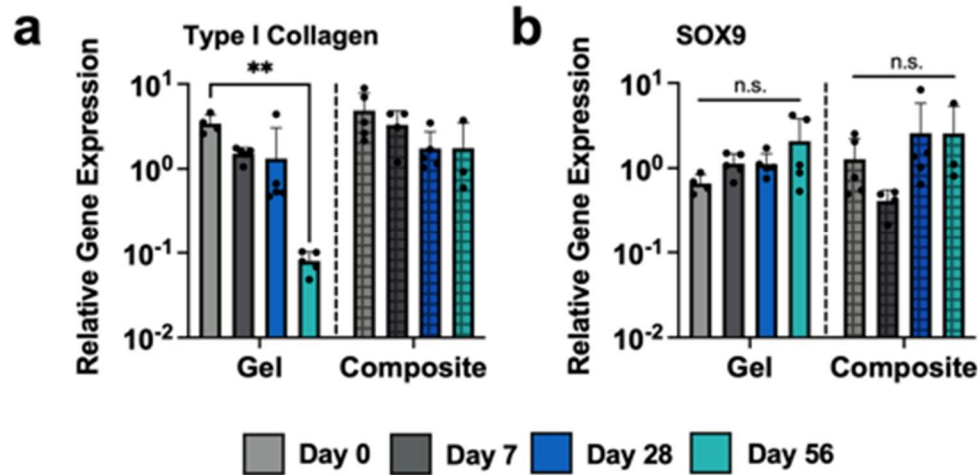


Figure 5.14: Influence of MEW Mesh on MSC chondrogenic gene expression. Relative gene expression of (a) type I collagen and (b) SOX9 in hydrogels and composites cultured in chondrogenic media, ** $p < 0.01$, n.s. = not significant, $n \geq 3$, with individual Kruskal–Wallis tests performed for each hydrogel formulation.

Composites exhibited a higher compressive modulus than hydrogels alone initially and continued to increase in their mechanical properties over culture time, possessing a significantly higher modulus (367 ± 95 kPa) than hydrogels alone (239 ± 119 kPa) after 56 days of culture (**Figure 5.12c**). Moreover, the compressive moduli of composites approached previously reported values for the Young's modulus of native articular cartilage (0.1-1.6 MPa).^{54,55} The observed increases in mechanical properties can be attributed to the deposition of ECM by encapsulated MSCs, since acellular hydrogels and composites cultured for 56 days exhibited modest decreases in compressive properties over time due to degradation (**Figure 5.15**). While all the experimental groups exhibited increases in DNA content, no significant differences were observed across culture timepoints or between hydrogels and composites (**Figure 5.12d**). The sGAG and COL contents for hydrogels and composites increased with culture time, with no significant differences between hydrogels or composites observed at the same culture times. Small differences in the absolute amount of sGAG or COL between composites and hydrogels

alone may be attributed to the volume fraction of fibers, which slightly decreases the space available for matrix.

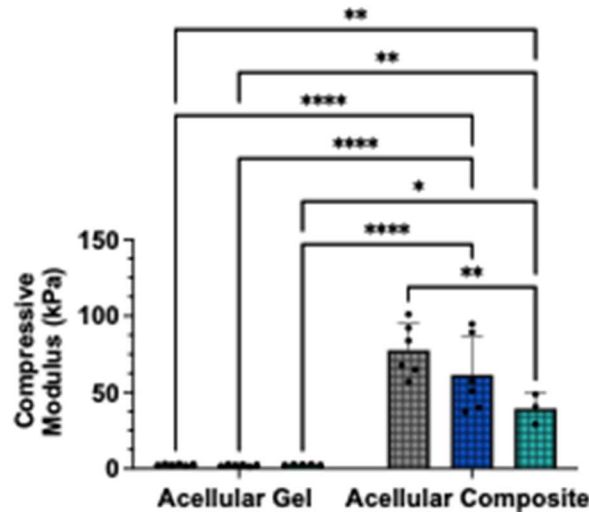


Figure 5.15: Compressive moduli of acellular hydrogels and composites. Compressive moduli measured after 56 days of incubation in chondrogenic media, illustrating slight decreases in mechanical properties due to material degradation. * $p < 0.01$, ** $p < 0.005$, **** $p < 0.0001$, $n \geq 3$.

After 28 and 56 days of culture, dense and opaque tissue was macroscopically visible in both hydrogels alone and in composites, such that the two were indistinguishable upon qualitative observation (**Figure 5.16**). The distribution of sGAG within both hydrogels and composites was comparable, with no significant differences observed in Alcian blue staining intensity (**Figure 5.17a**). Similarly, both hydrogels and composites supported the deposition of homogeneously distributed type II collagen, with no appreciable differences in staining intensity over culture time (**Figure 5.17b**). In addition, MSCs in both hydrogels and composites deposited minimal amounts of type I collagen, consistent with a hyaline cartilage-like phenotype (**Figure 5.18**). Although the staining intensity for type I collagen was significantly higher in composites at day 28 of culture, this may be attributed to the presence of additional surfaces along fibers, which may modulate gene expression and local mechanosensing of some cells.^{56,57} However, no significant differences in type I

collagen staining intensity between hydrogels and composites were observed after 56 days of culture. Importantly, the observed similarities in chondrogenic gene expression, biochemical content, and matrix staining between hydrogels and composites suggests that the inclusion of PCL meshes within cell-laden NorHA hydrogels does not attenuate the ability of cells to synthesize and distribute ECM. Thus, the higher initial mechanical properties and improved handling of the composites further motivates additional exploration of their use in cartilage repair.

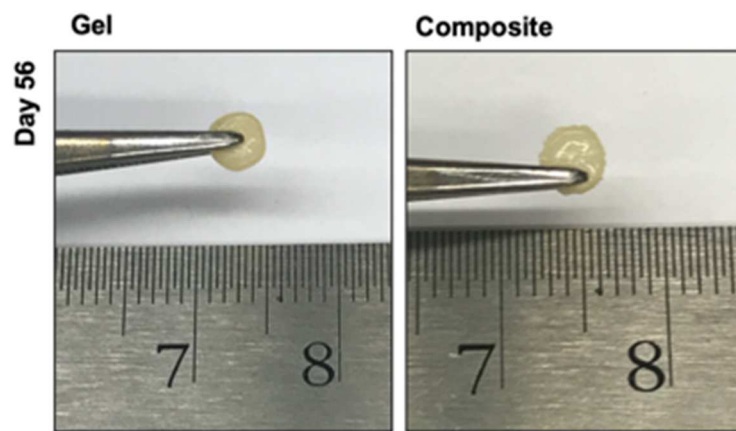


Figure 5.16: Representative gross images of MSC-laden 2 kPa hydrogels and composites. After 56 days of culture in chondrogenic media, both hydrogels alone and composites were opaque and consisted of dense tissue.

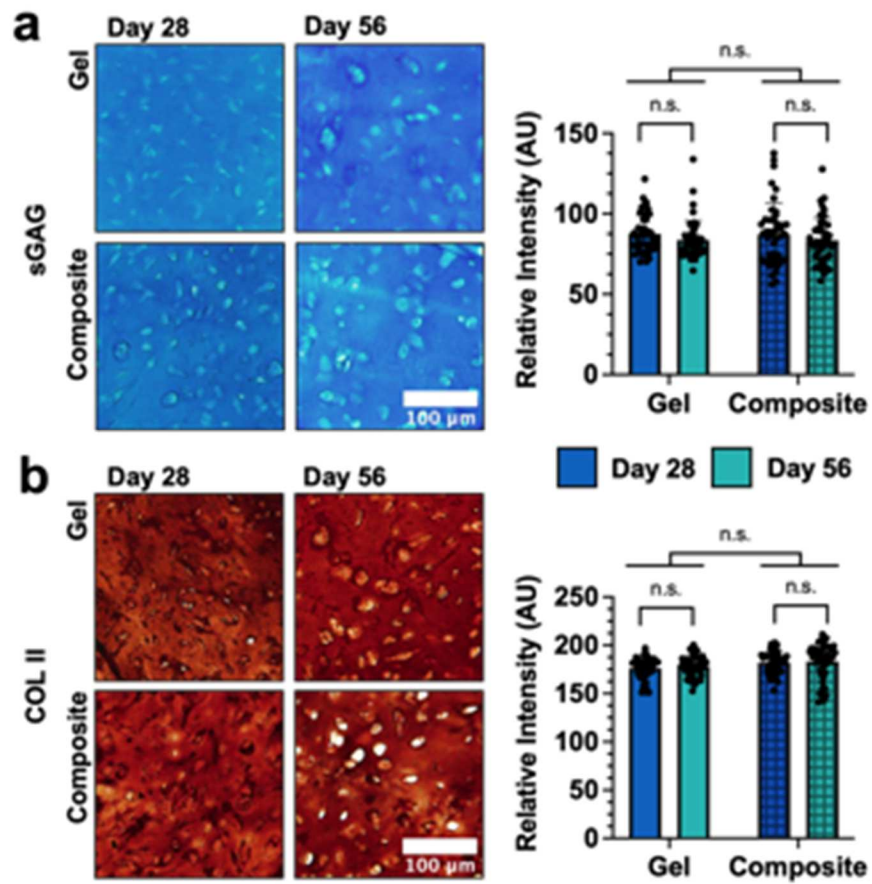


Figure 5.17: Influence of MEW Meshes on matrix production and distribution. Representative images and quantification of matrix distribution within NorHA hydrogels and composites after 28 and 56 days of culture for (a) sulfated glycosaminoglycans (sGAG) via Alcian blue staining or (b) type II collagen (COLII) via immunohistochemistry. n.s. = not significant, n=45 images, 5 sections, 3 constructs.

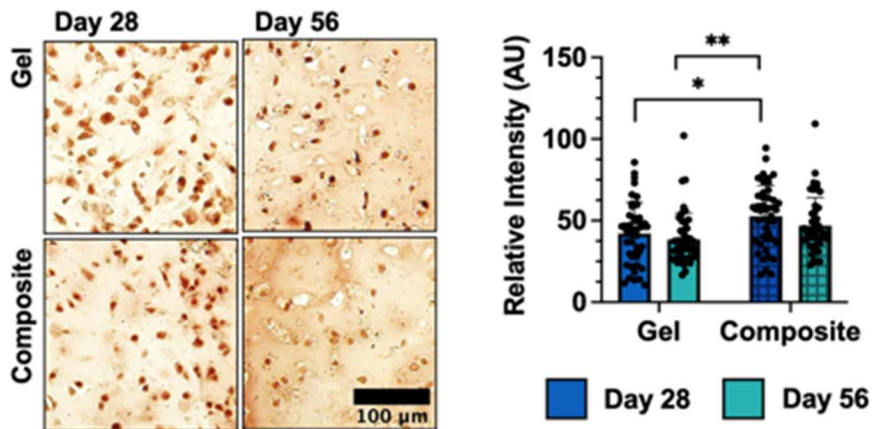


Figure 5.18: Influence of MEW Meshes on type I collagen elaboration and distribution. Representative images (day 28 and day 56) and quantification of type I collagen (COL1) distribution within hydrogels and composites via type I collagen immunohistochemistry. * $p < 0.05$, ** $p < 0.01$, n.s. = not significant, $n = 45$ images, 5 sections, 3 constructs.

5.3.4 Integration of Composites Within Cartilage Explants

Towards translating the developed composites for the repair of focal cartilage defects, we assessed the ability of composites to integrate with explanted native cartilage *ex vivo* (**Figure 5.19a**). After culture in chondrogenic media for 28 days, the formation of tissue resulted in changes in the opacity of press-fit cell-laden and cell-laden+PC composites; specifically, the appearance of cell-laden+PC composites started to resemble the autologous cartilage controls (**Figure 5.20**). The integration strength of press-fit constructs was then measured via push-out testing (**Figure 5.21**). While acellular composites were easily displaced from the center of cartilage rings, cell-laden composites exhibited a much higher integration strength (113 ± 74 kPa; **Figure 5.19b,c**). The addition of a pre-culture period and time for nascent matrix to form within composites further improved the integration strength of cell-laden+PC composites with surrounding cartilage (221 ± 115 kPa), which did not differ significantly from autologous tissue controls (272 ± 120 kPa) or previously reported integration strengths for autologous controls.³³ Uniaxial

compressive testing was performed on central regions that were pushed out to confirm that culture within cartilage rings did not significantly impede cartilage formation (Figure 5.22).

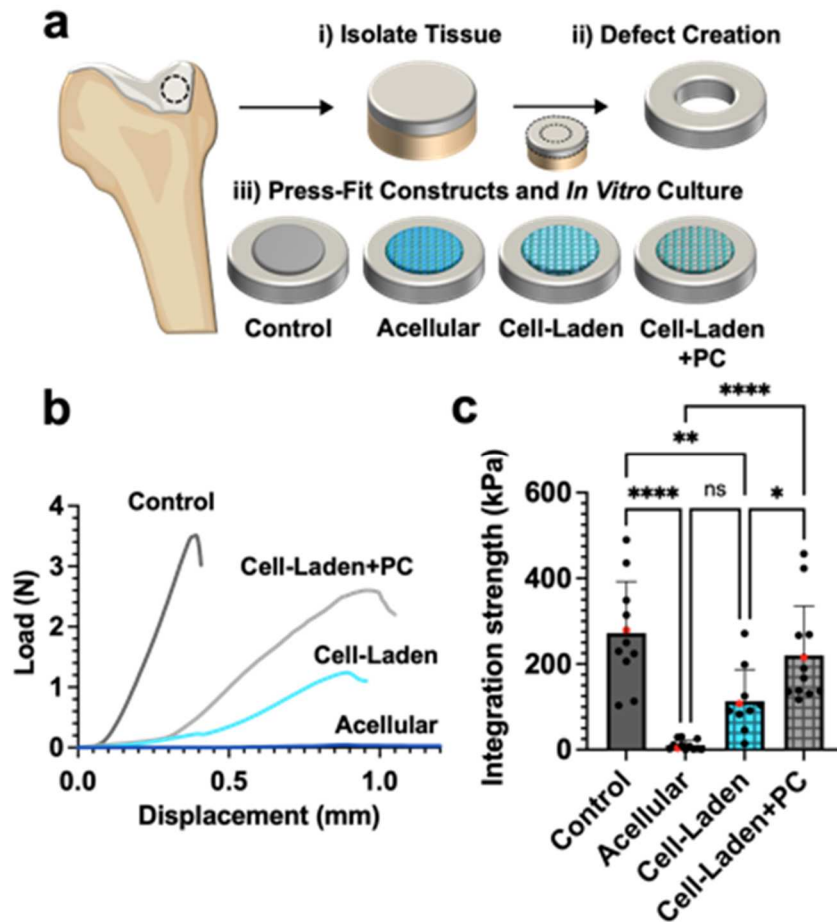


Figure 5.19: Integration of composites within explanted cartilage rings. (a) Schematic of integration studies. (i) Osteochondral plugs are isolated from the trochlear groove of juvenile bovine knee joints and (ii) defects are created to produce cartilage rings with an outer diameter of 8mm and an inner diameter of 4mm. (iii) Autologous cartilage or composites (acellular, cell-laden, and cell-laden with 28 days of chondrogenic pre-culture (+PC)) are then press-fit into cartilage rings, cultured for 28 days, and then subjected to push-out testing. (b) Representative load-displacement curves generated during push-out testing. (c) Quantification of the integration strength of press-fit constructs with surrounding tissue (red data points correspond to respective load-displacement curves in (b)). * $p < 0.05$, ** $p < 0.01$, **** $p < 0.0001$, $n \geq 10$. Created with BioRender.com.

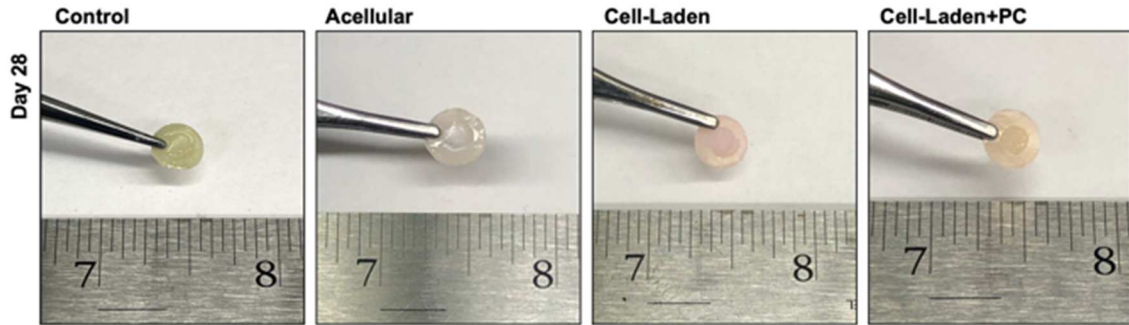


Figure 5.20: Representative gross images of constructs press-fit into explanted cartilage rings. After 28 days of culture in chondrogenic media, tissue resembling neocartilage is visible within the center of cartilage rings containing cell-laden and cell-laden+PC constructs, while acellular constructs remain translucent.

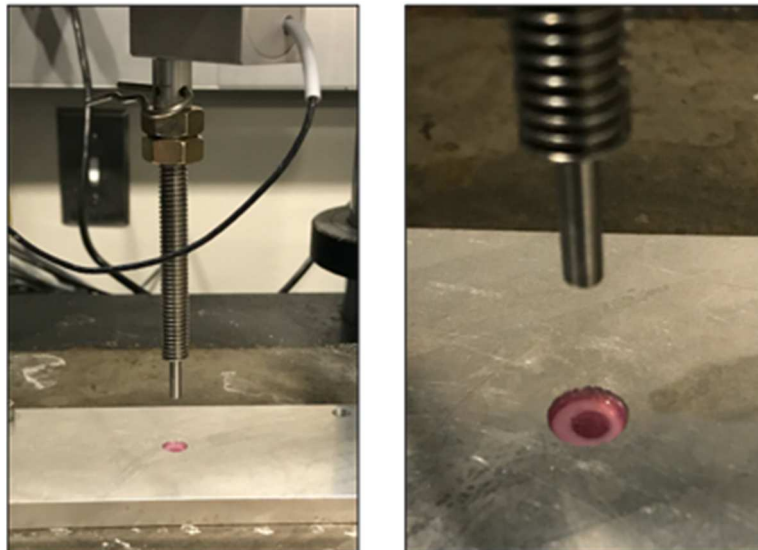


Figure 5.21: Push-out testing set-up. Representative images demonstrate sample placement for loading to obtain the integration strengths of constructs press-fit into explanted cartilage rings.

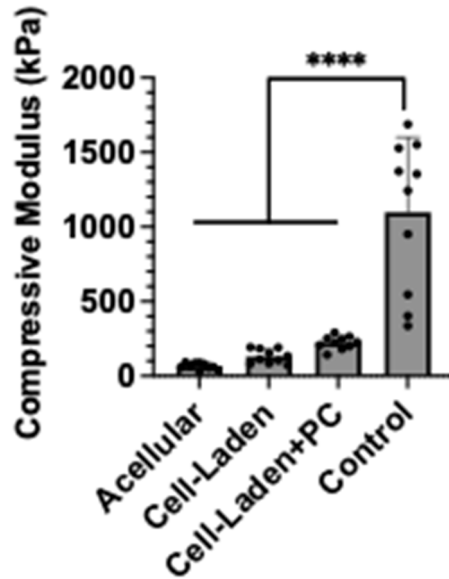


Figure 5.22: Mechanical analysis after push-out testing. The compressive moduli of constructs that were press-fit within explanted cartilage rings. **** $p < 0.0001$, $n = 10$.

In addition to push-out testing, microCT was performed on samples to assess the interfacial contact area between press-fit composites (or autologous cartilage) and explanted cartilage rings (Figures 5.23, 5.24).

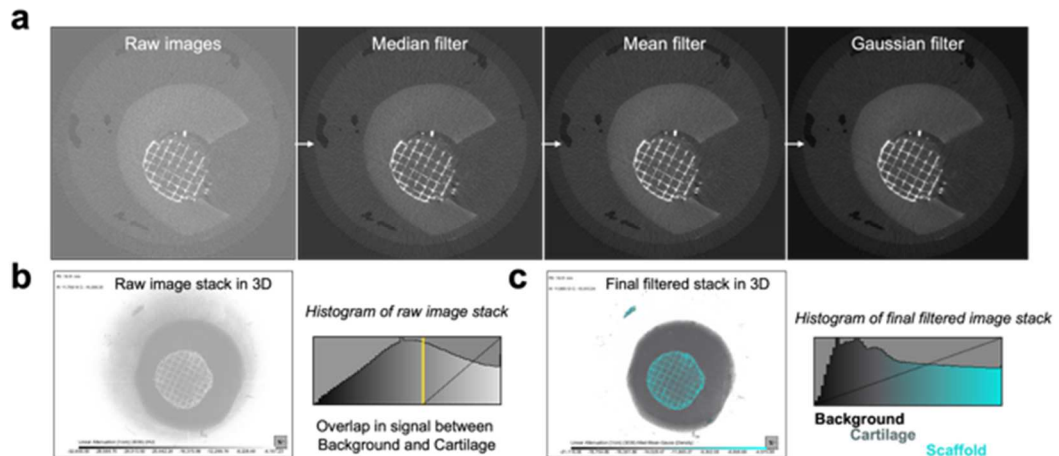


Figure 5.23: Image filtering of MicroCT scans. (a) The raw MicroCT images were sequentially filtered using a median filter, a mean filter, and then a gaussian filter. (b,c) Image filters were applied to obtain greater signal-to-noise ratios between the background signal and cartilage.

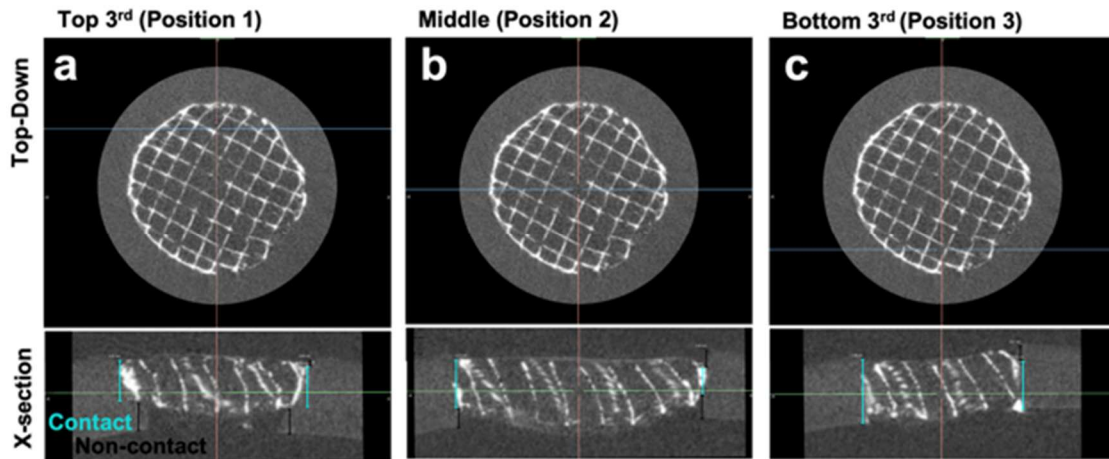


Figure 5.24: Quantification of composite-cartilage contact area from MicroCT scans. Contact area between the scaffold and cartilage rings was quantified from MicroCT scans at 3 cross-sectional (x-section) locations of the (a) top 3rd, (b) middle, and (c) bottom 3rd of the scaffold from the top-down view (Positions 1, 2, and 3 respectively, see Figure 8). In the Top-Down views, the blue plane represents the location of each x-section that was used to quantify the contact area. The cyan scale bars are representative regions of contact between the scaffold and cartilage ring in each location, while the black scale bars are representative regions of non-contact between the scaffold and cartilage ring. The contact area at each location was averaged to quantify the final contact area for each sample.

The inclusion of cells within composites and the addition of a pre-culture period significantly improved composite integration with surrounding tissue (**Figures 5.25a, 5.26**). The contact area between samples and cartilage rings was quantified at three different cross sections (**Figures 5.24, 5.25b**) and then normalized to represent a fraction of the total possible contact area between each sample and the surrounding cartilage (**Figure 5.25c**). While the normalized contact area was largest in control samples (0.85 ± 0.06), there were no significant differences from either of the cell-laden groups either without (0.66 ± 0.25) or with (0.78 ± 0.04) pre-culture. Notably, the normalized contact area was different between the acellular samples (0.33 ± 0.17) and both the cell-laden+PC samples and the autologous cartilage control samples. It is likely that the lack of tissue formation in acellular composites over culture time resulted in attenuated interfacial strength, as reflected by the displacement of composites and gaps visible between composites and native cartilage in the microCT reconstructions (**Figures 5.25a, 5.26**).

While these features are also pronounced in some cell-laden constructs, cell-laden+PC constructs generally showed intimate contact with the surrounding cartilage rings.

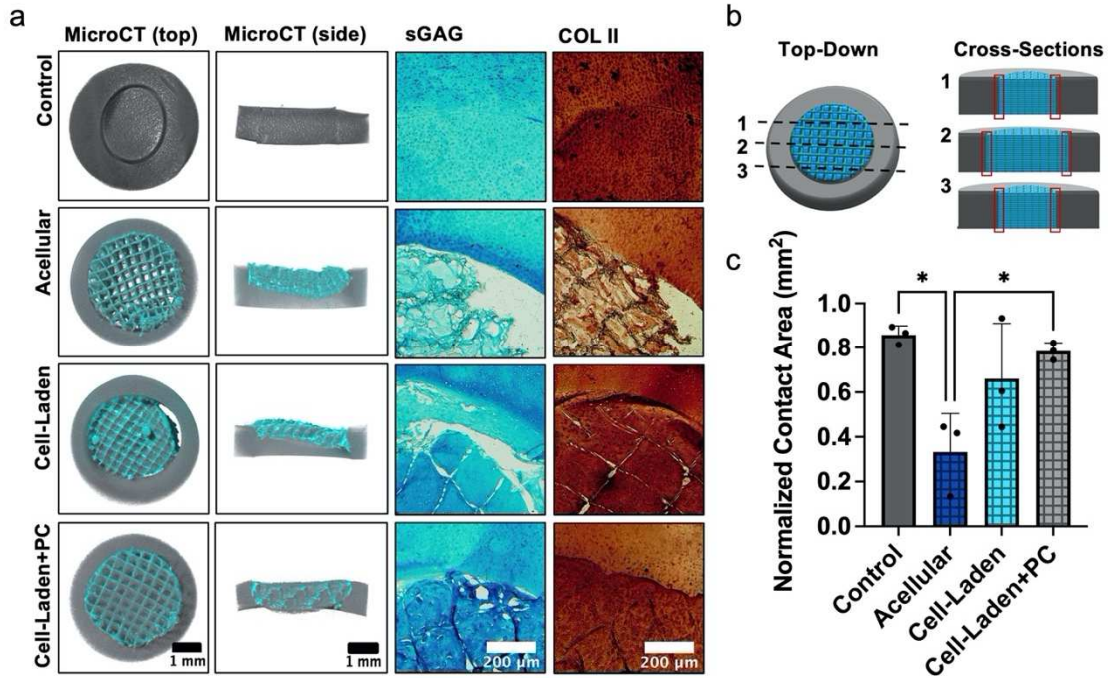


Figure 5.25: Characterization of composite-cartilage interfaces. (a) Representative MicroCT reconstructions, Alcian blue staining, and type II collagen (COLII) immunohistochemistry for constructs press-fit and cultured within explanted cartilage rings. (b) Schematic illustrating the three cross-sections (i.e., dashed lines; midplane, and planes 1 mm from the midplane in each respective direction) analyzed to determine the interfacial contact area (indicated by red boxes). (c) Quantification of normalized contact area between press-fit constructs and native cartilage at their interfaces. * $p < 0.05$, $n = 3$.

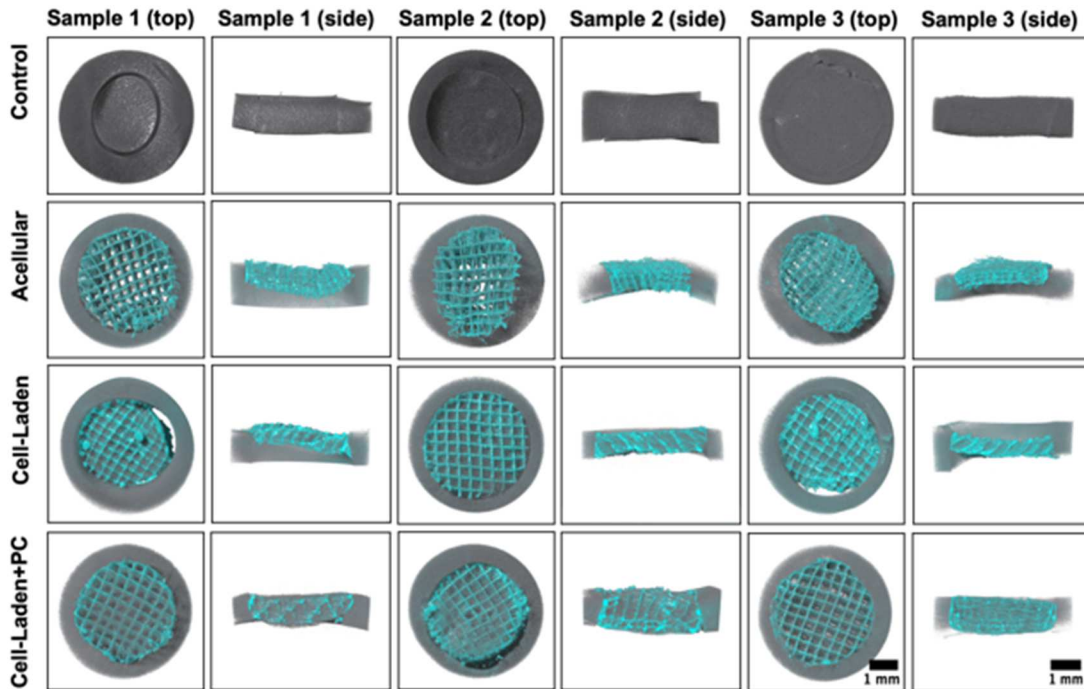


Figure 5.26: MicroCT reconstructions of constructs press-fit and cultured within explanted cartilage rings. Representative images of all constructs employed for quantification of contact area at the construct-native cartilage interface.

To further elucidate the interface of composites and cartilage, we stained constructs for sGAG and COLII to visualize local ECM organization (**Figure 5.25a**). Acellular composites failed to show sGAG or COLII along the entire perimeter of the interface, consistent with our microCT quantification. While cell-laden samples similarly possessed some gaps between composites and surrounding cartilage, cell-laden samples also showed increased sGAG and COLII staining when compared to acellular samples, suggesting that the presence of nascent ECM improved overall integration. While significant changes in composite volume were not observed over culture time, the formation of GAGs within composites might increase overall composite swelling, which may further improve composite integration within cartilage rings. Of the three composite groups, cell-laden+PC constructs contained interfaces with the most continuous sGAG

and COLII staining and most closely resembled autologous cartilage controls. Taken together, these results highlight the importance of hydrogel stabilization with MEW composites, as well as composite pre-culture towards developing a nascent ECM template that improves tissue integration with cartilage *ex vivo*.

5.4 CONCLUSIONS

In this study we demonstrated that loosely crosslinked NorHA hydrogels support MSC chondrogenesis and neocartilage formation with greater properties after culture for 56 days when compared to more densely crosslinked hydrogels. Specifically, softer NorHA hydrogels provided embedded MSCs with a local microenvironment more conducive to the production and distribution of ECM consistent with hyaline-like cartilage (i.e., high sGAG and COLII contents). To address the low initial mechanical properties and stability of these hydrogels, we reinforced the NorHA hydrogels with melt-electrowritten PCL scaffolds and showed that this did not inhibit MSC chondrogenesis or neocartilage formation while simultaneously providing improved mechanics and handling characteristics. Finally, we demonstrated that the chondrogenic pre-culture of NorHA-MEW composites resulted in improved tissue integration within explanted cartilage rings relative to acellular controls, informing future approaches for the fixation and maturation of cartilage implants within cartilage defects *in vivo*. Future work will implement these NorHA-MEW composites in the repair of articular cartilage defects *in vivo*.

5.5 REFERENCES

1. Martín A R, Patel J M, Zlotnick H M, Carey J L and Mauck R L 2019 Emerging therapies for cartilage regeneration in currently excluded ‘ red knee ’ populations *npj Regen. Med.* **4**
2. Widuchowski W, Widuchowski J and Trzaska T 2007 Articular cartilage defects: Study of 25,124 knee arthroscopies *Knee* **14** 177–82
3. Sadtler K, Singh A, Wolf M T, Wang X, Pardoll D M and Elisseeff J H 2016 Design, clinical translation and immunological response of biomaterials in regenerative medicine *Nat. Rev. Mater.* **1** 16040
4. Heir S, Nerhus T K, Rotterud J H, Loken S, Ekeland A, Engebretsen L and Aroen A 2010 Focal cartilage defects in the knee impair quality of life as much as severe osteoarthritis: a comparison of knee injury and osteoarthritis outcome score in 4 patient categories scheduled for knee surgery. *Am. J. Sports Med.* **38** 231–7
5. Kalson N S, Gikas P D and Briggs T W R 2010 Current strategies for knee cartilage repair *Int. J. Clin. Pract.* **64** 1444–52
6. Carey J L 2012 Fibrocartilage Following Microfracture Is Not as Robust as Native Articular Cartilage *J. Bone Jt. Surg. Am.* **94** e80
7. Devitt B M, Bell S W, Webster K E, Feller J A and Whitehead T S 2017 Surgical treatments of cartilage defects of the knee: Systematic review of randomised controlled trials *Knee* **24** 508–17
8. Balakrishnan B and Banerjee R 2011 Biopolymer-based hydrogels for cartilage tissue engineering *Chem. Rev.* **111** 4453–74
9. Yang J, Shrike Zhang Y, Yue K and Khademhosseini A 2017 Cell-Laden Hydrogels for Osteochondral and Cartilage Tissue Engineering *Acta Biomater.* **57**

1–25

10. Di Bella C, Duchi S, O'Connell C D, Blanchard R, Augustine C, Yue Z, Thompson F, Richards C, Beirne S, Onofrillo C, Bauquier S H, Ryan S D, Pivonka P, Wallace G G and Choong P F 2018 In situ handheld three-dimensional bioprinting for cartilage regeneration *J. Tissue Eng. Regen. Med.* **12** 611–21
11. O'Connell C D, Di Bella C, Thompson F, Augustine C, Beirne S, Cornock R, Richards C J, Chung J, Gambhir S, Yue Z, Bourke J, Zhang B, Taylor A, Quigley A, Kapsa R, Choong P and Wallace G G 2016 Development of the Biopen: A handheld device for surgical printing of adipose stem cells at a chondral wound site *Biofabrication* **8** 015019
12. Levato R, Jungst T, Scheuring R G, Blunk T, Groll J and Malda J 2020 From Shape to Function: The Next Step in Bioprinting *Adv. Mater.* **32** 1906423
13. Lim K S, Levato R, Costa P F, Castilho M D, Alcala-Orozco C R, van Dorenmalen K M A, Melchels F P W, Gawlitta D, Hooper G J, Malda J and Woodfield T B F 2018 Bio-resin for high resolution lithography-based biofabrication of complex cell-laden constructs *Biofabrication* **10** 034101
14. Bernal P N, Delrot P, Loterie D, Li Y, Malda J, Moser C and Levato R 2019 Volumetric Bioprinting of Complex Living-Tissue Constructs within Seconds *Adv. Mater.* **31** 1904209
15. Bryant S J and Anseth K S 2002 Hydrogel properties influence ECM production by chondrocytes photoencapsulated in poly(ethylene glycol) hydrogels *J. Biomed. Mater. Res.* **59** 63–72
16. Erickson I E, Huang A H, Sengupta S, Kestle S, Burdick J A and Mauck R L 2009 Macromer density influences mesenchymal stem cell chondrogenesis and maturation in photocrosslinked hyaluronic acid hydrogels *Osteoarthr. Cartil.* **17**

1639–48

17. Sridhar B V., Dailing E A, Brock J L, Stansbury J W, Randolph M A and Anseth K S 2015 A Biosynthetic Scaffold that Facilitates Chondrocyte-Mediated Degradation and Promotes Articular Cartilage Extracellular Matrix Deposition *Regen. Eng. Transl. Med.* **1** 11–21
18. Roberts J J, Nicodemus G D, Greenwald E C and Bryant S J 2011 Degradation improves tissue formation in (Un)loaded chondrocyte-laden hydrogels *Clin. Orthop. Relat. Res.* **469** 2725–34
19. Sahoo S, Chung C, Khetan S and Burdick J A 2008 Hydrolytically degradable hyaluronic acid hydrogels with controlled temporal structures *Biomacromolecules* **9** 1088–92
20. Chung C, Beecham M, Mauck R L and Burdick J A 2009 The influence of degradation characteristics of hyaluronic acid hydrogels on in vitro neocartilage formation by mesenchymal stem cells *Biomaterials* **30** 4287–96
21. Xu C, Dai G and Hong Y 2019 Recent advances in high-strength and elastic hydrogels for 3D printing in biomedical applications *Acta Biomater.* **95** 50–9
22. Andrew C D, Susan E C, Emily M R and Daniel J K 2016 A comparison of different bioinks for 3D bioprinting of fibrocartilage and hyaline cartilage *Biofabrication* **8** 45002
23. Xu T, Binder K W, Albanna M Z, Dice D, Zhao W, Yoo J J and Atala A 2013 Hybrid printing of mechanically and biologically improved constructs for cartilage tissue engineering applications *Biofabrication* **5** 015001
24. Lee J S, Hong J M, Jung J W, Shim J H, Oh J H and Cho D W 2014 3D printing of composite tissue with complex shape applied to ear regeneration *Biofabrication* **6** 024103

25. Kundu J, Shim J-H, Jang J, Kim S-W and Cho D-W 2015 An additive manufacturing-based PCL–alginate–chondrocyte bioprinted scaffold for cartilage tissue engineering *J Tissue Eng Regen Med* **9** 1286–97
26. Critchley S, Sheehy E J, Cunniffe G, Diaz-Payno P, Carroll S F, Jeon O, Alsberg E, Brama P A J and Kelly D J 2020 3D printing of fibre-reinforced cartilaginous templates for the regeneration of osteochondral defects *Acta Biomater.* **113** 130–43
27. Yoon Y, Kim C H, Lee J E, Yoon J, Lee N K, Kim T H and Park S H 2019 3D bioprinted complex constructs reinforced by hybrid multilayers of electrospun nanofiber sheets *Biofabrication* **11**
28. Schipani R, Scheurer S, Florentin R, Critchley S E and Kelly D J 2020 Reinforcing interpenetrating network hydrogels with 3D printed polymer networks to engineer cartilage mimetic composites *Biofabrication* **12**
29. Huang C-Y, Mow V C and Ateshian G A 2001 The Role of Flow-Independent Viscoelasticity in the Biphasic Tensile and Compressive Responses of Articular Cartilage *J. Biomech. Eng.* **123** 410–7
30. Moutos F T and Guilak F 2010 Functional properties of cell-seeded three-dimensionally woven poly(ϵ -Caprolactone) scaffolds for cartilage tissue engineering *Tissue Eng. - Part A* **16** 1291–301
31. Visser J, Melchels F P W, Jeon J E, Van Bussel E M, Kimpton L S, Byrne H M, Dhert W J A, Dalton P D, Hutmacher D W and Malda J 2015 Reinforcement of hydrogels using three-dimensionally printed microfibrils *Nat. Commun.* **6** 6933
32. de Ruijter M, Ribeiro A, Dokter I, Castilho M and Malda J 2019 Simultaneous Micropatterning of Fibrous Meshes and Bioinks for the Fabrication of Living Tissue Constructs *Adv. Healthc. Mater.* **8**

33. Robinson T M, Hutmacher D W and Dalton P D 2019 The Next Frontier in Melt Electrospinning : Taming the Jet *Adv. Funct. Mater.* **29** 1904664
34. Hochleitner G, Jüngst T, Brown T D, Hahn K, Moseke C, Jakob F, Dalton P D and Groll J 2015 Additive manufacturing of scaffolds with sub-micron filaments via melt electrospinning writing *Biofabrication* **7** 035002
35. Kim I L, Mauck R L and Burdick J A 2011 Hydrogel design for cartilage tissue engineering : A case study with hyaluronic acid *Biomaterials* **32** 8771–82
36. Vega S L, Kwon M Y, Song K H, Wang C, Mauck R L, Han L and Burdick J A 2018 Combinatorial hydrogels with biochemical gradients for screening 3D cellular microenvironments *Nat. Commun.* **9** 614
37. Livak K J and Schmittgen T D 2001 Analysis of relative gene expression data using real-time quantitative PCR and the $2^{-\Delta\Delta CT}$ method *Methods* **25** 402–8
38. Kim M, Erickson I E, Choudhury M, Pleshko N and Mauck R L 2012 Transient exposure to TGF- β 3 improves the functional chondrogenesis of MSC-laden hyaluronic acid hydrogels *J. Mech. Behav. Biomed. Mater.* **11** 92–101
39. Kwon M Y, Vega S L, Gramlich W M, Kim M, Mauck R L and Burdick J A 2018 Dose and Timing of N-Cadherin Mimetic Peptides Regulate MSC Chondrogenesis within Hydrogels *Adv. Healthc. Mater.* **7** 1701199
40. Castilho M, Hochleitner G, Wilson W, Van Rietbergen B, Dalton P D, Groll J, Malda J and Ito K 2018 Mechanical behavior of a soft hydrogel reinforced with three-dimensional printed microfibre scaffolds *Sci. Rep.* **8** 1245
41. Ragelle H, Tibbitt M W, Wu S Y, Castillo M A, Cheng G Z, Gangadharan S P, Anderson D G, Cima M J and Langer R 2018 Surface tension-assisted additive manufacturing *Nat. Commun.* **9** 1184
42. Liebesny P H, Mroszczyk K, Zlotnick H, Hung H H, Frank E, Kurz B, Zanotto G,

- Frisbie D and Grodzinsky A J 2019 Enzyme Pretreatment plus Locally Delivered HB-IGF-1 Stimulate Integrative Cartilage Repair In Vitro *Tissue Eng. - Part A* **25** 1191–201
43. Erickson I E, Kestle S R, Zellars K H, Dodge G R, Burdick J A and Mauck R L 2012 Improved cartilage repair via in vitro pre-maturation of MSC-seeded hyaluronic acid hydrogels *Biomed. Mater.* **7** 024110
44. Dicker K T, Gurski L A, Pradhan-Bhatt S, Witt R L, Farach-Carson M C and Jia X 2014 Hyaluronan: A simple polysaccharide with diverse biological functions *Acta Biomater.* **10** 1558–70
45. Highley C B, Prestwich G D and Burdick J A 2016 Recent advances in hyaluronic acid hydrogels for biomedical applications *Curr. Opin. Biotechnol.* **40** 35–40
46. Lim K S, Galarraga J H, Cui X, Lindberg G C J, Burdick J A and Woodfield T B F 2020 Fundamentals and Applications of Photo-Cross-Linking in Bioprinting *Chem. Rev.* **120** 10662–94
47. Loebel C, Kwon M Y, Wang C, Han L, Mauck R L and Burdick J A 2020 Metabolic Labeling to Probe the Spatiotemporal Accumulation of Matrix at the Chondrocyte–Hydrogel Interface *Adv. Funct. Mater.* **30** 1909802
48. Akiyama H, Chaboissier M C, Martin J F, Schedl A and De Crombrughe B 2002 The transcription factor Sox9 has essential roles in successive steps of the chondrocyte differentiation pathway and is required for expression of Sox5 and Sox6 *Genes Dev.* **16** 2813–28
49. Dhote V, Skaalure S, Akalp U, Roberts J, Bryant S J and Vernerey F J 2013 On the role of hydrogel structure and degradation in controlling the transport of cell-secreted matrix molecules for engineered cartilage *J. Mech. Behav. Biomed. Mater.* **19** 61–74

50. Castilho M, Mouser V, Chen M, Malda J and Ito K 2019 Bi-layered micro-fibre reinforced hydrogels for articular cartilage regeneration *Acta Biomater.* **95** 297–306
51. Bas O, De-Juan-Pardo E M, Meinert C, D'Angella D, Baldwin J G, Bray L J, Wellard R M, Kollmannsberger S, Rank E, Werner C, Klein T J, Catelas I and Hutmacher D W 2017 Biofabricated soft network composites for cartilage tissue engineering. *Biofabrication* **9** 025014
52. Bas O, Lucarotti S, Angella D D, Castro N J, Meinert C, Wunner F M, Rank E, Vozi G, Klein T J, Catelas I, De-Juan-Pardo E M and Hutmacher D W 2018 Rational design and fabrication of multiphasic soft network composites for tissue engineering articular cartilage: A numerical model-based approach *Chem. Eng. J.* **340** 15–23
53. Vernerey F J and Bryant S 2020 The role of percolation in hydrogel-based tissue engineering and bioprinting *Curr. Opin. Biomed. Eng.* **15** 68–74
54. Wang C C B, Chahine N O, Hung C T and Ateshian G A 2003 Optical determination of anisotropic material properties of bovine articular cartilage in compression *J. Biomech.* **36** 339–53
55. Töyräs J, Lyyra-Laitinen T, Niinimäki M, Lindgren R, Nieminen M T, Kiviranta I and Jurvelin J S 2001 Estimation of the Young's modulus of articular cartilage using an arthroscopic indentation instrument and ultrasonic measurement of tissue thickness *J. Biomech.* **34** 251–6
56. Hogrebe N J, Reinhardt J W and Gooch K J 2017 Biomaterial microarchitecture: a potent regulator of individual cell behavior and multicellular organization *J. Biomed. Mater. Res. - Part A* **105** 640–61
57. Eichholz K F and Hoey D A 2018 Mediating human stem cell behaviour via

defined fibrous architectures by melt electrospinning writing *Acta Biomater.* **75**

140–51

CHAPTER 6: EVALUATION OF MEW-NORHA COMPOSITES IN A PORCINE CARTILAGE DEFECT MODEL

6.1 INTRODUCTION

A variety of surgical approaches have been developed to treat full-thickness cartilage defects due to trauma and disease, including arthroscopic debridement, microfracture, and autologous chondrocyte implantation.¹ Importantly, if cartilage defects are left untreated they may progress to osteoarthritis (OA), which results in significant pain and dysfunction to the patient.² Unfortunately, these approaches typically fail to restore the full function of the damaged cartilage, as the repair cartilage formed in strategies such as microfracture typically exhibits inferior properties to healthy articular cartilage.³ However, the relative success of each of these respective approaches is a strong function of the damaged defect size, which dictates the indication for each procedure.¹ Bone marrow stimulation via subchondral microfracture is widely considered to be the first option for treating relatively small lesions ($<2.5 \text{ cm}^2$), with defects ranging between 1 - 2.5 cm^2 responding well to the treatment.¹ However, microfracture has previously demonstrated poor patient outcomes in the treatment of larger defects ($\geq 4 \text{ cm}^2$),¹ which typically must be repaired with osteochondral allografts. For intermediate defect sizes (2 cm^2), ACI is typically used to mediate repair;¹ however, ACI is not usually employed for larger defects ($\geq 4 \text{ cm}^2$), since there is typically a limited number of donor cells that can be readily isolated.

In response to the limitations of current approaches for cartilage repair,⁴⁵ a variety of new tissue engineering therapies are being developed and several have been evaluated for cartilage repair in large animals.⁶⁻⁹ These have been met with varied success, but highlight the importance of selecting models and timepoints that best recapitulate human cartilage damage in a clinically relevant manner. To this end, canine, caprine, porcine, and equine models are most commonly used for the investigation of new cartilage repair

strategies.¹⁰ Porcine models are often employed as large animal models for cartilage damage because they permit easy operative access to non-load bearing articular cartilage (i.e., along the femoral trochlea) and possess cartilage with thickness comparable to human articular cartilage.¹¹ For example, composite scaffolds consisting of woven polycaprolactone (PCL) and either infilled hydrogels (i.e., self-assembling peptide-based hydrogels and HA hydrogels) or bone marrow aspirate were previously investigated for the treatment of cartilage lesions (4mm diameter) in Yucatan minipigs.⁹ 12-months after implantation, the quality of repair cartilage formed by these composites was characterized via gross scoring, mechanical testing, MicroCT, and histology. Despite the early observation of scaffold retention in defects at 6-weeks, ultimately defects treated with composites performed worse than those treated with microfracture. Similarly, biphasic composites of PCL and cell-laden PEG hydrogel were evaluated in minipig cartilage defects for 6 months; explanted composites resulted in O'Driscoll scores (i.e., histological scoring) that were worse than empty defect controls and significant bone resorption was observed.⁶

One challenge to such therapies is the successful fixation and retention of implants within full-thickness cartilage defects.^{12,13} A range of approaches have been investigated for implant fixation,¹⁴ including press-fitting, suturing with an overlying periosteal flap, application of fibrin glue/sealant, and the use of bone anchors to integrate implants with the underlying bone. While simple press fitting of implants may be appropriate for osteochondral defects or instances in which full thickness cartilage defects are surrounded by healthy thick cartilage,¹⁵ often times samples are dislodged from defects due to the complex loads experienced within the joint.^{14,16} Fibrin glue has similarly been combined with press-fitting of implants, but only marginally improved the fixation strength and retention of implants.¹⁶⁻¹⁸ Suturing of periosteal flaps to secure implants within defects

unfortunately leads to loss of chondrocytes and ECM at the local suture site, as well as the formation of fissures reminiscent of partial thickness defects.¹⁹ Bone anchors have been shown to more reliably ensure the retention of implants within defects,⁹ but they often lead to underlying subchondral bone remodeling or voids.^{18,20} In a recent study, biphasic scaffolds composed of hydroxyapatite and PCL microfiber meshes fabricated via MEW were evaluated in an equine model of osteochondral damage. 6 months after implantation, marginal cartilaginous ECM was observed in the chondral phase of implants, while MicroCT results showed the collapse of bone anchors used to fix the implants within defects.⁷ Generally, both the cartilage defect size and geometry, as well as the properties of the implant itself must be considered when selecting the optimal fixation method for scaffolds.

In Chapter 5, MEW-NorHA composites were shown to support MSC chondrogenesis and neocartilage formation while also achieving high initial construct mechanical properties, using juvenile bovine MSCs. The impressive compressive moduli and biochemical contents achieved in these composites *in vitro*, taken together with their ability to integrate with native articular cartilage *ex vivo* motivates additional exploration of their therapeutic potential in a clinically-relevant model of cartilage damage. Thus, the aims of this study were to (i) explore adult porcine MSC behavior within composites, (ii) to elucidate the fixation of MEW-NorHA composites within cartilage defects, and (iii) to assess the ability of the composites to support the repair of full-thickness cartilage defects in a minipig model.

6.2 METHODS

6.2.1 Materials

Sodium hyaluronic acid was obtained from Lifecore Biomedical (Chaska, MN) and lithium phenyl-2,4,6-trimethylbenzoylphosphinate (LAP) was obtained from Colorado Photopolymer Solutions (Boulder, CO). Unless otherwise specified, all other reagents and materials were purchased from Sigma-Aldrich (St. Louis, MO).

6.2.2 MEW Mesh-NorHA Composite Fabrication and Cell Culture

Adult mesenchymal stromal cells (MSCs) were isolated from bone marrow aspirate derived from the iliac crest of three adult Yucatan minipigs (12-14 years old; Sinclair Research, Auxvasse, MO) via plastic adherence during culture in Dulbecco's modified eagle medium (DMEM) supplemented with 10% fetal bovine serum (FBS) and 1% penicillin/streptomycin (P/S).

NorHA was synthesized as previously described in Chapter 5 and dissolved in phosphate buffered saline (PBS) with LAP photoinitiator (0.05%) and DTT crosslinker (0.54 mM) to obtain macromer precursor solution.²¹ Similarly, polycaprolactone (Purasorb PC 12, Corbion Inc., Gorinchem, Netherlands) MEW meshes (diameter ~4 mm, height~1mm, 400 μm fiber interspacing) were fabricated as described in Chapter 5.²² The macromer solution was then used to fill in the box-structure PCL MEW meshes with or without porcine MSCs (pMSCs, P1, 20×10^6 cells/mL) and irradiated with blue light (400-500 nm, Omnicure lamp with an affixed collimator, $I=10 \text{ mW/cm}^2$) for 5 minutes to obtain composites similar to those investigated in Chapter 5 (i.e., 400 μm spacing PCL MEW meshes, 2 kPa NorHA gel). Composites were then cultured in chondrogenic media (1% ITS+; 2.50 $\mu\text{g/mL}$ amphotericin B; $1 \times 10^{-3} \text{ M}$ sodium pyruvate; 50 $\mu\text{g/mL}$ ascorbic acid 2-

phosphate; 40 µg/mL L-proline; 1×10^{-7} M dexamethasone; 10 ng/mL TGF-B3) for up to 28 days.

6.2.3 Screening of Porcine Donors for pMSC Chondrogenic Potential

After culture in chondrogenic media for 28 days, the compressive moduli of composites were determined via unconfined, uniaxial compressive testing with a constant loading rate of 0.2 N/min (Q800 DMA, TA Instruments) and the modulus was quantified as the slope of the stress-strain curves between 10-20% strain.

The biochemical contents of composites were quantified as detailed in Chapter 5. Samples were minced and digested via incubation with papain and hyaluronidase overnight at 60°C. Sulfated glycosaminoglycan content, collagen content, and DNA content were then determined via the dimethylmethylene blue assay, the hydroxyproline (OHP) assay (Abcam Hydroxyproline Assay Kit, ab222941), and the Picogreen dsDNA assay.²³

To evaluate the deposition and distribution of extracellular matrix (ECM) by encapsulated cells within composites, composites were first fixed (10% buffered formalin), paraffin embedded, and sectioned (5 µm). Alcian blue staining and immunohistochemistry for type I (COL I, mouse monoclonal anti-collagen type 1 antibody, Millipore Sigma) and type II collagen COL II, mouse monoclonal anti-collagen type II antibody, Developmental Studies Hybridoma Bank) were then performed as described in Chapter 5. The mean staining intensities of sGAGs, COL I, and COL II in composites were quantified using Image J software.²⁴

6.2.4 Cell Viability

To evaluate the cytocompatibility of cell-laden composites prepared for implantation, live/dead staining with calcein AM and ethidium homodimer was performed

in accordance with manufacturer's instructions (Invitrogen) after 7 days of culture in chondrogenic media. Cell viability was quantified using Image J software as the number of live cells per total cells within images acquired via epifluorescence microscopy (n ≥ 3 hydrogels, 9 images per sample).

6.2.5 Animal Procedures and Stifle Joint Surgery

Skeletally mature (12-14 mo old at time of surgery) male Yucatan minipigs were acquired (Sinclair Bioresources, Auxvasse, MO, USA) for the evaluation of composites in the repair of cartilage defects *in vivo* (n=9). All animal procedures were approved by the Institutional Animal Care and Use Committee at the University of Pennsylvania. Adult animals were selected over skeletally immature animals to better recapitulate the patient populations that develop full-thickness cartilage defects and to mitigate the degree of subchondral bone remodeling that occurs with cartilage defect creation.²⁵ Unilateral stifle joint surgeries were performed on the right hind limb of each animal as previously described.^{16,26,27}

Animals were first anesthetized with inhaled isoflurane before undergoing endotracheal intubation according to the protocol. The right stifle joint was then shaved, cleaned, and surgically prepared with Betadine. Bupivacaine was injected into the joint prior to a 4 cm medial parapatellar skin incision. The subcutaneous tissue was then incised, homeostasis was attained, and the medial patellar tendon border was palpated prior to leg extension. Thereafter, an incision was made through the joint capsule under the patellar tendon and the trochlea was exposed via medial parapatellar arthrotomy (and patella dislocation laterally). A minimum of four full-thickness chondral defects were then created (two proximal and distal medial defects and two proximal and distal lateral defects) using a 4mm biopsy punch and a curette to excise cartilage within the bounds of the scored defect while ensuring the underlying subchondral bone was not damaged.

Groups included empty defects, microfracture, acellular composites, and composites containing pMSCs that were precultured for 28 days. In formed defects treated with microfracture, a surgical awl was used to create three holes to stimulate the underlying bone marrow. After the fixation of composites (described below) within defects and the creation of microfracture holes, the patella was relocated, all instruments and retractors were removed, and the knee was then ranged to ensure that the patella was stable. The joint capsule was then closed with 0 Vicryl interrupted sutures, the subcutaneous tissue layer was closed with 2-0 Vicryl simple interrupted sutures, and the skin layer was closed with a 3-0 monocryl running suture (all sutures were from Ethicon). All animals received postoperative analgesia, antibiotics, and anti-inflammatories, with unrestricted cage activity permitted 2 to 3 hours after recovery from anesthesia.

Either PLDLLA pins (Aesculap FR736, Center Valley, PA) or fibrin glue (Tisseel, Baxter) were used to fix composites within created defects as previously reported.¹⁶ To pin composite implants within defects, composites were press-fit into the defects and pilot holes were then created through the implant and into the subchondral bone. A 3-pronged fixation guide (Aesculap FR720, Center Valley PA) was then placed on top of composites and used to insert the pins into the created pilot holes. In two animals (Surgeries 1-2), an additional fifth defect was introduced on the lateral side of the femoral trochlea to replace medial distal defects in which insufficient fixation of implants with PLA pins was initially achieved (i.e., poor seating of composites within the created defect and misaligned pinning at the time of fixation). Each of these additional, lateral distal defects were evaluated in lieu of the medial distal defects in all the performed analyses.

To fix composites within defects using Tisseel, the fibrin glue was first applied to the underlying subchondral bone. Tisseel fibrin glue was selected since it has been previously shown to possess higher compressive properties than alternative commercial

(Evicel, Ethicon) and autologous (Angel, Anthrex; ProPlaz, Biorich) fibrin glue products.²⁸ Composites were then press-fit into defects on top of the glue and manually held in place for 3 minutes via application of force with a spatula and a surgical curette. Additional fibrin glue was then applied along the top of the composite interface, and force was again manually applied on top of the composite for 3 minutes.

6.2.6 Arthroscopy and Gross Observations

12 weeks after cartilage defect creation, animals were euthanized, and the stifle joints were retrieved for post-mortem analyses. Dry arthroscopy was first performed to visualize the cartilage defects *in situ* using an adapted protocol.¹⁶ A 1 cm vertical incision was made to establish a medial subpatellar arthroscopic portal, which allowed for placement of a trocar and arthroscopic probe within the medial aspect of the stifle joint. Images of each defect were then taken to qualitatively evaluate the smoothness of repair cartilage and its integration with the surrounding tissue.²⁹

The stifle joint was then dissected to expose the patellofemoral joint, and both the trochlea and patella were explanted. To characterize any potential damage along the surface of the patella due to the presence of pins or fibrin glue on the opposing articulating surface, India ink staining was performed. Cartilage defects along the trochlear groove were then macroscopically imaged to qualitatively assess the retention of implants and the quality of repair cartilage formed in defects.³⁰

6.2.7 Indentation Testing of Composites and Repair Cartilage

To evaluate the mechanical properties of composites prior to implantation and repair cartilage 12 weeks after defect creation, creep indentation testing was performed as previously described using an Instron 5948 Universal Testing System (Instron Inc, Norwood, MA) with an affixed 1mm diameter spherical indenter.³¹ Since large

deformations during physiologic creep testing may significantly alter the local compositional characteristics of immature tissue constructs (i.e., acellular composites), relatively lower loads were employed during all indentation testing to ensure the accurate quantification of composite mechanical properties prior to implantation.³² Generally, a load of 0.1 N was applied to all samples at a loading rate of 0.1 N/s and then held for 900 s (after the load setpoint was reached) while the creep displacement was measured. Acellular and precultured composites were submerged in PBS prior to indentation testing.

Alternatively, osteochondral samples were first fixed into place within a low-melting temperature bismuth alloy to secure samples while maintaining the cartilage defect surface upright. Samples were then submerged in PBS and positioned under the indenter setup using a custom XY positioning stage and a goniometer to ensure that the cartilage surface was perpendicular to the indenter. Repair cartilage within the center of defect samples (or directly adjacent to pins in instances where pins were still visible and exposed on the cartilage surface) was then indented.

After osteochondral sample fixation and decalcification, defects were cut along their midplane to determine the thickness of cartilage samples. The compressive modulus, tensile modulus, and permeability of all indented samples was then quantified by fitting the collected creep data to a Hertzian biphasic model.³³

6.2.8 MicroCT and Histological Evaluation of Cartilage Defects

To qualitatively visualize any subchondral bone remodeling or bone resorption that occurred during the 12-week time course, explanted cartilage defects (and healthy tissue controls) were imaged via microCT as previously described.³⁴ Osteochondral samples were incubated in Lugol's solution overnight at room temperature and then imaged using a Scanco MicroCT 45 system (Scanco Medical, Southeastern, PA, USA; exposure: 600 ms, voltage: 55 kVp, isotropic voxel size: 10 μ m), with cross-sectional and top-down

images of samples acquired via DragonFly software (Object Research Systems, Montreal, Canada).

After microCT imaging, samples were fixed (10% formalin, 24-48h incubation overnight at 4°C) and decalcified via incubation in Formical-2000 for 4 weeks (solution changed weekly). Thereafter, samples were embedded in paraffin, sectioned (8 µm), and stained with Safranin O/Fast Green to visualize proteoglycan content and collagen content, respectively, within the repair cartilage and the underlying subchondral bone.

6.2.9 Statistical Analysis

All statistical analyses were performed using GraphPad Prism 9 software, with data reported as mean±standard deviation and significance for all performed analyses determined at $p < 0.05$. One-way ANOVAs were performed with Tukey's honestly significant difference (HSD) post-hoc testing to compare functional outcomes between porcine donors, cell viability across precultured composites (for different surgeries), and functional outcomes for the experimental groups investigated in the porcine model. Alternatively, Two-way ANOVAs were performed for the analysis of acellular and precultured composites' compressive moduli initially and 12 weeks after implantation, and multiple comparisons were performed with $\alpha = 0.05$ and Tukey's HSD post-hoc test.

6.3 RESULTS AND DISCUSSION

6.3.1 pMSC Donor Screen for Chondrogenic Potential

To evaluate the therapeutic efficacy of MEW-NorHA hydrogel composites for the repair of full-thickness cartilage defects, it was necessary to first validate that the composites support the chondrogenesis of adult porcine MSCs toward the formation of neocartilage. Importantly, adult pMSCs were selected as an allogenic cell source to

mitigate any potential immune responses upon implantation into porcine models.³⁵ Moreover, isolated pMSCs were age-matched to the host animals (12-14 mo.) to ensure that they best represented the clinically-relevant scenario in which autologous cells are sourced and used within implants.

Since donor variability is known to influence human MSC properties such as proliferation and differentiation,³⁶ pMSCs from three prospective porcine donors (Donors 1, 2, 3) were screened to identify a cell source with the requisite chondrogenic potential to form neocartilage when cultured in chondrogenic media for 28 days (**Figure 6.1a**). Given the age of the encapsulated adult pMSCs, it was expected that the mechanical properties and relative amounts of cartilaginous ECM components in these composites would be inferior to those observed in composites containing juvenile bovine MSCs (Chapter 5). However, increases in the compressive moduli of pMSC-laden composites were still observed over 28 days when compared to acellular composite controls (~100 kPa; Chapter 5, Figure 10).

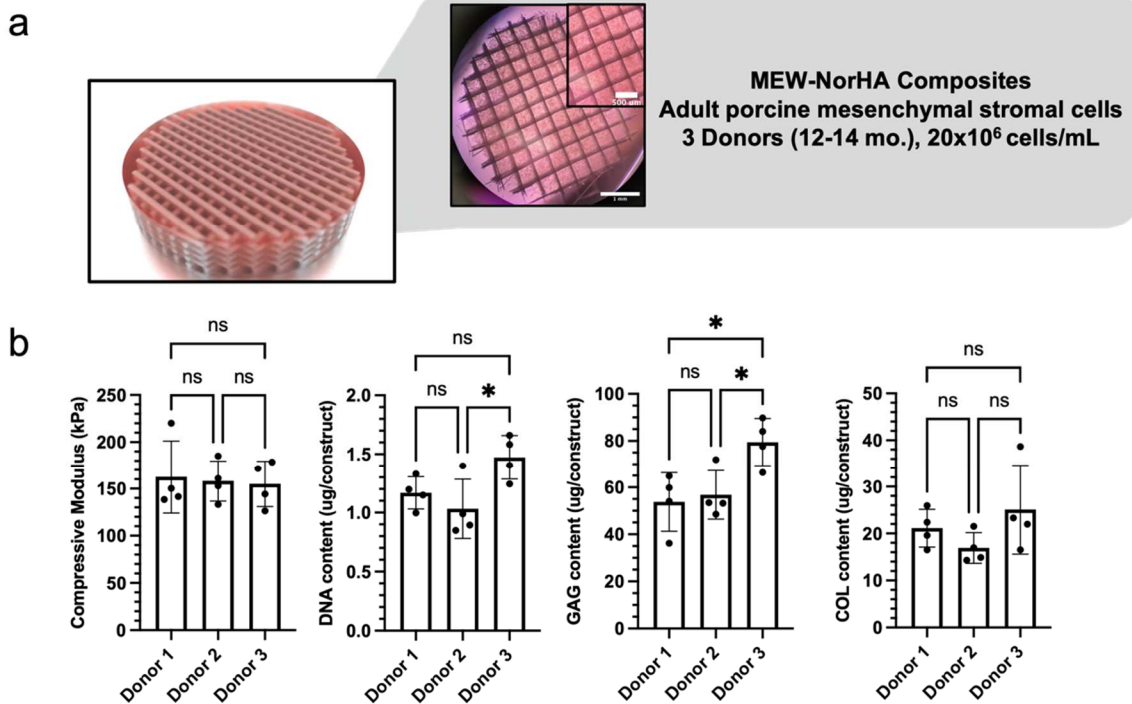


Figure 6.1: *In vitro* screening of porcine MSC donors. a) (Left) Schematic of the MEW-NorHA composites used to evaluate adult porcine mesenchymal stromal cells (pMSCs) sourced from three porcine donors. (Right) Images of MEW-NorHA composites containing encapsulated pMSCs during culture. b) (Left to right) Compressive modulus and biochemical contents (i.e., DNA, glycosaminoglycan (GAG) and collagen (COL) contents) of composites containing encapsulated adult porcine MSCs from 3 donors and cultured for 28 days in chondrogenic media. n=4, One-way ANOVA, *p<0.05, ns = not significant.

Minimal differences were observed across the donors with respect to the compressive moduli of composites cultured for 28 days (**Figure 6.1b**). However, The DNA content of composites cultured with pMSCs from Donor 3 was significantly higher than the DNA content of composites containing pMSCs from Donor 2 despite all the cell-laden composites being fabricated with the same density of encapsulated cells, suggesting that cells from Donor 3 may have an innately higher proliferative capacity. This data is qualitatively corroborated by the observation of faster expansion times for Donor 3 cells plated on tissue culture plastic (TCP) at a density of 6.67×10^3 cells/cm² when compared to other donors (data not shown). In addition, pMSCs isolated from Donor 3 and

encapsulated in composites led to neotissue with significantly higher sulfated glycosaminoglycan contents than composites containing pMSCs from Donor 1 or 2 (**Figure 6.1b**).

Evaluation of these composites via histology and immunohistochemistry also demonstrated that composites containing cells from Donors 1 and 3 stained significantly more intensely for sGAG and type I collagen (COL I) than composites containing cells from Donor 2 (**Figure 6.2**). However, the morphology of the encapsulated pMSCs, the relative distribution and organization of ECM, and the overall staining intensity was qualitatively comparable across all donors (**Figure 6.2**). Based on all these results, Donor 3 was selected as the primary allogenic cell source for all of the cell-laden composites fabricated and cultured for the animal study to maximize the chondrogenic potential and efficacy of precultured composite implants.

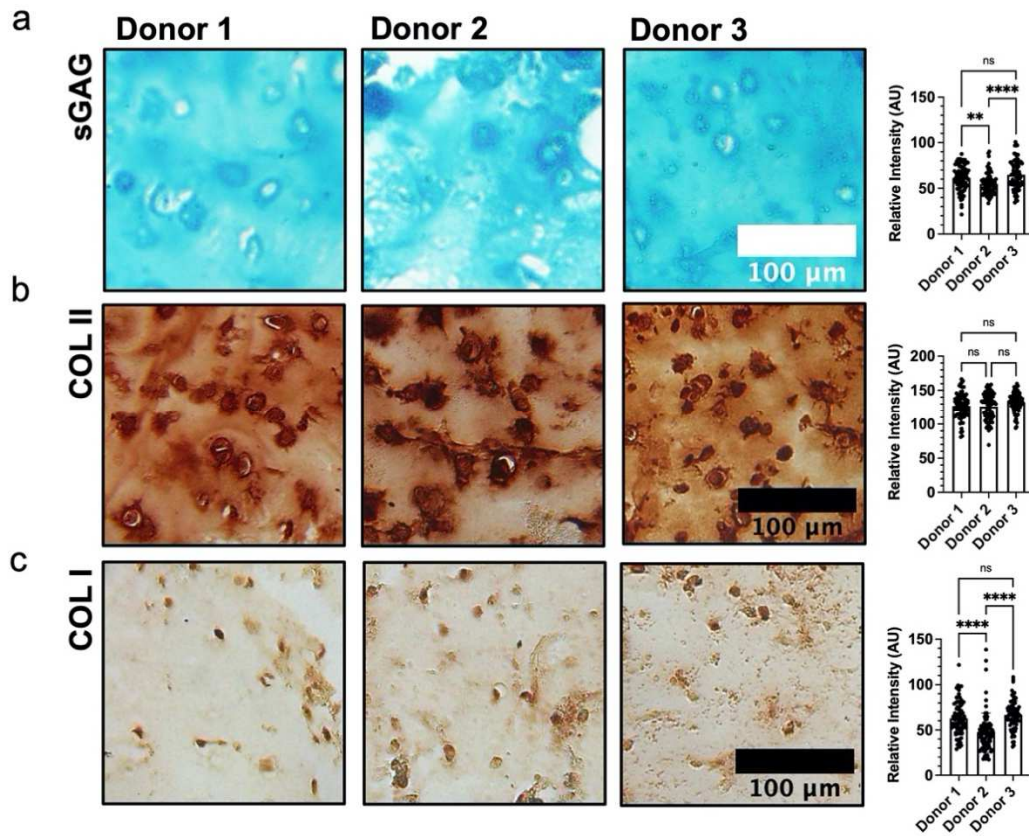


Figure 6.2: ECM staining of composites across porcine MSC donors. After 28 days of culture in chondrogenic media, ECM within composites containing encapsulated MSCs from three porcine donors is visualized via a) Alcian Blue staining (for sulfated glycosaminoglycans, sGAG), b) type II collagen (COL II) immunohistochemistry, and c) type I collagen (COL I) immunohistochemistry. a-c) Representative images (left) and quantification of staining intensity (right) to characterize a) sGAG, b) COL II, and c) COL I distribution and organization for 3 porcine donors. n=81 images, 9 sections, 3 composites; One-way ANOVA, ****p<0.0001, ns = not significant.

6.3.2 Animal Study Design

After screening porcine donors, the ability of MEW-NorHA composites to facilitate cartilage repair *in vivo* was evaluated in a porcine model of full-thickness cartilage damage (Figure 6.3a).¹⁰ Cartilage defects were created along the femoral trochlea of Yucatan minipigs to investigate the performance of implanted acellular and precultured (i.e., chondrogenic culture for 28 days in chondrogenic media) composites in comparison to

empty defect controls or defects treated with microfracture. To mitigate the potential influence of defect location on the performance of different experimental groups, treatment location was randomized across the performed surgeries.

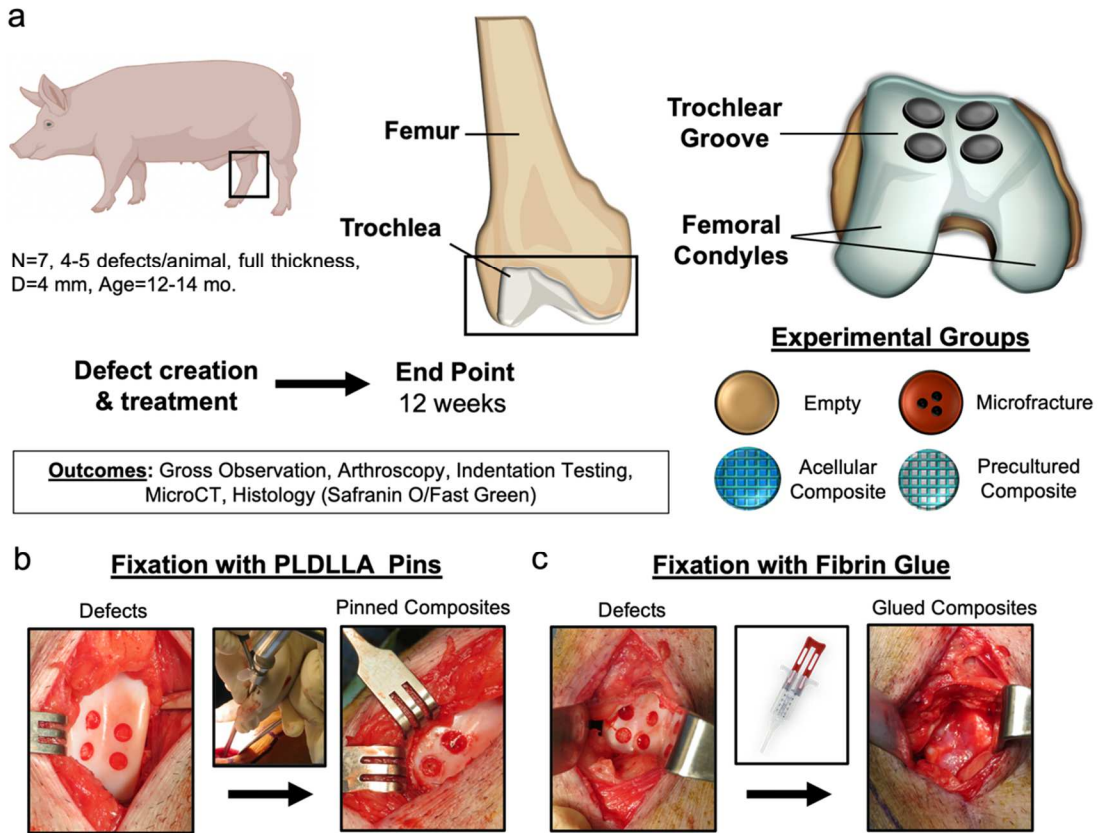


Figure 6.3: Overview of in vivo study design. a) Schematic of the animal model, experimental groups, and study design employed to evaluate MEW-NorHA composites for cartilage repair. Full-thickness cartilage defects are created along the trochlear groove of the patellofemoral joint (right, hind stifle joint) for seven pigs, with empty and microfracture controls and either acellular or precultured (chondrogenic media, Donor 3 pMSCs, 28 days) MEW-NorHA composites. 12 weeks after implantation, the quality of repair cartilage within each of these respective defects is evaluated via gross observation, arthroscopic imaging, mechanical testing, microCT, and histology. To ensure that implants are retained within the created cartilage defects, composites are fixed with either b) bioresorbable polylactic acid (PLA) pins or c) fibrin glue sealant. b-c) Representative images of defects formed along the trochlear groove (left) and composites fixed with either b) pins or c) fibrin glue (right).

Two distinct fixation methods were also investigated to identify how best to implant MEW-NorHA composites within cartilage defects: 1) pinning of composites to the underlying subchondral with bioresorbable PLDLLA (poly(l-lactide- co-d,l-lactide)) pins,

which degrade on the order of months, and 2) fixation with fibrin glue (**Figure 6.3b**). While the former fixation method has been previously shown to retain nanofibrous HA-based scaffolds within full-thickness porcine defects, it is also associated with appreciable subchondral bone remodeling.¹⁶ Alternatively, past results suggest that subchondral bone remodeling is attenuated with the use of fibrin glue,¹⁶ but that the retention of implants within defects is not significantly improved when compared to press-fitting alone.¹⁷ Given the previously reported advantages and limitations of these respective approaches, this study aimed to identify the fixation method most appropriate for use with MEW-NorHA composites.

Unilateral stifle joint surgeries were performed on a total of nine animals, such that $n \geq 4$ defects were created for each of the respective experimental groups: empty defects (n=5), defects treated with microfracture (n=5), pinned acellular composites ('Acellular+Pin', n=6), pinned precultured composites ('Precultured+Pin', n=4), glued acellular composites ('Acellular+FG', n=4), and glued precultured composites ('Precultured+FG', n=4). In two of the nine total animals, post-operative lateral patellar luxation was observed approximately 3 weeks after the initially performed surgery, compromising the animals' ability to ambulate or bear load on the right stifle; therefore, early euthanasia was elected. The observed patellar luxation in the first animal may likely be attributed to recovery-related complications, while the second instance of patellar luxation was accompanied by urticaria and incisional dehiscence consistent with a previously reported case of suture hypersensitivity in a Yucatan minipig.³⁷ For all other animals, repair cartilage within defects was evaluated via arthroscopy, gross observation, mechanical testing, microCT, and histology 12 weeks after the initial defect formation and treatment (**Figure 6.4**).

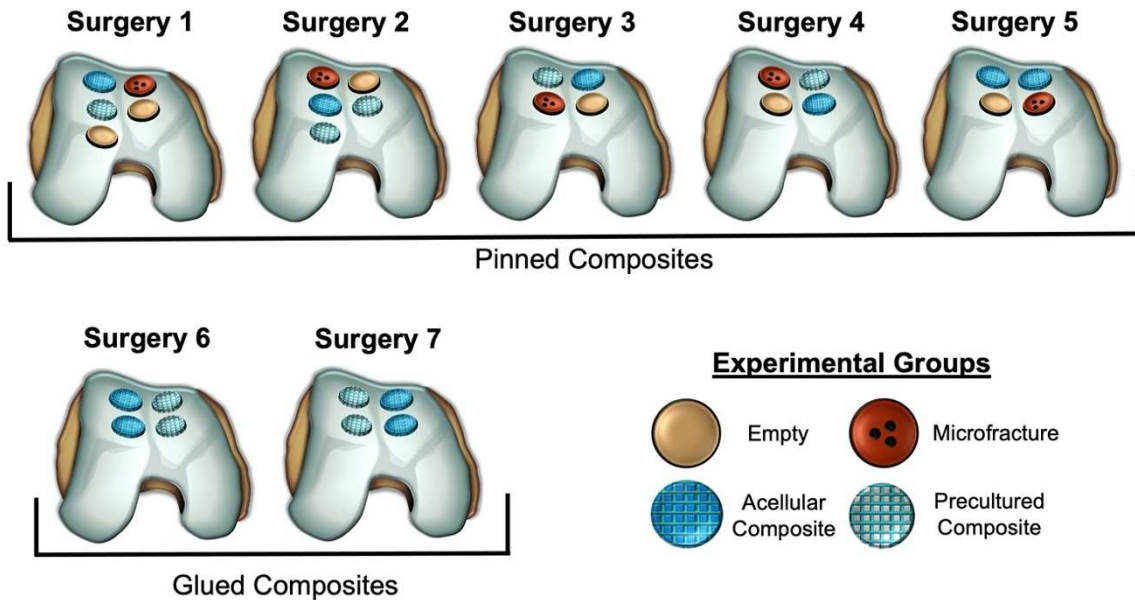


Figure 6.4: Overview of implant distributions for porcine surgeries. Representative schematics detailing the location of each experimental group (empty defect, microfracture therapy, acellular composite, precultured composite) along the operated trochlear groove for each respective animal. The location of experimental groups is varied across surgeries to account for any potential differences associated with defect location. Two animals experienced operation-related complications and did not complete the 12-week time course. For surgeries 1 and 2, an additional fifth defect is created on the lateral distal portion of the trochlea, as initial attempts to pin composites within the medial distal defects resulted in poor composite fixation. Composites are fixed within created cartilage defects using PLA pins for surgeries 1-5 and fibrin glue for surgeries 6 and 7.

Across all the surgeries in which precultured composites were implanted (Surgeries 1-4, 6-7), the viability of implants was investigated via live/dead staining of constructs after the first 7 days of culture in chondrogenic media (**Figure 6.5**). Importantly, no differences in cell viability were observed across precultured composites prepared for separate surgeries, and cell viability that is suitable for adult pMSCs was achieved across all the implants (~80%).

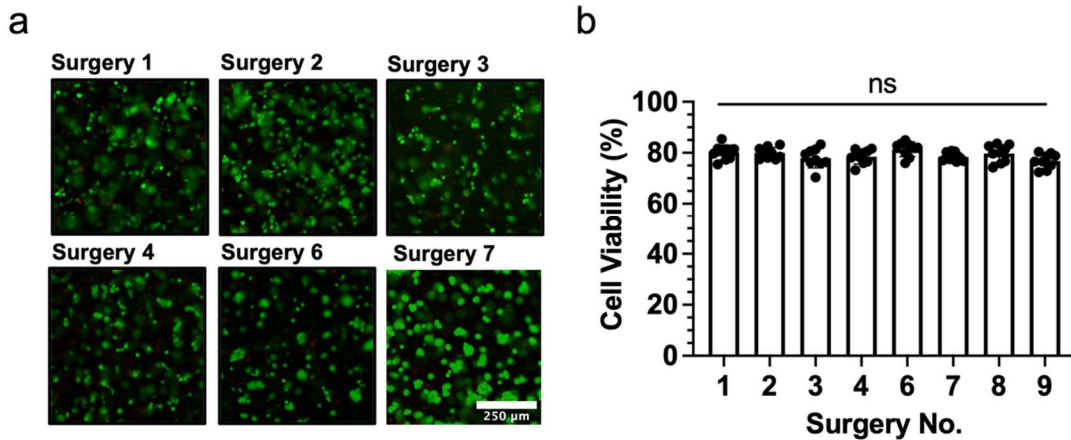


Figure 6.5: Cell viability of precultured composites for implantation in vivo. a) Representative images and b) quantification of cell viability for precultured composite implants stained 7 days after encapsulation for each of the respective performed animal surgeries to ensure the viability of implanted constructs. n=3, 9 images, One-way ANOVA, ns=not significant.

6.3.3 Evaluation of Repair Cartilage

To characterize the healing response within cartilage defects 12 weeks after surgery, repair cartilage was first assessed via arthroscopy (**Figure 6.6**).^{29,38} Although the appearance of defects varied across different animals, a number of features were conserved within each of the treatment groups. For example, empty defects were consistently filled and generally smooth but exhibited some fibrillation at the defect interface. Similarly, defects that were treated with microfracture consistently exhibited a smooth surface and complete defect filling, with intimate integration along the border of the defect. Given the size of the created defects (~0.13 cm²), these observations are consistent with the short-term repair outcomes seen clinically for defects <4 cm² that are treated with microfracture.³⁹ Pinned and glued composites however exhibited heterogeneous and incomplete defect filling, with apparent fissures along the defect border in defects treated with pinned composite. Glued composites resulted in similarly heterogeneous repair cartilage; however, in some instances, glued composites facilitated

complete defect filling and the formation of smooth cartilage that integrated with the surrounding tissue.

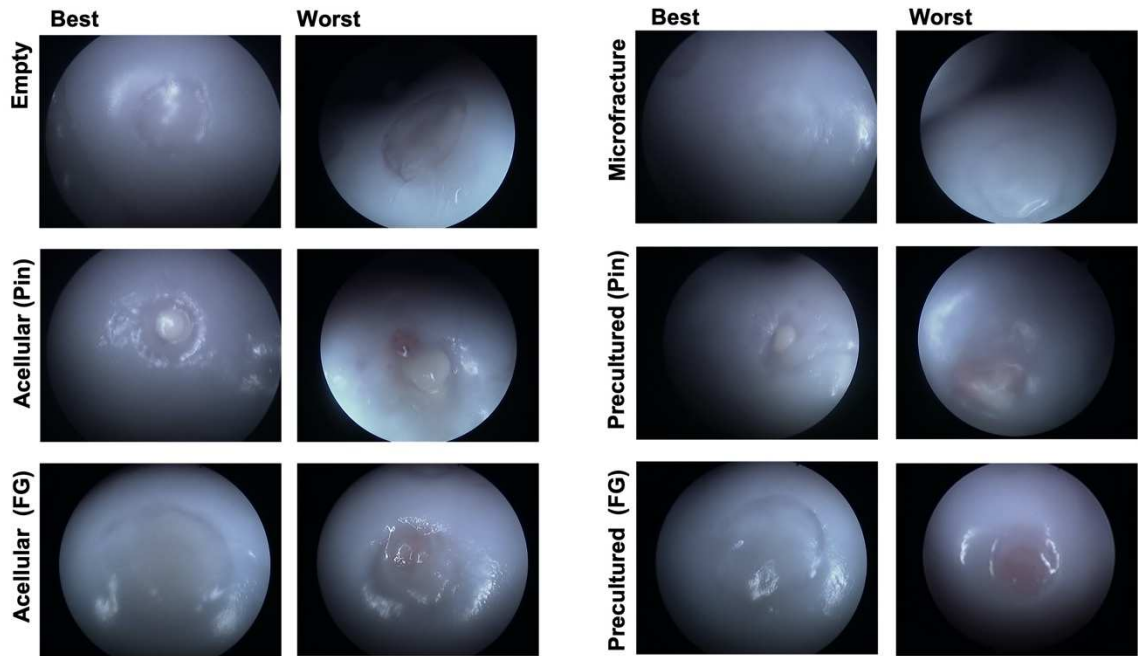


Figure 6.6: Arthroscopic observation of repair cartilage. Representative arthroscopy images of repair cartilage corresponding to each of the respective experimental groups 12 weeks after surgeries (FG = fibrin glue).

Macroscopic gross imaging of the femoral trochlea corroborated the trends observed via arthroscopy (**Figure 6.7**). Interestingly, 8 of the 10 defects investigated with pinned composites contained a visible pinhead after explanting the femoral trochlea; although it is expected that the pin would be retained within all defects after 12 weeks based on their previously reported degradation behavior, a 75% success rate of implant fixation was previously reported with the use of these pins in the same animal model. However, retention of implants within the two defects where the pin may not be readily seen may still have been achieved. Given the observation of pin failure in at least one instance (i.e., lateral distal defect in Surgery 2), it is possible that the pin head may have translocated away from the defect post-operatively. Alternatively, the formation of repair

cartilage around and/or above the pin may be obscuring the presence of underlying pins. For example, pinheads were observed in both lateral defects in Surgery 1, albeit further way from the articular surface (i.e., deeper) than what was observed in other samples.

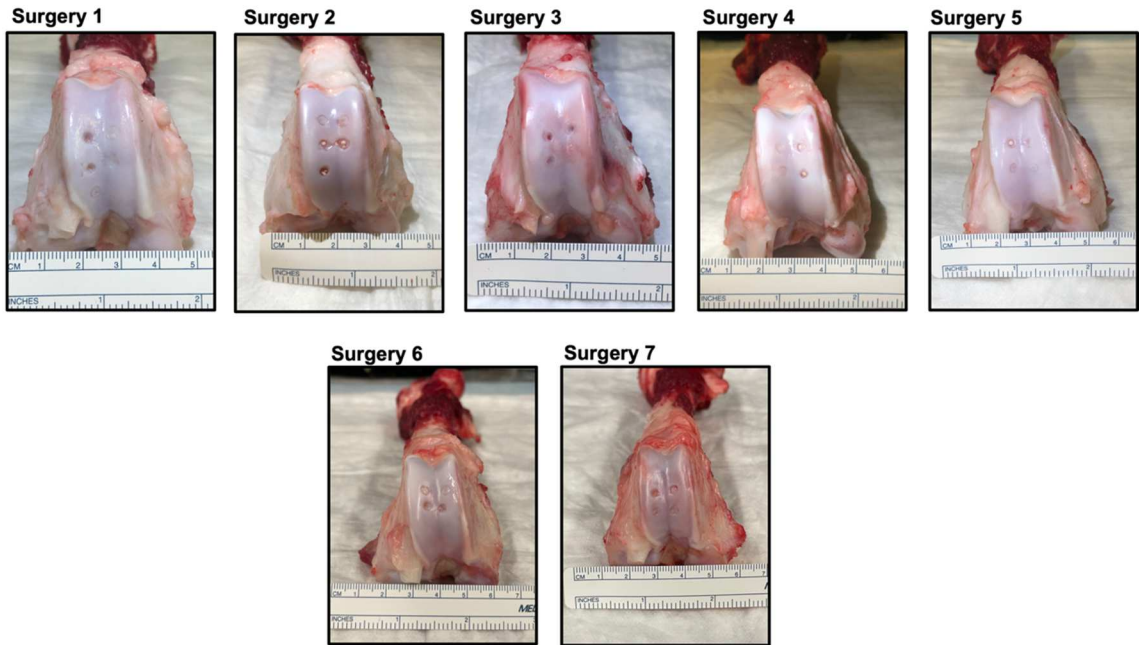


Figure 6.7: Gross observation of repair cartilage. Representative gross images of explanted trochlea 12 weeks after composite implantation.

Despite the apparent presence of pins in most defects after 12 weeks, India Ink staining of the opposing patellar surface did not reveal any damage or defects that may have been caused by the pins (**Figure 6.8**). Similarly, India ink staining confirmed that the patella remained undamaged by the use of fibrin glue for composite fixation.

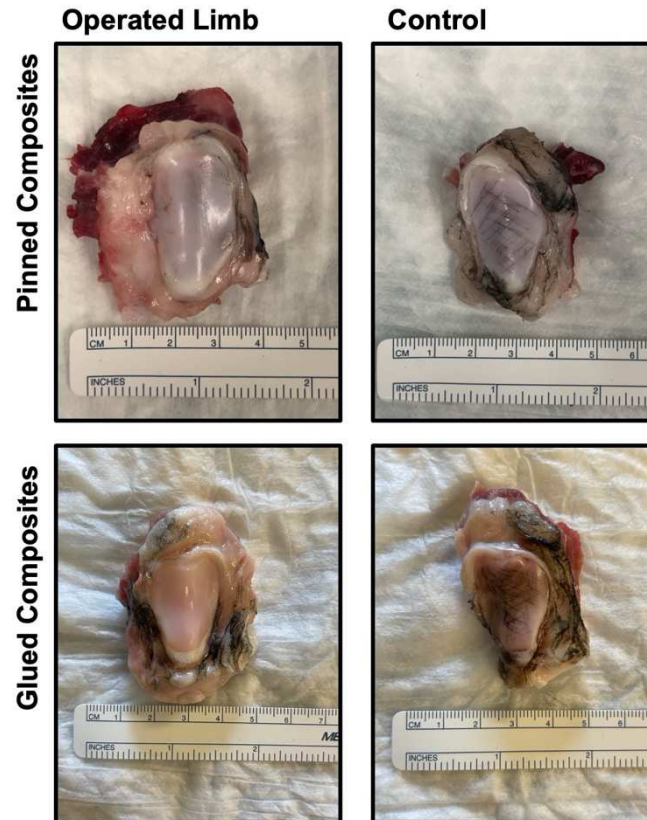


Figure 6.8: Gross observation of the opposing articulating surface. Representative images of patella explants 12 weeks after composite implantation. Patella explants are stained with India ink to reveal any potential damage caused by the presence of pins or glue on the opposing articulating surface. No appreciable staining is observed on the surface of the patella for joints that contained pinned or glued composites (left) when compared to positive controls (i.e., contralateral patella explants that were damaged with a scalpel) (right).

Generally, macroscopic images show that the volume of the pin used to fix composites qualitatively impeded the complete filling of defects containing acellular or precultured composites (**Figure 6.7**). Moreover, the potential contraction of composites upon formation of pilot holes or the application of the fixation guide (for the insertion of pins through composites and into the subchondral bone) may have perturbed the composite-native tissue interface, further influencing defect fill and repair cartilage integration. The appearance of repair cartilage in defects treated with acellular and

precultured composites varied considerably. In some instances, damage to the subchondral bone and adjacent cartilage was evident (e.g., Surgery 2), while in other examples repair tissue adjacent to the pin was white and level with the adjacent tissue (e.g. Surgery 4).³⁰ Empty defects and defects treated with microfracture consistently filled with white repair cartilage, but possessed fissures and fibrillated rough surfaces in most instances (**Figure 6.7**).³⁰

Improved defect fill and macroscopic appearance was observed for composites fixed within defects using fibrin glue in lieu of pins; however, at least one defect appeared to be entirely empty (Surgery 7, lateral proximal defect), while the appearance of repair cartilage in defects containing glued acellular and precultured composites was variable (**Figure 6.7**). Specifically, both groups exhibited instances where complete defect fill was achieved and a homogenous, smooth cartilage surface was observed; in parallel, other defects partially filled at smaller depths with more apparent fissures.³⁰

MicroCT was performed on all the cartilage defects to qualitatively assess the relative amounts of bone resorption associated with each of the respective treatment groups (**Figure 6.9**). While some degree of bone resorption is qualitatively observed across all experimental groups via microCT, including in empty defects alone as previously reported,²⁷ resorption is especially pronounced in defects treated with microfracture or pinned composites. Importantly, subchondral bone remodeling may compromise the long-term stability of any repair cartilage formed in the overlying defect, or alternatively give rise to differential osteochondral loading, leading to the progression of OA.⁴⁰

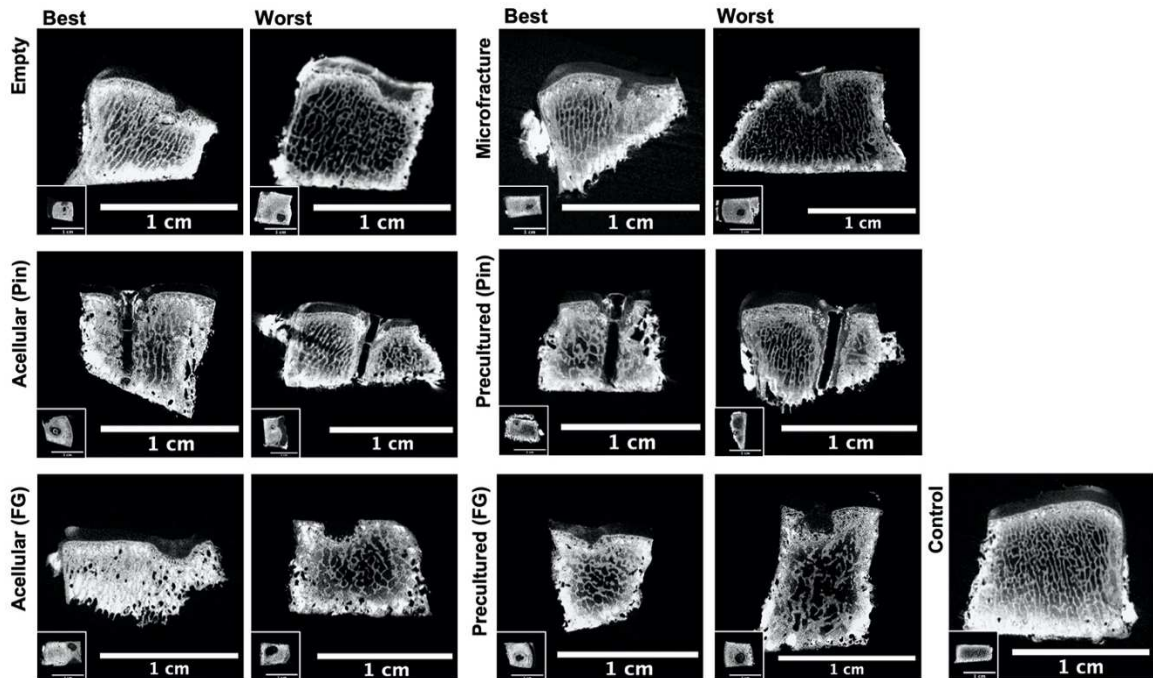


Figure 6.9: MicroCT scans of cartilage defects and underlying subchondral bone. Representative cross-sectional images 12 weeks after surgeries (FG=fibrin glue). Insets show the top-down view for each defect. Control osteochondral samples are isolated from the most distal portion of the trochlea for qualitative comparisons.

To gain insight into the composition of repair cartilage within each of the cartilage defects, Safranin O/Fast Green staining was performed (**Figure 6.10**).⁴¹ All the experimental groups resulted in variable repair tissue staining and morphology across animals. Empty and microfracture groups however stained with Safranin O and Fast Green consistently, suggesting the abundant presence of both proteoglycans and collagen within defects. Importantly, integration of nascent tissue can be visualized with the adjacent healthy tissue. Acellular and precultured composites that were pinned however exhibited marginal Safranin O staining, even adjacent to the pin. When composites were fixed within defects via application of fibrin glue, the best-performing samples exhibited significant proteoglycan content and distribution, as evidenced by Safranin O staining comparable to what was observed for control groups. To this end, the

Safranin O staining intensity was higher in precultured composites than in acellular composites, suggesting that the formation of nascent tissue prior to implantation via chondrogenic preculture period may help to mediate repair cartilage maturation. However, across all the defects that filled with significant proteoglycans, tissue morphology consistent with fibrocartilage was observed.

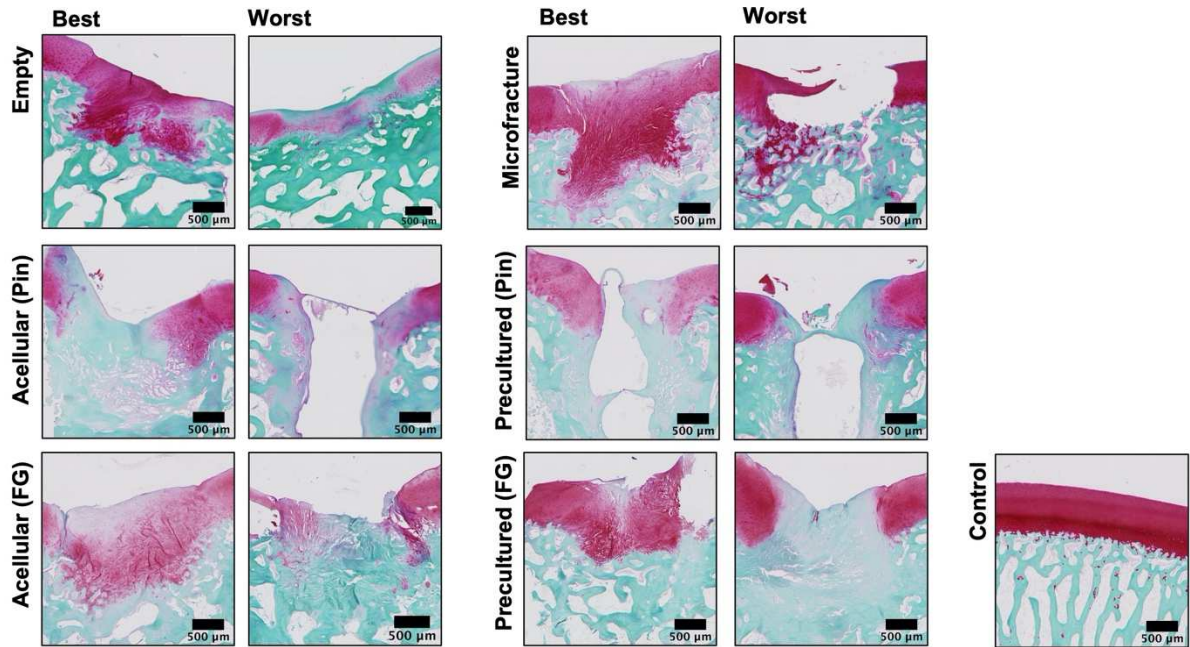


Figure 6.10: Safranin O /Fast Green staining of repair cartilage. Representative cross-sectional images showing the center of cartilage defects for each of the respective experimental groups 12 weeks after surgeries (FG=fibrin glue). Control osteochondral samples are isolated from the most distal portion of the trochlea for qualitative comparisons.

Finally, the functional properties of repair cartilage were evaluated via indentation creep testing, which enables the *in situ* mechanical testing of tissues within defects to elucidate the compressive modulus, tensile modulus, and permeability (**Figure 6.11**). The measured average compressive modulus of repair cartilage across all the experimental groups did not exceed 0.4 MPa, suggesting that repair cartilage possessed inferior mechanical properties when compared to previously reported modulus values for native cartilage.⁴² Indentation testing of healthy tissue controls isolated from the most distal

region of the lateral trochlear groove (compressive modulus = 2.00 ± 0.64 MPa) confirmed that each treatment group led to only partial restoration of the defect's biomechanical function.

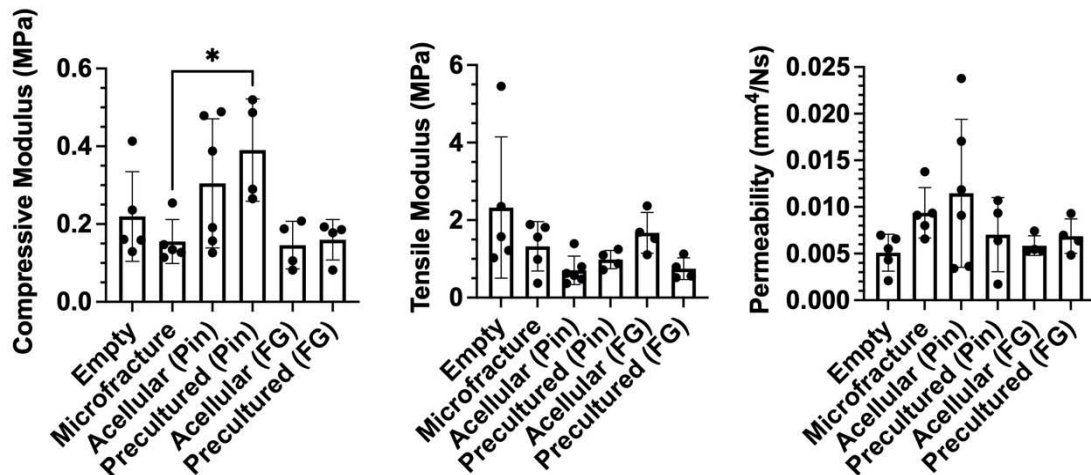


Figure 6.11: Indentation testing of repair cartilage. The compressive moduli (left), tensile moduli (middle) and permeability (right) of explanted repair cartilage quantified via Hertzian biphasic creep testing 12 weeks after surgeries (FG=fibrin glue). $n \geq 4$, One-way ANOVA, * $p < 0.05$.

Statistical differences in compressive modulus were observed between defects treated with microfracture and pinned precultured composites, and pinned composites possessed higher compressive moduli than glued composites. However, the elevated compressive moduli observed for pinned acellular and precultured composites may potentially be due to the presence of the pin within the defect. Careful attention was given to ensure that all indentation tests were performed on tissues adjacent and away from pins toward to avoid any contribution of the pin to the mechanical properties. Since the pins were also inserted into composites perpendicular to the cartilage surface, it is unlikely that pins were inadvertently underlying tested regions of interest. An alternative source for these observed differences in compressive modulus may be the recruitment of endogenous cells during the formation of pilot holes into the subchondral bone, (i.e., combinations of composites with a single microfracture hole).

In accordance with the tension-compression non-linearity observed in healthy articular cartilage, the repair cartilage in all of the experimental groups exhibited tensile moduli that were appreciably larger than their respective compressive moduli;⁴³ however, no significant trends were otherwise observed across groups. The permeability of repair cartilage across experimental groups is expected to have an inverse relationship with the compressive and tensile moduli, but this trend is only observed for the latter, further highlighting the variability of the measured mechanical properties.

Despite the variability in healing response observed across all the experimental groups, when comparing composites only with their baseline properties prior to implantation, the compressive modulus of all implanted composites increased over time, suggesting delivered and/or endogenous cells mediated the elaboration, maturation, and/or remodeling of nascent repair tissue (**Figure 6.12**).

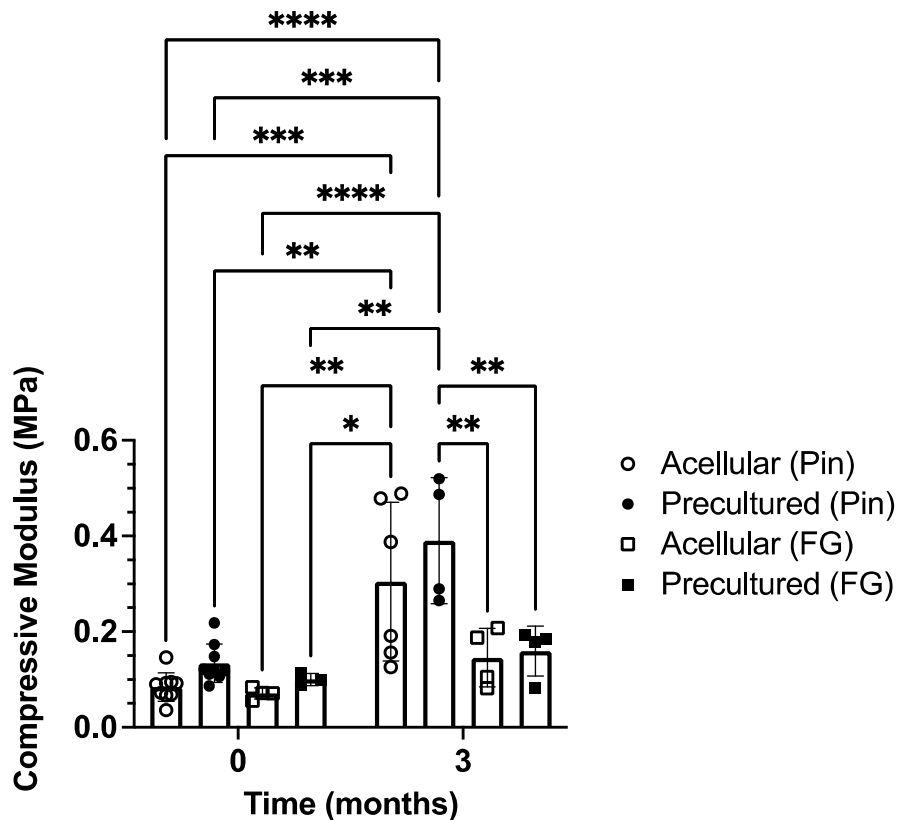


Figure 6.12: Mechanical properties of composites before and after implantation. The compressive moduli of acellular and precultured composites quantified via Hertzian biphasic creep testing both prior to implantation in animals (for both fixation methods; FG=fibrin glue) and 12 weeks after the initial surgeries. Increases in the mechanical properties of all composites are observed 12 weeks after implantation. $n \geq 4$, Two-way ANOVA, $*p < 0.05$.

6.4 CONCLUSIONS

Previously developed composites of MEW-NorHA were successfully translated to adult porcine MSCs that exhibited viability, chondrogenesis, and cartilage formation during culture. Further, fixation methods and the capacity of MEW-NorHA composites to facilitate repair cartilage within full-thickness chondral defects were evaluated. Despite their ability to form neocartilage *in vitro* with multiple porcine donors, composites with chondrogenic preculture did not exhibit any marked improvements over the quality of cartilage formed via control microfracture treatment. Arthroscopic and gross observation of defects

demonstrated that significant variability exists across all the experimental groups, with the most pronounced differences observed within composite groups. While the use of PLDLLA pins appears to have ensured the retention of composites within defects, the size of the pins relative to the defect size may have compromised the ability for repair tissue to completely fill defects; moreover, the loading imparted by the pinning process itself could have adversely impacted the outcomes of pinned composite groups by compromising the mechanical properties of composites and or contracting the composites, causing them to sink in defects and poorly integrate with peripheral tissue. In contrast, fixation of composites with fibrin glue led to repair cartilage with improved gross appearance and more complete defect filling.

With these results in mind, it is clear that further improvements in fixation, overall cartilage properties, and the animal model selected are needed for a thorough assessment of composites. While retention of samples with fibrin glue may be less reliable, the reduced subchondral bone remodeling taken together with the improved ECM contents, as evidenced by histology, suggests that future approaches for cartilage repair with MEW-reinforced hydrogels should leverage fibrin glue over bioresorbable pins. To this end, the composite design may be further improved towards increasing the prospects of this approach. Namely, improved fixation and integration may be achieved through the incorporation of tissue-adhesive hydrogels,⁴⁴ while the chondrogenic potential of adult pMSCs may be augmented via coculture with chondrocytes,⁴⁵ the presentation of signaling cues that recapitulate the cell-cell interactions present during mesenchymal condensation (i.e. N-cadherin mimetic peptide HAVDI), or the sustained delivery of growth factor such as TGF- β 3 *in vivo*.^{21,45,46} Lastly, the 4 mm defect selected in this model is quite small ($\sim 0.13 \text{ cm}^2$) and repaired well with both untreated and microfracture controls. To this end, it is important to note that this defect size is within the indicated range that

microfracture would be clinically recommended.¹ Therefore, the comparisons made between microfracture surgery and composite implantation in this study likely do not illustrate the composites' potential advantages in repairing defects that would be otherwise challenging to repair (i.e., larger defects approaching or greater than 4 cm²).

6.5 REFERENCES

1. Kalson, N. S., Gikas, P. D. & Briggs, T. W. R. Current strategies for knee cartilage repair. *Int. J. Clin. Pract.* **64**, 1444–1452 (2010).
2. Everhart, J. S., Abouljoud, M. M. & Flanigan, D. C. Role of full-thickness cartilage defects in knee osteoarthritis (OA) incidence and progression: Data from the OA Initiative. *J. Orthop. Res.* **37**, 77–83 (2019).
3. Carey, J. L. Fibrocartilage Following Microfracture Is Not as Robust as Native Articular Cartilage Commentary. *J. Bone Jt. Surg.* **94**, e80 (2012).
4. Martín, A. R., Patel, J. M., Zlotnick, H. M., Carey, J. L. & Mauck, R. L. Emerging therapies for cartilage regeneration in currently excluded ‘ red knee ’ populations. *npj Regen. Med.* **4**, (2019).
5. Johnstone, B., Stoddart, M. J. & Im, G. II. Multi-Disciplinary Approaches for Cell-Based Cartilage Regeneration. *J. Orthop. Res.* **38**, 463–472 (2020).
6. Bothe, F. *et al.* Treatment of focal cartilage defects in minipigs with zonal chondrocyte/mesenchymal progenitor cell constructs. *Int. J. Mol. Sci.* **20**, 1–17 (2019).
7. Diloksumpan, P. *et al.* The Complexity of Joint Regeneration: How an Advanced Implant could Fail by Its In Vivo Proven Bone Component. *J. Trial Error* (2021). doi:10.36850/e3
8. Mancini, I. A. D. *et al.* A composite hydrogel-3D printed thermoplast osteochondral anchor as example for a zonal approach to cartilage repair: In vivo performance in a long-term equine model. *Biofabrication* **12**, (2020).
9. Sennett, M. L. *et al.* Long term outcomes of biomaterial -mediated repair of focal cartilage defects in a large animal model. *Eur. Cells Mater.* **41**, 40–51 (2021).

10. McIlwraith, C. W. & Frisbie, D. D. Animal models for cartilage regeneration. *Eur. Cells Mater.* **20**, 22 (2010).
11. Ahern, B. J., Parvizi, J., Boston, R. & Schaer, T. P. Preclinical animal models in single site cartilage defect testing: a systematic review. *Osteoarthr. Cartil.* **17**, 705–713 (2009).
12. Mancini, I. A. D. *et al.* Fixation of Hydrogel Constructs for Cartilage Repair in the Equine Model: A Challenging Issue. *Tissue Eng. - Part C Methods* **23**, 804–814 (2017).
13. Gotterbarm, T., Breusch, S. J., Schneider, U. & Jung, M. The minipig model for experimental chondral and osteochondral defect repair in tissue engineering: Retrospective analysis of 180 defects. *Lab. Anim.* **42**, 71–82 (2008).
14. Drobnič, M., Radosavljevič, D., Ravnik, D., Pavlovčič, V. & Hribernik, M. Comparison of four techniques for the fixation of a collagen scaffold in the human cadaveric knee. *Osteoarthr. Cartil.* **14**, 337–344 (2006).
15. Duchow, J., Hess, T. & Kohn, D. Primary stability of press-fit-implanted osteochondral grafts: Influence of graft size, repeated insertion, and harvesting technique. *Am. J. Sports Med.* **28**, 24–27 (2000).
16. Patel, J. M. *et al.* Resorbable Pins to Enhance Scaffold Retention in a Porcine Chondral Defect Model. *Cartilage* (2020). doi:10.1177/1947603520962568
17. Efe, T. *et al.* Fibrin glue does not improve the fixation of press-fitted cell-free collagen gel plugs in an ex vivo cartilage repair model. *Knee Surgery, Sport. Traumatol. Arthrosc.* **20**, 210–215 (2012).
18. Friedman, J. M. *et al.* Comparison of Fixation Techniques of 3D-Woven Poly(ϵ -Caprolactone) Scaffolds for Cartilage Repair in a Weightbearing Porcine Large Animal Model. *Cartilage* **9**, 428–437 (2018).

19. Hunziker, E. B. & Stähli, A. Surgical Suturing of Articular Cartilage Induces Osteoarthritis- Like Changes. *Bone* **23**, 1–7 (2008).
20. Vikingsson, L. *et al.* Implantation of a polycaprolactone scaffold with subchondral bone anchoring ameliorates nodules formation and other tissue alterations. *Int. J. Artif. Organs* **38**, 659–666 (2015).
21. Vega, S. L. *et al.* Combinatorial hydrogels with biochemical gradients for screening 3D cellular microenvironments. *Nat. Commun.* **9**, 614 (2018).
22. Castilho, M. *et al.* Mechanical behavior of a soft hydrogel reinforced with three-dimensional printed microfibre scaffolds. *Sci. Rep.* **8**, 1245 (2018).
23. Kim, M., Erickson, I. E., Choudhury, M., Pleshko, N. & Mauck, R. L. Transient exposure to TGF- β 3 improves the functional chondrogenesis of MSC-laden hyaluronic acid hydrogels. *J. Mech. Behav. Biomed. Mater.* **11**, 92–101 (2012).
24. Kwon, M. Y. *et al.* Dose and Timing of N-Cadherin Mimetic Peptides Regulate MSC Chondrogenesis within Hydrogels. *Adv. Healthc. Mater.* **7**, (2018).
25. Pfeifer, C. G. *et al.* Age-Dependent Subchondral Bone Remodeling and Cartilage Repair in a Minipig Defect Model. *Tissue Eng. - Part C Methods* **23**, 745–753 (2017).
26. Zlotnick, H. M. *et al.* Marked differences in local bone remodelling in response to different marrow stimulation techniques in a large animal. *Eur. Cells Mater.* **41**, 546–557 (2021).
27. Fisher, M. B. *et al.* Cartilage repair and subchondral bone remodeling in response to focal lesions in a mini-pig model: Implications for tissue engineering. *Tissue Eng. - Part A* **21**, 850–860 (2015).
28. Cravens, M. G., Behn, A. W. & Dragoo, J. L. Comparison of mechanical compressive properties of commercial and autologous fibrin glues for tissue

- engineering applications. *Clin. Biomech.* **49**, 34–39 (2017).
29. Smith, G. *et al.* Arthroscopic Assessment of Cartilage Repair: A Validation Study of 2 Scoring Systems. *Arthrosc. J. Arthrosc. Relat. Surg.* **21**, 1462–1467 (2005).
 30. Goebel, L. *et al.* Experimental scoring systems for macroscopic articular cartilage repair correlate with the MOCART score assessed by a high-field MRI at 9.4 T - comparative evaluation of five macroscopic scoring systems in a large animal cartilage defect model. *Osteoarthr. Cartil.* **20**, 1046–1055 (2012).
 31. Stoeckl, B. D. *et al.* The porcine accessory carpal bone as a model for biologic joint replacement for trapeziometacarpal osteoarthritis. *Acta Biomater.* **129**, 159–168 (2021).
 32. Patel, J. M., Wise, B. C., Bonnevie, E. D. & Mauck, R. L. A Systematic Review and Guide to Mechanical Testing for Articular Cartilage Tissue Engineering. *Tissue Eng. - Part C Methods* **25**, 593–608 (2019).
 33. Moore, A. C., DeLucca, J. F., Elliott, D. M. & Burris, D. L. Quantifying Cartilage Contact Modulus, Tension Modulus, and Permeability with Hertzian Biphasic Creep. *J. Tribol.* **138**, 1–7 (2016).
 34. Erickson, I. E. *et al.* Improved cartilage repair via in vitro pre-maturation of MSC-seeded hyaluronic acid hydrogels. *Biomed. Mater.* **7**, (2012).
 35. Fisher, M. B. *et al.* Effects of Mesenchymal Stem Cell and Growth Factor Delivery on Cartilage Repair in a Mini-Pig Model. *Cartilage* **7**, 174–184 (2016).
 36. Qayed, M., Copland, I. & Galipeau, J. *Allogeneic Versus Autologous Mesenchymal Stromal Cells and Donor-to-Donor Variability. Mesenchymal Stromal Cells* (Elsevier Inc., 2017). doi:10.1016/b978-0-12-802826-1.00004-0
 37. Collins, D. & Simons, B. Significantly delayed polyglactin 910 suture-related pseudoinfection in a Yucatan pig. *BMC Vet. Res.* **16**, 1–7 (2020).

38. Brittberg, M. & Winalski, C. S. Evaluation of cartilage injuries and repair. *J. Bone Jt. Surg. - Ser. A* **85**, 58–69 (2003).
39. Mithoefer, K., Mcadams, T., Williams, R. J., Kreuz, P. C. & Mandelbaum, B. R. Clinical efficacy of the microfracture technique for articular cartilage repair in the knee: An evidence-based systematic analysis. *Am. J. Sports Med.* **37**, 2053–2063 (2009).
40. Donell, S. Subchondral bone remodelling in osteoarthritis. *EFORT Open Rev.* **4**, 221–229 (2019).
41. Mainil-Varlet, P. *et al.* A new histology scoring system for the assessment of the quality of human cartilage repair: ICRS II. *Am. J. Sports Med.* **38**, 880–890 (2010).
42. Mansour, J. M. Biomechanics of Cartilage. *Kinesiol. Mech. pathomechanics Hum. Mov.* 66–79 (2009). doi:10.1002/art.23548
43. Huang, C.-Y., Mow, V. C. & Ateshian, G. A. The Role of Flow-Independent Viscoelasticity in the Biphasic Tensile and Compressive Responses of Articular Cartilage. *J. Biomech. Eng.* **123**, 410–417 (2001).
44. Zhang, X., Jiang, Y., Han, L. & Lu, X. Biodegradable polymer hydrogel-based tissue adhesives: A review. *Biosurface and Biotribology* **7**, 163–179 (2021).
45. Kim, M., Steinberg, D. R., Burdick, J. A. & Mauck, R. L. Extracellular vesicles mediate improved functional outcomes in engineered cartilage produced from MSC/chondrocyte cocultures. *Proc. Natl. Acad. Sci. U. S. A.* **116**, 1569–1578 (2019).
46. Patel, J. M., Saleh, K. S., Burdick, J. A. & Mauck, R. L. Bioactive factors for cartilage repair and regeneration: Improving delivery, retention, and activity. *Acta Biomater.* **93**, 222–238 (2019).

CHAPTER 7: DIGITAL LIGHT PROCESSING OF MACROPOROUS AND HYDROLYTICALLY DEGRADABLE NORHA_{CA} HYDROGELS FOR USE WITH AUTOLOGOUS MATRIX-INDUCED CHONDROGENESIS

7.1 INTRODUCTION

Despite the multitude of biofabrication approaches implemented for the repair of articular cartilage to date, including a large number of bioprinting strategies for the fabrication of cell-laden implants,¹ few if any have successfully translated into the clinic and improved patient outcomes. Existing clinical repair strategies that employ the delivery of cells to afflicted patients such as autologous chondrocyte implantation (ACI) and matrix-assisted ACI (MACI) also suffer from several limitations. For example, therapies that employ autologous cells from patients require multiple surgeries and significant time to both isolate and expand cells *in vitro* to achieve sufficient cell numbers for therapeutic benefit. Moreover, these autologous cells may exhibit attenuated chondrogenic potential if isolated from either older patients and/or diseased tissues. Donor site morbidity has also been previously reported for instances in which chondrocytes are isolated for ACI. Even with the successful isolation and expansion of a cell source, additional challenges remain such as ensuring the retention of viable cells and maintaining their chondrogenic differentiation.

An alternative approach to these therapies and the cell-based approaches explored in Chapters 4-6 is the use of acellular scaffolds as a medium to provide both mechanical support and physiochemical cues to endogenous cells. Autologous matrix-induced chondrogenesis (AMIC) is clinically employed to treat isolated osteochondral lesions ($\leq 1.5 \text{ cm}^2$ in size) via combining subchondral microfracture with the fixation of a collagen membrane using fibrin glue.^{2,3} As a one-stage procedure, AMIC circumvents a number of the highlighted challenges associated with MACI and other cell-based

approaches, while achieving comparable patient outcomes in the short term (i.e., 2 years). The inclusion of a collagen scaffold with microfracture has been shown to improve the retention of recruited stromal cells, while also providing mechanical support to the blood clot against shear forces generated within the joint.⁴ Moreover, it is believed that AMIC addresses a number of the limitations associated with conventional microfracture alone, including insufficient defect filling and limited formation of hyaline tissue.⁵ To this end, a randomized control trial comparing patient outcomes for 47 patients treated with either AMIC or microfracture showed that AMIC results in significantly improved cartilage repair, with filled defects and functional tissue observed 5 years after treatment.⁶ While additional studies are needed to characterize the performance of AMIC relative to other repair strategies such as ACI and MACI,³ the general prospects for AMIC may be significantly improved, especially in instances where cartilage defects are large,⁵ by enhancing the ability of implanted scaffolds to promote and facilitate MSC chondrogenesis.

While collagen has been used in clinical AMIC procedures, there is interest in the engineering of alternatives that may provide improved outcomes through their design. The ideal scaffold for AMIC should exhibit a degradation rate that is matched to the rate of neocartilage formation, such that tissue maturation and remodeling can occur over time without impedance from the presence of the scaffold.⁷ However, the scaffold must also persist long enough to ensure that recruited cells are able to deposit and engage with nascent matrix at early timepoints.^{7,8} Additionally, scaffolds for AMIC must enable or support the infiltration of endogenous cells from the bone marrow to ensure that ECM is deposited throughout the entirety of the scaffold and integrates with the surrounding tissue.⁹ To this end, macroporous constructs with high degree of interstitial pores are required to facilitate the filling and distribution of marrow throughout the full thickness of the scaffold and defect. It is also important that the scaffold possess suitable mechanical

properties so that it may stabilize the initial blood clot formed during microfracture, ensuring that cartilage defect remains entirely filled with recruited cells. Finally, scaffolds engineered for AMIC should be amenable to growth factor delivery towards improving the chondrogenic potential of cells. There have been a number of approaches to engineer scaffolds that meet these properties, including with multipolymer electrospun scaffolds (i.e., composed of PCL and HA),¹⁰ electrospun HA scaffolds,¹¹ and a number of commercial scaffolds;¹² these include photocrosslinkable PEG hydrogels (ChonDux), freeze-dried polyglycolic-HA scaffolds with loaded chemoattractant (Chondrotissue), and autologous scaffolds that form upon mixing of patient's whole blood with chitosan glycerol phosphate (BSTCarGel).¹² In addition, composite hydrogels with these properties were recently bioprinted with chondroprogenitor cells into porous films towards the delivery of paracrine signals to recruited MSCs in an adapted AMIC approach.¹³

In response to the challenges of cell-based approaches for cartilage repair and the findings of Chapter 6, the aim of this study is to fabricate a novel acellular scaffold that encompasses each of these design considerations for future investigation in the treatment of cartilage defects via AMIC. NorHA macromers are engineered using an alternative chemistry from that which was used in Chapters 4-6 to obtain NorHA with hydrolytically labile pendant norbornene groups (NorHA_{CA}). Hydrolytically degradable step-growth hydrogels with a range of mechanical properties and degradation behaviors are then fabricated, and a computational model is developed to relate the stochastic degradation of NorHA_{CA} crosslinks to macroscopic gel properties over time. It is expected that the continued development of this model will assist with hydrogel characterization, and eventually, help predict the degradation behavior of prospective NorHA_{CA} hydrogel formulations for use in AMIC. Unlike the scaffolds currently employed clinically in AMIC, the developed NorHA_{CA} hydrogels are processed via digital light processing (DLP), which

permits precise control over the scaffold geometry towards achieving optimal infilling of marrow (from subchondral microfracture) within the implant.

7.2 METHODS

7.2.1 Materials

Sodium hyaluronic acid was purchased from Lifecore Biomedical (Chaska, MN) and lithium phenyl-2,4,6-trimethylbenzoylphosphinate (LAP) was purchased from Colorado Photopolymer Solutions (Boulder, CO). Unless otherwise specified, all other reagents and materials were purchased from Sigma-Aldrich (St. Louis, MO).

7.2.2 NorHA_{CA} Synthesis, Hydrogel Fabrication, and Photocrosslinking

HA modified with hydrolytically labile norbornene functional groups (NorHA_{CA}) was synthesized via an esterification reaction with carbic anhydride. HA was dissolved in DI water and titrated to pH~8.7 with 1 N NaOH. Carbic anhydride was then added dropwise (20 molar equivalents relative to HA) throughout the first two hours of the reaction. pH was maintained between 8.4 and 8.6 by continued addition of NaOH for the duration of the reaction (3 to 3.5 hours). Thereafter, the reaction solution was stirred overnight at 4 °C, and further titrated to a pH of 8.5 (so that the HA would react with any remaining carbic anhydride that had not yet been hydrolyzed) the next day. The reaction solution was then frozen and lyophilized. Multiple degrees of modification of HA with norbornene were targeted by changing the concentration of HA and the reaction time. To quantify degree of modification, samples were analyzed via ¹H-NMR spectroscopy (Bruker Neo400 360 MHz; **Figure 7.1**).

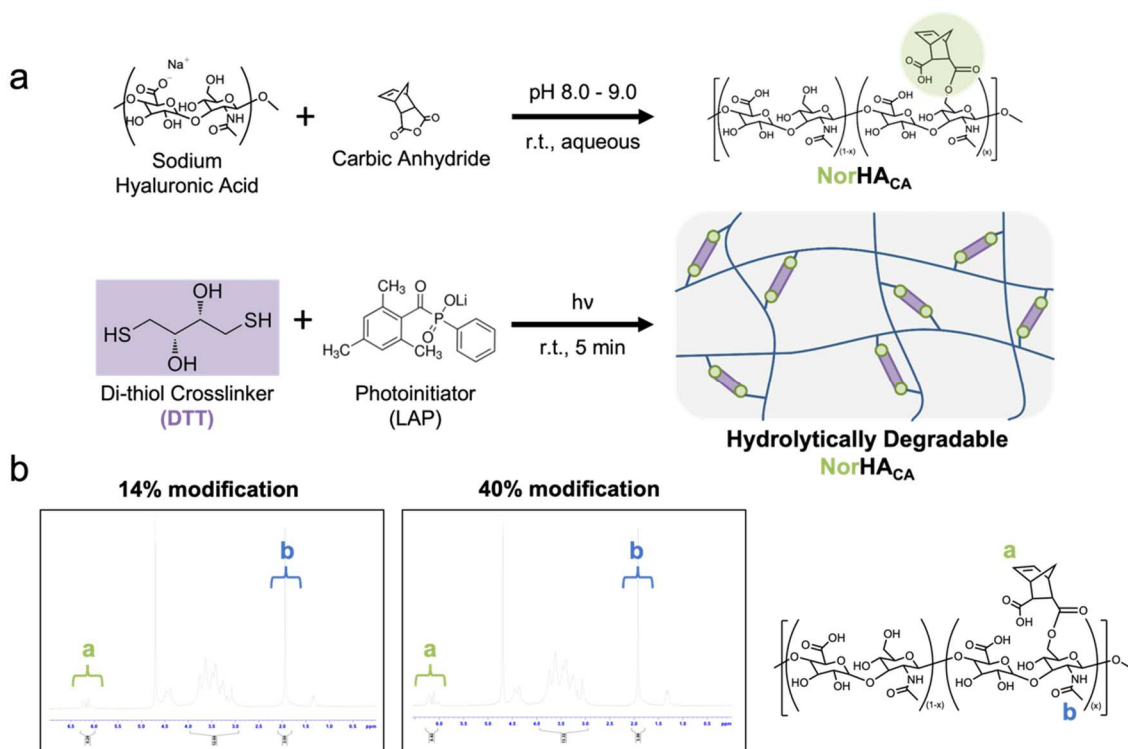


Figure 7.1: Overview of hydrolytically degradable NorHACA hydrogel formation. a) Schematic of the synthesis and photocrosslinking of hydrogels from norbornene-modified hyaluronic acid (HA). Sodium HA is reacted with carbic anhydride under basic conditions to yield NorHACA, which is then photocrosslinked via a thiol-ene reaction in the presence of di-thiol crosslinker (DTT, dithiothreitol) and LAP photoinitiator (0.05%). b) $^1\text{H-NMR}$ spectra of synthesized NorHACA macromer. To quantify the degree of norbornene modification, the vinyl protons of norbornene (2H, $\delta\sim 5.9\text{-}6.4$ ppm) are integrated relative to the methyl protons found on the backbone of HA (3H, $\delta\sim 1.8\text{-}2.1$ ppm). Norbornene modifications of (left) $\sim 14\%$ and (right) $\sim 40\%$ of the disaccharide repeat units of HA were obtained.

Hydrogels were formed via thiol-ene crosslinking by dissolving NorHACA macromer in PBS with LAP photoinitiator (0.05%) and DTT ($X_{\text{DTT}}=1.0$), casting the hydrogel precursor into molds (diameter $\sim 4.78\text{mm}$), and curing with blue light (Exfo Omnicure S1500 lamp, 400–500 nm filter, $I=10\text{mW}/\text{cm}^2$) for 5 min. To characterize reaction kinetics, the storage (G') and loss (G'') moduli of NorHACA hydrogels were monitored during gelation using an AR2000 stress-controlled rheometer (TA Instruments) fitted with a 20 mm diameter cone and plate geometry, 59 min 42 s cone angle, and 27 μm gap. All time sweeps (0.5% strain,

1 Hz) were performed in the presence of visible blue light (Exfo Omnicure S1500 lamp, 400–500 nm filter, $I=10\text{mW}/\text{cm}^2$, $t=5$ min).

7.2.3 Compression Testing

The compressive moduli of hydrogels were determined via unconfined uniaxial compressive testing (Q800, TA Instruments), with a loading rate of 0.2N/min and the modulus calculated as the slope of generated stress-strain curves between 10% and 20% strain. To determine the Poisson ratio (ν_p) of hydrogels, the compression of samples ($n=3$, 5% NorHACA, 40%mod) to 30% strain was recorded (loading rate of 0.2 N/min). Images from the beginning and the end of the loading ramps were then processed using Image J software, and strains in the transverse direction for each experiment were measured to determine $\nu_p = 0.441 \pm 0.019$. Therefore, $\nu_p \sim 0.44$ was assumed for all the hydrogel formulations investigated.

7.2.4 Characterization of NorHACA Hydrogel Bulk Degradation

Hydrogels were incubated in 1 mL of phosphate buffered saline (PBS) at 37°C ($n=3$) until the complete degradation of the hydrogel (i.e., reverse gelation) was observed. Throughout the incubation time course, the PBS was regularly replaced (at a minimum 2-3 times per week), and the supernatant collected (and stored frozen until future analysis) to quantify the cumulative release of HA from the hydrogel. After reverse gelation was observed, samples were incubated overnight at 37°C in hyaluronidase (1 mg/mL, 750-3000 U/mg) solution to ensure the complete degradation of any residual entangled or covalently linked macromers.

The release of HA from crosslinked hydrogels was quantified as previously described via reaction of collected supernatant with carbazole to detect uronic acid (a degradation product of HA), using a 96-well assay.¹⁴ In each well, samples containing

released HA (50 μL) were mixed with 25 mM sodium tetraborate decahydrate (200 μL) in sulfuric acid and incubated at 100°C for 10 min. After cooling to room temperature, samples were then reacted with 0.125% carbazole in ethanol at 100°C for 10 min. The absorbance of samples at 550 nm was then quantified on a Tecan Infinite M200 spectrometer, with a four-parameter logistic regression used to fit generated 8-point standard curves (concentrations ranging from 0-1 mg/mL HA).

The dry and wet masses of hydrogels were measured as previously described to calculate the mass swelling ratio (Q_m) of hydrogels in the relaxed state (i.e., immediately after crosslinking), the equilibrium state (i.e., 24h after crosslinking), and at different time points (t) over the course of their degradation.¹⁵ Q_m was calculated using Equation 7.1:

$$(7.1) \quad Q_m(t) = \frac{M_{wet}}{M_{dry}}$$

where M_{wet} and M_{dry} are the wet and dry masses, respectively, of hydrogels.

Following wet weight measurements, compression testing was performed as described in the preceding section to quantify the compressive modulus of NorHA_{CA} hydrogels over the course of degradation.

7.2.5 Modeling of Hydrogel Degradation Behavior

A custom MATLAB script was developed using an object-oriented programming approach to simulate the random degradation of crosslinks and subsequent release of macromer chains from a network. This model is based on a previously described model by Jahanmir and colleagues, who modeled the hydrolysis of high molecular weight dextran hydrogels (40 kDa) crosslinked via thiol-Michael addition.¹⁶ Specifically, an array of crosslinkable ‘nodes’ was first constructed based on input macromer properties and hydrogel formulation, where each column (n) represents an individual polymer chain

($n=1000$ polymer chains simulated per each modeled network) and each row (m) corresponds to a discrete norbornene group attached to the polymer chain backbone, such that an index ($X_{n,m}$) is assigned to every norbornene actively forming a crosslink within the network.

Model inputs included the macromer concentration, macromer molecular weight, repeat unit molecular weight, and the hydrogel volume, all of which inform the total number of crosslinks incorporated into the simulated network. For example, assuming a homogenous distribution of norbornene modifications and molecular weights across all the polymer chains prior to crosslinking, as well as the formation of an ideal network (i.e., every norbornene reacts with another norbornene to form a functional crosslink), a 5wt% NorHA_{CA} hydrogel with a 40% degree of modification yields an array composed of 1000 columns and 109 rows. Every index of the array is randomly coupled to another index, representing the random formation of crosslinks between macromers. Since the network architecture that arises from this process is unique for every iteration, multiple network structures were generated and simulated ($n=25$).

Within each simulated network, the number of degraded crosslinks and released polymer chains was monitored as a function of time. As a result, the mole number of macromers retained between crosslinks and the average number of active functional groups participating within crosslinks may be determined and thereafter related to hydrogel properties of interest. Several simplifying assumptions were made to ensure that this model framework could be applied to the NorHA_{CA} hydrogels.¹⁷ The reactivity of norbornenes across all macromer backbones is assumed to be equal and to remain constant independent of the extent of crosslinking. Similarly, the probability of any pendant norbornene functional group undergoing hydrolysis is assumed to be the same across all

norbornenes. Finally, no intermolecular or non-specific interactions are assumed to occur between pendant norbornenes.

At any given time, a crosslink within the NorHA_{CA} network may exist in three states (1-3): (1) entirely intact, such that the two esters attaching norbornenes to HA backbones are both retained (2) partially intact, where one of the two esters attaching norbornenes to HA backbones is hydrolytically cleaved, and (3) completely degraded, where both esters attaching norbornenes to HA backbones are cleaved so that the crosslinker is released from the network (**Figure 7.2**).

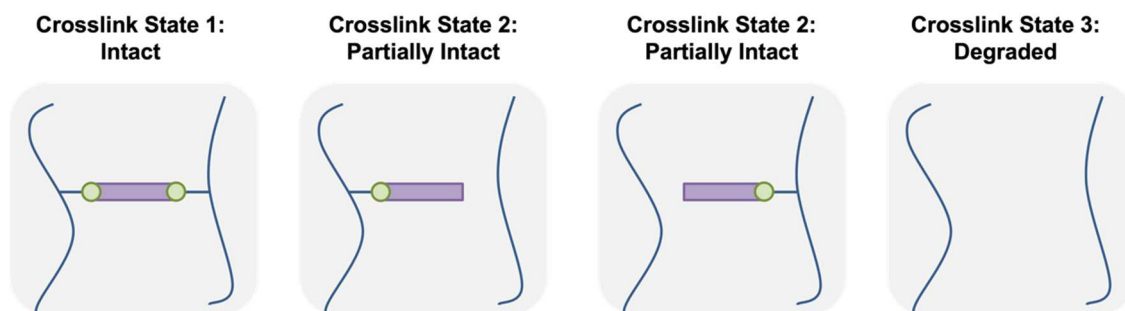


Figure 7.2: Overview of possible crosslink states within NorHA_{CA} hydrogels. Every crosslink within the network exists in one of three possible states (shown from left to right): intact, partially intact, or fully degraded. Each of these crosslink states have their own respective probabilities of existing during the degradation of the hydrogel, which are defined by the hydrolysis kinetics. When a norbornene (green) group is hydrolytically cleaved, the parent macromer is disconnected from the DTT crosslinker (purple). For any given macromer, when all the pendant norbornenes participating in crosslinks are cleaved, the parent macromer is released from the continuous network. Macroscopically, a minimum average of two crosslinks must be attached to each macromer backbone for a stable gel to persist. When this condition is no longer met, the network undergoes reverse gelation and macromers are released as uncrosslinked polymer chains. Thus, the number of active functional groups participating in crosslinks per each macromer backbone (N) is directly related to the degradation rate (k) and the degradation time (t). Importantly, N varies as a function of the hydrogel formulation (i.e., macromer molecular weight and degree of modification) and the effective crosslinking efficiency (η) during gelation (i.e., macromer concentration, X_{DTT} , and photocrosslinking parameters such as the photoinitiator concentration and molar absorptivity, the light intensity, and the light exposure time).

Assuming that the hydrolysis of NorHA_{CA} hydrogels is a first order process that abides by pseudo first order degradation kinetics (i.e., constant concentration of PBS, constant pH, homogenous exposure of water to degradable ester bonds throughout the

hydrogel network), the molar concentration of esters ($[ester]$) incorporated within the network as functional crosslinks over time (t) can be described by Equation 7.2 as follows:

$$(7.2) \quad \frac{d[ester]}{dt} = -k[ester]$$

where k is the degradation rate constant. Solving this rate equation yields the concentration profile of esters within functional crosslinks over the course of degradation (Equation 7.3).

$$(7.3) \quad [ester] = [ester]_0 e^{-kt}$$

Moreover, the probability of an ester bond (within crosslinks) hydrolyzing (P_{deg}) can be described by Equation 7.4:

$$(7.4) \quad P_{deg} = \frac{[ester]_0 - [ester]}{[ester]_0} = 1 - e^{-kt}$$

which describes the extent of ester hydrolysis degradation within the network. With this probability defined, each of the respective crosslink states previously described may be assigned probabilities in accordance with the law of conditional probability.

Since the probability of a single ester bond being intact can be described as $(1 - P_{deg})$ the probability of any crosslink being fully intact (P_1) is given by Equation 7.5:

$$(7.5) \quad P_1 = (1 - P_{deg})^2$$

Alternatively, the probability of any crosslink being partially intact (P_2) is given by Equation 7.6:

$$(7.6) \quad P_2 = 2P_{deg}(1 - P_{deg})$$

since there are two possible scenarios in which one ester bond within a crosslink is cleaved and the other is intact.

Finally, the probability of any crosslink being fully degraded (P_3) is given by Equation 7.7:

$$(7.7) \quad P_3 = P_{deg}^2$$

A first-order Erlang distribution is employed to model the random hydrolysis of esters within NorHA_{CA} networks at discrete simulation time steps (0.05 days), since a similar approach has been previously used to model the surface degradation of polymers.¹⁸ Every crosslink node is assigned a random variable, ϵ , that is equally distributed and exists in between 0 and 1.¹⁶ An exponential distribution of node lifetimes (in accordance with the probability of a single ester bond undergoing hydrolysis) is then established by setting ϵ equal to P_{deg} (Equation 7.8).

$$(7.8) \quad \epsilon = 1 - e^{-kt}$$

This expression may then be solved explicitly to relate the randomly assigned variables to an arbitrary node lifetime (Equation 7.9).

$$(7.9) \quad t_{n,m} = -\frac{1}{k} \ln(1 - \epsilon)$$

During simulation timesteps, the lifetime of individual crosslinks corresponding to the n^{th} polymer and the m^{th} norbornene along the backbone ($t_{n,m}$) is compared to the simulation time. When the latter value is larger than the randomly assigned lifetime, the crosslink

node is considered hydrolyzed; this is reflected by the variable $x_{n,m}$, which is assigned to every index within the network and is defined by Equations 7.10 and 7.11 as follows:

$$(7.10) \quad x_{n,m} = 0 \text{ if crosslink node is intact}$$

$$(7.11) \quad x_{n,m} = 1 \text{ if crosslink node is intact}$$

While non-idealities such as the reaction of DTT crosslinkers with only one norbornene, unreacted norbornenes, and cyclization of norbornenes (i.e., reactions between pendant norbornenes on the same macromer, also known as ‘back biting’) are known to occur during the crosslinking of long chain step-growth hydrogels, ideal networks do not account for this. Therefore, empirical swelling data from hydrogels in the relaxed and equilibrium swollen state was used to characterize the number of functional groups that effectively participate in crosslinks.

To account for non-idealities that occur during the crosslinking of norbornenes, or ‘nodes’ within the simulated network, the effective crosslinking efficiency, η , was determined using Equation 7.12:

$$(7.12) \quad \eta = \frac{v_{e,actual}}{v_{e,ideal}}$$

where $v_{e,ideal}$ and $v_{e,actual}$ are the mole numbers of macromer chains in between crosslinks for an idealized network and for actual hydrogel samples. While $v_{e,ideal}$ may be theoretically calculated based on the molar concentration of macromer and the degree of norbornene modification used, $v_{e,actual}$ was determined via the well-characterized Bray Merrill Equation,¹⁹ which relates the polymer volume fraction within the hydrogel to the mole number of macromer chains in between crosslinks, and as a result, the crosslink density (ρ_x). Specifically, the crosslink density of any hydrogel may be defined by Equation 7.13:

$$(7.13) \quad \rho_x = \frac{v_{e,actual}}{V_{gel,r}} = -\frac{1}{V_1} \frac{(\ln(1 - v_{2,s}) + v_{2,s} + v_{2,s}^2)}{\left(\frac{v_{2,s}}{v_{2,r}}\right)^{1/3} - \frac{1}{2} \frac{v_{2,s}}{v_{2,r}}}$$

where $V_{gel,r}$ is the initial hydrogel volume in the relaxed state, V_1 is the molar volume of the solvent (i.e., $V_1=18$ mL/mol for water), $v_{2,s}$ is the polymer volume fraction in the equilibrium swollen state, χ_1 is the Flory polymer–solvent interaction parameter ($\chi_1 \sim 0.473$ for HA and water),²⁰ and $v_{2,r}$ is the polymer volume fraction in the relaxed state.

To solve for $v_{e,actual}$ in Equation 7.13, empirical mass swelling ratios (Q_m) are first used to determine the polymer fractions $v_{2,s}$ and $v_{2,r}$ using Equation 7.14:

$$(7.14) \quad v_2 = \frac{\bar{v}_2}{\bar{v}_1 (Q_m - 1) + \bar{v}_2}$$

where \bar{v}_1 is the specific volume of water ($\bar{v}_1=1$ mL/g) and \bar{v}_2 is the specific volume of hyaluronic acid ($\bar{v}_2=0.547$ mL/g for HA in water at 37°C).²¹

Once a value for $v_{e,actual}$ was quantified, η was calculated using Equation 12 and used to determine the maximum possible number of crosslinks within the true network in the equilibrium swollen state ($t=1$ day). The network architecture was initialized to reflect this, yielding an updated array of crosslink nodes.

The final requirement for the simulation to proceed is the selection of the rate constant k to determine the rate at which random ester hydrolysis events occur. Importantly, this rate constant may be determined via theoretical relationships to the degradation time.

To identify the point of reverse gelation, Macosko and Miller previously developed a recursive model that describes the evolution of network architecture during crosslinking,

such that the transition of macromer molecular weight from finite (when macromers exist as soluble species) to infinite (when macromers are covalently crosslinked into a continuous network) can be elucidated.^{22,23} The reverse of this transition period is considered the reverse gelation point, or the extent of hydrolysis at which bulk degradation of a continuous hydrogel is complete. The law of conditional probability was applied to describe changes in hydrogel molecular weight over time towards identifying the reverse gelation time.

For step-growth reactions in which stoichiometric mixtures of reagents are used (as is the case for all the NorHA_{CA} hydrogels investigated; i.e., $X_{DTT}=1.0$), gelation is observed when an average of at least two crosslinks are attached to every macromer backbone.²⁴ At the gel point, the extent of reaction is predicted by the Carothers Equation (Equation 7.15):

$$(7.15) \quad X_c = \frac{2}{N}$$

where X_c is the critical extent of crosslinking at which gelation occurs and N is the average number of active functional groups participating in crosslinks on the NorHA_{CA} macromer backbone.²⁴ Importantly, N can be determined using model inputs for the hydrogel formulation (Equation 7.16):

$$(7.16) \quad N = \frac{MW_{HA}}{MW_{disaccharide}} * DM * \eta$$

where MW_{HA} is the molecular weight of the unmodified HA macromer (~88 kDa), $MW_{disaccharide}$ is the molecular weight of the disaccharide repeat unit (~378.3 g/mol), and DM is the degree of norbornene modification.

At the critical time at which the gel point occurs (t_c), the critical extent of crosslinking $X(t_c)$ may be described as the probability of ester bonds being intact.²⁴ Since this probability is defined by Equation 7.5, the degradation time of a hydrogel with N active functional groups contributing to crosslinks is given by Equation 7.17:

$$(7.17) \quad X(t_c) = [1 - P_{deg}(t_c)]^2$$

Substitution of $X(t_c)$ (Equation 7.15) and $P_{deg}(t_c)$ (Equation 7.4) into Equation 7.17 and solving for the rate constant reveals the relationship between k , t_c and N (Equations 7.18 - 7.21):

$$(7.18) \quad P_{deg} = 1 - \left(\frac{2}{N}\right)^{\frac{1}{2}}$$

$$(7.19) \quad (1 - e^{-kt_c}) = 1 - \left(\frac{2}{N}\right)^{\frac{1}{2}}$$

$$(7.20) \quad e^{-kt_c} = 1 - \left(1 - \left(\frac{2}{N}\right)^{\frac{1}{2}}\right)$$

$$(7.21) \quad k = -\frac{\ln\left(\left(\frac{2}{N}\right)^{\frac{1}{2}}\right)}{t_c}$$

This approach may be implemented to determine input rate constants from empirically observed degradation times and swelling behavior. Alternatively, rate constants may be determined via model recursion to predict the time at which reverse gelation occurs for distinct hydrogel formulations. Simulations were performed with the number of intact crosslinks and released macromer chains recorded at each time step.

The mole number of macromers retained between crosslinks ($v_{e,actual}$) and the average number of active functional groups participating within crosslinks (N) were calculated from these model outputs, such that mass swelling ratios could then be predicted using Equations 7.13 and 7.14.

The compressive modulus was also predicted (E_{pred}) as previously described using calculated crosslink densities at discrete simulation times and the Poisson's ratio ($v_p=0.44$ for all hydrogels investigated) of the hydrogel (Equation 7.22).²⁵

$$(7.22) \quad E_{pred} = -\frac{RT\rho_x}{(1 - 2v_p)}$$

where R is the universal gas constant ($R=8.3145 \text{ m}^3 \text{ Pa mol}^{-1} \text{ K}^{-1}$) and T is the temperature ($T=310.15 \text{ K}$).

7.2.6 Preparation of Copolymer Hydrogels

Non-degradable NorHA was synthesized as previously described via BOP coupling of HA and 5-norbornene-2-methylamine.²⁶ NorHA_{CA} macromer and non-degradable NorHA were then dissolved in PBS along with LAP photoinitiator (0.05%) and DTT ($X_{DTT}=1.0$), cast into molds (diameter~4.78mm), and crosslinked via irradiation with blue light (Exfo Omnicure S1500 lamp, 400–500 nm filter, $I=10 \text{ mW/cm}^2$) for 5 min.

7.2.7 Digital Light Processing of Hydrogels

NorHA_{CA} hydrogels (5% NorHA_{CA}, 40% modification, 0.5% LAP, $X_{DTT}\sim 1.0$) were printed on a Lumen Alpha Prototype Projector (Volumetric Inc., Houston, TX) with a 405 nm LED light source ($I=15 \text{ mW/cm}^2$), 100 μm step size, and a print speed of 30 mm/min. Variable concentrations of tartrazine photoabsorber (TTz, 0.5-1 mM) and light exposure times (4-10 s) were initially investigated to identify the requisite resin formulation and

printing conditions required for the fabrication of stable constructs with internal negative features. Ultimately, 1 mM TTz and 6 s exposure time were selected used to print 2D patterns, as well as 3D bulk and macroporous structures. Porous constructs printed for the characterization of bulk degradation were washed post-printing with PBS containing 1% LAP and 15 mM DTT, and then stabilized with post-print curing (Exfo Omnicure S1500 lamp, 400–500 nm filter, $I=10\text{mW}/\text{cm}^2$, and $t=5$ min, with constructs flipped after 2.5 min of curing). Visualization of 2D printed constructs was achieved via swelling of constructs in rhodamine-labeled dextran (which is then pseudo-colored green), while the visualization of 3D printed constructs was achieved via the presence of TTz.

7.2.8 Statistical Analysis

All data are reported as mean \pm standard deviation and were analyzed using GraphPad Prism 9 software. One-way ANOVAs were performed with Tukey's honestly significant difference (HSD) post-hoc testing and significance determined at $p<0.05$ to compare the compressive modulus of casted and 3D printed NorHA_{CA} hydrogels.

7.3 RESULTS AND DISCUSSION

7.3.1 Rational Design of Degradable Hydrogels for AMIC

To create a scaffold that can be implemented in the AMIC approach for cartilage repair, it is of interest to target degradation times that match the rate of neocartilage formation by endogenous cells. Although candidate degradable hydrogels have been previously engineered with protease-sensitive crosslinkers,²⁷ enzymatic degradation is typically dependent on the local environment and varies dynamically with both local enzyme concentration and cellular behaviors.²⁸ Conversely, hydrolytically degradable hydrogels may be engineered with degradation timescales that are defined *a priori* by the selection of the hydrogel chemistry and network structure. Additionally, the crosslinking

method used to form scaffolds for AMIC should be well controlled to ensure that the resultant mechanical properties, crosslink density, and mesh size are defined, since each of these properties will influence both the overall hydrogel degradation behavior and cellular infiltration into the hydrogel network overtime.^{15,29}

HA macromers with hydrolytically sensitive functional groups have been previously synthesized, including methacrylated-HA with incorporated caprolactone or lactic acid units between the HA backbone and methacrylate groups.^{30,31} However, these macromers are all crosslinked via free radical crosslinking, which leads to heterogenous network architectures and variable mesh sizes. In contrast, macromers that undergoes step-growth crosslinking may offer more precise control over network structure and hydrolysis.

Although hydrolytically degradable crosslinkers could be employed to achieve the degradation of step-growth hydrogels crosslinked via thiol-ene reaction, there are very few thiol-modified crosslinkers that possess the requisite hydrolytically sensitive bonds, miscibility in aqueous conditions, and size (i.e., small molecule) desired for this system. Thus, alternative methods were needed. Generally, biopolymers may be modified with norbornenes via esterification or amidation reactions with molecules containing norbornenes and terminal carboxylic acid or amine groups;³² however, recent studies have also shown that modification of polymers (e.g., gelatin, carboxymethyl cellulose, PEG) with norbornene may also be achieved via reaction with carbic anhydride.³³⁻³⁶ In contrast to traditional norbornene synthesis routes, the use of carbic anhydride results in the conjugation of norbornenes with an additional attached carboxylic acid group; the presence of this carboxylic acid group significantly increases the overall hydrophilicity of the pendant norbornene, enabling the hydrolysis of ester bonds found between the norbornene and the macromer backbone.

To this end, NorHA_{CA} macromer with hydrolytically labile norbornene groups was synthesized via esterification of HA with carbic anhydride (**Figure 7.3a**). Hydrogels were then formed via thiol-ene photocrosslinking with blue light, and the resultant mechanical properties were readily achieved via changes to the macromer concentration or the degree of norbornene modification (**Figure 7.3b**). Across a range of hydrogel formulations, NorHA_{CA} undergoes rapid crosslinking, as evidenced by photorheological time sweeps, which also illustrate changes in storage moduli with variations in crosslink density (**Figure 7.3c**).

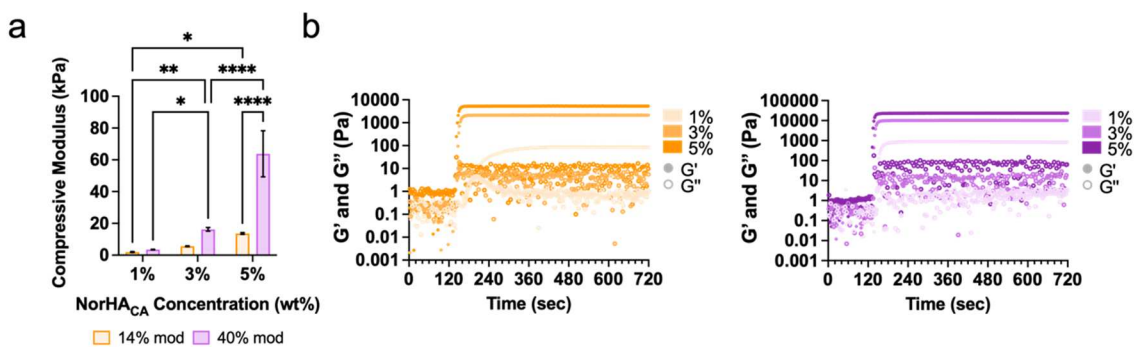


Figure 7.3: Characterization of NorHA_{CA} hydrogel mechanical properties. a) Compressive moduli of NorHA_{CA} hydrogels across changes in NorHA_{CA} concentration (1, 3, 5%) and extent of norbornene modification (14, 40% mod) (n=5). b) Photoreological time sweeps (1Hz, 0.5% strain) showing increases in the storage (G') and loss (G'') moduli during the gelation of 14% modified (left, orange) and 40% modified (right, purple) NorHA_{CA} hydrogels of varying macromer concentrations (1, 3, 5%) with exposure to visible light (400-500 nm, light on at t=120 seconds). Two-way ANOVA, *p<0.05, **p<0.01, ****p<0.0001.

7.3.2 Characterization and Modeling of Bulk Degradation in NorHA_{CA} Hydrogels

The ability for NorHA_{CA} hydrogels incubated in PBS to degrade via ester hydrolysis was validated qualitatively via observation of reverse gelation. Quantitative release assays, swelling measurements, and compression testing were also performed to elucidate the temporal evolution of the network with degradation (**Figure 7.4**). Across all of the investigated NorHA_{CA} hydrogel formulations, the sustained release of HA polymer chains was observed, consistent with a bulk mode of degradation.²⁹ The swelling ratios

and compressive moduli of all the investigated NorHA_{CA} formulations also exponentially increased and decreased, respectively, consistent with the first order process of ester hydrolysis. However, relative differences existed between hydrogel formulations, as the rate at which hydrolysis occurred was mediated not only by the pendant group chemistry, but also the overall network architecture. Increases in the macromer concentration or the degree of modification resulted in corresponding increases in the hydrogel crosslink density as expected, which was proportional to the compressive modulus and inversely proportional to the swelling ratio.²⁹ With increasing crosslink density, the total number of crosslinks required to hydrolyze prior to reverse gelation also increased; therefore, increases in the macromer concentration and the degree of modification also resulted in prolonged reverse gelation times. Generally, NorHA_{CA} hydrogels degraded after 3-12 days of incubation in PBS at 37 °C.

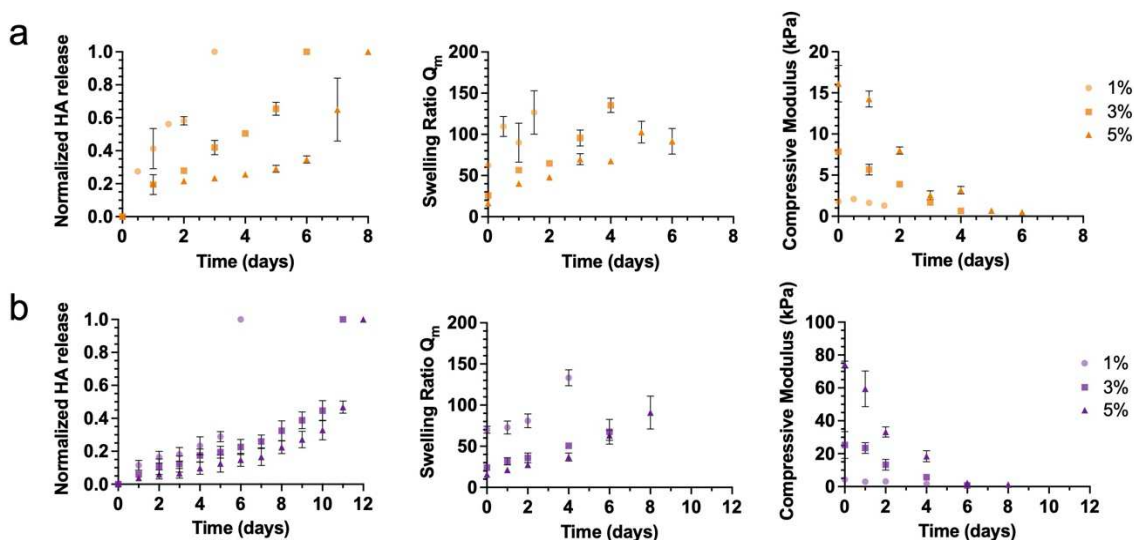


Figure 7.4: Characterization of NorHA_{CA} hydrogel degradation. HA release (left), swelling ratio (middle), and compressive moduli (right) of hydrogels across changes in NorHA_{CA} concentration (1, 3, 5wt%) at either a) 14% modification or b) 40% modification upon incubation in PBS at 37°C until complete degradation (i.e., reverse gelation) is observed (n=3).

Modeling can be useful to better understand synthesized networks towards their use in biomedical applications. For example, a multiscale computational model was

developed to characterize the transition of cell-laden, enzymatically degradable hydrogels into neocartilage.³⁷ Motivated by this, the work herein described aims to use computational modeling to inform the design of NorHA_{CA} hydrogels. Specifically, a kinetics-based model was combined with Monte Carlo simulations of NorHA_{CA} hydrogel degradation to relate changes in hydrogel mesh size over time to macroscopic gel properties.¹⁶ In doing so, the rate of NorHA_{CA} hydrogel degradation might be precisely defined via alterations to the hydrogel formulation to match desired rates.

Several theoretical models have been previously developed to describe the bulk degradation of hydrogels crosslinked via free radical crosslinking,^{24,38,39} step growth crosslinking,^{25,40,41} and even mixed modes of crosslinking (i.e., concurrent radical and step growth crosslinking).⁴² However, many of the models that characterize the degradation of step-growth hydrogels involve hydrogels composed of small molecule monomers and/or multi-arm macromers with a fixed number of functional groups, resulting in relatively simple network structures.⁴⁰ In contrast, the step-growth crosslinking of long NorHA_{CA} macromers, which may exhibit a distribution of molecular weights or degrees of modification, results in random network architectures with variable mesh sizes throughout the hydrogel.

To recapitulate the randomness observed during crosslinking, a statistical-co-kinetic model was developed and combined with Monte Carlo simulations.¹⁶ Through this generalizable approach, probability functions were employed to capture the random and differential hydrolysis of crosslinks. Moreover, the averaging of these random and discrete events at the microscale provides insights into the overall mesh size of the hydrogel over time. As a result, the crosslink density and macroscopic properties such as mass swelling ratios and compressive moduli may be predicted (**Figure 7.5**). Model simulations were performed across randomly generated network architectures using the inputs shown in

Table 7.1, including theoretical rate constants that were determined recursively based on the hydrogel composition and empirically observed swelling behavior (**Figure 7.4**). The model generated swelling and compressive modulus profiles comparable to those obtained empirically, demonstrating its potential use in the future as a predictive tool for NorHA_{CA} hydrogel design. However, the degradation timescales predicted by the model using these input rate constants were generally shorter than those observed empirically for NorHA_{CA} hydrogels. This may be due to the additional contributions of polymer chain entanglement and intermolecular interactions to the overall hydrogel stability, both of which are not currently captured by the model (which only accounts for covalent crosslinks within the network). Importantly, the model may be further adapted to account for these phenomena so that eventually only swelling data at early time points is needed to accurately predict degradation timescales, and as a result, swelling and mechanical properties as a function of time.

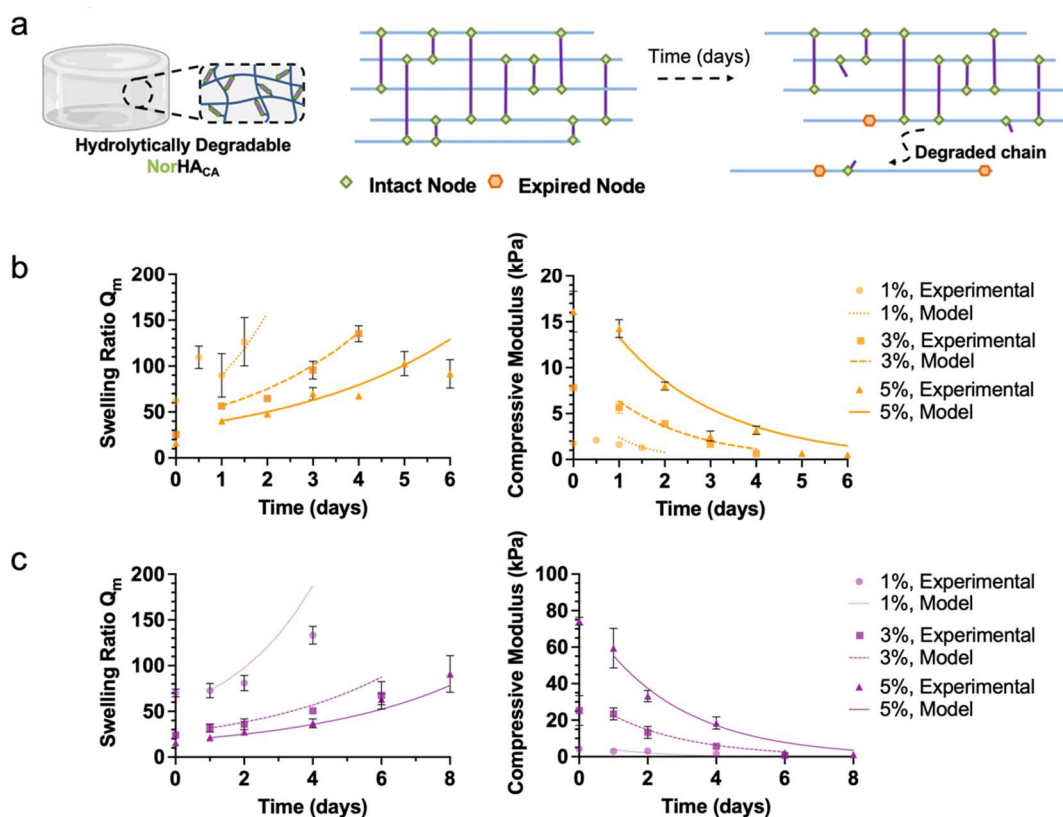


Figure 7.5: Modeling the degradation behavior of NorHA_{CA} hydrogels via Monte Carlo simulations. a) Overview of the modeling approach employed to characterize NorHA_{CA} hydrogel degradation. Empirical mass swelling data collected immediately after hydrogel formation (i.e., in the relaxed state; $Q_{m,r}, \nu_{2,r}$) and 24 h afterwards (i.e., in the equilibrium swollen state; $Q_{m,s}, \nu_{2,s}$) is used to determine the effective crosslinking (η) achieved between pendant norbornene groups. The moles of norbornene incorporated into crosslinks is then calculated ($\nu_{e,actual}$) and used to create an initial network architecture composed solely of intact nodes, recapitulating the covalent network of the hydrogel in the equilibrium swollen state. Simulations are then performed to model the stochastic transition of intact nodes to expired nodes, representing the hydrolysis of pendant norbornene groups and the disruption of hydrogel crosslinks (for each hydrogel formulation, $n=25$ simulations of unique networks, 1000 polymer chains per network). Throughout each simulation, the remaining moles of norbornenes contributing to crosslinks ($\nu_{e,actual}$) are monitored and related to the hydrogel crosslink density (ρ_x) to predict mass swelling ratios and compressive moduli over time. The degradation kinetics (i.e., degradation rate constant, k) for each simulation are determined via a recursion that optimizes generated predictions for mass swelling ratios and compressive moduli. b) Model predictions for the swelling behavior and mechanical properties of 14% modified NorHA_{CA} hydrogels (1,3,5%) during degradation, with comparisons to empirical data shown ($n=3$). c) Model predictions for the swelling behavior and mechanical properties of 40% modified NorHA_{CA} hydrogels (1,3,5%) during degradation, with comparisons to empirical data shown ($n=3$).

Table 7.1: Model inputs for network initialization prior to Monte Carlo simulation.

Hydrogel Formulation	$Q_{m,r}$	$Q_{m,s \text{ initial}}$	$v_{2,r}$	$v_{2,s \text{ initial}}$	$v_{e, \text{actual initial}}$	k (day⁻¹)
14% mod, 1%	62.300	89.905	0.00884	0.00612	5.602 nmol	1.17
14% mod, 3%	25.585	56.566	0.0218	0.00975	14.766 nmol	0.57
14% mod, 5%	16.494	40.222	0.0341	0.0138	30.945 nmol	0.44
40% mod, 1%	70.111	84.500	0.00785	0.00757	9.309 nmol	0.67
40% mod, 3%	24.121	31.724	0.0231	0.0175	52.487 nmol	0.43
40% mod, 5%	15.742	21.270	0.0358	0.0263	113.636 nmol	0.39
Copolymer 1	15.202	20.101	0.0371	0.0278	112.216 nmol	0.33
Copolymer 2	15.432	19.832	0.0365	0.0282	110.795 nmol	0.23

While NorHA_{CA} hydrogels exhibit promise as degradable scaffolds for AMIC, longer degradation timescales may be needed for clinical translation. To this end, the degradation of hydrolytically sensitive biopolymers has been previously modulated via the incorporation of additional macromers to form copolymers.^{30,31} For example, non-degradable macromers have been previously combined with hydrolytically degradable macromers to achieve prolonged degradation times;³⁰ alternatively, macromers that are sensitive to enzymatic degradation have also been introduced to endow hydrogels with dual modes of degradation.³¹

The degradation behavior of NorHA_{CA} hydrogels is further tuned via combinations of non-degradable NorHA macromer with NorHA_{CA} macromer to yield copolymers (**Figure 7.6**). The incorporation of small amounts of non-degradable NorHA into hydrogels results in prolonged degradation behavior in comparison to pure NorHA_{CA} hydrogels alone (**Figure 7.6a**). However, at some critical concentration, the addition of NorHA macromer into copolymers results in the formation of a network that transiently degrades overtime but does not undergo reverse gelation (**Figure 7.6b**).

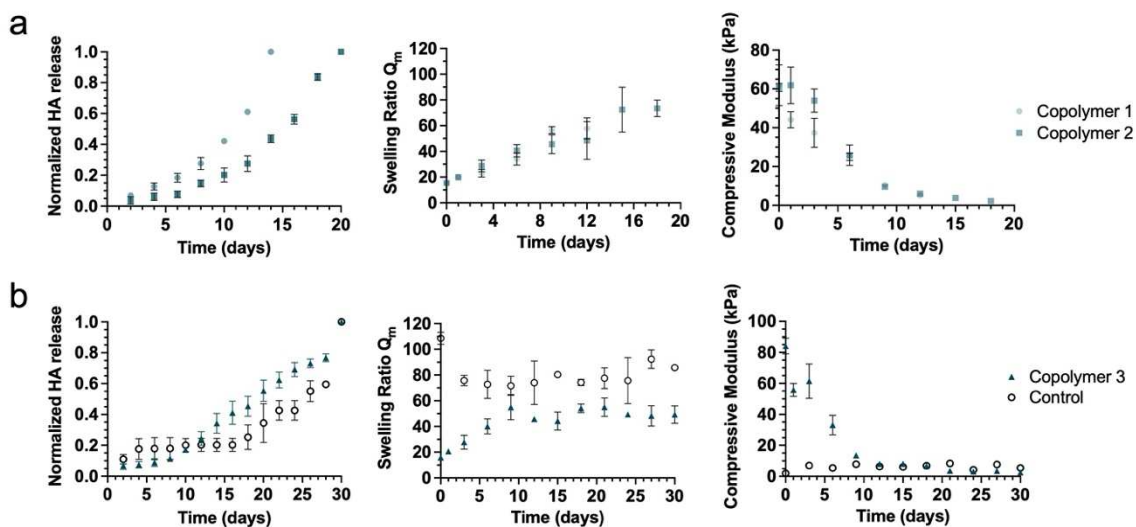


Figure 7.6: Degradation behavior of NorHA_{CA}:NorHA hydrogels. To modulate the degradation behavior of NorHA_{CA} hydrogels without changing the degree of norbornene modification or the macromer concentration, NorHA_{CA} macromer is mixed with a non-degradable, hydrolytically stable NorHA macromer. a) Macromer mixtures (Copolymer 1= 4.75% NorHA_{CA}:0.25% NorHA; Copolymer 2= 4.5% NorHA_{CA}:0.5% NorHA) extend degradation timescales, as evidenced by prolonged HA release (left) and swelling behavior (middle), and higher compressive moduli (right) over time (n=3). b) The incorporation of excessive amounts of stable NorHA into macromer mixtures (Copolymer 3= 4% NorHA_{CA}:1% NorHA) results in hydrogels that do not degrade after 30 days and that exhibit plateaus in both swelling ratios and compressive moduli, similar to non-degradable controls (0.5% NorHA alone). After 30 days, Copolymer 3 and control hydrogels are degraded via treatment with hyaluronidase (n=3). In these studies, 40% modification NorHA_{CA} and 30% modification NorHA are used.

Interestingly, the statistical-co-kinetic model that was developed enables the prediction of swelling ratios and compressive moduli for copolymers that undergo reverse gelation (**Figure 7.7**), capturing the unique features observed in these systems and not in pure NorHA_{CA} hydrogels. To this end, potential copolymer formulations may eventually be screened to obtain hydrogels with extended degradation timescales or complex, non-linear release profiles.

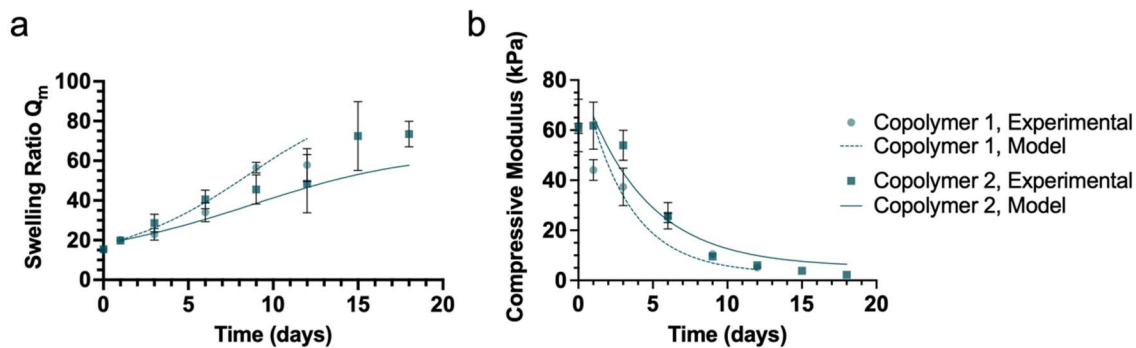


Figure 7.7: Modeling the degradation behavior of NorHACA:NorHA hydrogels. The model is adapted to accommodate the incorporation of non-degradable norbornene crosslinks such that the a) mass swelling ratios and b) compressive moduli of mixed macromer formulations can be characterized over simulation time. Model predictions for the a) swelling behavior and b) mechanical properties of Copolymers 1 and 2 during degradation, with comparisons to empirical data shown (n=3).

7.3.3 Digital Light Processing of NorHACA Hydrogels

Digital light processing (DLP) is a powerful biofabrication approach that enables the formation of hydrogel constructs with complex internal features and print resolutions superior to those accessible via extrusion printing (**Figure 7.8a**).^{43,44} To this end, a number of studies have investigated the use of DLP for cartilage tissue engineering.^{45–48} Increased attention has also been focused on the development of hydrolytically degradable resins for DLP.⁴⁹

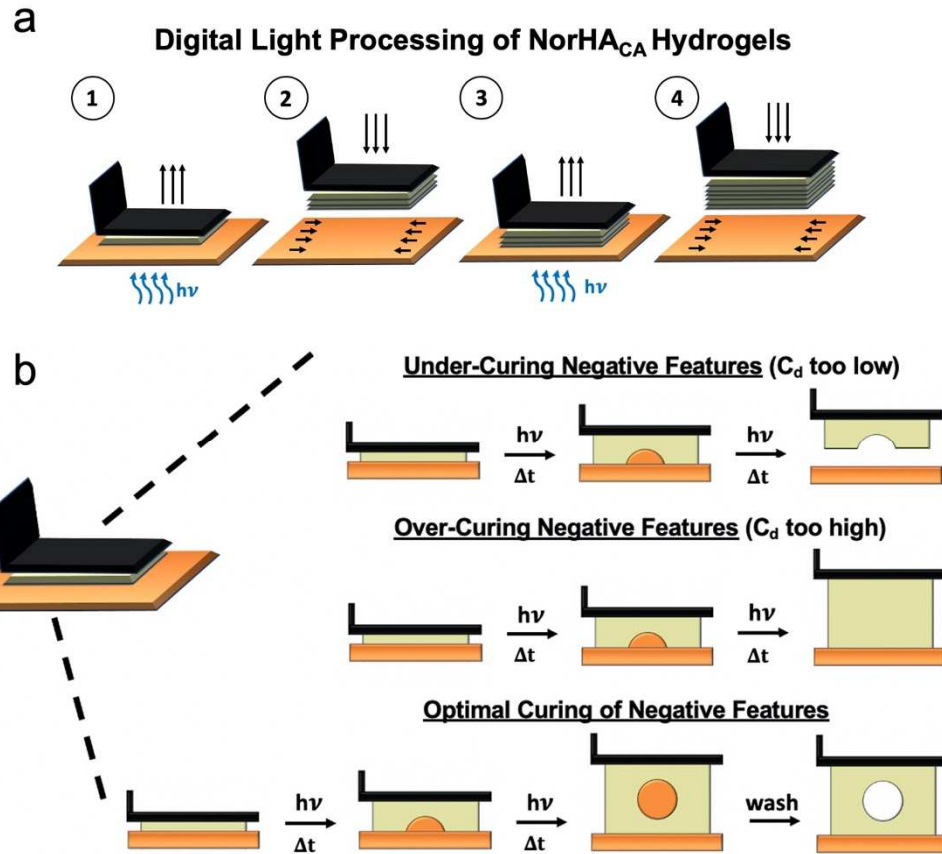


Figure 7.8: Overview of digital light processing (DLP) and considerations for printability. a) In DLP, non-viscous resin is contained within a vat and is brought into contact with a build-plate (black). Light is projected through an underlying lens (into a 2D light pattern of interest, which is achieved via digital micromirror devices) to cure the resin onto the build-plate (1). Thereafter, the build-plate rises, allowing uncured resin (orange) to flow underneath the cured resin (yellow), which is attached to the build-plate (2). The replenished resin may then be cured with projected and patterned light, so that it integrates with the preceding layer of resin (3), and the cycle proceeds to achieve layer-by-layer fabrication of photosensitive constructs (4). If the resin does not flow underneath the build-plate (2,4) in between successive curing steps (1,3), then the printed construct will contain defects and/or be incomplete. Therefore, the resin viscosity cannot be too high, or else the resin will not regularly interface with the build-plate. Important consideration must also be given to the build-plate retraction height/speed and the wait time whenever the build-plate is retracted. b) Schematic detailing the importance of cure depth (C_d) in DLP. The printing parameters, curing conditions, and resin formulation must be balanced to achieve desired print resolution, especially toward the fabrication of constructs with negative features. If the cure depth is too low, failure between successive layers of material might occur during the printing process. However, if the cure depth is too high, negative features such as pores, which are critical for tissue engineering applications, may be inadvertently cured.

In one study, DLP was used to fabricate a scaffold that could be press fit into a focal cartilage defect and then infilled with an injectable, photocrosslinkable cell-laden hydrogel to create a composite scaffold that slowly degrades over time and facilitates cartilage repair *in situ*.⁵⁰ Similarly, PEGDA structures with a range of possible mechanical properties were previously printed via DLP into macroporous structures, which were then combined with cell-instructive, soft hydrogels. Specifically, MSC-laden hydrogels (PEG-norbornene) containing ECM molecules (chondroitin sulfate) and tethered growth factors or peptide sequences (i.e., RGD) were infilled into these structures to achieve the requisite microenvironments required for cartilage formation. The composite system was evaluated in *ex vivo* porcine osteochondral plugs and subsequently employed to create a biphasic scaffold for OC tissue engineering.⁵¹

It is expected that DLP may be similarly leveraged to form degradable macroporous scaffolds for implementation in AMIC, where infilling of the scaffold with marrow occurs. However, to process NorHA_{CA} hydrogels via DLP, permissible printing conditions need to first be identified (**Figure 7.8b**).

An adapted form of the Beer-Lambert Law is commonly used to describe the light attenuation that occurs as light is projected through a resin during DLP. For a given resin formulation, the Jacobs Equation (Equation 7.23) relates the thickness of a single cured layer (i.e., the cure depth, C_d) to the penetration depth of projected light (D_p) and the energy dosage E applied for photo crosslinking.^{43,52}

$$(7.23) \quad C_d = D_p \ln\left(\frac{E}{E_c}\right)$$

where E_c is the critical energy dosage required for resin crosslinking (i.e., gelation only occurs when $E > E_c$). When the light intensity used for printing is constant, t_c describes the critical exposure time required for gelation. Ideally, the relative amount of macromer

photocrosslinking at the layer-layer interface (in between successive z-steps during printing) should be just slightly higher than what is required for the gel point to ensure that successful integration between printed layers is achieved. By tuning printing parameters such as the light intensity and exposure time (E), layers of different thickness can be targeted.

The cure depth of a resin is significantly influenced by the crosslinking kinetics, which is dictated by the rate of radical species generation and consumption and the irradiation conditions (e.g., the photoinitiator concentration and molar absorptivity, the applied energy dosage).⁵³ Therefore, the incorporation of photoabsorbers into resins is often exploited to increase the E_c such that the light penetration depth for a given energy dosage is decreased, increasing the achievable print resolution (i.e., smaller cure depths).

46,54

NorHA_{CA} resin was supplemented with variable amounts of tartrazine photoabsorber (TTz, 0.5 mM-1mM) and photocrosslinked with a range of energy dosages to elucidate how the cure depth varies with curing conditions. Logarithmic-linear plots of cure depth versus energy dosage, which are also known as working curves, were used to identify the D_p (slope of working curve) and E_c (x-intercept of working curve) of resin formulations (**Figure 7.9a**).

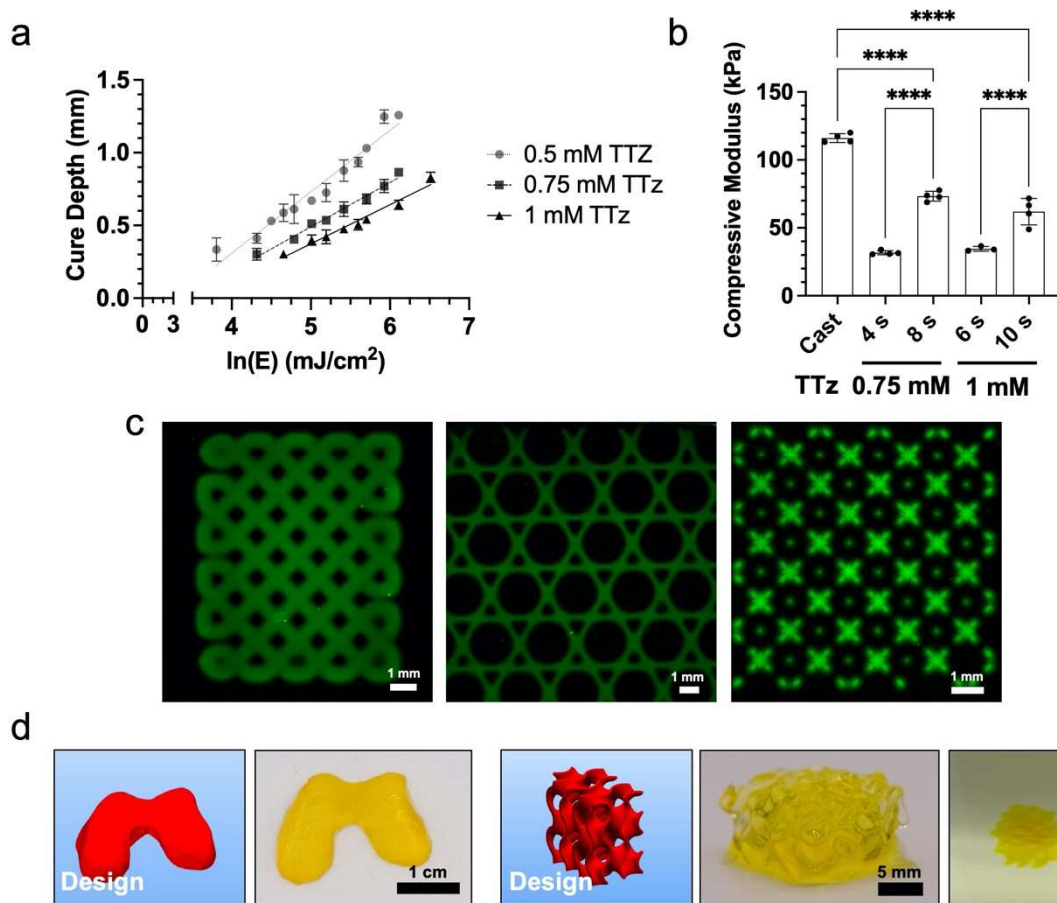


Figure 7.9: DLP of NorHACA hydrogels for tissue engineering applications. a) Working curves to determine the requisite curing conditions (i.e., light intensity, exposure time) and resin formulation required to achieve desired cure depths (C_d) for DLP. NorHA_{CA} resin (40% modification, 5wt%) containing 0.5% LAP, DTT ($X_{DTT}=1.0$), and variable concentrations of tartrazine photoabsorber (TTz, 0.5, 0.75, 1mM) is exposed to a range of different energy dosages (E , mJ/cm²) to identify the penetration depth (D_p) of light through each resin formulation, as well as the critical energy dosage (E_c) required for the conversion of liquid NorHA_{CA} resin into a hydrogel. b) The compressive moduli of casted NorHA_{CA} hydrogels and printed NorHA_{CA} hydrogels with variable concentrations of TTz (0.75, 1mM) and light exposure times (4,6,8,10s). NorHA_{CA} resin containing 1 mM TTz is selected with an exposure time of 6 seconds since it exhibits good printability while conserving sufficient mechanical integrity. c) Representative images of NorHA_{CA} hydrogels printed into a range of porous, 2D geometries with features ranging from ~100-500 μ m. d) Representative images of NorHA_{CA} hydrogels printed into complex 3D geometries, including a model femoral condyle (left) and a gyroid structure (right), which possesses macroporous features that are visible when submerged in PBS (far right).

Increasing the concentration of TTz within the NorHA_{CA} resin led to decreases in the light penetration depth and critical exposure times, effectively increasing the possible resolution of stable features (**Table 7.2**).

Table 7.2: DLP working curve fit parameters for NorHA_{CA} resin.

[TTz]	D_p	E_c	t_c
0.5 mM	0.45 mm	29.6 mJ/cm ²	2 s
0.75 mM	0.31 mm	31 mJ/cm ²	2.1 s
1 mM	0.26 mm	34.7mJ/cm ²	2.3 s

The compressive modulus of printed NorHA_{CA} discs however were lower than casted hydrogel controls across permissible printing conditions (**Figure 7.9b**) since complete crosslinking of layers is avoided to ensure that successive layers of resin crosslink with one another. A final TTz concentration of 1 mM and an exposure time of 6 s was selected to fabricate a range of complex, 2D porous structures, highlighting the printability of NorHA_{CA} resins (**Figure 7.9c**). Impressively, NorHA_{CA} resin could also be processed into complex 3D structures, including a model femoral condyle and a gyroid with macroporous porosity (**Figure 7.9d**).

To demonstrate that NorHA_{CA} resin can be 3D printed into degradable scaffolds, porous discs were fabricated and incubated in PBS at 37°C to monitor hydrogel degradation over time (**Figure 7.10a**). After 10 days, reverse gelation was observed in all the printed constructs. Although the compressive modulus and the swelling ratio of these constructs were lower than casted hydrogels composed of the same macromer concentration and degree of modification (**Figure 7.4**), a comparable HA release profile,

swelling profile, and drop in mechanical properties was observed, indicating that NorHA_{CA} scaffolds may be processed via DLP towards their use in AMIC (**Figure 7.10b-d**).

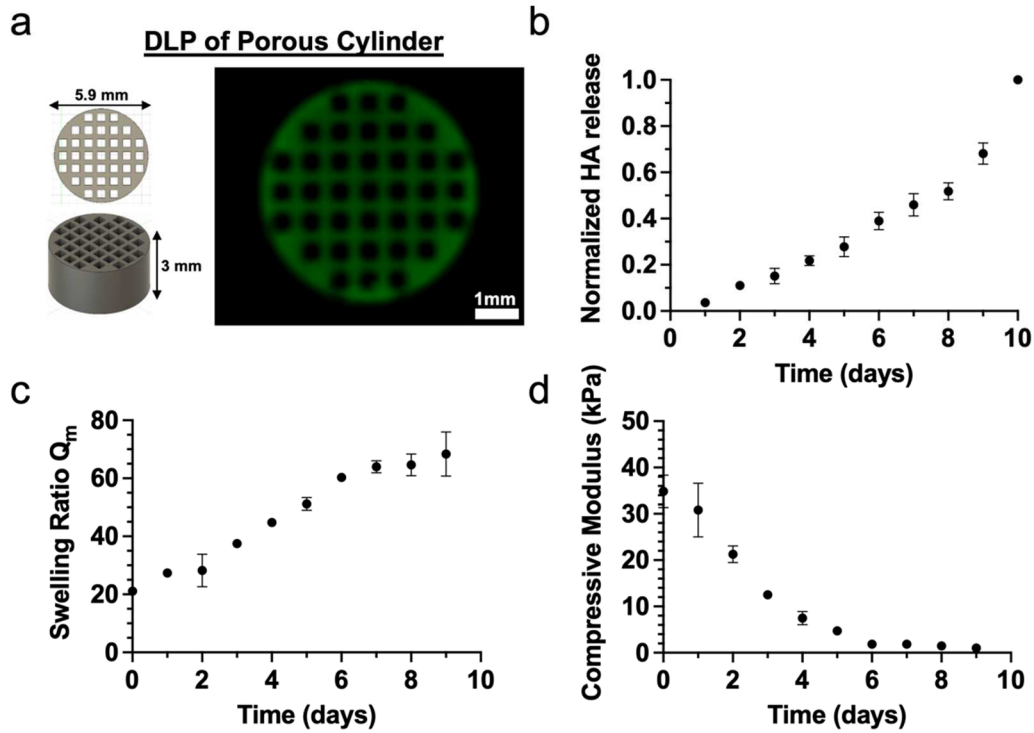


Figure 7.10: Degradation behavior of porous NorHA_{CA} hydrogels fabricated via DLP. a) NorHA_{CA} hydrogels (40% modification, 5wt%) are printed via DLP to yield porous cylinders (green) and then incubated in PBS at 37°C until complete degradation (i.e., reverse gelation) is observed. b) The relative amounts of HA released during the incubation, c) the mass swelling ratio, and d) the compressive moduli of printed hydrogels during degradation (n=3).

Several ECM biopolymers have been modified via reaction with carbic anhydride to develop inks or resins for biofabrication. For example, collagen has been previously reacted with carbic anhydride to achieve a bioink that could be processed via extrusion printing while conserving its helical conformation.⁵⁵ In addition, Rizzo and colleagues synthesized norbornene-modified gelatin via reaction of free amines with carbic anhydride for the rapid volumetric printing of cellularized tissue constructs.⁵⁶ However, it is believed that this study encompasses the first use of carbic anhydride to obtain a norbornene-

modified ECM resin toward use for DLP. The amenability of NorHA_{CA} hydrogels to DLP was demonstrated through the characterization of working curves and representative prints of both bulk and porous structures. In addition, the degradability of NorHA_{CA} constructs fabricated via DLP is confirmed, suggesting that these scaffolds may be further designed for use in AMIC.

7.4 CONCLUSIONS

As a first step towards the design of macroporous hydrogel scaffolds for AMIC in cartilage repair, a new hydrolytically degradable hydrogel was synthesized, characterized, modeled, and processed with DLP. Specifically, NorHA_{CA} hydrogels were fabricated with compressive modulus ranging from ~2-70 kPa and degradation times ranging between three days and two weeks. Importantly, the hydrogel's mechanical properties and degradation behavior were readily modulated through the selection of different macromer concentrations and degrees of modification. Moreover, the use of copolymers composed of both degradable and non-degradable macromers extends the degradation times of hydrogels to nearly 3 weeks. A statistical-co-kinetics model was also developed to describe changes in network mesh size and macroscopic hydrogel properties as a function of crosslink hydrolysis.

Ongoing work is focused on investigating the degradation behavior of NorHA_{CA} hydrogels with high degrees of modification, which are expected to exhibit different degradation timescales than the formulations herein characterized. Early results suggest that reactions of HA with carbic anhydride can yield fully modified NorHA_{CA} macromers (i.e., ~100% norbornene modification). As a result, the crosslink density may be significantly increased, potentially increasing hydrogel degradation times. In addition, high modification NorHA_{CA} macromer may be combined with non-degradable NorHA to form additional copolymer formulations with prolonged degradation times. However, important

consideration must be given to the potential for high degrees of norbornene modification to attenuate the innate bioactivity of HA, such as its ability to interact with MSCs via cell-surface receptors (e.g. CD44).⁵⁷ Each of these respective approaches will be explored towards achieving degradation timescales that better match the required time need for neocartilage to form (i.e., ~ 1 month, as evidenced by the in vitro studies performed in Chapters 4-6 with MSC-laden hydrogels).

The developed model may also be further adapted to predict mass loss profiles for hydrogel formulations of interest,^{24,25,38,39,42} which may be related to the generated HA release profiles obtained by uronic acid assay. However, while past theoretical models assume that the rate of diffusion of degradation products is significantly faster than the rate of degradation,²⁴ this assumption is likely invalid in the case of NorHA_{CA} hydrogels, where the use of high molecular weight macromers leads to chain entanglement and perturbations to the polymer chain dynamics. Additional features may also be incorporated into the model to account for complex non-idealities such as intermolecular interactions between functional groups and restricted mobilities due to diffusion limitations that arise with crosslinking.⁵⁸ It is expected that with these alterations, initial swelling data collected at short time scales (i.e., days) for any arbitrary hydrogel formulation may be used to fit optimized rate constants using the model, permitting predictions of mass swelling ratios, compressive modulus, and mass loss profiles at long time scales (i.e., weeks to months). Moreover, the incorporation of these model features will improve the model's ability to accurately predict degradation timescales observed in NorHA_{CA} hydrogels.

Lastly, growth factors such as TGF-B3 may eventually be incorporated into printed NorHA_{CA} scaffolds, allowing for sustained delivery to MSCs after microfracture to improve chondrogenesis and ECM formation.^{59,60} Importantly, the developed model framework in

this study may be adapted to model the kinetics of TGF-B3 release from the gel,⁶¹ and a three-dimensional stochastic model may be used to account for random variations in payload diffusivity due to network architecture and heterogenous mesh sizes if needed.⁶²

7.5 REFERENCES

1. Wu, Y. *et al.* Three-Dimensional Bioprinting of Articular Cartilage: A Systematic Review. *Cartilage* **12**, 76–92 (2021).
2. Benthien, J. P. & Behrens, P. Autologous matrix-induced chondrogenesis (AMIC): Combining microfracturing and a collagen I/III matrix for articular cartilage resurfacing. *Cartilage* **1**, 65–68 (2010).
3. Gao, L., Orth, P., Cucchiari, M. & Madry, H. Autologous Matrix-Induced Chondrogenesis: A Systematic Review of the Clinical Evidence. *Am. J. Sports Med.* **47**, 222–231 (2019).
4. Schiavone Panni, A., Cerciello, S. & Vasso, M. The management of knee cartilage defects with modified amic technique: preliminary results. *Int. J. Immunopathol. Pharmacol.* **24**, 149–152 (2011).
5. Lee, Y. H. D., Suzer, F. & Thermann, H. Autologous Matrix-Induced Chondrogenesis in the Knee: A Review. *Cartilage* **5**, 145–153 (2014).
6. Volz, M., Schaumburger, J., Frick, H., Grifka, J. & Anders, S. A randomized controlled trial demonstrating sustained benefit of Autologous Matrix-Induced Chondrogenesis over microfracture at five years. *Int. Orthop.* **41**, 797–804 (2017).
7. Vernerey, F. J. & Bryant, S. The role of percolation in hydrogel-based tissue engineering and bioprinting. *Curr. Opin. Biomed. Eng.* **15**, 68–74 (2020).
8. Loebel, C., Mauck, R. L. & Burdick, J. A. Local nascent protein deposition and remodelling guide mesenchymal stromal cell mechanosensing and fate in three-dimensional hydrogels. *Nat. Mater.* (2019). doi:10.1038/s41563-019-0307-6

9. Hunziker, E. B. Biologic Repair of Articular Cartilage. *Clin. Orthop. Relat. Res.* **367**, S135–S146 (1999).
10. Kim, I. L. *et al.* Fibrous Scaffolds with Varied Fiber Chemistry and Growth Factor Delivery Promote Repair in a Porcine Cartilage Defect Model. *Tissue Eng. - Part A* **21**, 2680–2690 (2015).
11. Martin, A. R. *et al.* Nanofibrous hyaluronic acid scaffolds delivering TGF- β 3 and SDF-1 α for articular cartilage repair in a large animal model. *Acta Biomater.* **126**, 170–182 (2021).
12. Huddleston, H. P., Haunschild, E. D., Wong, S. E., Cole, B. J. & Yanke, A. B. Microfracture Augmentation Options for Cartilage Repair. in *Cartilage Injury of the Knee: State-of-the-Art Treatment and Controversies* (eds. Krych, A. J. *et al.*) 205–217 (Springer International Publishing, 2021). doi:10.1007/978-3-030-78051-7_18
13. Zhou, Y., Qin, R., Chen, T., Zhang, K. & Gui, J. 3D bioprinting modified autologous matrix-induced chondrogenesis (AMIC) technique for repair of cartilage defects. *Mater. Des.* **203**, 109621 (2021).
14. Cesaretti, M., Luppi, E., Maccari, F. & Volpi, N. A 96-well assay for uronic acid carbazole reaction. *Carbohydr. Polym.* **54**, 59–61 (2003).
15. Burdick, J. A., Chung, C., Jia, X., Randolph, M. A. & Langer, R. Controlled degradation and mechanical behavior of photopolymerized hyaluronic acid networks. *Biomacromolecules* **6**, 386–391 (2005).
16. Jahanmir, G., Abdekhodaie, M. J. & Chau, Y. Stochastic Modeling of Degradation Behavior of Hydrogels. *Macromolecules* **51**, 3941–3952 (2018).
17. Flory, P. J. *Principles of Polymer Chemistry*. (Cornell University Press Ithaca, NY, 1953).
18. Göpferich, A. & Langer, R. Modeling of Polymer Erosion. *Macromolecules* **26**,

- 4105–4112 (1993).
19. Bray, J. C. & Merrill, E. W. Poly(vinyl alcohol) hydrogels. Formation by electron beam irradiation of aqueous solutions and subsequent crystallization. *J. Appl. Polym. Sci.* **17**, 3779–3794 (1973).
 20. Leach, J. B., Bivens, K. A., Patrick, C. W. & Schmidt, C. E. Photocrosslinked hyaluronic acid hydrogels: Natural, biodegradable tissue engineering scaffolds. *Biotechnol. Bioeng.* **82**, 578–589 (2003).
 21. Gómez-Alejandre, S., Sánchez de la Blanca, E., Abradelo de Usera, C., Rey-Stolle, M. F. & Hernández-Fuentes, I. Partial specific volume of hyaluronic acid in different media and conditions. *Int. J. Biol. Macromol.* **27**, 287–290 (2000).
 22. Macosko, C. W. & Miller, D. R. A New Derivation of Average Molecular Weights of Nonlinear Polymers. *Macromolecules* **9**, 199–206 (1976).
 23. Miller, D. R. & Macosko, C. W. A New Derivation of Post Gel Properties of Network Polymers. *Macromolecules* **9**, 206–211 (1976).
 24. Metters, A. T., Bowman, C. N. & Anseth, K. S. A statistical kinetic model for the bulk degradation of PLA-b-PEG-b-PLA hydrogel networks: Incorporating network non-idealities. *J. Phys. Chem. B* **104**, 7043–7049 (2000).
 25. Rydholm, A. E., Reddy, S. K., Anseth, K. S. & Bowman, C. N. Development and Characterization of Degradable Thiol-Allyl Ether Photopolymers. *Polymer (Guildf)*. **13**, 4589–4600 (2007).
 26. Vega, S. L. *et al.* Combinatorial hydrogels with biochemical gradients for screening 3D cellular microenvironments. *Nat. Commun.* **9**, 614 (2018).
 27. Sridhar, B. V. *et al.* Development of a cellularly degradable PEG hydrogel to promote articular cartilage extracellular matrix deposition. *Adv. Healthc. Mater.* **4**, 702–713 (2015).

28. Burdick, J. A. & Murphy, W. L. Moving from static to dynamic complexity in hydrogel design. *Nat. Commun.* **3**, (2012).
29. Ifkovits, J. L. & Burdick, J. A. Review: Photopolymerizable and degradable biomaterials for tissue engineering applications. *Tissue Eng.* **13**, 2369–2385 (2007).
30. Chung, C., Beecham, M., Mauck, R. L. & Burdick, J. A. The Influence of Degradation Characteristics of Hyaluronic Acid Hydrogels on In Vitro Neocartilage Formation by Mesenchymal Stem Cells. *Biomaterials* **30**, 4287–4296 (2009).
31. Sahoo, S., Chung, C., Khetan, S. & Burdick, J. A. Hydrolytically degradable hyaluronic acid hydrogels with controlled temporal structures. *Biomacromolecules* **9**, 1088–1092 (2008).
32. Muir, V. G. & Burdick, J. A. Chemically Modified Biopolymers for the Formation of Biomedical Hydrogels. *Chem. Rev.* **121**, 10908–10949 (2021).
33. Perera, M. M. & Ayres, N. Gelatin based dynamic hydrogels via thiol-norbornene reactions. *Polym. Chem.* **8**, 6741–6749 (2017).
34. Muñoz, Z., Shih, H. & Lin, C. C. Gelatin hydrogels formed by orthogonal thiol-norbornene photochemistry for cell encapsulation. *Biomater. Sci.* **2**, 1063–1072 (2014).
35. McOscar, T. V. C. & Gramlich, W. M. Hydrogels from norbornene-functionalized carboxymethyl cellulose using a UV-initiated thiol-ene click reaction. *Cellulose* **25**, 6531–6545 (2018).
36. Lin, F. Y. & Lin, C. C. Facile Synthesis of Rapidly Degrading PEG-Based Thiol-Norbornene Hydrogels. *ACS Macro Lett.* **10**, 341–345 (2021).
37. Schneider, M. C., Lalitha Sridhar, S., Vernerey, F. J. & Bryant, S. J. Spatiotemporal neocartilage growth in matrix-metalloproteinase-sensitive

- poly(ethylene glycol) hydrogels under dynamic compressive loading: An experimental and computational approach. *J. Mater. Chem. B* **8**, 2775–2791 (2020).
38. Metters, A. T., Anseth, K. S. & Bowman, C. N. A statistical kinetic model for the bulk degradation of PLA-b-PEG-b-PLA hydrogel networks: Incorporating network non-idealities. *J. Phys. Chem. B* **105**, 8069–8076 (2001).
 39. Martens, P., Metters, A. T., Anseth, K. S. & Bowman, C. N. A generalized bulk-degradation model for hydrogel networks formed from multivinyl cross-linking molecules. *J. Phys. Chem. B* **105**, 5131–5138 (2001).
 40. Shih, H. & Lin, C. C. Cross-linking and degradation of step-growth hydrogels formed by thiol-ene photoclick chemistry. *Biomacromolecules* **13**, 2003–2012 (2012).
 41. Metters, A. & Hubbell, J. Network formation and degradation behavior of hydrogels formed by Michael-type addition reactions. *Biomacromolecules* **6**, 290–301 (2005).
 42. Reddy, S. K., Anseth, K. S. & Bowman, C. N. Modeling of network degradation in mixed step-chain growth polymerizations. *Polymer (Guildf)*. **46**, 4212–4222 (2005).
 43. Ng, W. L. *et al.* Vat polymerization-based bioprinting - process, materials, applications and regulatory challenges. *Biofabrication* **12**, (2020).
 44. Chartrain, N. A., Williams, C. B. & Whittington, A. R. A review on fabricating tissue scaffolds using vat photopolymerization. *Acta Biomater.* **74**, 90–111 (2018).
 45. Sun, A. X., Lin, H., Beck, A. M., Kilroy, E. J. & Tuan, R. S. Projection Stereolithographic Fabrication of Human Adipose Stem Cell-incorporated Biodegradable Scaffolds for Cartilage Tissue Engineering. *Front. Bioeng.*

- Biotechnol.* **3**, 1–9 (2015).
46. Lim, K. S. *et al.* Bio-resin for high resolution lithography-based biofabrication of complex cell-laden constructs. *Biofabrication* **10**, (2018).
 47. Shie, M. Y. *et al.* 3D printing of cytocompatible water-based light-cured polyurethane with hyaluronic acid for cartilage tissue engineering applications. *Materials (Basel)*. **10**, (2017).
 48. Kim, S. H. *et al.* Precisely printable and biocompatible silk fibroin bioink for digital light processing 3D printing. *Nat. Commun.* **9**, 1–14 (2018).
 49. Muralidharan, A., McLeod, R. R. & Bryant, S. J. Hydrolytically Degradable Poly(β -amino ester) Resins with Tunable Degradation for 3D Printing by Projection Micro-Stereolithography. *Adv. Funct. Mater.* (2021). doi:10.1002/adfm.202106509
 50. Aisenbrey, E. A. *et al.* A Stereolithography-Based 3D Printed Hybrid Scaffold for In Situ Cartilage Defect Repair. *Macromol. Biosci.* **18**, 1–8 (2018).
 51. Schoonraad, S. A. *et al.* Biomimetic and mechanically supportive 3D printed scaffolds for cartilage and osteochondral tissue engineering using photopolymers and digital light processing. *Biofabrication* **13**, 044106 (2021).
 52. Li, Y. *et al.* Theoretical prediction and experimental validation of the digital light processing (DLP) working curve for photocurable materials. *Addit. Manuf.* **37**, 101716 (2021).
 53. Lim, K. S. *et al.* Fundamentals and Applications of Photo-Cross-Linking in Bioprinting. *Chem. Rev.* **120**, 10662–10694 (2020).
 54. Grigoryan, B. *et al.* Multivascular networks and functional intravascular topologies within biocompatible hydrogels. *Science (80-.)*. **364**, 458–464 (2019).
 55. Guo, K. *et al.* Collagen-Based Thiol-Norbornene Photoclick Bio-Ink with Excellent Bioactivity and Printability. *ACS Appl. Mater. Interfaces* **13**, 7037–7050 (2021).

56. Rizzo, R., Ruetsche, D., Liu, H. & Zenobi-Wong, M. Optimized Photoclick (Bio)Resins for Fast Volumetric Bioprinting. *Adv. Mater.* (2021).
doi:10.1002/adma.202102900
57. Kwon, M. Y. *et al.* Influence of hyaluronic acid modification on CD44 binding towards the design of hydrogel biomaterials. *Biomaterials* **222**, (2019).
58. De Keer, L., Van Steenberge, P. H. M., Reyniers, M. F. & D'hooge, D. R. Going beyond the carothers, flory and stockmayer equation by including cyclization reactions and mobility constraints. *Polymers (Basel)*. **13**, 1–26 (2021).
59. Kim, M., Erickson, I. E., Choudhury, M., Pleshko, N. & Mauck, R. L. Transient exposure to TGF- β 3 improves the functional chondrogenesis of MSC-laden hyaluronic acid hydrogels. *J. Mech. Behav. Biomed. Mater.* **11**, 92–101 (2012).
60. Martín, A. R., Patel, J. M., Zlotnick, H. M., Carey, J. L. & Mauck, R. L. Emerging therapies for cartilage regeneration in currently excluded 'red knee' populations. *npj Regen. Med.* **4**, (2019).
61. Lin, C. C. & Metters, A. T. Hydrogels in controlled release formulations: Network design and mathematical modeling. *Adv. Drug Deliv. Rev.* **58**, 1379–1408 (2006).
62. Jahanmir, G., Lau, C. M. L., Abdekhodaie, M. J. & Chau, Y. Dual-Diffusivity Stochastic Model for Macromolecule Release from a Hydrogel. *ACS Appl. Bio Mater.* **3**, 4208–4219 (2020).

CHAPTER 8: CONCLUSIONS, LIMITATIONS, AND FUTURE DIRECTIONS

8.1 OVERVIEW

The overarching goal of the work described in this dissertation was to employ light-based biofabrication technologies to engineer hydrogels composed of hyaluronic acid for the repair of articular focal defects. Specifically, extrusion bioprinting, melt-electrowriting, and digital light processing were leveraged to design three complex and distinct scaffolds, each of which aimed to improve upon the limitations of scaffolds currently employed in the clinic for the treatment of cartilage defects. (e.g., collagen scaffolds). The design and fabrication of these respective scaffolds was informed by the fundamental theories of photocrosslinking described in Chapter 3, such that HA hydrogel properties were controlled through understanding of thiol-ene reaction behavior and the applied biofabrication technology. Norbornene-modified hyaluronic acid (NorHA) was used in the development of each of these scaffolds, since the use of step-growth hydrogels permits the fabrication of hydrogels with well-defined crosslink densities and predictable reaction behavior.

First, a novel *in situ* crosslinking technique for the 3D printing of living MSCs in HA hydrogels was characterized to demonstrate the ability to create large-scale neocartilage constructs with anatomical features. Many implants that are clinically employed in the repair of articular focal defects fail due to poor integration with the surrounding tissue, whereas this bioprinting technique enabled the formation of implants with patient-specific geometries to improve defect filling. Thereafter, the influence of HA hydrogel crosslink density on encapsulated MSC chondrogenesis and ECM production was investigated to identify HA hydrogel formulations that best support the formation of cartilage. MSC-laden hydrogels that are soft and loosely crosslinked are shown to form dense neocartilage *in vitro*, but their low initial mechanical properties preclude their use

in vivo. To address this, polycaprolactone (PCL)-based microfiber meshes were fabricated via melt electrowriting to mechanically reinforce soft hydrogels without compromising their chondrogenic potential. Importantly, composites of PCL meshes and HA hydrogels resulted in the formation of cartilage with mechanical properties approaching those of native tissues. Therefore, composites were evaluated for their ability to repair focal defect lesions in a porcine model of cartilage damage, and their performance was compared to microfracture. Implanted composites supported the formation of repair cartilage in some animals, suggesting that this repair approach may potentially be employed with additional refinement. Finally, novel HA hydrogels with tunable degradability were synthesized and 3D printed via digital light processing for use as scaffolds in autologous matrix induced chondrogenesis (AMIC), a clinical procedure that combines microfracture surgery with scaffolds containing cellular signals to improve the quality of tissue formed by recruited MSCs. The ability to fabricate macroporous implants amenable to infilling with marrow during AMIC is shown, and a computational model is developed to characterize how the hydrogel formulation may be tuned to match the rates of implant degradation and neotissue formation.

8.2 SPECIFIC AIM 1

Employ an *in situ* crosslinking bioprinting technique to fabricate MSC-laden HA constructs for the formation of cartilage.

Conclusions

Extrusion bioprinting is a promising approach for the repair of cartilage tissue after damage due to injury or disease; however, the design of 3D printed scaffolds has

been limited by the availability of bioinks with requisite printability, cytocompatibility, and bioactivity.¹ In Aim 1, an approach termed *in situ* crosslinking was developed and characterized to permit the printing of non-viscous, photocrosslinkable bioinks via the direct-curing of the bioink with light through a photopermeable capillary prior to deposition. NorHA macromer was used as a representative bioink to demonstrate how thiol-ene crosslinking kinetics and the printing parameters (e.g., capillary length, flow rate, light intensity) could be tuned to identify printing conditions that were optimal for the ink. The printing process was cytocompatible, with high cell viability and homogenous distribution of mesenchymal stromal cells (MSCs) observed throughout printed constructs. Over 56 days of culture in chondrogenic media, printed constructs increased in compressive moduli, biochemical content (i.e., sulfated glycosaminoglycans, collagen), and histological staining of matrix associated with cartilage tissue. This generalizable printing approach may be used towards the repair of focal defects in articular cartilage or broadly towards widespread biomedical applications across a range of photocrosslinkable bioinks that can now be printed.

Limitations and Future Directions

Although the developed *in situ* crosslinking technique was used to successfully print large tissue constructs with centimeter-scale dimensions, large filament diameters were required to do so; otherwise, the required print times would have been prohibitively long, and the viability of cells would have been compromised. In addition, prolonged print times could potentially lead to cell settling prior to the *in situ* crosslinking of filaments in the print head, which would lead to the heterogeneous printing of cells within a construct.

In most cases, the developed photorheological models were able to identify appropriate printing conditions for a given ink formulation; however, the permissible

printing regime for some bioinks is inherently narrow, limiting the relative flexibility of certain printing setups. To this end, even small perturbations to the steady state flow of bioink during printing may lead to extents of crosslinking within the photopermeable capillary that either impede the continuous extrusion of filaments or result in heterogeneously crosslinked filaments. Future studies may therefore explore the use of photoabsorbers to modulate crosslinking kinetics in a manner similar to their use in DLP.²

Conversely, printed filaments must also undergo sufficient crosslinking to achieve stable filaments. While NorHA hydrogel formulations with compressive modulus of ~6 kPa were consistently and reliably printed with the *in situ* crosslinking technique, softer hydrogel formulations (compressive modulus of ~2 kPa) that were identified in Aim 2 as better alternatives for the formation of neocartilage could not be easily printed.

8.3 SPECIFIC AIM 2

Fabricate composites of soft hydrogels with supporting melt electrowritten polycaprolactone and evaluate their potential for neocartilage formation.

Conclusions

NorHA hydrogels were shown to support MSC chondrogenesis and neocartilage formation *in vitro* in Aim 1. However, in Aim 2 a range of hydrogel formulations were investigated to elucidate the influence of NorHA crosslink density on the formation of repair cartilage. In keeping with previously reported findings, it was shown that NorHA hydrogel networks with lower crosslink densities are generally more amenable to the deposition and distribution of nascent matrix by encapsulated MSCs.^{3,4} However, the low initial mechanics of these hydrogels rendered them ill-suited for implantation into a

cartilage defect, where complex and dynamic loading forces are present. Therefore, melt-electrowriting was employed as a method to mechanically reinforce soft NorHA hydrogels. MEW-NorHA composites were engineered with high compressive properties, which significantly increased with the encapsulation and chondrogenic culture of MSCs. Moreover, MSC-laden MEW-NorHA composites demonstrated the capacity to integrate with native cartilage tissue *ex vivo*.

Limitations and Future Directions

While previous examples of MEW-reinforced hydrogels involve the molding of MEW meshes within hydrogels,⁵ MEW-NorHA composites were fabricated via infilling of hydrogel precursor into the PCL mesh, allowing for the potential fabrication of composites with irregular geometries or topographies. For instance, this may be of interest in potential applications where composites are prepared intraoperatively (with or without cells) during the surgical repair of cartilage, as the MEW mesh may be processed into a shape of interest (i.e., a patient-specific defect shape) and hydrogel precursor may then be crosslinked *in situ* within the mesh. However, the decision to process composites in this manner necessitates the use of excess amounts of macromer and cells (relative to the amount needed to form a casted composite of the same volume). For example, in this study ~100 μL of macromer suspension containing MSCs was used to fill a single MEW mesh (~15 μL), which is important to consider if these composites are to be scaled toward the repair of large cartilage defects (4 cm^2). Further, the addition of hydrogel precursor into the MEW mesh does not always yield a perfectly homogenous construct, as the presence of misaligned MEW fibers may give rise to imperfections in hydrogel filling. In instances where this occurs, additional macromer and cells are required.

Fiber misalignment within fabricated MEW meshes is typically observed as the fiber density and/or mesh thickness is increased (e.g., 200 μm interfiber spacing in box-structure meshes, and heights greater than 1mm).⁶ However, thicker MEW meshes with precisely patterned architectures could yield composites with even higher compressive properties, and more importantly, enable improved integration and/or filling of full thickness defects in instances where the defect thickness is greater than 1 mm.

Conventional MEW systems employ a fixed voltage and collector distance, such that over time as the height of the mesh increases, excessive charge accumulates within deposited fibers, resulting in mesh distortion and inaccurate fiber deposition.⁶ However, if the electrostatic force is maintained throughout the print, the accumulation of this excess charge may be circumvented, allowing for the fabrication of thick MEW scaffolds (e.g., 7 mm).⁷ Thus, future improvements to MEW hardware may facilitate the generation of dynamic electric fields through the digital control of the applied voltage and the collector distance, allowing for the fabrication of meshes with improved fiber alignment at higher thicknesses.⁶

Although not investigated in these studies, past examples of MEW-reinforced hydrogels have also demonstrated poor mechanical properties under dynamic loading conditions.⁸ Towards eventually employing these composites for the repair of focal defects at load bearing sites, alternate MEW structures and combinations therein should be explored with NorHA hydrogels to elucidate if the mechanical properties can be further improved.⁸⁹ Alternatively, combinations of MEW meshes and interpenetrating network hydrogels, which typically possess mechanical properties that significantly supersede their single hydrogel network counterparts, may be explored if tough IPNs with suitable chondrogenic potential can be achieved.¹⁰

8.4 SPECIFIC AIM 3

Evaluate implantation of MEW-NorHA composites to facilitate cartilage repair in a porcine model of articular cartilage damage

Conclusions

In Aim 3, MEW-NorHA composites were investigated in a porcine model of cartilage damage to evaluate their ability to promote cartilage repair *in vivo*. In some animals, composites successfully facilitated the formation of repair cartilage over 3 months. However, observed outcomes were highly variable and dependent on the method used for composite fixation. Qualitative assessment of defects via arthroscopic, gross, and histology images three months after performed surgeries suggests that fibrin glue was better suited than resorbable pins for the fixation of MEW-NorHA composites in small defects, as the resorbable pins used accounted for a significant fraction of the total defect area. Safranin O/Fast Green staining also revealed that the repair cartilage formed in defects was not hyaline-like, suggesting that defects may have filled with tissue resembling fibrocartilage. These results were corroborated by indentation testing. While implanted composites exhibited significant increases in compressive modulus after implantation, repair cartilage across all the experimental groups was inferior to healthy cartilage controls.

Limitations and Future Directions

While large animal models are necessary to evaluate the efficacy of novel cartilage repair strategies,¹¹ careful consideration must be given to the selection of appropriate models and timepoints. As discussed in Chapter 6, the composites' true

ability to facilitate cartilage repair in focal lesions cannot yet be fully assessed given the significant variability that was observed across outcomes. In addition, appreciable defect fill and tissue repair was observed in both defects treated with microfracture and empty defect controls. These outcomes suggest that the cartilage defect size employed may have been too small to reliably compare the performance of composites and microfracture; alternatively, longer time points may have better illustrated any differences between these repair strategies. Moreover, both of the fixation methods investigated in this study demonstrated varied results, highlighting the demand for improved fixation techniques.¹²⁻¹⁴

Future studies may employ hydrogels with tissue adhesiveness towards ensuring successful composite retention and integration with the surrounding tissue.¹⁵ For example, HA has previously been modified with gallol moieties via EDC-coupling for use as a tissue adhesive biomaterial ink.¹⁶ A similar approach could be readily employed to adorn NorHA with adhesive moieties. Towards improving the quality of neocartilage formed in composites prior to implantation, the chondrogenic potential of adult pMSCs may be improved via coculture with chondrocytes or the presentation of N-cadherin mimetic peptides (HAVDI) during culture.^{17,18}

8.5 SPECIFIC AIM 4

Engineer hydrolytically degradable, thiol-ene step growth hydrogels amenable to digital light processing (DLP) for cartilage repair applications.

Conclusions

In Aim 4, hydrolytically degradable NorHA_{CA} was synthesized for use as a DLP resin toward the development of scaffolds for autologous matrix induced chondrogenesis

(AMIC). Importantly NorHA_{CA} hydrogels were engineered with tunable mechanical properties and a range of degradation behaviors, allowing for the rational design of a hydrogel that can promote cartilage formation endogenously (via combination with microfracture). A computational model was also developed using Monte Carlo simulations and gelation theory to simulate the stochastic process of crosslink hydrolysis in NorHA_{CA} hydrogels. As a result, empirical hydrogel degradation behavior could be predicted, establishing a framework that may be potentially used to predict and screen the degradation behavior of various NorHA_{CA} hydrogel formulations. Finally, NorHA_{CA} hydrogels were successfully processed via DLP to construct macroporous, degradable scaffolds with user-defined geometries. Ultimately, the development of this new, modular hydrogel system may inform the next generation of degradable and cell-instructive scaffolds used in AMIC.

Limitations and Future Directions

NorHA_{CA} hydrogel formulations investigated in this aim exhibit relatively rapid degradation times; while this could be beneficial for the rapid release and transient exposure of MSCs to TGF- β 3,¹⁹ generally much longer degradation time scales are required to ensure the mechanical integrity of blood clots formed in AMIC is retained long enough for the formation of neotissue to begin. To this point, the *in vitro* culture of MSC-laden hydrogels in Specific Aims 1-3 suggests that cells require on the order of 1 month to form stable, continuous ECM toward the formation of neocartilage. Ongoing work is focused on the characterization of high modification NorHA_{CA} and copolymer formulations incorporating non-degradable NorHA macromer. It is expected that these alternatives may yield hydrogels that degrade over significantly longer timescales (more

than two weeks) than what has been observed for either 14% modified or 40% modified NorHA_{CA} (less than two weeks).

The engineered NorHA_{CA} hydrogels exhibit rapid swelling with the hydrolysis of crosslinks, such that the initial print resolution of hydrogels fabricated via DLP is quickly lost; this is especially true for macroporous constructs (as opposed to bulk hydrogel constructs) in which the surface area for mass contact is significantly increased.

Interestingly, the developed copolymers composed of degradable and non-degradable macromers exhibited prolonged degradation times and attenuated swelling over time when compared to NorHA_{CA} hydrogels alone. Future work will investigate the DLP of these copolymers to determine if they may achieve the requisite balance of printability, degradability, and swelling required to ensure successful integration with bone marrow during AMIC.

If both increased degrees of modification and/or the use of copolymers results in degradation times that are still too short, modification of the second carboxylic acid group on the pendant norbornene group may be explored to impede hydrolysis, either through changes to the functional group's hydrophobicity or overall steric hindrance.

The developed Monte Carlo model may be improved to account for several non-idealities, which better approximate the true nature of hydrogel crosslinking and degradation over time. These include relative changes to norbornene reactivities and rates of ester hydrolysis due to intermolecular interactions and diffusion limitations within the crosslinked network.²⁰ In addition, random distributions of polymer chain lengths and degrees of modification will be incorporated into the model to better capture the stochastic nature of NorHA_{CA} macromer synthesis prior to hydrogel formation. Since the goal for this model is to ultimately provide predictive capabilities toward screening prospective

NorHA_{CA} formulations for AMIC, future work should validate the predictive capabilities of the model for polymer species with long degradation times.

8.6 OVERALL SUMMARY

This dissertation work provides an instructional overview of how biomaterials, biofabrication techniques, and tissue engineering may be combined to inform and develop future strategies for cartilage repair, and more broadly, for regenerative medicine. The use of NorHA hydrogels for cell-based therapies was systematically investigated through a series of *in vitro*, *ex vivo*, and *in vivo* studies, providing insights on how engineered biomaterials may be used to elicit therapeutic outcomes. In addition, new biomaterials were synthesized and characterized with the goal of instructing cells behaviors toward guiding the formation of new tissues.

8.7 REFERENCES

1. Kyle, S., Jessop, Z. M., Al-Sabah, A. & Whitaker, I. S. 'Printability' of Candidate Biomaterials for Extrusion Based 3D Printing: State-of-the-Art'. *Adv. Healthc. Mater.* **6**, 2017 (2017).
2. Ng, W. L. *et al.* Vat polymerization-based bioprinting - process, materials, applications and regulatory challenges. *Biofabrication* **12**, (2020).
3. Erickson, I. E. *et al.* Macromer density influences mesenchymal stem cell chondrogenesis and maturation in photocrosslinked hyaluronic acid hydrogels. *Osteoarthr. Cartil.* **17**, 1639–1648 (2009).
4. Loebel, C. *et al.* Metabolic Labeling to Probe the Spatiotemporal

- Accumulation of Matrix at the Chondrocyte-Hydrogel Interface. *Adv. Healthc. Mater. In Review*, 1–29 (2019).
5. Visser, J. *et al.* Reinforcement of hydrogels using three-dimensionally printed microfibrils. *Nat. Commun.* **6**, 6933 (2015).
 6. Kade, J. C. & Dalton, P. D. Polymers for Melt Electrowriting. *Adv. Healthc. Mater.* **10**, (2021).
 7. Wunner, F. M. *et al.* Melt Electrospinning Writing of Highly Ordered Large Volume Scaffold Architectures. *Adv. Mater.* **30**, (2018).
 8. Castilho, M., Mouser, V., Chen, M., Malda, J. & Ito, K. Bi-layered microfibre reinforced hydrogels for articular cartilage regeneration. *Acta Biomater.* **95**, 297–306 (2019).
 9. de Ruijter, M. *et al.* Out-of-Plane 3D-Printed Microfibers Improve the Shear Properties of Hydrogel Composites. *Small* **14**, 1–6 (2018).
 10. Dhand, A. P., Galarraga, J. H. & Burdick, J. A. Enhancing Biopolymer Hydrogel Functionality through Interpenetrating Networks. *Trends Biotechnol.* **39**, 519–538 (2021).
 11. McIlwraith, C. W. & Frisbie, D. D. Animal models for cartilage regeneration. *Eur. Cells Mater.* **20**, 22 (2010).
 12. Patel, J. M. *et al.* Resorbable Pins to Enhance Scaffold Retention in a Porcine Chondral Defect Model. *Cartilage* (2020).
doi:10.1177/1947603520962568
 13. Efe, T. *et al.* Fibrin glue does not improve the fixation of press-fitted cell-free collagen gel plugs in an ex vivo cartilage repair model. *Knee Surgery,*

- Sport. Traumatol. Arthrosc.* **20**, 210–215 (2012).
14. Friedman, J. M. *et al.* Comparison of Fixation Techniques of 3D-Woven Poly(ϵ -Caprolactone) Scaffolds for Cartilage Repair in a Weightbearing Porcine Large Animal Model. *Cartilage* **9**, 428–437 (2018).
 15. Zhang, X., Jiang, Y., Han, L. & Lu, X. Biodegradable polymer hydrogel-based tissue adhesives: A review. *Biosurface and Biotribology* **7**, 163–179 (2021).
 16. Shin, M., Galarraga, J. H., Kwon, M. Y., Lee, H. & Burdick, J. A. Gallol-derived ECM-mimetic adhesive bioinks exhibiting temporal shear-thinning and stabilization behavior. *Acta Biomater.* (2018).
doi:10.1016/j.actbio.2018.10.028
 17. Kim, M., Steinberg, D. R., Burdick, J. A. & Mauck, R. L. Extracellular vesicles mediate improved functional outcomes in engineered cartilage produced from MSC/chondrocyte cocultures. *Proc. Natl. Acad. Sci. U. S. A.* **116**, 1569–1578 (2019).
 18. Vega, S. L. *et al.* Combinatorial hydrogels with biochemical gradients for screening 3D cellular microenvironments. *Nat. Commun.* **9**, 614 (2018).
 19. Kim, M., Erickson, I. E., Choudhury, M., Pleshko, N. & Mauck, R. L. Transient exposure to TGF- β 3 improves the functional chondrogenesis of MSC-laden hyaluronic acid hydrogels. *J. Mech. Behav. Biomed. Mater.* **11**, 92–101 (2012).
 20. De Keer, L., Van Steenberge, P. H. M., Reyniers, M. F. & D'hooge, D. R. Going beyond the carothers, flory and stockmayer equation by including

cyclization reactions and mobility constraints. *Polymers (Basel)*. **13**, 1–26 (2021).